

# **INTER-SCALE ENERGY TRANSFER IN TURBULENT PREMIXED COMBUSTION**

A Dissertation  
Presented to  
The Academic Faculty

By

Askar Kazbekov

In Partial Fulfillment  
of the Requirements for the Degree  
Doctor of Philosophy in the  
School of Aerospace Engineering

Georgia Institute of Technology

December 2022

© Askar Kazbekov

# **INTER-SCALE ENERGY TRANSFER IN TURBULENT PREMIXED COMBUSTION**

Thesis committee:

Dr. Adam M. Steinberg, Advisor  
Aerospace Engineering  
*Georgia Institute of Technology*

Dr. Jerry M. Seitzman  
Aerospace Engineering  
*Georgia Institute of Technology*

Dr. Timothy C. Lieuwen  
Aerospace Engineering  
*Georgia Institute of Technology*

Dr. Ellen Yi Chen Mazumdar  
Mechanical Engineering  
*Georgia Institute of Technology*

Dr. Joseph Oefelein  
Aerospace Engineering  
*Georgia Institute of Technology*

Date approved: December 5, 2022

## ACKNOWLEDGMENTS

I would like to take a moment and acknowledge the numerous people who have been a part of my graduate school experience. Decision to pursue a Ph.D. in any field is a choice one makes to dedicate multiple years of their life to advancing a state of human knowledge. Having people who support you makes this experience easier and more enjoyable. My graduate research experience began 6 years ago at the University of Toronto and ended here at Georgia Tech. In these years, I have been given an opportunity to dive deeply into experimental research, meet people from all over the world, and learn from the world-class scholars. It has truly been a pleasure and honour to be a part of the academic community. Consequently, I wish to acknowledge all of the folks who have made this work possible.

I would like to first express my deepest gratitude to my advisor and mentor, Professor Adam M. Steinberg. I first started working with Prof. Steinberg in my senior year of undergraduate studies at the University of Toronto. He has served as my undergraduate thesis advisor and he provided me with an opportunity to perform real-life research in the field of aerospace - a goal I had since finishing high school. Suffice to say, the mentorship he offered and the cutting-edge research performed in his group has convinced me to pursue further graduate work under his supervision, both at the University of Toronto and Georgia Tech. I want to thank Professor Steinberg for giving me an opportunity to work on this project, providing constant support and guidance, offering a plethora of ideas and solutions when help was needed, and pushing me to do my best. Moreover, I also want to express my gratitude for exposing me to projects beyond the scope of my research. While this seemed like extra work at the time, I appreciate the experience and I value all of the knowledge and skills I gained from those projects. Without a doubt, the work presented in this thesis would not have been possible without his valuable guidance and input.

I also want to thank all of the members of my doctoral advisory committee: Prof. Lieuwen, Prof. Oefelein, Prof. Seitzman, and Prof. Mazumdar. All of the members are

leading experts in the fields of combustion, fluid dynamics, numerical tools, and diagnostics. I would like to truly express my gratitude to all of the members for taking time out of their busy schedule to review my proposal and thesis, attend the defense, and providing excellent feedback that resulted in a much better research work. I have also taken classes with Prof. Lieuwen and Prof. Seitzman, in subjects that have direct relevance to my research and of personal interest. Their knowledge and teaching approach have definitely made me learn the concepts from a new angle and expanded my well of knowledge in the fields of combustion and aerospace propulsion.

Next, I want to acknowledge the supporters of my research. This project was supported by two organizations: the US Air Force Office of Scientific Research (AFOSR) and Natural Sciences and Engineering Research Council of Canada (NSERC). AFOSR has provided the grant funding that has enabled my research for the duration of both my masters and my Ph.D. I would like to offer my gratitude to NSERC who have provided financial support in a form of a postgraduate scholarship that extended to Canadian students studying abroad. Their support was truly invaluable.

Finally, I would like to extend my thanks to many of the awesome lab mates, undergraduate assistants, research engineers, and post-doctoral fellows who have been a part of my journey. Firstly, special thanks goes to Qiang, who has taught me most of what I needed to know about laser diagnostics and running experiments in the lab. I have carried that knowledge throughout my research career. Similarly, I want to thanks the folks at UTIAS - Keishi, Ketana, and Rahul for offering a helping hand in the lab, helping me process the data, and teaching me everything I need to know about the laser diagnostics outside my expertise. I also want to extend my special thanks to Ketana for setting an unachievable standard for cleanliness and organization in the workspace. I have tried and miserably failed at meeting that standard in my research.

For my folks at Georgia Tech, and there are many of you, it has been truly a pleasure to work alongside you and being a part of your life. First are my immediate group-mates



- Mitchell, Manya, Sam, Jeremiah, Adhiraj, Cathy, Boni, Jean Luis, Shrey, and Ari. We spent a lot of time together, both in the lab and outside of it. Thank you for offering a lending hand in almost anything I've been involved (from doing experiments to processing data), giving valuable feedback and advice on my work, keeping me sane, and always being there for me. As much as I value your professional and academic support, I also enjoyed our countless break-time trivia and geo-guessing! To the research engineers and post-doctoral fellows - Vedanth, Sam, Subodh, David, and Kris - thank you for your ever-present support and continuous teaching in experimental setup, diagnostics, data analysis, and rig management. To other members of the combustion lab, including but not limited to Dan, Hanna, Connor, Hari Priya, Henderson, Shivam, and Aravind, you have been an integral part of the lab and made the combustion lab as I will remember it. Of course, I must also acknowledge all of the undergraduate research engineers who have helped me along the way - Wyatt, Cathy, Adhiraj, and Andrew; you have made the list of never-ending tasks shorter and helped my research progress much quicker. To the others, whom I may have forgotten to mention, I appreciate your support throughout all of these years.

I want to also extend my gratitude to the folks outside the lab, who has made the previous four years enjoyable, especially my Sunday soccer crew and the Tuesday league team. Specifically, I wish to extend my deepest gratitude to Yura for organizing the Sunday games and always being there first, Hikari for pushing me to always improve, Slava for being an unexpected but much appreciated countryman, and Almambet for supporting me in everything from joining new leagues to helping me fix my car. I am really grateful to have come to know you all and become close friends. It has truly been a pleasure.

Finally, I must express my most profound gratitude to my parents and my sister for providing me with ever-present support and continuous encouragement throughout my years of graduate study. Thank you for being there for me and for going above and beyond when I needed you. I can always rely on you in time of need. This accomplishment would not have been possible without you. Thank you.

## TABLE OF CONTENTS

<b>Acknowledgments</b> . . . . .	iii
<b>List of Tables</b> . . . . .	x
<b>List of Figures</b> . . . . .	xi
<b>Nomenclature</b> . . . . .	.xviii
<b>Summary</b> . . . . .	xxi
<b>Chapter 1: Introduction and Theory</b> . . . . .	1
1.1 Motivation . . . . .	1
1.2 Outline . . . . .	2
1.3 Structure and Dynamics of Turbulence . . . . .	5
1.3.1 Richardson Energy Cascade . . . . .	6
1.3.2 Kolmogorov's Theory . . . . .	8
1.4 Premixed Combustion . . . . .	11
1.4.1 Laminar Flames . . . . .	11
1.4.2 Regime Diagrams . . . . .	13
1.4.3 Properties of Reacting Turbulence . . . . .	16
1.5 SFS modeling in LES . . . . .	18

1.6	Inter-scale Energy Transfer . . . . .	24
1.7	Hypothesis and Objectives . . . . .	29
<b>Chapter 2: Experimental Approach . . . . .</b>		<b>34</b>
2.1	Experimental Configuration . . . . .	35
2.2	Test Conditions . . . . .	39
2.3	Laser Diagnostics . . . . .	42
2.3.1	Tomographic Particle Image Velocimetry . . . . .	43
2.3.2	CH <sub>2</sub> O Planar Laser Induced Fluorescence . . . . .	58
<b>Chapter 3: Analysis Methods . . . . .</b>		<b>67</b>
3.1	Progress variable and density estimation . . . . .	67
3.2	Computation of $\alpha_{\text{sfs}}$ . . . . .	72
3.3	Filtering . . . . .	76
3.4	Identification of coherent structures . . . . .	77
3.5	Data conditioning and convergence . . . . .	82
<b>Chapter 4: Deconvolution . . . . .</b>		<b>86</b>
4.1	Brief Overview of Deconvolution Methods . . . . .	87
4.1.1	Normal and Wiener Deconvolution . . . . .	89
4.1.2	Scale-Similarity (SS) . . . . .	91
4.1.3	Approximate Gaussian Method (AGM) . . . . .	92
4.1.4	Approximate Deconvolution Model (ADM) . . . . .	94
4.1.5	Regularized Deconvolution . . . . .	95

4.2	Test Setup and Data Analysis . . . . .	96
4.2.1	Deconvolution Analysis . . . . .	96
4.2.2	Identification of TPIV Filter . . . . .	98
4.3	Application of Deconvolution Methods on DNS . . . . .	102
4.3.1	Target test filter range . . . . .	106
4.4	Estimation of PIV filter kernel . . . . .	113
<b>Chapter 5: Characterization of the Flow and Flames . . . . .</b>		<b>117</b>
5.1	Characterization of the flow field . . . . .	117
5.2	Characterization of turbulence conditions . . . . .	126
5.3	Determination of fully-resolved cases . . . . .	130
<b>Chapter 6: Inter Scale Energy Transport . . . . .</b>		<b>133</b>
6.1	Instantaneous and mean $\alpha_{\text{sfs}}$ fields . . . . .	133
6.2	$c$ - and $S_{ij}S_{ij}$ - conditioned statistics at $\Delta/\delta_L^0 = 1.5$ . . . . .	140
6.3	Effect of filter size . . . . .	145
6.4	Effect of Coherent Flow Structures . . . . .	149
6.4.1	Instantaneous Data and Conditional Statistics . . . . .	149
6.4.2	Phase-Conditioned Analysis . . . . .	151
6.5	Effects of swirl number, equivalence ratio, jet velocity, and mean pressure gradient . . . . .	155
<b>Chapter 7: Conclusions . . . . .</b>		<b>161</b>
7.1	Future Work . . . . .	167

<b>Appendices</b> . . . . .	170
Appendix A: Swirl Number Calculation for Radial Swirler . . . . .	171
<b>References</b> . . . . .	173

## LIST OF TABLES

2.1	Geometrical parameters of the radial swirlers considered. . . . .	39
2.2	Test conditions, using a methane-air mixture. Shaded cases represent data taken from an earlier experiment. . . . .	41
2.3	Orientations of cameras around the domain of interest. . . . .	47
2.4	Estimated $d_{\text{blur}}$ and DOF for Infinity K2 microscope with CF1/B objective. Values used in computation: $M = 0.8$ , $f = \text{WD} = 388 \text{ mm}$ , $\lambda = 532 \text{ nm}$ , $e = 6.5 \mu\text{m}$ , $n = 1$ . . . . .	49
2.5	Seeding density statistics for case D-E100-S3-U05. . . . .	50
2.6	Summary of final interrogation box sizes and the corresponding vector resolutions. . . . .	58
4.1	Physical model parameters of the highly turbulent premixed methane–air flame simulated in the present study. . . . .	96
5.1	Statistics of swirl number measurements. . . . .	122
5.2	Measured properties of turbulence and mean flow. The cases marked with * are those, for which the high resolution velocity dataset is fully resolved. .	129

## LIST OF FIGURES

1.1	Schematic representation of the turbulent kinetic energy cascade. . . . .	6
1.2	Schematic representation of length scales and ranges in the turbulent kinetic energy cascade. . . . .	10
1.3	Illustration of one-dimensional unstretched laminar premixed flame. . . . .	11
1.4	Regime diagram as proposed by Peters [23] with estimated conditions for various engines. . . . .	14
1.5	Model energy spectrum for homogeneous isotropic turbulence. . . . .	25
2.1	Swirl burner with measurement locations. . . . .	36
2.2	Schematic representation of a swirl stabiled combustor, showing the central and outer recirculation zones (CRZ and ORZ) and the associated pressure gradients [75]. . . . .	37
2.3	Geomerty of three radial swirlers used to vary the swirl number. . . . .	40
2.4	Laser diagnostics for “standard-resolution” velocity measurement. Long-distance microscopes replace TPIV camera lenses in “high-resolution” TPIV configuration. . . . .	43
2.5	The basic principle of PIV [78]. . . . .	44
2.6	Camera orientations with respect to the laser propagation direction. . . . .	47
2.7	Distribution of particle counts per interrogation box from a typical tomographic reconstructed particle field (case D-E100-S3-U05 used). . . . .	50
2.8	Reconstructed z-intensity profile from TPIV tomograms, compared to the beam profiler (case D-E100-S3-U05 used). . . . .	51

2.9	Aggregate of TPIV beam profiles and vertically averaged profiles for individual snapshots. . . . .	52
2.10	Calibration setup of the laser diagnostics. . . . .	55
2.11	Calibration images for TPIV. . . . .	56
2.12	Corrected images from TPIV camera calibration. . . . .	57
2.13	Variation of $\text{CH}_2\text{O}$ mole fraction, temperature-based progress variable, and fluid density in a laminar premixed flame at $\phi = 0.75$ . . . . .	60
2.14	The measured spectra of the 11-band filter designed for imaging formaldehyde, overlaid with the emission spectra of $\text{CH}_2\text{O}$ [99] . . . . .	61
2.15	Schematic representation of laser sheet thickness measurement using knife edge traversal technique. . . . .	62
2.16	The laser power intensity profiles for $\text{CH}_2\text{O}$ PLIF measured at 5 locations. . . . .	63
2.17	Images of the 1951 USAF resolution target in TPIV and $\mu$ -TPIV configurations. . . . .	63
2.18	$\text{CH}_2\text{O}$ PLIF image pre-processing. . . . .	65
3.1	Schematic representation of mapping $\text{CH}_2\text{O}$ to $c$ . . . . .	68
3.2	Illustration of instantaneous progress variable and density computation from planar $\text{CH}_2\text{O}$ distribution. Measurement from Case 1 is shown. Red lines show the boundaries of the two $\text{CH}_2\text{O}$ containing regions. . . . .	69
3.3	$\text{CH}_2\text{O}$ and $\rho$ mapping to $c$ . . . . .	70
3.4	Comparison of the $\alpha_{\text{sfs}}$ computed using different PLIF- $c$ mapping methods; $\Delta/\delta_{\text{L}}^0 = 1.5$ . . . . .	71
3.5	JPDF of $\alpha_{\text{sfs}}$ computed using Equation 3.2 and Equation 3.3 vs. Equation 3.10 for case E085-S1-U15. . . . .	74
3.6	Convergence of doubly-conditioned statistics with $\Delta/\delta_{\text{L}}^0 = 1.5$ for E085-S1-U15. . . . .	75
3.7	Convergence of $\langle \alpha_{\text{sfs}}   c \rangle$ for E085-S1-U15. . . . .	75



3.8	JPDF of $\alpha_{\text{sfs}}$ computed using box filter vs. Gaussian filter for E085-S1-U15.	77
3.9	Joint probability density function of $\hat{n}_z$ and the polar angle $\phi$ of the normal vector in the $x$ - $y$ plane.	79
3.10	Distribution of eigenvalues $\psi_i$ of POD analysis and phase portrait between coefficients of mode 1 and 2 for case E085-S1-U15.	80
3.11	First two spatial POD modes for the reacting flow.	80
3.12	Phase averaged evolution of the dominant coherent vortex $\langle \lambda_{\text{ci}}   \theta_i \rangle$ , with every second phase shown. White dashed curve represents $\langle c   \theta_i \rangle = 0.1$ and 0.9. Solid green curve is an isocontour of $\langle \lambda_{\text{ci}}   \theta_i \rangle = \frac{1}{8} \langle \lambda_{\text{ci}}   \theta_i \rangle_{\text{max}}$ .	82
4.1	Instantaneous snapshot of gas density along the central slice of the DNS volume. The red rectangle represents the region of interest used for deconvolution analysis.	96
4.2	Schematic representation of the DNS grid and the sampling grid in a single dimension for overlaps typically used for TPIV. Grey and green blocks depict the $\Delta$ and $\Delta_T$ filters.	98
4.3	A flowchart for the process to obtain the TPIV filter from an analytical velocity field.	101
4.4	Comparison of deconvolved velocity and estimated $\alpha_{\text{sfs}}$ using four deconvolution methods. Top row: $u$ -velocity; middle row: $\alpha_{\text{sfs}}$ across $\Delta_T$ ; bottom row: joint PDF between $\alpha_{\text{sfs}}$ and $\alpha_{\text{sfs}}^*$ . Left column shows true velocity velocity and $\alpha_{\text{sfs}}$ .	103
4.5	Variation of correlation coefficient between $\alpha_{\text{sfs}}$ and $\alpha_{\text{sfs}}^*$ across $\Delta_T = 14 \text{ vx}$ with filter overlap, size of the measurement filter, and presence of noise for the four deconvolution methods.	105
4.6	Demonstration of double filtering a noisy sine wave using a spatial box filter of width $\Delta = 15$ . Top: original signal (blue circles), filtered signal (red), and doubly filtered signal (black). Bottom: difference between single- and doubly-filtered signal.	107
4.7	Convolution of a box filter $\mathcal{G}$ (red) with a hypothetical TPIV filter $\mathcal{G}_{\text{PIV}}$ (blue) that has a shape of a box (left column), Gaussian (middle column), and sharp spectral cutoff (right column). Black curve shows the result of the convolution $\mathcal{G} * \mathcal{G}_{\text{PIV}}$ .	109

4.8	Trends in doubly-filtered convolution kernel. . . . .	110
4.9	Comparison of filtered velocity fields and $\alpha_{\text{sfs}}$ across $\Delta_T$ with estimates obtained by filtering the results twice. Here, both $\Delta_T$ and $\Delta$ are box filters. .	111
4.10	Variation of RMS residual of filtered velocity and $\alpha_{\text{sfs}}$ with filter scale ratio. .	112
4.11	Central slice of the identified filter kernels with IB of 24 vx. . . . .	113
4.12	One dimensional profiles of the result from applying TPIV on the step-response velocity field. . . . .	114
4.13	Original and filtered velocity fields. Filtering is performed using estimated $\mathcal{G}_{\text{PIV}}$ , corresponding to IB of 24 vx. Filtered velocity is compared to the TPIV velocity field. . . . .	115
4.14	Original and filtered velocity fields. Filtering is performed using estimated $\mathcal{G}_{\text{PIV}}$ , corresponding to IB of 24 vx. Filtered velocity is compared to the TPIV velocity field. . . . .	116
5.1	Mean velocity fields in cylindrical coordinates of equivalent non-reacting and reacting flows along the $z = 0$ mm and $y = 1$ mm planes. Every third velocity vector is shown. Flame brush is denoted by the contours at $\langle c \rangle = 0.1$ and $\langle c \rangle = 0.9$ . . . . .	118
5.2	Radial profiles of mean velocity components along $y = 1$ mm and $z = 0$ mm line in a series of non-reacting flows as $U_j$ is varied; $\mathcal{S}$ and chemistry are fixed. . . . .	119
5.3	Radial profiles of mean velocity components along $y = 1$ mm and $z = 0$ mm line in a series of non-reacting flows as $\mathcal{S}$ is varied; $U_j$ and chemistry are fixed. . . . .	119
5.4	Radial profiles of mean velocity components along $y = 1$ mm and $z = 0$ mm line in a series of reacting flows as $U_j$ is varied; $\mathcal{S}$ and $\phi$ are fixed. . .	120
5.5	Radial profiles of mean velocity components along $y = 1$ mm and $z = 0$ mm line in a series of reacting flows as $\mathcal{S}$ is varied; $U_j$ and $\phi$ are fixed. . .	120
5.6	Radial profiles of mean velocity components along $y = 1$ mm and $z = 0$ mm line in a series of reacting flows as $\phi$ is varied; $U_j$ and $\mathcal{S}$ are fixed. . .	121

5.7	Box and whiskers plot of the measured swirl numbers in both reacting and non-reacting flows. Marker 'x' denotes the mean across all cases for each swirler; red circle represents the mean across reacting cases; green square represents the mean across non-reacting cases. . . . .	123
5.8	Profiles of the mean radial pressure gradient along $z = 0$ mm and $y = 1$ mm planes for different swirl numbers. Flame brush is denoted by the contours at $\langle c \rangle = 0.1$ and $\langle c \rangle = 0.9$ . . . . .	124
5.9	Radial profiles of mean radial pressure gradient along $y = 1$ mm and $z = 0$ mm line in a series of reacting flows where $\phi$ , $U_j$ , and $\mathcal{S}$ are varied. . . . .	125
5.10	Turbulence characterization inside the inner shear layer for case E085-S2-U10. . . . .	128
5.11	Proposed test conditions plotted on a turbulent premixed combustion regime diagram by Peters [23]. . . . .	130
5.12	Joint probability density plots of $u_i$ , $\partial u_i / \partial x_j$ , $\partial^2 u_i / \partial x_j^2$ , $\partial^3 u_i / \partial x_j^3$ , as computed using 32 vx and 40 vx grids for cases E085-S100-U05 and E085-S1-U10. Low resolution dataset used for E085-S100-U05 (top row); high resolution dataset used for E085-S1-U10 (bottom row). . . . .	131
6.1	Instantaneous inter-scale energy transfer $\langle \alpha_{\text{sfs}}^* \rangle \cdot \ell / u'^3$ for $\mathcal{S}_1$ swirler across at $\Delta = 2.3$ mm ( $\Delta / \delta_L^0 = 4.7$ for reacting cases). Black contours denote $c = 0.1$ and $c = 0.9$ . Left column: reacting flow at $\phi = 0.85$ ; right column: non-reacting flow. . . . .	134
6.2	One dimensional $\alpha_{\text{sfs}}$ across a premixed methane-air laminar flame at $\phi = 0.75$ . Profiles of density, temperature, and axial velocity used to compute $\alpha_{\text{sfs}}$ were obtained using Cantera; filtering performed using a box filter of width $\Delta = 1.5$ mm or $\Delta / \delta_L^0 = 2.6$ . . . . .	136
6.3	Mean inter-scale energy transfer $\langle \alpha_{\text{sfs}}^* \rangle \cdot \ell / u'^3$ for non-reacting flows at $U_j = 5$ m/s for three available swirlers; $\alpha_{\text{sfs}}^*$ computed at $\Delta = 2.3$ mm. . . . .	137
6.4	Mean inter-scale energy transfer $\langle \alpha_{\text{sfs}} \rangle \cdot \ell / u'^3$ for $\phi = 0.85$ at $\Delta = 2.3$ mm ( $\Delta / \delta_L^0 = 4.7$ ). Black lines represent $\langle c \rangle = 0.1$ and $\langle c \rangle = 0.9$ contours of the flame brush. . . . .	138
6.5	Mean inter-scale energy transfer $\langle \alpha_{\text{sfs}} \rangle \cdot \ell / u'^3$ for varying $\phi$ using $\mathcal{S}_1$ at $U_j = 10$ m/s across $\Delta = 2.3$ mm. Black lines represent $\langle c \rangle = 0.1$ and $\langle c \rangle = 0.9$ contours of the flame brush. . . . .	139

6.6	Doubly-conditioned statistics with $\Delta/\delta_L^0 = 1.5$ . Top row: mean cross-scale energy transport as a function of progress variable and strain rate. Bottom row: JPDFs between progress variable and strain rate. . . . .	141
6.7	Probability density functions of $\alpha_{\text{sfs}}$ conditioned on $c$ with $\Delta/\delta_L^0 = 1.5$ . . .	142
6.8	Mean and skewness of $P(\alpha_{\text{sfs}} c)$ with $\Delta/\delta_L^0 = 1.5$ . . . . .	143
6.9	Probability density functions of $\alpha_{\text{sfs}}$ conditioned on $S_{ij}S_{ij}$ with $\Delta/\delta_L^0 = 1.5$	144
6.10	Mean and skewness of $P(\alpha_{\text{sfs}} S_{ij}S_{ij})$ with $\Delta/\delta_L^0 = 1.5$ . Filled markers: reacting flow, empty markers: non-reacting flow. . . . .	144
6.11	Contours (solid dots) where $\langle \alpha_{\text{sfs}} \rangle = 0$ for increasing $\Delta$ . Open circles indicate the location of maximum $\langle \alpha_{\text{sfs}} \rangle$ for each $\Delta$ . . . . .	146
6.12	Probability density functions of $\alpha_{\text{sfs}}$ , conditioned on progress variable, at different filter scales for E085-S1-U15. . . . .	147
6.13	Variation of $\langle \alpha_{\text{sfs}} c \rangle$ with the filter scale. . . . .	147
6.14	Mean of $\alpha_{\text{sfs}} S_{ij}S_{ij}$ in reacting and non-reacting flows, as filtered using near the scales of the flame. . . . .	148
6.15	Instantaneous realization of $\lambda_{\text{ci}}$ and $\alpha_{\text{sfs}}$ for $\Delta/\delta_L^0 = 1.5$ . Magenta curves correspond to $c = 0.1$ and $c = 0.9$ contours. Green curve is an isocontour of $\lambda_{\text{ci}} = \frac{1}{2} \max(\lambda_{\text{ci}})$ at this instant. Regions that do not have valid velocity measurements are filled black. . . . .	150
6.16	Variation of instantaneous $\alpha_{\text{sfs}}$ with $\lambda_{\text{ci}}$ for reacting and non-reacting flows.	150
6.17	Schematic of the regions used for conditioning the phase-averaged statistics, taken from an instantaneous image at phase 7. . . . .	152
6.18	Phase-averaged statistics as a function of phase for the most dominant coherent structure in the reacting and non-reacting flows. . . . .	153
6.19	Variation of $c$ -conditioned $\alpha_{\text{sfs}}^*$ with $U_j$ at $\phi = 0.75, 0.85$ , and $1.00$ ; swirl number fixed at $\mathcal{S}_1$ and $\alpha_{\text{sfs}}^*$ computed across $\Delta = 1.1$ mm. Top row: non-normalized; bottom row: normalized by $\ell/u'^3$ . . . . .	155
6.20	Variation of $c$ -conditioned $\alpha_{\text{sfs}}$ with $\phi$ at $U_j = 5, 10$ , and $12$ m/s; swirl number fixed at $\mathcal{S}_1$ and $\alpha_{\text{sfs}}$ computed across $\Delta = 1.1$ mm. . . . .	156

6.21	Variation of $c$ -conditioned $\alpha_{\text{sfs}}$ with $\mathcal{S}$ at $U_j = 5, 10$ , and $12$ ; equivalence ratio is fixed at $0.85$ and $\alpha_{\text{sfs}}$ computed across $\Delta = 1.1$ mm. Top row: non-normalized; bottom row: normalized by $\ell/u'^3$ . . . . .	156
6.22	Scaling between maximum measured $\langle \alpha_{\text{sfs}} c \rangle$ and $\langle \nabla p_{\text{r}} \rangle$ ; $\Delta = 2.3$ mm. . . .	158
6.23	Scaling between maximum measured $\langle \alpha_{\text{sfs}} c \rangle$ and $\text{Ka}$ ; $\Delta = 2.3$ mm. . . .	159
6.24	Scaling between maximum measured $\langle \alpha_{\text{sfs}} c \rangle$ and $\text{Re}$ ; $\Delta = 2.3$ mm. . . .	160
A.1	Schematic of a singular channel in a swirler and relevant angles. . . . .	172

## NOMENCLATURE

### Acronyms

<b>ADM</b>	Approximate Deconvolution Model	<b>PM</b>	Particulate Matter
<b>AGM</b>	Approximate Gaussian Method	<b>POD</b>	Proper Orthogonal Decomposition
<b>CRZ</b>	Central Recirculation Zone	<b>RANS</b>	Reynolds-Averaged Navier-Stokes
<b>DOF</b>	Depth of Field	<b>RDM</b>	Regularized Deconvolution Method
<b>HIT</b>	Homogenous Isotropic Turbulence	<b>RMS</b>	Root-Mean-Squared
<b>LES</b>	Large Eddy Simulations	<b>RZ</b>	Reaction Zone
<b>MART</b>	Multiplicative Algebraic Reconstruction Technique	<b>SFS</b>	Sub-filter-scales
<b>NA</b>	Numerical Aperture	<b>SS</b>	Scale similarity
<b>ORZ</b>	Outer Recirculation Zone	<b>SSC</b>	Swirl Stabilized Combustor
<b>PHZ</b>	Preheat Zone	<b>TPIV</b>	Tomographic Particle Image Velocimetry
<b>PLIF</b>	Planar Laser Induced Fluorescence	<b>WD</b>	Working Distance

### Chemical Compounds

$\text{Al}_2\text{O}_3$	Aluminum Oxide	$\text{HCO}$	Formyl Radical
$\text{CH}_4$	Methane	$\text{NO}_x$	Oxides of nitrogen
$\text{CH}_2\text{O}$	Formaldehyde	$\text{O}_2$	Oxygen
$\text{H}_2$	Hydrogen	$\text{OH}$	Hydroxyl Radical

## Nomenclature

$C_S$	Smagorinsky constant	$k$	Filtered kinetic energy
$\mathcal{D}$	Diffusivity	$k_{\text{sfs}}$	Sub-filter scale kinetic energy
$D_e$	Nozzle diameter	$\ell$	Integral length scale
Da	Damköhler number	$\ell_{DI}$	Length scale between dissipation and inertial ranges
$\mathcal{G}$	Filter kernel	$\ell_{EI}$	Length scale between energy-containing and inertial ranges
$\mathcal{G}_{\text{PIV}}$	Filter kernel imposed by PIV	$p$	Fluid pressure
$I$	Intensity in the recorded image	$q$	Quantity of interest
$K$	Filtered kinetic energy of the full flow	$q_i$	Flux of quantity of interest
Ka	Karlovitz number	$s_L^0$	Unstretched laminar flame speed
$\mathcal{L}_{ij}$	Resolved stress	$u'$	Root-mean-squared velocity fluctuation
$M$	Magnification	$u_{ax}$	Axial velocity component of velocity
$N$	Image noise	$u_i$	Velocity vector
$\mathcal{Q}$	Deconvolution kernel	$u_\eta$	Kolmogorov velocity scale
$\dot{Q}'''$	Volumetric heat release rate	$u_\theta$	Circumferential velocity component of velocity
$R$	Nozzle radius	$\dot{w}_r$	Volumetric reaction rate of the fuel
$R_{ij}$	Autocorrelation function	$\Delta$	Filter scale
Re	Reynolds number	$\Delta_T$	Test filter scale
$\mathcal{S}$	Swirl number	$\Pi$	Rate of turbulent kinetic energy production by mean flow
$\mathcal{S}_g$	Geometric swirl number	$\alpha_p$	Work done by the resolved pressure
$S_{ij}$	Strain-rate tensor	$\alpha_p^{\text{sfs}}$	Sub-filter scale pressure-velocity gradient correlation
$T$	Temperature	$\alpha_r$	Thermal diffusivity of the reaction
$\mathcal{T}_{ij}$	Sub-filter scale stress		
$U_j$	Jet velocity		
$\mathcal{W}$	Wiener filter kernel		
$c$	Progress variable		
$c_T$	Temperature-based progress variable		
$d$	Distance between points inside the flame to edges of the flame		
$d_{\text{blur}}$	Diffraction-limited spot size		

	tant mixture	$\nu$	Kinematic viscosity
$\alpha_{\text{sfs}}$	Work done by the unresolved turbulent stress	$\nu_{\text{sfs}}$	Eddy viscosity
$\alpha_\nu$	Work done by the resolved viscous shear	$\rho$	Fluid density
$\alpha_\nu^{\text{sfs}}$	Sub-filter scale viscous work	$\rho_p$	Pearson correlation coefficient
$\gamma$	Regularization parameter	$\tau_c$	Chemical time scale
$\delta_L^0$	Unstretched laminar flame thickness	$\tau_{ij}$	Viscous stress tensor
$\varepsilon$	Dissipation rate	$\tau_\ell$	Integral time scale
$\varepsilon_{\text{AV}}$	Local spatial average of dissipation rate	$\tau_\eta$	Kolmogorov time scale
$\varepsilon_{\text{sfs}}$	Sub-filter scale dissipation rate	$\phi$	Equivalence ratio
$\eta$	Kolmogorov length scale	$\phi_j$	Eigenvector
$\theta$	Angle between camera and the laser sheet normal	$\phi_{\text{sfs}}$	Unclosed flux term
$\theta_i$	POD phase angle	$\chi$	Mole fraction
$\lambda$	Wavelength	$\psi_j$	Eigenvalue
$\lambda_{\text{ci}}$	Swirling strength	$\langle \cdot \rangle$	Ensemble average
$\lambda_\nu$	Dissipative length scale	$(\bar{\cdot})$	Reynolds filter across filter scale $\Delta$
$\mu$	Dynamic viscosity	$(\tilde{\cdot})$	Favre filter across filter scale $\Delta$
		$(\hat{\cdot})$	Reynolds filter across filter scale $\Delta_T$
		$(\check{\cdot})$	Favre filter across filter scale $\Delta_T$



## SUMMARY

Turbulent premixed combustion is of tremendous practical importance and scientific interest. However, despite its widespread use in a variety of industries and decades of research, there are many aspects of turbulent combustion that require further scientific inquiry. The complexity of turbulent premixed combustion arises from the non-linear, multi-scale, and multi-physics nature of the problem, which involves interactions between fluid dynamic and chemical processes across a myriad of length and time scales. One of the key consequences of this interaction is the production of turbulence at the scales of the flame, which has the potential to reverse the classical turbulent energy cascade in a process termed as ‘backscatter’.

The existing literature has showed that the inter-scale energy transfer in turbulent combustion do not necessarily follow the same phenomenology as in non-reacting incompressible turbulence. Moreover, these differences were shown to potentially depend on the magnitude of the pressure gradients across the flames. Hence, the mean pressure fields, generated by various flow configurations, have the potential to induce significantly different turbulence dynamics as compared to non-reacting turbulence. The goal of the presented research is thus to explore the conditions at which significant energy backscatter occurs in an aerospace relevant configuration, and attempt to identify the underlying physical mechanisms that have a leading order impact on this process. This is done by analyzing the transport equations for the filtered and sub-filter-scale turbulent kinetic energy and computing conditional statistics of inter-scale energy flux. The data is obtained experimentally by employing simultaneous laser diagnostics to measure velocity and thermo-chemical state fields. Tomographic particle image velocimetry and planar laser induced fluorescence are used to measure the 3D velocity fields and planar distribution of formaldehyde, respectively; relevant thermodynamic properties (e.g. density and progress variable) are estimated from the distribution of formaldehyde in the flow.

The range of operating conditions achieved in this work ranges from weak to moderate turbulence intensities ( $21 \lesssim Ka \lesssim 164$ ) across three different swirler geometries. Such flames possess a large-scale pressure field that in addition to the pressure fields associated with small-scale turbulent vortices can perform significant pressure-work. Mean kinetic energy transfer from sub-filter scales to larger scales was observed internal to the flame structure across the range of conditions studied, with the maximum backscatter occurring towards the center of the flame and at relatively moderate local strain-rates. Compared to equivalent non-reacting cases, considerably more backscatter occurred in the reacting flows.

The research presented herein seeks to extend the existing state of knowledge by considering an expanded set of operating conditions, including higher turbulence intensities and stronger flow-induced pressure fields. A systematic study of inter-scale energy transfer across a wide range of conditions helps to determine the range of conditions across which backscatter is significant. Ultimately, this work provides a rigorous assessment of the extent to which current turbulence modeling paradigms hold in aerospace-relevant combustion, as well as the data necessary to develop and validate new models if required.

# CHAPTER 1

## INTRODUCTION AND THEORY

### 1.1 Motivation

Combustion is one of the most important classes of chemical reactions and it is essential to human society due to its wide use in industrial processes, chemical processing, energy generation, and transportation [1]. Currently, propulsion devices in aircraft and space launch vehicles operate by burning fossil fuels. Although alternative sources of energy are becoming available, devices used for propulsion and other high-power density applications are expected to rely on combustion of fossil fuels for the foreseeable future [2]. Two major critiques of the combustion devices are utilization of non-renewable fuels and emission of harmful pollutants into the atmosphere. In recent decades, the environmental concerns regarding  $\text{NO}_x$  and particulate matter (PM) emissions have resulted in increasingly strict emission requirements. Thus, design of next-generation combustion systems is driven by environmental impact of pollutants, efficiency, and safety considerations.

Development of physics-based combustion models to aid in the design of next-generation combustion devices requires fundamental understanding of turbulence-flame interactions, particularly in aerospace-relevant configurations. Large Eddy Simulations (LES) provide a good compromise between accuracy and cost, and thus are suitable for engineering-focused simulations. LES resolves large scale flow features in space and time, but models the impact of the small scale fluid behaviour – below the size of the filter used by the simulation – on the resolved scales. Combustion simulations also must model flame-related diffusion and reaction length scales, which typically are less than the filter scale. While numerous models have been developed to describe the sub-filter-scales (SFS), LES of turbulent combustion in realistic configurations remains an active area of research.

Turbulence models typically are based on energy transfer principles, and rely on various assumptions regarding the behaviour of small-scale turbulence [3]. Unfortunately the interaction between chemical reactions and turbulence is still not completely understood and remains an open research question, particularly at the high turbulence intensities found in aerospace and power generation applications [2, 4]. To date, the majority of experimental studies have focused on the interaction between the large-scale turbulent flow structures and the flame [5–8]. Studies of fine-scale turbulence behaviour in reacting flows predominantly have been done using the Direct Numerical Simulations (DNS) in low Mach number homogenous isotropic turbulence (HIT) [9, 10]. However, it is unknown whether this idealization accurately reflects real combustors.

Developing a thorough understanding of flame-turbulence interactions that govern turbulent premixed combustion is thus of vital importance, and will allow for creation of more accurate predictive turbulence and combustion models that will permit engineers to design more efficient and environmentally responsible combustion systems. The overall goal of this thesis is to experimentally measure inter-scale energy dynamics in turbulent premixed flames which would enable formulation of more accurate and robust LES models in the future.

## **1.2 Outline**

### *Introduction and Theory*

The remainder of this chapter is dedicated to the introduction of relevant concepts in turbulence and premixed combustion. A brief overview is given on the SFS models that are used in LES and the issues with applying them in simulations of reacting flows are discussed. Basics of inter-scale energy transfer is presented and the chapter closes with the thesis objectives.

### *Experimental Approach*

The experimental setup, laser diagnostics, test conditions, and the experimental considerations are introduced in this chapter. This thesis uses two laser diagnostics: tomographic particle image velocimetry (TPIV) and planar laser induced fluorescence (PLIF) of formaldehyde ( $\text{CH}_2\text{O}$ ), to simultaneously measure the three-dimensional velocity fields and distribution of formaldehyde in the flow field. The setup of each diagnostic is discussed, evaluating the resolution and accuracy of both TPIV and  $\text{CH}_2\text{O}$  PLIF.

### *Analysis Methods*

Data analysis methods are presented in this chapter. Methods used to estimate the local properties of the fluid (density and temperature) and the combustion progress variable from the distribution of  $\text{CH}_2\text{O}$  are presented and its impact on the results is evaluated. The challenges of computing inter-scale energy transfer and the methods of dealing with such challenges is discussed. Finally, proper orthogonal decomposition (POD) is introduced, which is used to identify the coherent structures in the flow.

### *Characterization of the flow and flames*

In this chapter, characterization of relevant flow field in the swirl-stabilized combustor are documented. Low and high resolution TPIV measurements are used to evaluate the mean flow, turbulence intensity, integral length scale, and dimensionless quantities of relevance in turbulence. Grid convergence is also discussed to identify the test cases that contain a fully resolved flow field. Lastly, identification of coherent structures in the flow using POD is performed and document in this chapter.

### *Deconvolution*

In this chapter, methods of deconvolution are presented. Fully-resolved velocity fields are usually not captured in TPIV measurements; hence, these must first be estimated from the

raw measurements in order to evaluate the inter-scale energy transfer in moderate to high intensity turbulent flows. A brief overview on commonly used deconvolution methods is presented and they are tested on data from DNS of turbulent premixed flames. Moreover, determination of the TPIV convolution kernel is presented here as well.

### *Inter-Scale Energy Transport*

Measurements of inter-scale energy transport at various conditions are discussed here. First, the instantaneous distribution of cross-scale energy transport in the flow field and in the flame is presented. Next, the conditional statistics of inter-scale transport on the progress variable and local strain-rate are evaluated and compared against the equivalent non-reacting flow fields. Next, the interaction between coherent flow structures and the turbulent flame is considered and the magnitude and direction of inter-scale energy transport is examined in regions of flame-vortex interactions. Finally, the effects of the filter scale, turbulence intensity, and externally-imposed pressure gradients are examined on the measurements of inter-scale energy transport.

### *Conclusions*

Summary of key takeaways from this thesis is presented in this chapter. The results of inter-scale energy transfer and its dependence on turbulence intensity, equivalence ratio, and externally-imposed pressure gradients is summarized. Although this thesis presents interesting and novel observations in the area of energy dynamics, there is considerable work that needs to happen in further developing our understanding of turbulence-flame interaction and implication it has on LES models. These will be discussed in the closing chapter of this thesis.

### 1.3 Structure and Dynamics of Turbulence

To understand the effects of turbulence and combustion on each other, it is critical to first highlight the theoretical framework of non-reacting turbulence. Theories of constant density non-reacting turbulence have historically received more attention than compressible and reacting turbulence, and thus serve as a baseline for studying the effects of combustion on turbulence properties and dynamics. It should also be noted that many closure models used in simulations of both reacting and non-reacting flows are based on the theories of classical non-reacting turbulence. Finally, recent studies have shown that the properties of non-reacting turbulence are similar to those in highly turbulent combustion [11]. Hence, a brief discussion of constant density turbulence is presented here.

The governing equations for the evolution of a turbulent flow are the coupled set of partial differential equations describing the conservation of mass and momentum of a viscous fluid, i.e.

$$\begin{aligned}\frac{\partial \rho}{\partial t} + \frac{\partial \rho u_j}{\partial x_j} &= 0, \\ \frac{\partial \rho u_i}{\partial t} + \frac{\partial \rho u_i u_j}{\partial x_j} &= -\frac{\partial p}{\partial x_i} + \frac{\partial \tau_{ij}}{\partial x_j},\end{aligned}\tag{1.1}$$

where  $u_i$  is the velocity vector,  $\rho$  is fluid density,  $p$  is pressure, and  $\tau_{ij}$  is the viscous stress tensor. These equations contain a non-linear inertial term, which is typically damped by the linear viscous diffusion term. However, the non-linear inertial term typically dominates over viscous diffusion, resulting in a deterministic but chaotic (turbulent) fluid motion. The system under such conditions is highly sensitive to initial and boundary conditions; infinitesimal perturbations lead to drastically different flow fields. The Reynolds number  $Re$ , which characterizes the relative magnitudes of non-linear advection and viscous diffusion, is typically used to delineate between laminar (small  $Re$ ) and turbulent (large  $Re$ ) flows [12, 13].

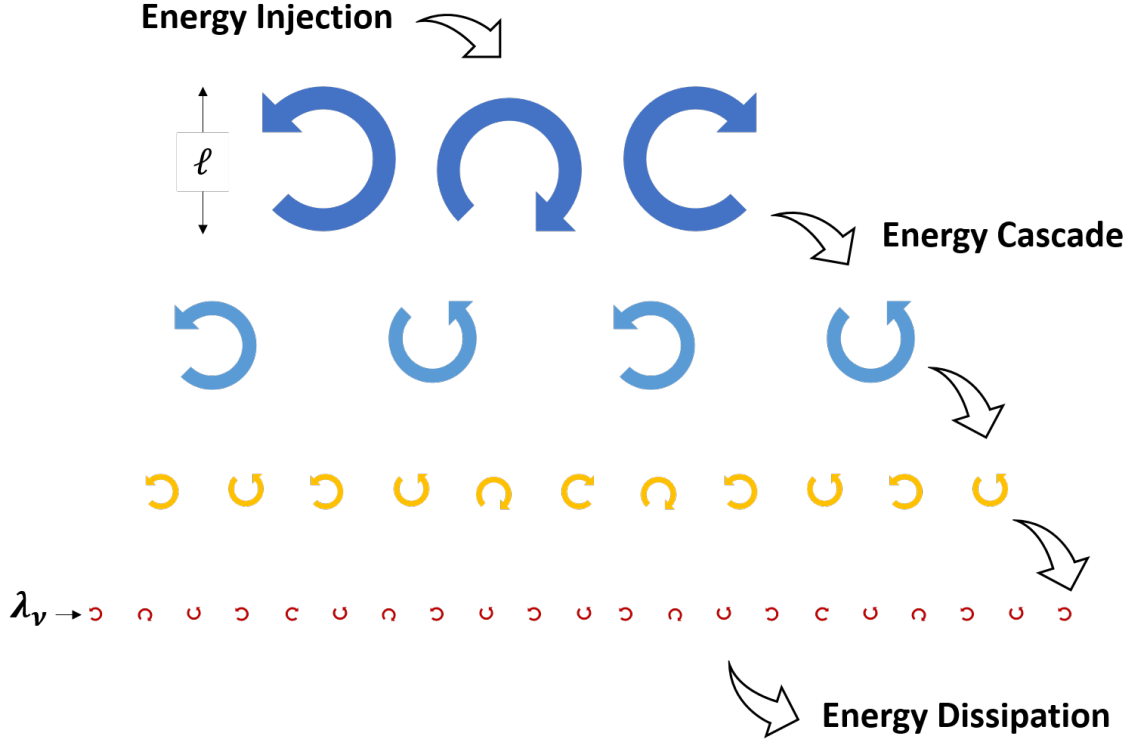


Figure 1.1: Schematic representation of the turbulent kinetic energy cascade.

### 1.3.1 Richardson Energy Cascade

The non-linearity of the Navier-Stokes equations lies at the root of turbulence [12]. Richardson [14] has observed that, at large  $Re$ , large spatial and temporal variations in flow properties are created over a broad range of length and time scales, and that the dissipation of turbulent kinetic energy is associated predominantly with the smallest scales of turbulence. Consequently, Richardson introduced the concept of *energy cascade* for high- $Re$  turbulence, which is schematically demonstrated in Figure 1.1.

The classical energy cascade is initiated through creation of turbulent kinetic energy at the largest scales of motion (i.e. the integral length scale  $\ell$ ) by the mean fluid dynamic shear. Inertial instabilities cause the largest eddies to break-up into smaller vortices, transferring their turbulent kinetic energy in the process. At high  $Re$  numbers, the inertial forces continue to drive the break-up of eddies into continuously smaller structures, transferring



energy in a non-dissipative manner. The process continues until the eddy size is small enough that  $Re$ , based on the size of smallest turbulence structure, is of order unity. Note that the magnitude of viscous stresses acting on larger eddies is negligible; the energy cascade is driven by inertial forces [15]. The role of viscosity is to convert turbulent kinetic energy at the smallest scales (i.e. the dissipative scale  $\lambda_\nu$ ), at which viscous diffusion balances non-linear advection; the energy is converted from turbulent kinetic energy to internal energy of the fluid. Note that the process of eddy breakup is purely notional; the physical mechanism by which energy is transferred between scales occurs predominantly via stretching or distortion of smaller structures by larger ones (i.e. vortex-stretching), but it may also occur due to disintegration of a larger eddy.

The timescale over which the largest eddies pass most of their energy to smaller structures is on the order of their turnover time  $\ell/u'$ , where  $u'$  is the root-mean-squared velocity fluctuation. Consequently, the rate at which the turbulent kinetic energy is passed down the cascade is [12, 15]

$$\Pi \sim \frac{u'^2}{\ell/u'} = \frac{u'^3}{\ell}. \quad (1.2)$$

The rate at which turbulent kinetic energy is dissipated depends on the strain-rate tensor  $S_{ij} = \frac{1}{2}(\frac{\partial u_i}{\partial x_j} + \frac{\partial u_j}{\partial x_i})$ , and is defined as [12, 13, 15]

$$\varepsilon \sim \nu S_{ij} S_{ij}. \quad (1.3)$$

At smallest scales,  $S_{ij} \sim u_\eta/\eta$ , where  $u_\eta$  and  $\eta$  are velocity and length scales associated with smallest turbulent structures, respectively; consequently,  $\varepsilon \sim \nu(u_\eta^2/\eta^2)$ . At statistically steady flow conditions, the rate of energy injection must be balanced by the rate of dissipation at smallest turbulence scales to avoid accumulation of energy at intermediate scales. The balance between production  $\Pi$  and dissipation  $\varepsilon$  leads to

$$\frac{u'^3}{\ell} \sim \nu \frac{v^2}{\eta^2}. \quad (1.4)$$

Combined with the knowledge that  $\text{Re}$ , based on scales of the smallest turbulence scales, is of order unity –  $u_\eta \eta / \nu \sim 1$ , the range of length, velocity, and time scales can be defined [12]

$$\eta \sim \ell \text{Re}^{-3/4} \quad \text{or} \quad \eta = \left( \frac{\nu^3}{\varepsilon} \right)^{1/4}, \quad (1.5)$$

$$u_\eta \sim u' \text{Re}^{-1/4} \quad \text{or} \quad u_\eta = (\nu \varepsilon)^{1/4}, \quad (1.6)$$

$$\tau_\eta \sim (\ell / u') \text{Re}^{-1/2} \quad \text{or} \quad \tau_\eta = (\nu / \varepsilon)^{1/2}, \quad (1.7)$$

where  $\text{Re} = \ell u' / \nu$  is the turbulent Reynolds number. The scales  $\eta$ ,  $u_\eta$ , and  $\tau_\eta$  are the *Kolmogorov microscales*, while  $\ell$  is the *integral scale*. The separation between the largest ( $\ell$ ) and smallest ( $\eta$ ) length scales is shown to depend on the turbulent Reynolds number; at large  $\text{Re}$ , the range of length scales can span multiple orders of magnitude. It is noted, that the actual observed smallest length scales – the dissipation scale  $\lambda_\nu$  – are approximately 5-6 times larger than  $\eta$  [11, 16–18].

### 1.3.2 Kolmogorov's Theory

Richardson's energy cascade model is a multi-stage process which involves a hierarchy of turbulence structures. In 1941, Andrey Nikolaevich Kolmogorov introduced equilibrium theories that build upon the energy cascade model to describe how energy is transferred from one scale to another, how much energy is contained at different scales, and how much energy is dissipated at each scale [19]. Based on physical reasoning and dimensional arguments, Kolmogorov introduced three hypotheses that form the basis for statistical analysis of turbulence.

Kolmogorov's hypothesis of local isotropy states that the smallest turbulence (i.e. eddies of size  $r \ll \ell$  with a lifetime  $t \ll \ell / u'$ ) can be approximated as being locally homogeneous, isotropic, and stationary. In homogeneous flow, fluctuation statistics are the same at all locations in the flow; statistics only depend on relative distance between two

points. In an isotropic flow, the fluctuation statistics do not have directional preference. In a stationary flow, turbulence statistics do not vary in time. Due to the complex non-linear processes that lead to formation of smallest turbulence, it is plausible that there is no memory of the original anisotropy or other large-scale features associated with a particular flow. Moreover, since the lifetime of the smallest turbulent eddies is much smaller than those of large eddies, it is reasonable that smallest scale turbulence is in approximate *statistical equilibrium* with the large scales to the extent that  $\varepsilon = \Pi(t)$ . The regime  $r \ll \ell$  is known as the *universal equilibrium range*.

Kolmogorov's first similarity hypothesis states that the statistics of small scale turbulence are universal and are uniquely determined by  $\varepsilon$  and  $\nu$  at sufficiently high Reynolds number. Under this hypothesis, the role of the smallest eddies – Kolmogorov microscales – is to dissipate energy cascading from larger eddies; the size of smallest scales adjusts to changes in  $\varepsilon$  and  $\nu$  (see Equation 1.5 and Equation 1.6). In the dissipation range of scales, the turbulence statistics have the functional form  $\langle \cdot \rangle = f(\varepsilon, \nu, r)$ , where  $r$  is the length scale and  $\langle \cdot \rangle$  denotes ensemble averaging. In dimensionless form, the functional relationship may be rewritten as

$$\frac{\langle \cdot \rangle}{\varepsilon^a \nu^b} = \mathcal{F}(r/\eta), \quad r \ll \ell, \quad \text{or} \quad \frac{\langle \cdot \rangle}{\varepsilon^a \nu^b} = \mathcal{F}(k\eta), \quad k \gg \ell^{-1}, \quad (1.8)$$

where  $k$  is the wavenumber, and  $a$  and  $b$  are chosen accordingly to non-dimensionalize the statistic of interest.  $\mathcal{F}$  represents the universal function, expected to be valid for all forms of turbulence. In fact, experimental evidence verified universality of  $\mathcal{F}$  in a variety of flows, including wakes, jets, pipes, boundary layers, and grids [20].

Kolmogorov's second similarity hypothesis states that for sufficiently high Reynolds number, the statistical properties have a universal form that is uniquely determined by  $\varepsilon$  and independent of  $\nu$  in the range  $\eta \ll r \ll \ell$ . This is motivated by the fact that the range of length scales increases with larger Re. Consequently, it is expected to find a range of

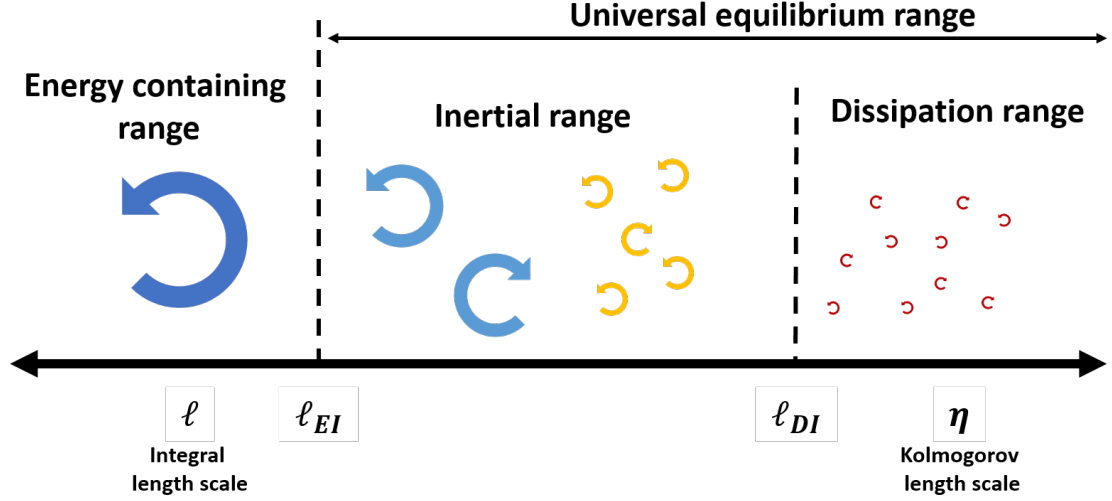


Figure 1.2: Schematic representation of length scales and ranges in the turbulent kinetic energy cascade.

scales, called the *inertial range*, such that  $r \gg \eta$  where effects of viscosity are negligible and  $r \ll \ell$  where no memory of large scales is retained. In this range, turbulence statistics are expected to have the form

$$\langle \cdot \rangle = \varepsilon^c r^d, \quad \eta \ll r \ll \ell, \quad \text{or} \quad \langle \cdot \rangle = \varepsilon^c k^d, \quad \eta^{-1} \gg k \gg \ell^{-1}, \quad (1.9)$$

where exponents  $c$  and  $d$  are chosen to match the dimensions of  $\langle \cdot \rangle$ . It should be noted that higher-order statistics (of order 3 and higher) deviate from the universal scaling, due to the intermittent nature of  $\varepsilon$  in space and time [12, 13]. To account for this discrepancy, Kolmogorov [21] has refined his second similarity hypothesis in 1962 to replace  $\varepsilon$  with  $\varepsilon_{AV}$ , which is a local spatial average of dissipation in a spherical volume of radius  $r$ .

Schematic representation of the length scale ranges in the energy cascade is shown in Figure 1.2. The length scales  $\ell_{EI}$  and  $\ell_{DI}$  represent the demarcation lines between energy-inertial ranges and inertial-dissipation ranges, respectively.

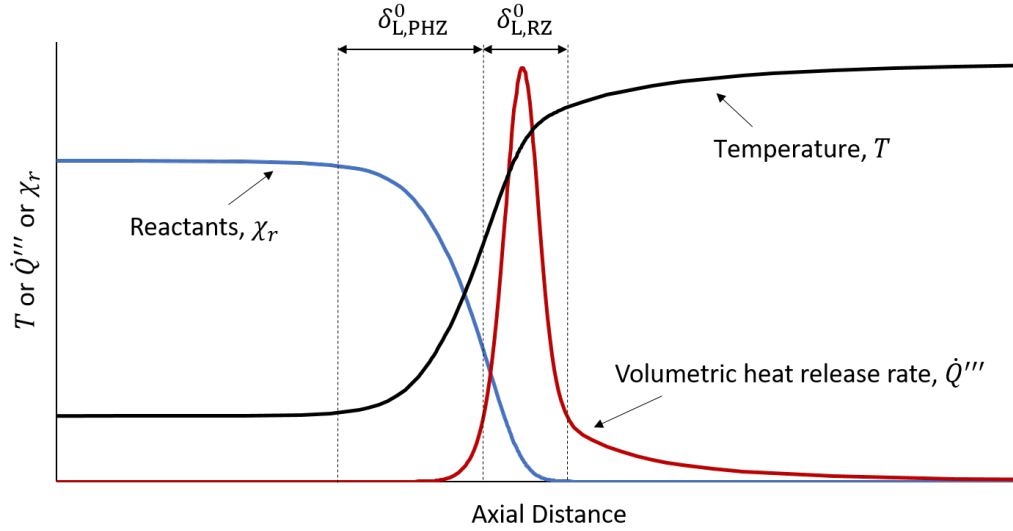


Figure 1.3: Illustration of one-dimensional unstretched laminar premixed flame.

## 1.4 Premixed Combustion

### 1.4.1 Laminar Flames

A brief overview of laminar premixed combustion is also necessary before examining the interaction between turbulence and premixed flames. In subsonic premixed combustion reactants are converted to products through a localized combustion zone [1]. This region of self-sustaining chemical reactions is commonly referred to as a *flame*. The structure of a steady flame can be examined in one dimension in the reference frame of a fixed observer. A representative schematic of a laminar premixed flame is shown in Figure 1.3.

The structure of the unstretched laminar flame is typically separated into two regions: the preheat zone (PHZ) and the reaction zone (RZ); these regions are indicated by the vertical dashed lines in Figure 1.3. For methane/air flames, the preheat zone is a relatively chemically inert region dominated by heat and mass diffusion processes. Here, the mixture is gradually heated by the heat conducted from the heat release region downstream; continuously rising temperature enables lower temperature endothermic reactions, such as fuel pyrolysis, and creation of free radicals [22, 23]. The reaction zone is characterized by the rapid heat release occurring within this region. For high activation energy reactions, includ-

ing those involved in combustion, it is expected that the reactions are activated close to the expected maximum temperature [22]; once initiated, such reactions are also expected to be completed rapidly. Consequently, the reactants are rapidly consumed and the many radicals are created by chain-branching reactions in the reaction zone. In the region downstream of the reaction zone, commonly labeled as the oxidation layer, slower oxidation reactions take place as temperature slowly approaches equilibrium condition.

Two laminar flame properties that are frequently used to characterize turbulent combustion and used for scaling analysis are the unstretched laminar flame thickness ( $\delta_L^0$ ) and flame speed ( $s_L^0$ ). Laminar flame thickness is a measure of how quickly chemical reactions can occur against the oncoming flow. From Figure 1.3, it is evident that it is the sum of the preheat layer thickness and reaction zone thickness (i.e.  $\delta_L^0 \sim \delta_{L,PHZ}^0 + \delta_{L,RZ}^0$ ). Typically, the overall thermal thickness is estimated as

$$\delta_L^0 = \frac{T_p - T_r}{\max(|\nabla T|)}, \quad (1.10)$$

where  $T$  is the local temperature, and subscripts  $r$  and  $p$  correspond to reactants and products, respectively. However, analysis of mass, species, and energy conservation equations also suggest that  $\delta_L^0 \sim \alpha_r/s_L^0$ , where  $\alpha_r$  is the thermal diffusivity of the reactant mixture [1, 23]; this thickness approximately represents the thickness of the thin reaction zone (i.e.  $\delta_{L,RZ}^0 = \alpha_r/s_L^0$ ). In hydrocarbon/air flames, the thermal thickness of the flame is approximately an order of magnitude larger than the thickness of the reaction zone (i.e.  $\delta_{L,RZ}^0 = \mathcal{O}(10^{-1})\delta_L^0$ ) [11].

The laminar flame speed can be defined in two main ways: as a displacement speed of a specific iso-surface in the flame, or as a global consumption speed of reactants, typically obtained by integrating the volumetric reaction rate of fuel. The difference between the displacement and consumption speeds arises due to the choice of the isosurface used to compute the displacement speed [24]. Since the flow accelerates across the flame, displace-

ment speed at iso-surface  $T = T_p$  will be greater than displacement speed at iso-surface  $T = T_r$ . Moreover, stretched flames introduce variations in propagation rate of the flame due to local curvature of iso-surfaces and differential mass diffusion, amplifying the difference between consumption and displacement speeds; in the tip of a Bunsen flame, the displacement speed can be an order of magnitude larger than the consumption speed [24]. Experimentally,  $s_L^0$  is typically taken as the velocity of the gas upstream of the preheat zone and is approximately equal to the consumption speed. For the purposes of this dissertation, the global consumption speed of an unstretched laminar flame will be considered, defined as

$$s_L^0 = \frac{1}{\rho_r} \int_{-\infty}^{\infty} \dot{w}_r dx, \quad (1.11)$$

where  $\dot{w}_r$  is the volumetric reaction rate for the fuel, and  $\rho_r$  is the density of the reactant mixture. The consumption speed of a stretched flame can be computed in a similar manner, integrating over the volume occupied by the flame instead.

#### 1.4.2 Regime Diagrams

The broad range of turbulent scales, which often encompass the thermal thickness of laminar flames ( $\delta_L^0$ ) in flows of practical interest, allow for chemical and fluid-dynamic processes to interact across a myriad of scales that may be local or distant in scale space [25–28]. This leads to modification of both the flame structure and turbulence characteristics, resulting in different flame structures observed at various turbulence conditions. The Karlovitz number ( $Ka = \tau_c/\tau_\eta$ ) and the Damköhler number ( $Da = \tau_\ell/\tau_c$ ) are typically used to characterize the turbulence/flame interactions;  $\tau_c$ ,  $\tau_\eta$ , and  $\tau_\ell$  represent the time scales associated with the laminar flame, Kolmogorov scale, and integral turbulent scales, respectively. These dimensionless numbers are typically expressed in terms of physical operating parameters in the combustor as

$$Ka = \left( \frac{u'}{s_L^0} \right)^{3/2} \left( \frac{\delta_L^0}{\ell} \right)^{1/2}, \quad (1.12)$$

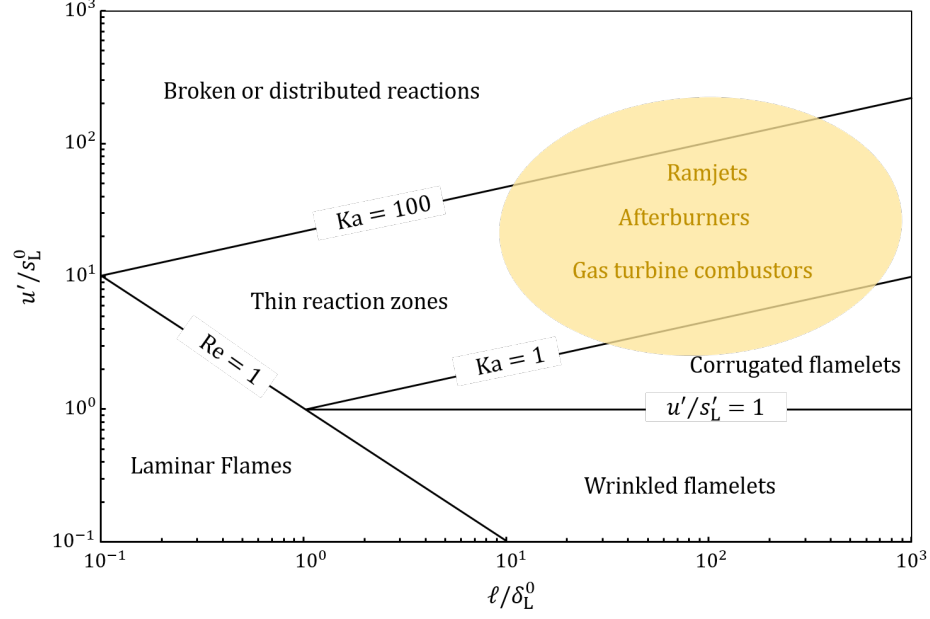


Figure 1.4: Regime diagram as proposed by Peters [23] with estimated conditions for various engines.

$$Da = \left( \frac{s_L^0}{u'} \right) \left( \frac{\ell}{\delta_L^0} \right). \quad (1.13)$$

Numerous attempts have been made to classify the turbulent flames into different regimes of turbulent combustion, including by Williams [29], Borghi [30], and Peters [23]. The boundaries between the regimes is typically defined in terms of a ratio of turbulence and chemistry length and time scales,  $Ka$ , or  $Da$ . One of the most commonly used regime diagrams is the one proposed by Peters [23], which uses  $\ell/\delta_L^0$  and  $u'/s_L^0$  as the abscissa and the ordinate, respectively. An example of this diagram is shown in Figure 1.4.

The laminar flames are characterized by small  $\ell/\delta_L^0$  and  $u'/s_L^0$  and are separated from the turbulent flames by  $Re = 1$  line. In the presence of “weak” turbulence, the instantaneous flame surface behaves as a thin *flamelet*; this behavior typically encompasses the wrinkled flamelet and corrugated flamelet regimes. A flamelet was originally defined by Williams [29] as the flame where gradients in thermo-chemical properties (i.e. temperature, heat release, etc.) are much larger in flame-normal direction than in tangential direction;



the local flame structure essentially resembles that of a laminar flame. In these regimes reactions occur in thin sheets, as the combustion time scales are smaller than the turbulence time scales [23]. In the wrinkled flamelets regime, turbulence can only wrinkle the flame front, but not sufficiently enough for the flame to interact with itself [31]. The Kolmogorov length scales are typically larger than the flame thickness and the magnitude of velocity fluctuations are smaller than  $s_L^0$ . As the magnitude of turbulence velocity fluctuations exceeds the local flame speed,  $u'/s_L^0 > 1$ , the flame front is not able to keep up with turbulent fluctuations, resulting in a highly convoluted flame front, to the point where isolated pockets of reactants or burned products appear. This is the corrugated flamelet regime.

The line separating the thin flamelet regimes from the thin reaction zones is called the Klimov-Williams (K-W) condition [29, 32], formally defined by  $Ka = 1$  (here,  $\eta = \delta_L^0$  and  $u_\eta = s_L^0$ ). Above the K-W condition, the Kolmogorov length scale is smaller than the thermal thickness of the flame and the turbulence fluctuations are greater than the laminar flame thickness [11]. As turbulence is increased, structures of smaller and smaller size appear in the flow. It is generally thought that turbulent eddies larger than  $\delta_L^0$  increase the flame surface area through wrinkling and strain mechanisms, hence increasing the turbulent flame speed [33]. On the other hand, turbulence smaller than  $\delta_L^0$  is able to penetrate the flame structure and alter the scalar gradients. Hence, the enhanced stirring internal to the flame results in increased diffusion of species and enthalpy, which affects the burning rate [4, 34, 35]. In the thin reaction zone regime, it is hypothesized that the presence of small scale turbulence,  $\eta < \delta_L^0$ , leads to broadening of the flame structure, specifically the preheat layer upstream of the thin reaction zone [4]. Consequently, the flame structure has a characteristic broadened preheat layer and a thin reaction zone. Some suggest that incoming turbulence is attenuated in the preheat zone due to increasing temperature, leaving no small scale turbulence strong enough to affect the structure of the thin reaction zone [36, 37].

Lastly, if the Kolmogorov length scale is small enough to penetrate the thin reaction zone of the flame, the flames may be broadly thickened and reactions could occur over

vastly distributed regions of space. However, the ability of the smallest turbulence to modify the flame structure is still unclear since the Kolmogorov time scale is shorter than the reaction time scales. On the regime diagram, the broken or distributed reaction regime is delineated from thin reaction zones by  $Ka = 100$  line; this corresponds to  $\eta \approx \delta_{L,RZ}^0$  in methane/air flames. The broken reactions have only been observed in compression ignition engines and are a result of rapid heat-release in a homogeneous mixture, rather than turbulence itself [31].

Figure 1.4 shows a shaded region, which coarsely outlines the range of typical operating conditions in practical devices, including gas turbine combustors, afterburners, and ramjets [11]. Clearly, most combustion devices are operated in the thin reaction zones regime between  $1 < Ka < 100$ . In the present work, this range of  $Ka$  number is investigated.

#### 1.4.3 Properties of Reacting Turbulence

To date, many studies focused on the effects of turbulence on premixed combustion, driven by the need to understand the increased reaction rate in presence of turbulence, as compared to laminar flames [4, 34, 35]. The results indicate that the effect of turbulence on premixed flames is reflected in the rate at which energy and species are mixed between the products and reactants. For example, it has been observed that a turbulent premixed flame consumes reactants much quicker than a laminar flame occupying the same volume [38].

However, combustion can also have a significant impact on turbulence [11, 39, 40]. As an example of how turbulence is modified by the flame, spectral and multi-scale structure properties of reacting turbulence in DNS of flames in HIT have been observed to deviate from the form observed in most constant-density flows. Towery *et al.* [41] examined the 2D kinetic energy spectra at various locations within a  $Ka \approx 20$ ,  $Da \approx 0.8$  statistically planar flame in HIT using single-step chemistry, and observed that small-scale turbulence is monotonically suppressed from reactants to products. Kolla *et al.* [42] and Kolla *et al.* [43] identified a spectral bump in the 1D kinetic energy spectrum near the scale of

the laminar flame at  $Ka \approx 0.7$ ,  $Da \approx 0.1$ , which was linked to the dilatation from the flame. Additionally, conditional analysis of the velocity structure functions has shown that dilatation is the cause of significant deviation from constant-density scaling at  $Ka \lesssim 20$  [44–46]. In flows with mean shear, the turbulent kinetic energy dynamics were found to be dominated by the velocity-pressure gradient term for  $Ka \lesssim 7$  [47, 48], whereas the kinetic energy transport equation is typically balanced by production and dissipation in most constant-density flows. Finally, the presence of a premixed flame alters the vorticity dynamics through combustion-induced terms in the transport equation (i.e. dilation and baroclinic torque) and modifying the magnitude of local transport coefficients [9, 49–57].

The literature clearly shows that there are critical differences between the physics of reacting turbulence – with variable density, temperature, compositions, etc. – and the classical phenomenology of incompressible non-reacting turbulence. It is shown that (1) production of turbulence may occur at the length scales associated with the flame (i.e.  $\delta_L^0$ ), (2) the turbulent kinetic energy may be transferred to larger scales, and (3) these processes may also depend on the configuration. Consequently, the coupling between chemical and mechanical (kinetic) energies may alter the phenomenological picture of the classical equilibrium turbulent energy cascade.

This consequence is especially significant in the context of LES, which model the influence of the SFS scales on the larger resolved scales. At highly turbulent conditions, most of the flame-induced turbulence dynamics exists in the SFS scales and must be modelled. Most SFS models currently used in LES of reacting flows have been designed for non-reacting turbulent flows and concur with the phenomenology of Richardson [14] and Kolmogorov [19]. Answering the questions of whether the flame disrupts the predominant net forward cascade of kinetic energy and whether there is a net backscatter (i.e. upscale transfer) of energy by the flame is necessary to create physics-based SFS models in LES of reacting flows. Thus, it is critical to understand the mechanisms of flame-scale turbulence production, transfer of momentum and energy flame scales and larger scales, and identify

the conditions at which these effects are important. This thesis focuses on the details of inter-scale energy transfer.

## 1.5 SFS modeling in LES

Large eddy simulations separate large scale fluid motion from small scales through convolution of the governing equations with a spatial filter. For LES of compressible flows, the basic governing equations are filtered Navier-Stokes equations. The filtered continuity and momentum equations are

$$\begin{aligned}\frac{\partial \bar{\rho}}{\partial t} + \frac{\partial \bar{\rho} \tilde{u}_j}{\partial x_j} &= 0, \\ \frac{\partial \bar{\rho} \tilde{u}_i}{\partial t} + \frac{\partial \bar{\rho} \tilde{u}_i \tilde{u}_j}{\partial x_j} &= -\frac{\partial \bar{p}}{\partial x_i} + \frac{\partial \tilde{\tau}_{ij}}{\partial x_j} - \frac{\partial \mathcal{T}_{ij}}{\partial x_j},\end{aligned}\tag{1.14}$$

where  $\tilde{u}_i$  is the filtered velocity field that is also a solution to the problem,  $\bar{p}$  is the filtered pressure,  $\tilde{\tau}_{ij}$  is the filtered viscous stress, and  $\mathcal{T}_{ij}$  is the SFS stress. Here, Favre filtering operation is denoted as  $(\tilde{\cdot}) = \overline{\rho(\cdot)}/\bar{\rho}$ , where the spatial filtering operation  $(\bar{\cdot})$  is performed by convolution of the filter kernel  $\mathcal{G}$ , characterized by the filter scale  $\Delta$ , with the quantity of interest  $q(\mathbf{x}, t)$ , [58]

$$\bar{q}(\mathbf{x}, t) = \mathcal{G} * q(\mathbf{x}, t) = \int_{-\infty}^{\infty} q(\mathbf{x}', t) \mathcal{G}(\mathbf{x} - \mathbf{x}') d\mathbf{x}'.\tag{1.15}$$

The term containing the SFS stress (i.e.  $\partial_j \mathcal{T}_{ij}$  in Equation 1.14) physically represents the exchange of momentum between scales larger and smaller than  $\Delta$  and is defined as

$$\mathcal{T}_{ij} \equiv \bar{\rho}(\widetilde{u_i u_j} - \tilde{u}_i \tilde{u}_j).\tag{1.16}$$

The filtered product of two velocity components  $\widetilde{u_i u_j}$  appears in the definition, which creates a closure problem in LES since the unfiltered velocity  $u_i$  is unknown. It is critical that  $\mathcal{T}_{ij}$  is modelled properly, since it has a direct effect on the dynamics of resolved scales

and the accuracy of the solution. As is commonly done in turbulence simulations, the problem is closed by expressing the unclosed term  $-\mathcal{T}_{ij}$  – as a function of the filtered quantities (i.e.  $\tilde{u}_i$  and  $\bar{p}$ ) [13]. However, one must be mindful when using this approach, since the effects of higher-order moments in the unfiltered velocity field are not captured by such closure models [59]. The three main classes of LES models are presented in this section: eddy viscosity models, dynamic models, and scale-similarity models.

At this point, it is beneficial to briefly introduce the SFS ‘dissipation’  $\varepsilon_{\text{sfs}}$ , defined as

$$\varepsilon_{\text{sfs}} = \mathcal{T}_{ij} \tilde{S}_{ij}, \quad (1.17)$$

where  $\tilde{S}_{ij} = \frac{1}{2}(\frac{\partial \tilde{u}_i}{\partial x_j} + \frac{\partial \tilde{u}_j}{\partial x_i})$  is the filtered strain rate tensor. Physically,  $\varepsilon_{\text{sfs}}$  represents the dissipation of turbulent kinetic energy by energy transfer to the sub-filter scales. Instantaneously, it can be either positive or negative, denoting either up-scale or down-scale energy transfer, respectively. The equation for  $\varepsilon_{\text{sfs}}$  is exact, but it depends on unclosed  $\mathcal{T}_{ij}$ . Hence, performance of the model for  $\mathcal{T}_{ij}$  has a direct effect on the energy dynamics. Discussion on  $\varepsilon_{\text{sfs}}$  and its link to the inter-scale energy transfer parameter  $\alpha_{\text{sfs}}$  will be discussed in more detail in Section 1.6.

### *Eddy Viscosity Models*

The eddy viscosity models in LES are conceptually very similar to the eddy viscosity models used in Reynolds-averaged Navier-Stokes (RANS) equations closure. Specifically, the *gradient transport approximation* is applied to the unresolved small-scales. Since turbulence contains a great deal of fine-scale structures that appears to be random and stochastic, it is believed that fine-scale motions can be modeled using stochastic transport mechanisms.

This is analogous to the molecular transport of mass, momentum, energy, and scalars governed by small-scale stochastic molecular motion. Fourier’s law of heat conduction, Fick’s law of mass diffusion, and momentum diffusion via viscosity are all examples of

diffusive transport mechanisms that takes the form

$$q_i = -\mathcal{D} \frac{\partial \phi}{\partial x_i}, \quad (1.18)$$

where  $\mathcal{D}$  is a proportionality constant,  $\phi$  is any quantity of interest and  $q_i$  is the net flux of said quantity per unit mass. Since the net flux is proportional to the mean gradient of  $\phi$ , this is referred to as a *gradient transport mechanism*. Turbulent transport is commonly modelled using this mechanism, assuming that small-scale stochastic vortical structures (i.e. eddies) dominate turbulent transport. Under this model, the SFS stress is modelled as

$$\mathcal{T}_{ij} \approx 2\nu_{\text{sfs}} \tilde{S}_{ij}, \quad (1.19)$$

where  $\nu_{\text{sfs}}$  is the eddy viscosity (i.e. the proportionality constant in Equation 1.18). Under this formulation, it is required that the SFS stress is aligned with the resolved strain rate tensor. Using a constant eddy viscosity is possible, but it gives very poor results [59]. The various sub-filter-scale models in the category of eddy viscosity models differ in the manner in which  $\nu_{\text{sfs}}$  is modelled.

One of the most popular models in use to date is the *Smagorinsky model*. Originally developed for atmospheric flows in 1963 [60], Smagorinsky expressed the eddy viscosity in the following form

$$\nu_{\text{sfs}} = (C_S \Delta)^2 (\tilde{S}_{ij} \tilde{S}_{ij})^{1/2}, \quad (1.20)$$

where  $C_S$  is the Smagorinsky coefficient, and  $\Delta$  is the filter scale. This is a fairly simple model, which is relatively straightforward to implement and is computationally efficient.

However, its primary issue is that it is a purely dissipative model:

$$\begin{aligned}
\varepsilon_{\text{sfs}} &= \mathcal{T}_{ij} \tilde{S}_{ij} \\
&= (2\nu_{\text{sfs}} \tilde{S}_{ij}) \tilde{S}_{ij} \\
&= 2C_S^2 \Delta^2 (\tilde{S}_{ij} \tilde{S}_{ij})^{3/2}.
\end{aligned} \tag{1.21}$$

Since,  $\tilde{S}_{ij} \tilde{S}_{ij}$  is strictly positive,  $\varepsilon_{\text{sfs}} > 0$ ; only forward scatter of energy is permitted by the Smagorinsky model. However, locally and instantaneously in a real turbulent flow, the energy exchange between larger (resolved) and smaller (sub-filter) scales can occur in either direction [61]. While this limitation can be acceptable if mean energy transfer direction occurs from resolved to sub-filter scales, Smagorinsky model can lead to completely incorrect prediction if mean energy transfer occurs in the up-scale direction.

Moreover, model predictions tend to be sensitive to the Smagorinsky constant  $C_S$  [61]. Typically,  $C_S$  is determined by equating mean SFS dissipation rate to true kinetic energy dissipation, *viz.*  $\langle \varepsilon_{\text{sfs}} \rangle = \langle \varepsilon \rangle$ . A standard value of  $C_S$  is typically taken as 0.17, but can range between 0.1-0.2 in shear flows, and value of 0.23 is commonly used in homogeneous isotropic turbulence [3, 13]. Clearly, there is a dependence of  $C_S$  on the flow regime. Eddy viscosity models perform reasonably well in predicting mean flows away from boundaries, but often overpredict shear stress [59]. Generally, the eddy viscosity models tend to correctly model the mean down-scale energy dissipation, but poorly represent the sub-filter-stress terms on a local basis [62].

### *Dynamic Models*

The class of dynamic models builds upon the eddy viscosity type models, but allows the coefficient to vary in space and time. These models do not require the coefficient to be specified explicitly, but are computed dynamically during the LES calculation in response to the local turbulence conditions. The first such model was applied to the Smagorinsky eddy-viscosity model by Germano *et al.* [63], creating the dynamic Smagorinsky model.

The idea that  $C_S$  can be determined *in situ* during LES calculation is based on the assumption that the same Smagorinsky coefficient can be applied at the original filter scale and at a test filter level that is larger than the original filter width (typically twice as large). If the operation  $(\hat{\cdot})$  denotes filtering at the test scale  $\Delta_T$ , the “test stress tensor” can be computed as

$$\mathcal{T}_{ij}^{\Delta_T} = \widehat{\widetilde{u_i u_j}} - \hat{\widetilde{u_i}} \hat{\widetilde{u_j}}. \quad (1.22)$$

Note that the test-filtered sub-filter-stress has the following form

$$\hat{\mathcal{T}}_{ij} = \widehat{\widetilde{u_i u_j}} - \hat{\widetilde{u_i}} \hat{\widetilde{u_j}}. \quad (1.23)$$

Determination of the dynamic Smagorinsky coefficient is enabled using the *Germano identity* to calculate the resolved stress  $\mathcal{L}_{ij}$  as

$$\begin{aligned} \mathcal{L}_{ij} &= \mathcal{T}_{ij}^{\Delta_T} - \hat{\mathcal{T}}_{ij} \\ &= \widehat{\widetilde{u_i u_j}} - \hat{\widetilde{u_i}} \hat{\widetilde{u_j}}. \end{aligned} \quad (1.24)$$

Since the right hand side of the Germano identity can be explicitly calculated using the known  $\widetilde{u_i}$  fields by applying a test filter  $\Delta_T$ ,  $\mathcal{L}_{ij}$  is a known quantity. By modelling both  $\mathcal{T}_{ij}$  and  $\mathcal{T}_{ij}^{\Delta_T}$  using a Smagorinsky model (Equation 1.20) and assuming the same value of  $C_S$ , one can dynamically solve for the Smagorinsky constant at each point in the computational domain [63].

Performance of the dynamic Smagorinsky model shows a considerable improvement over the static version, including in shear flows [63] and in compressible flows [64]. Importantly, fluctuations in Smagorinsky coefficient allows for positive and negative energy transfer which simulates the forward- and back-scatter of energy [59]. However, large fluctuations in the coefficient are often observed, leading to numerical instabilities. Some sort of regularization is typically required for evaluation of the dynamic variables to avoid such instabilities (ex. smoothing, thresholding, averaging), resulting in a plethora of sub-models



determined by the regularization method [61]. A common approach is to average the dynamic constant over homogeneous directions (*ex.* planar cross-sections) which means that back-scatter or forward-scatter must occur uniformly over the averaging domain. While dynamic models are a definite improvement over the static eddy-viscosity models, their disadvantage is that they require increased computational time as two levels of filtering must be employed, as well as potentially averaging of the dynamic coefficient.

### *Scale Similarity Model*

Another class of models, termed *scale similarity*, were proposed by Bardina *et al.* [62] in an attempt to capture energy back-scatter  $\varepsilon_{\text{sfs}} > 0$ . The basic assumption in this model is that energy transfer between resolved and sub-filter scales is determined by eddies at the filter size  $\Delta$ ; these are simultaneously the largest sub-filter-scale eddies and smallest resolved eddies. In essence, the Bardina model assumes that the energy transferred through the filter scale is the same as that transferred through a slightly larger scale; hence, it is assumed that  $u_i = \tilde{u}_i$ . Similarly to the dynamic model, test filtering across the test filter scale  $\Delta_T > \Delta$  is performed, which results in

$$\begin{aligned} \mathcal{T}_{ij} &= \widehat{u_i u_j} - \tilde{u}_i \tilde{u}_j \\ &\approx C_L \underbrace{\left[ \widehat{\tilde{u}_i \tilde{u}_j} - \hat{\tilde{u}}_i \hat{\tilde{u}}_j \right]}_{\mathcal{L}_{ij}}. \end{aligned} \quad (1.25)$$

Here, the test filter is again at a larger scale than the original scale ( $\Delta_T > \Delta$ ). The separation between  $\Delta_T$  and  $\Delta$  was referred to as the *transfer range* by Bardina *et al.* [62] and is typically narrow (i.e.  $\Delta_T = 2\Delta$ ). Effectively, Bardina has assumed that the energy transfer between the resolved scales and the sub-filter scales occurs through the transfer range. Since the separation between the original and test filter scales is small, the local instantaneous energy transfer across  $\Delta_T$  is proportional to the local instantaneous energy

transfer across  $\Delta$ , i.e.

$$\mathcal{T}_{ij} = C_L \mathcal{L}_{ij}. \quad (1.26)$$

Modeled SFS stress in *a priori* tests using the scale similarity model exhibits a relatively high correlations with the exact SFS stress [59, 65]. Most importantly, these models allow for back-scatter of energy, making it a viable model for compressible and reacting flows where reversal of energy cascade may be important. Moreover, the SFS stress term modeled by scale similarity is Galilean invariant, whereas the those provided by eddy viscosity or dynamic models are not [66].

While the predictions of the SFS stresses is generally good, the scale similarity model does not dissipate enough energy [59, 61]. To remedy this issue, mixed models are used, which combine the scale similarity model with Smagorinsky model [62]. This allows the scale similarity portion of the model to predict energy back-scatter instantaneously, while the added eddy viscosity ensures sufficient energy dissipation to occur [65]. In general, mixed models give much improved correlations while allowing for adequate dissipation in non-reacting flows [61].

## 1.6 Inter-scale Energy Transfer

Practically speaking, the interest in the direction and magnitude of cross-scale energy transfer arises from the need in LES to close the residual stress-tensor  $\mathcal{T}_{ij} \equiv \bar{\rho}(\widetilde{u_i u_j} - \tilde{u}_i \tilde{u}_j)$ . It is therefore necessary to understand the physical processes governing  $\mathcal{T}_{ij}$  and how they depend on the local flow conditions and the filter scale. Models for  $\mathcal{T}_{ij}$  are generally based on energy transfer phenomenology and the constant density turbulence theories are predominantly relied upon to motivate such models.

The physics of constant density turbulence is typically described by the phenomenology of Richardson [14] and Komogorov's equilibrium theories [19, 21], as described in Section 1.3. Figure 1.5 shows a representative energy spectrum ( $E(k)$ ), with  $k$  the wavenum-

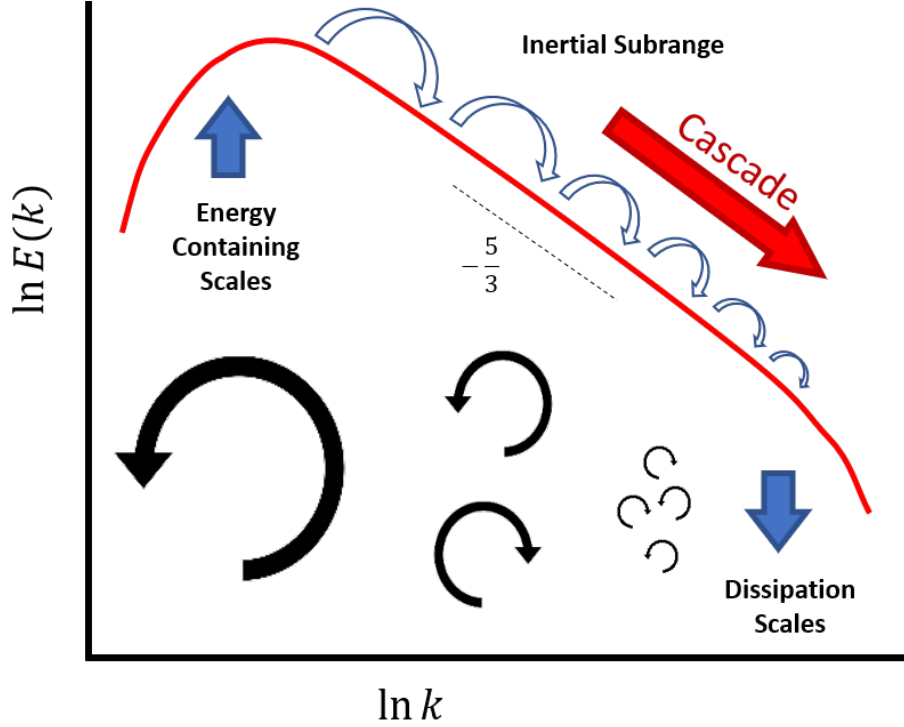


Figure 1.5: Model energy spectrum for homogeneous isotropic turbulence.

ber) observed in non-reacting HIT, from which key observations can be made. Firstly, turbulent kinetic energy is created by the mean fluid dynamic shear at the largest scales of motion (i.e.  $\ell$ ). The largest scales of turbulence (low wavenumbers) contain most of the energy; however, the details of the spectrum at low wavenumbers differs between various configurations. Secondly, the kinetic energy is transferred to subsequently smaller scales by non-linear advection in a non-dissipative manner in the middle range of the wavenumber range (i.e. inertial range). There is a power-law behaviour with slope  $d = -\frac{5}{3}$  in accordance with Equation 1.9. Finally, at high wavenumbers, the spectra decays more rapidly as the kinetic energy is dissipated by viscous action. Since the energy is input at the largest scale and energy is dissipated at the smallest scales, the overall transfer of turbulent kinetic energy occurs in the ‘forward’ direction.

As a result, most LES models predict a mean forward energy cascade; formulation of some models, such as the popular Smagorinsky eddy viscosity model, *only* allow the forward scatter of energy from large to small scales [3]. The mean forward cascade has

been confirmed in numerous flows [13]; however, the classical turbulence theories may not be valid in reacting flows since combustion enables mechanisms of turbulence production at the length scales of the flame, which are generally smaller than the integral scales in industry-relevant flows, and thermal expansion (dilatation) provides a mechanisms to transfer this energy to larger scales.

Recent DNS studies of planar premixed flames propagating in HIT, focusing on cross-scale kinetic energy transfer in turbulent premixed reacting flows, have identified significant deviations from equilibrium forward cascade behavior, including observation of mean backscatter. In the flame studied by Towery *et al.* [41], they noted significant variation of turbulent kinetic energy spectrum across the flame brush and observed reversal of advective energy transfer at scales of the laminar flame thickness. In a supersonic mixing layer, O’Brien *et al.* [67] studied the effects of compressibility and combustion on the dynamics of backscatter, finding that backscatter was strongly correlated to volumetric expansion. Based on scaling arguments, O’Brien *et al.* [68] hypothesized that backscatter should be significant for low to moderate turbulence intensities, roughly corresponding to the thin-reaction-zones regime of turbulent premixed combustion for flames in HIT. Studying similar conditions to Towery *et al.* [41], they used physical space analysis to identify combustion-induced mean backscatter when data were conditioned on the reaction progress variable  $c$ . Kim *et al.* [69] studied the same configuration, but at  $Ka \approx 70$  and  $Da \approx 0.3$  using a wavelet analysis method. They also reported an increase in the kinetic energy at small scales inside the flame, with the small scales becoming the donor of energy to larger scales at these locations. These various studies also highlighted the predominant roles of convective and pressure-gradient transfer terms in controlling the observed behaviors.

Clearly, the DNS evidence suggests that potentially significant small-to-large scale kinetic energy transfer occurs within the instantaneous premixed flames across a range of Karlovitz numbers that is relevant to practical devices. However, this has not yet been experimentally verified and, as pointed out by Kim *et al.* [69], it is important to consider (i)

different parameter spaces than are accessible to the DNS; (ii) realistic chemistry (beyond single-step Arrhenius models); and (iii) more practical configurations, including those with mean pressure gradients and shear flows.

In the literature, the behavior of the kinetic energy dynamics is studied using wavelets [69], in spectral space through application of the Fourier transform [41], or in physical space through spatial filtering of the velocity fields [67, 68]. The first two methods allow for direct analysis of interaction between pairs of scales; however, the Fourier space method requires homogeneity and periodicity in the domain – preventing analysis of non-planar flames – and the wavelet analysis is very challenging to perform on experimentally acquired data. The physical space approach does not provide any information on the interaction between the pairs of scales; however, it enables for explicit identification of physical processes associated with the cross-scale energy by studying the filtered transport equations. Moreover, the physical space method does not require homogeneity and periodicity in the test domain, making it possible to study more complex flame shapes experimentally.

The physical-space analysis of cross-scale energy transfer involves performing spatial filtering to separate the large and small scale dynamics; Favre filters are often used to simplify the analysis of the governing equations in compressible and reacting flows. The transport equation for the filtered kinetic energy of the flow ( $k = 2^{-1}\tilde{u}_i\tilde{u}_i$ ) is obtained by multiplying the filtered Navier-Stokes equation by the filtered velocity [68]:

$$\frac{\partial k}{\partial t} + \tilde{u}_i \frac{\partial k}{\partial x_i} = \underbrace{-\frac{\tilde{u}_i}{\bar{\rho}} \frac{\partial \bar{p}}{\partial x_i}}_{\alpha_p} + \underbrace{\frac{\tilde{u}_i}{\bar{\rho}} \frac{\partial \bar{\tau}_{ij}}{\partial x_j}}_{\alpha_\nu} - \underbrace{\frac{\tilde{u}_i}{\bar{\rho}} \frac{\partial \mathcal{T}_{ij}}{\partial x_j}}_{\alpha_{\text{sfs}}}. \quad (1.27)$$

The three terms on the right hand side of Equation 1.27 ( $\alpha_p$ ,  $\alpha_\nu$ , and  $\alpha_{\text{sfs}}$ ) represent the work done by the resolved pressure, resolved viscous shear, and the unresolved turbulent stresses, respectively.

A similar equation for the sub-filter-scale kinetic energy ( $k_{\text{sfs}} = 2^{-1}(\widetilde{u_i u_i} - \tilde{u}_i \tilde{u}_i)$ ) may be obtained by subtracting Equation 1.27 from the equation for filtered kinetic energy of

the full flow ( $K = \frac{1}{2}\widetilde{u_i u_i}$ ):

$$\begin{aligned} \frac{\partial k_{\text{sfs}}}{\partial t} + \tilde{u}_i \frac{\partial k_{\text{sfs}}}{\partial x_i} = & \underbrace{\frac{1}{\bar{\rho}} \left( \tilde{u}_i \frac{\partial \bar{p}}{\partial x_i} - \overline{u_i \frac{\partial p}{\partial x_i}} \right)}_{\alpha_p^{\text{sfs}}} + \underbrace{\frac{1}{\bar{\rho}} \left( u_i \frac{\partial \tau_{ij}}{\partial x_j} - \tilde{u}_i \frac{\partial \bar{\tau}_{ij}}{\partial x_j} \right)}_{\alpha_\nu^{\text{sfs}}} \\ & - \underbrace{\frac{1}{\bar{\rho}} \frac{\partial}{\partial x_i} (\bar{\rho} \widetilde{u_i K} - \bar{\rho} \tilde{u}_i \tilde{K})}_{\phi_{\text{sfs}}} - \alpha_{\text{sfs}}, \end{aligned} \quad (1.28)$$

where  $\alpha_p^{\text{sfs}}$  is the sub-filter-scale pressure-velocity gradient correlation,  $\alpha_\nu^{\text{sfs}}$  is sub-filter viscous work, and  $\phi_{\text{sfs}}$  is an unclosed flux term that contains a filtered product of three velocities.

There exists a two-way connection between the transport of  $k$  and  $k_{\text{sfs}}$ , via  $\alpha_{\text{sfs}}$ , which appears with opposite signs in Equation 1.27 and Equation 1.28. The sign convention implies that  $\alpha_{\text{sfs}} < 0$  is associated with the classical – downscale – energy cascade; upscale backscatter is represented by  $\alpha_{\text{sfs}} > 0$ . It should be noted that,  $\alpha_{\text{sfs}}$  is related to SFS ‘dissipation’  $\varepsilon_{\text{sfs}}$  via  $\varepsilon_{\text{sfs}} = -\bar{\rho}^{-1} \partial_j (\mathcal{T}_{ij} \tilde{u}_i) - \alpha_{\text{sfs}}$ ; in constant-density HIT, the prevailing mechanism of resolved/SFS kinetic energy transfer generally is given by  $\varepsilon_{\text{sfs}}$ . However, as shown by O’Brien *et al.* [68],  $\alpha_{\text{sfs}}$  is more expedient to identify energy transfer across the filter scale in systems with thermal expansion.

O’Brien *et al.* [68] observed a strong correlation between the SFS kinetic energy and SFS pressure work,  $\alpha_p^{\text{sfs}}$ , inside the flame. That is,  $\alpha_p^{\text{sfs}}$  acted as an energy source due to thermal expansion, leading to an increase in the SFS kinetic energy and enabling the transfer of excess energy to the resolved scales. In the planar flame studied by O’Brien *et al.* [68], the pressure gradients were primarily associated with the pressure decrease across the flame. However, practical combustor geometries frequently exhibit large-scale pressure gradients due to the mean flow, which often are stronger than those induced by the flame. It therefore is not unreasonable to expect that flow-induced pressure gradients can have a significant impact on the pressure-work, leading to larger SFS kinetic energy and increased

back-scatter.

The above discussion highlights the recent developments in the research of inter-scale energy transfer, highlighting the important roles of pressure-work and dilatation on modification of the classical energy cascade in premixed turbulent combustion. Nevertheless, the majority of research studies were performed on simple flames, in the absence of realistic flow features, and were done numerically with simplified reaction mechanisms. Further research is required to experimentally verify these findings and extend the research to practical combustor geometries.

## 1.7 Hypothesis and Objectives

The literature indicates that inter-scale energy transfer in turbulent combustion does not necessarily follow the same phenomenology as in non-reacting incompressible turbulence. Specifically, the evidence points to turbulence production and reversal of the classical down-scale energy transfer at scales around  $\delta_L^0$ . The above discussion has also identified the significance of thermal expansion and fluctuating pressure-work in transport of turbulent kinetic energy, which appears to strongly depend on local conditions and flow configuration. Given that pressure fields in practical turbulent combustors can arise from a variety of geometry- and condition-specific sources, this would potentially require a fundamental re-examination of quasi-universal turbulence closure models for the purposes of combustion.

However, quantification of cross-scale energy transfer has only been studied using DNS of flames in incompressible HIT at limited Re and without presence of potentially critical pressure effects. Since there is a very limited set of experimental efforts in these topics, there is a need for experimental quantification of (1) up-scale momentum/energy transfer, (2) the range of scales over which energy backscatter may occur, (3) the controlling parameters, and (4) whether these effects are significant in more practical configurations. This research gap thus presents an excellent opportunity to study inter-scale energy transfer in a

practical flow configuration.

Given previous observations of inter-scale energy dynamics, the direction and magnitude of inter-scale energy transfer is expected to depend on the magnitude of heat release from combustion, intensity of turbulence in the reactant mixture, and presence of large-scale pressure fields. The hypothesis to be tested in the presented work is that the magnitude of observed energy backscatter will (i) increase with the magnitude of the persistent pressure gradient induced over the flame region by the large-scale fluid dynamics, (ii) will increase with magnitude of heat release across the flame, and (iii) decrease in larger  $Re_T$  flows.

The effect of large-scale pressure gradients over the flame on  $\alpha_{sfs}$  is motivated by the DNS observations of flames in HIT. The pressure gradients driving the pressure-work in such flames arise solely from the turbulent eddies and from the expansion across a low Mach number deflagration, which become decreasingly significant at high  $Ka$ . Systems that induce the pressure gradients through other means have the potential to exhibit significant production of turbulence at scales of laminar flame thickness and at conditions beyond what would be predicted from flames in low Mach number HIT. One mechanism through which this can occur is baroclinic torque vorticity production [56]. In such situations, interactions between the flame-induced density gradients and the pressure field may give rise to considerable creation of turbulence at the flame scales, as opposed to the large-scale turbulence production by mean shear. The resultant excess energy in the sub-filter scales (as compared to equivalent non-reacting turbulence) can potentially lead to increased backscatter, as demonstrated by O’Brien *et al.* [68]. The first point of the hypothesis can thus be summarized as

$$(i) \quad \frac{\partial \alpha_p^{sfs}}{\partial |\langle \nabla p \rangle|} > 0 \quad \text{and} \quad \frac{\partial \alpha_{sfs}}{\partial |\langle \nabla p \rangle|} > 0, \quad (1.29)$$

where  $\langle p \rangle$  is the mean pressure field;  $\langle \cdot \rangle$  denotes ensemble averaging. Specifically, the small-scale pressure-work and  $\alpha_{sfs}$  will increase with the magnitude of the gradients associated with the mean pressure fields. The most common sources of large-scale pressure



gradients that can potentially affect the turbulence dynamics in low Mach number flames are associated with the large-scale flow features and the confinement geometry. The former frequently arises due to a coherent rotational fluid motion, such as in rotating (or swirling) flows, inside recirculation zones, or in large vortices generated by flow instabilities. The latter typically uses the geometrical constraints of the system to achieve large-scale pressure gradients in the system, such as in nozzles and diffusers. In cases when  $\langle \nabla p \rangle$  is stronger than  $\nabla p$  associated with the flames and small-scale turbulence, flame-scale turbulence production via  $\alpha_p^{\text{sfs}}$  may be significantly enhanced.

The amount of heat release due to combustion can similarly have a significant effect on the energy dynamics in turbulent flows. In cases when the rate of chemical energy release at the scales of laminar flame thickness is larger than the rate associated with turbulence production by mean shear at largest turbulent length scales, it is possible to overwhelm the classical downscale energy cascade with energy backscatter. It is thus entirely plausible to expect a larger amount of energy backscatter in weakly turbulent flames with high heat-release rates (ex. in  $\text{CH}_4$ -air flames at stoichiometric conditions). Conversely, in highly turbulent flows, the rate of large-scale turbulence production is presumed to be larger than heat-release rate; the magnitude of energy backscatter is expected to decrease with turbulence intensity or  $\text{Re}_T$ . As a result, the imbalance between rates of heat-release and turbulence production by mean shear can result in varying  $\alpha_{\text{sfs}}$ . This is summarized by points (ii) and (iii) of the hypothesis; mathematically,

$$(ii) \quad \frac{\partial \alpha_{\text{sfs}}}{\partial \dot{q}} > 0 \quad (1.30)$$

$$(iii) \quad \frac{\partial \alpha_{\text{sfs}}}{\partial \text{Re}_T} > 0. \quad (1.31)$$

For premixed hydrocarbon-air flames, and  $\text{CH}_4$ -air specifically, the heat-release rate is maximum in near-stoichiometric mixtures. Consequently, equivalence ratio can be used as a proxy for heat-release rate in such flames; the variation of  $\alpha_{\text{sfs}}$  with  $\dot{q}$  can be re-expressed

as

$$\frac{\partial \alpha_{\text{sfs}}}{\partial \phi} > 0 \quad \text{for } \phi < 1, \text{ and} \quad (1.32)$$

$$\frac{\partial \alpha_{\text{sfs}}}{\partial \phi} < 0 \quad \text{for } \phi > 1. \quad (1.33)$$

The overarching goal of research presented in this thesis is to experimentally determine the relationship between the pressure field, turbulence conditions, heat-release rate, and inter-scale energy transfer in an aerospace-relevant configuration. The research questions that will be addressed in the proposed work are

1. At what conditions, locations, and scales does significant energy back-scatter occur?
2. What are the underlying physical mechanisms responsible for energy back-scatter, and how are they related to (i.e. scale with) the controlling parameters ( $\text{Re}_T$ , average  $|\nabla p|$ , and  $\phi$ ; equivalently  $\text{Ka}$  and average  $|\nabla p|$ )?

The general approach is to measure the inter-scale energy transfer while systematically varying the available independent parameters. This strategy will involve adjustments of the mean pressure field (specifically the magnitude of the flow-induced pressure gradient  $|\nabla p|$ ),  $\text{Re}_T$ , and the equivalence ratio ( $\phi$ ) over a range of values that represent the turbulent and thermochemical conditions in practical combustor configurations.

For each test condition, the specific objectives are to:

1. Perform simultaneous measurements of the 3D velocity and planar distribution of  $\text{CH}_2\text{O}$ .
2. Estimate physically-reasonable density and progress variable fields from the  $\text{CH}_2\text{O}$  measurements. If necessary, obtain estimates of the fully-resolved velocity fields.
3. Favre filter the experimental data and calculate  $\alpha_{\text{sfs}}$  as a function of scale.

Ultimately, the results may require a re-examination of LES closure paradigms for compressible reacting turbulence and aid in the development of physically-reasonable turbulence closure models for combustion. This work will provide a rigorous assessment of the extent to which current turbulence modelling paradigms hold in aerospace-relevant combustion, as well as the data necessary to develop and validate new models if required.

## CHAPTER 2

### EXPERIMENTAL APPROACH

Study of turbulence-flame interactions requires simultaneous knowledge of the turbulent velocity field and scalar fields that characterize premixed combustion, such as temperature or reacting species, at all points in space and time. Moreover, the range of length and time scales under highly-turbulent flow conditions requires correspondingly high spatial and temporal resolutions. The number of independent variables one must measure depends on the nature of the reactants and the complexity of the reaction mechanism. For example, the simplest description of  $\text{H}_2\text{-O}_2$  combustion requires 8 species and 40 reactions (20 elementary reactions in forward and reverse directions) [1], while the simplest  $\text{CH}_4\text{-O}_2$  combustion mechanism uses 25 species and 150 elementary reactions [70]. Higher-order hydrocarbons and more complex fuels require even larger number of species to fully describe its oxidation. Hence, one must measure hundreds of chemical species and fine scale 3D velocity fluctuations with sufficient accuracy to fully describe the evolution of reacting turbulence. This is not yet possible experimentally and most fundamental studies of turbulence-flame interactions rely on DNS of premixed flames in low Re number turbulence [34].

Experimentally, only a few of these variables are measured simultaneously. One of the popular approaches involves a combination of PIV and PLIF for velocity fields and species distribution, respectively. The former can provide either two (2C) or three (3C) components of velocity in either a plane (2D) or a three-dimensional (3D) volume, based on the type of PIV used. The latter measures the concentration of a target species in a certain energy state. The PLIF signal is typically used to detect the presence of target species in the flow, or to measure local concentration, temperature, pressure, or velocity. Furthermore, there are limitations in the temporal and spatial resolution of the measurements due to the capabilities of the equipment used; often one is prioritized over the other. For example, study of how

turbulent flames evolve often requires high repetition rate measurements (on the order of kilohertz) at the cost of spatial resolution, while the studies of kinematic and dynamic properties of stationary turbulence often focus on maximizing the spatial resolution (on the order of micrometers).

In this dissertation, measurements are performed simultaneously in statistically stationary turbulent swirl flames using high-resolution tomographic PIV and formaldehyde ( $\text{CH}_2\text{O}$ ) PLIF in two optical configurations. The first configuration uses macro lenses to view a larger field of view with ‘standard’ spatial resolution. This setup allows for measurement of cross-scale energy transfer across large length scales (several times larger than  $\delta_L^0$ ) and identification of large-scale coherent structures in the flow. In the second configuration, long-distance microscopes are used to view a smaller field of view while maximizing the spatial resolution. In this layout, cross-scale energy transfer across smaller length scales (on the order of  $\delta_L^0$  and smaller) can be evaluated. It is shown that the configuration with ‘standard’ resolution is not fully resolved (see Chapter 5), and hence only the second configuration is able to accurately measure  $\alpha_{\text{sfs}}$  across scales on the order of  $\delta_L^0$ . In both cases, TPIV provided 3C-3D velocity fields that allow for computation of the full velocity gradient tensor, which is required for evaluation of  $\alpha_{\text{sfs}}$  directly. The distribution of  $\text{CH}_2\text{O}$  was used to identify the edges of the instantaneous flame and approximate the local fluid density and reaction progress variable along the central plane of the TPIV volume. The details of the experiment and optical diagnostic techniques are provided below.

## 2.1 Experimental Configuration

The burner used is a gas turbine model combustor, shown in Figure 2.1, identical to that originally described by Meier et al. [71] but with the combustion chamber removed to prevent seed deposition on the windows from interfering with the measurements. The swirl burner was mounted onto a three-directional motor-driven translation stage (Velmex, 5  $\mu\text{m}/\text{step}$ ), which allowed examining different regions of interest without moving the com-

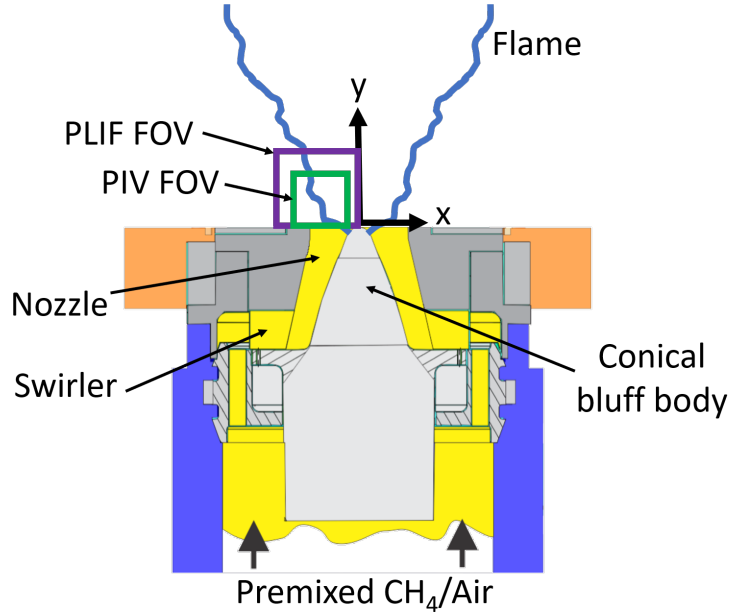


Figure 2.1: Swirl burner with measurement locations.

ponents of optical diagnostics. Air and fuel (methane) flow rates are metered using independent mass flow controllers (Brooks, 1% of set point); the reactants are premixed well upstream of the combustor plenum, passed through a fixed radial swirler, and expelled through a  $D_e = 27.85$  mm diameter nozzle having a conical bluff body along the center-line. The air was seeded with solid  $\text{Al}_2\text{O}_3$  particles for TPIV; the flow rate for the seeded air was also metered using a Brooks mass flow controller.

In practical devices, flame stability is one of the key considerations when designing a combustor. This usually requires the flame to be anchored at a desired location and be resistant to a variety of dynamical events, such as flashback, liftoff, and blowoff, over a range of operating conditions. The essential requirement for anchoring the flame in a usually turbulent flow is that the local turbulent flame speed matched the local mean flow velocity. This can be achieved through modification of the flow, combustor geometry, turbulent flame speed, or any combination of the above. Common methods of flame stabilization include the use of low-velocity bypass ports, refractory burner tiles, bluff-body flameholders, or through creation of recirculation zones in the flow [1].

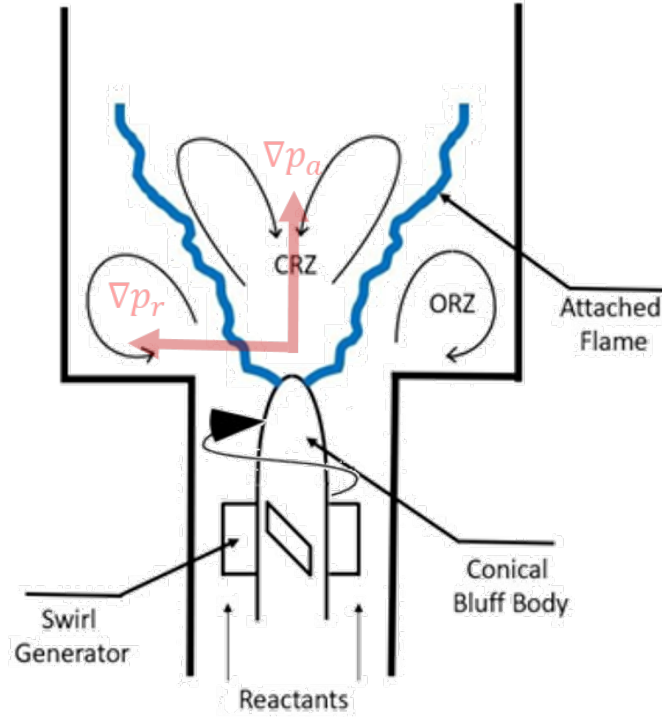


Figure 2.2: Schematic representation of a swirl stabilized combustor, showing the central and outer recirculation zones (CRZ and ORZ) and the associated pressure gradients [75].

Swirl stabilized combustion (SSC) is a popular flame stabilization technique in aeronautical gas-turbine engines because it increases the residence time inside the combustor of a given - usually constrained - length, while enhancing mixing close to the exit nozzle [72, 73]. Additionally, amounts of unburned hydrocarbons and soot in SSC are reduced, which makes it attractive to engine manufacturers in the face of increasingly stringent emission regulations [74]. Swirl-stabilized flames are typically compact in size, as compared to flames at equivalent thermal power but stabilized using other methods (ex. Bunsen or bluff-body stabilized flames). This reduces the overall weight of the combustor and consequently of the entire engine assembly.

Stabilization of the swirling flames is achieved through formation of recirculation zones by introducing a swirling velocity component to the incoming reactants, as shown in Figure 2.2. The geometry of SSC is such that the swirling vortex downstream of a dump plane undergoes a sudden expansion; the centripetal force of the swirling jet emitted from

the nozzle pushes the air-fuel mixture away from the center of the burner, inducing a low-pressure zone in the center and forming a radial pressure gradient. Axial expansion through the nozzle causes a decay in the tangential velocity and magnitude of the radial pressure gradient with downstream distance, thus forming a negative axial pressure gradient along the rotation axis of the burner. Formation of the central recirculation zone (CRZ) occurs when the adverse axial pressure gradient is sufficient to overcome the axial jet momentum [76]. In the case of confined combustion, outer recirculation zones (ORZ) also form between the swirling reactant jet and the combustion chamber, which allows the flame to stabilize in the outer shear layer at low bulk flow velocities.

Presence of the CRZ creates a region of low velocity at the nozzle exit, allowing the flame to stabilize there. Furthermore, the recirculation bubble transports hot combustion products and active chemical species to the flame root which leads to increased mixing of hot products and the reactant mixture. Thus a continuous ignition source exists at the nozzle exit, allowing for flame stabilization at flow rates that would not be possible in other flame configurations. However, recirculating swirling flows are only formed above a critical swirl number  $\mathcal{S}$ , which is defined as the ratio of the the axial flux of swirl momentum to the axial flux of axial momentum, i.e.

$$\mathcal{S} = \frac{\int_0^R \rho u_{ax} u_{\theta} r^2 dr}{R \int_0^R [\rho u_{ax}^2 + (p - p_{\infty})] r dr}, \quad (2.1)$$

where  $u_z$  and  $u_{\theta}$  are the axial and azimuthal velocity components and  $(p - p_{\infty})$  is the pressure difference between the swirling jet and the fluid at rest [77]. For low Mach number flows, contribution of the pressure term is very small compared to  $u_{ax}$  and its contribution to  $\mathcal{S}$  is generally neglected.

It is known that the swirl number can have significant effects on the mean flow field and flame dynamics. As discussed in the previous chapter, the magnitude of the imposed pressure gradient can potentially result in increased energy backscatter. In this thesis, the



magnitude of flow-induced pressure gradient is varied through modification of the swirl number. Three radial swirlers are considered, the geometry of which are shown in Figure 2.3; Table 2.1 summarizes the geometrical parameters of the three swirlers. The geometric swirl number ( $\mathcal{S}_g$ ) in Table 2.1 is the theoretical swirl number derived from the details of the swirler geometry; details of  $\mathcal{S}_g$  calculation for the radial swirler are shown in Appendix A. The angle of the radial vanes with respect to the radial coordinate is increased from  $19.4^\circ$  to  $34.0^\circ$ . Additionally, the width and height of individual channels was adjusted such that cross-sectional area of each channel is constant; this is required for  $\mathcal{S}_3$  specifically to ensure the channels do not overlap. Note, that  $\mathcal{S}_g$  is different from the measured swirl number  $\mathcal{S}$ . The swirl numbers are measured experimentally at the nozzle exit and the results are presented in Section 5.1.

## 2.2 Test Conditions

Due to the unique geometrical features of the SSC, explicit and *relatively independent* control of the magnitudes of turbulence intensity, mean pressure gradient, and density gradient are possible through separate manipulations of the jet velocity issuing from the nozzle ( $U_j$ ), the swirl number ( $\mathcal{S}$ ), and global equivalence ratio ( $\phi$ ). Variation in  $U_j$  can be interpreted in terms of the Reynolds number ( $Re = U_j D_e / \nu_r$ , where  $D_e$  is the nozzle exit diameter). As an example, low  $Re$  flow at a high  $\mathcal{S}$  will induce weak turbulence and a relatively strong gradients in the mean pressure field. It is noted that  $U_j$  and  $\mathcal{S}$  are not truly independent; however, a wide range of  $Re$  and pressure gradients can be achieved by manipulating  $U_j$  and  $\mathcal{S}$ . Changing  $\phi$  has a direct effect on the product temperature, flame speed, and laminar

Table 2.1: Geometrical parameters of the radial swirlers considered.

Swirler	Channel width (mm)	Channel height (mm)	$\theta$ (deg)	$\mathcal{S}_g$
$\mathcal{S}_1$	6 mm	11.3 mm	$19.4^\circ$	0.55
$\mathcal{S}_2$	6 mm	11.3 mm	$26.2^\circ$	0.75
$\mathcal{S}_3$	5 mm	13.6 mm	$34.0^\circ$	1.00

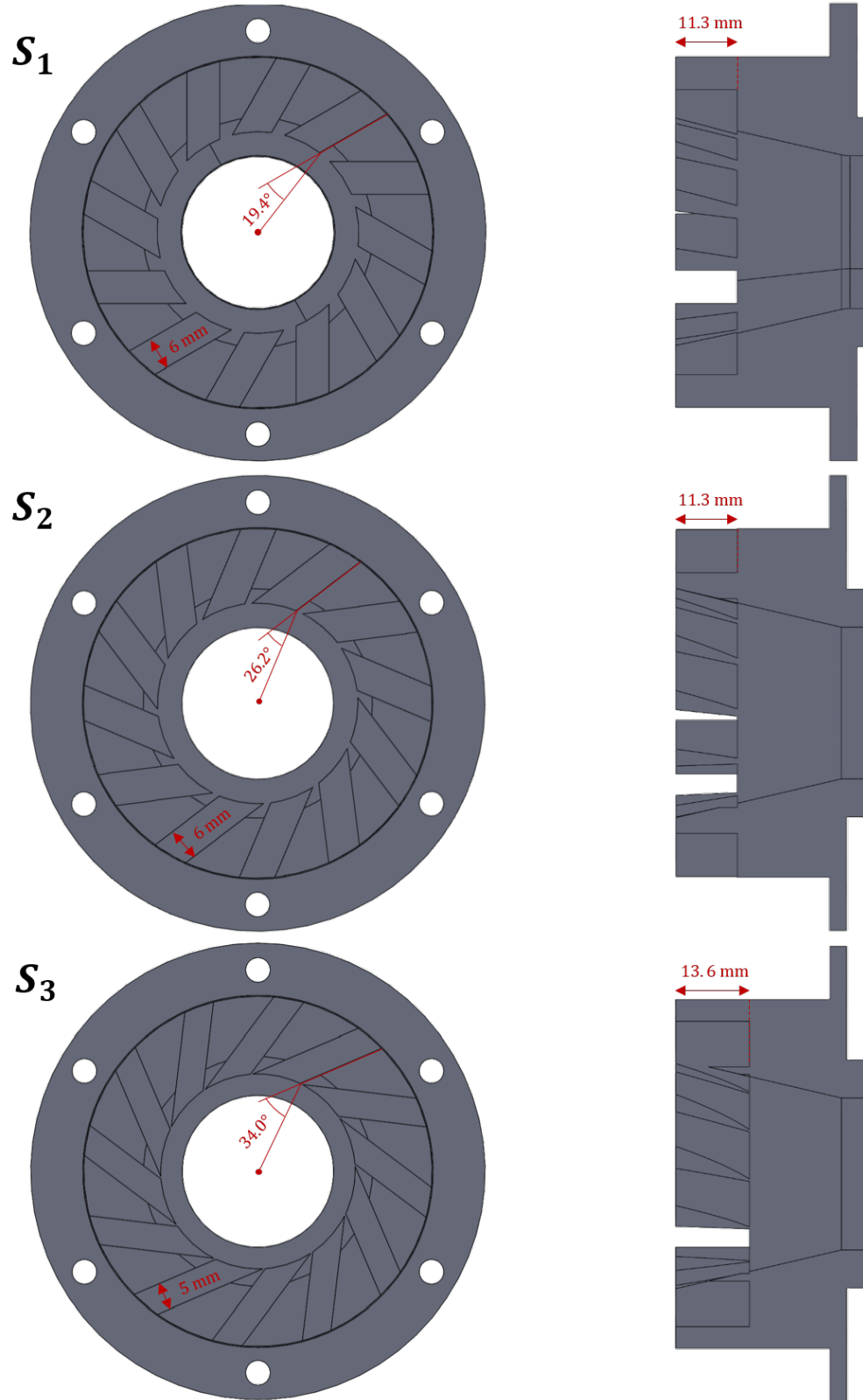


Figure 2.3: Geomerty of three radial swirlers used to vary the swirl number.

Table 2.2: Test conditions, using a methane-air mixture. Shaded cases represent data taken from an earlier experiment.

$\phi = 0.75$			$\phi = 0.85$			$\phi = 1.0$		
Case	$\mathcal{S}$	$U_j$ (m/s)	Case	$\mathcal{S}$	$U_j$ (m/s)	Case	$\mathcal{S}$	$U_j$ (m/s)
E075-S1-U04	$\mathcal{S}_1$	4	E085-S1-U05 E085-S1-U10 E085-S1-U12 E085-S1-U15 E085-S1-U20 E085-S1-U25 E085-S1-U27	$\mathcal{S}_1$	5	E100-S1-U05	$\mathcal{S}_1$	5
E075-S1-U05	$\mathcal{S}_1$	5		$\mathcal{S}_1$	10	E100-S1-U10	$\mathcal{S}_1$	10
E075-S1-U10	$\mathcal{S}_1$	10		$\mathcal{S}_1$	12	E100-S1-U12	$\mathcal{S}_1$	12
E075-S1-U12	$\mathcal{S}_1$	12		$\mathcal{S}_1$	15	E100-S1-U20	$\mathcal{S}_1$	20
E075-S1-U15	$\mathcal{S}_1$	15		$\mathcal{S}_1$	20			
				$\mathcal{S}_1$	25			
				$\mathcal{S}_1$	27			
E075-S2-U05	$\mathcal{S}_2$	5	E085-S2-U05	$\mathcal{S}_2$	5	E100-S2-U05	$\mathcal{S}_2$	5
E075-S2-U10	$\mathcal{S}_2$	10	E085-S2-U10	$\mathcal{S}_2$	10	E100-S2-U10	$\mathcal{S}_2$	10
E075-S2-U12	$\mathcal{S}_2$	12	E085-S2-U12	$\mathcal{S}_2$	12	E100-S2-U12	$\mathcal{S}_2$	12
			E085-S2-U17	$\mathcal{S}_2$	17	E100-S2-U20	$\mathcal{S}_2$	20
E075-S3-U05	$\mathcal{S}_3$	5	E085-S3-U05*	$\mathcal{S}_3$	5	E100-S3-U05	$\mathcal{S}_3$	5
E075-S3-U10	$\mathcal{S}_3$	10	E085-S3-U10	$\mathcal{S}_3$	10	E100-S3-U10	$\mathcal{S}_3$	10
E075-S3-U12	$\mathcal{S}_3$	12	E085-S3-U12	$\mathcal{S}_3$	12	E100-S3-U12	$\mathcal{S}_3$	12
			E085-S3-U20	$\mathcal{S}_3$	20	E100-S3-U20	$\mathcal{S}_3$	20

flame thickness, which allows to control the magnitude of the density gradient across the flame, and consequently the magnitude of pressure-work.

Table 2.2 summarizes the set of operating conditions considered in this work. Equivalence ratio is varied between  $\phi = 0.75$ ,  $\phi = 0.85$ ,  $\phi = 1.00$  to achieve two fuel-lean mixtures and one stoichiometric mixture. Swirl number is varied by physically replacing the radial swirler in the burner and takes on three distinct values:  $\mathcal{S}_1$ ,  $\mathcal{S}_2$ , and  $\mathcal{S}_3$ . All three swirlers have medium-to-high swirl numbers ( $\mathcal{S} \geq 0.55$ ) which ensures formation of the central recirculation zone and stabilization of the flame [57]. The jet velocity is defined as  $U_j^2 = U_b^2(\mathcal{S}^2 + 1)$ , where the bulk flow velocity  $U_b$  is determined from the ratio of volumetric flow rate and the nozzle exit area. It is also assumed that the characteristic swirl velocity  $U_\theta$  and  $U_b$  are the dominant velocity components at the nozzle exit and are related via  $\mathcal{S} \propto U_\theta/U_b$ . The jet velocity is varied between 4 m/s to 20 m/s. Furthermore, an additional measurement is taken for each entry in Table 2.2 at non-reacting conditions with an

equivalent flow rate (i.e. same  $Re$ ). This enables comparison of results between reacting and non-reacting conditions.

A brief discussion regarding the completeness of the operating conditions in Table 2.2 is warranted. Firstly, the test matrix appears sparsely populated. The goal was to construct the test matrix such that comparisons across one variable are possible, while holding the other two constant. However, preliminary testing has demonstrated that the flame was either unstable or was blown-off at high jet velocities, especially for lean reactant mixtures ( $\phi = 0.75$  and  $\phi = 0.85$ ). As a result, three primary jet velocities at which a stable flame exists at all  $\phi$  and  $\mathcal{S}$  were targeted ( $U_j = 5, 10$ , and  $12$  m/s) as base velocities. At each combination of  $\phi$  and  $\mathcal{S}$ , the highest jet velocity (above  $U_j = 12$  m/s but below  $U_j = 20$  m/s) at which the flame is stable was recorded. This additional test condition represents the most turbulent flame prior to flame blow-off and is meant to demonstrate the highly turbulent conditions. Secondly, there are more test points for  $\mathcal{S}_1$  than for other swirler numbers. The extra cases, which are shaded in Table 2.2, represent prior measurements that were taken at an earlier time using an identical experimental setup and laser diagnostics for another study [56]. However, the data is also useful for the purposes of this dissertation and is therefore included here for completeness.

## 2.3 Laser Diagnostics

Experiments were performed using simultaneous TPIV and  $CH_2O$  PLIF in unconfined premixed swirl flames. All measurements are performed directly above the nozzle as shown in Figure 2.1. It should be noted that only the left branch was imaged with a smaller field of view to increase the spatial resolution of the measurements. The laser diagnostics configuration is shown in Figure 2.4. The experimental measurements are performed in two blocks: the “standard-resolution” dataset is obtained using standard macro lenses to maximize the filter scale during data analysis; the second “high-resolution” dataset uses long-distance microscopes to maximize the spatial resolution of the velocity field. All of

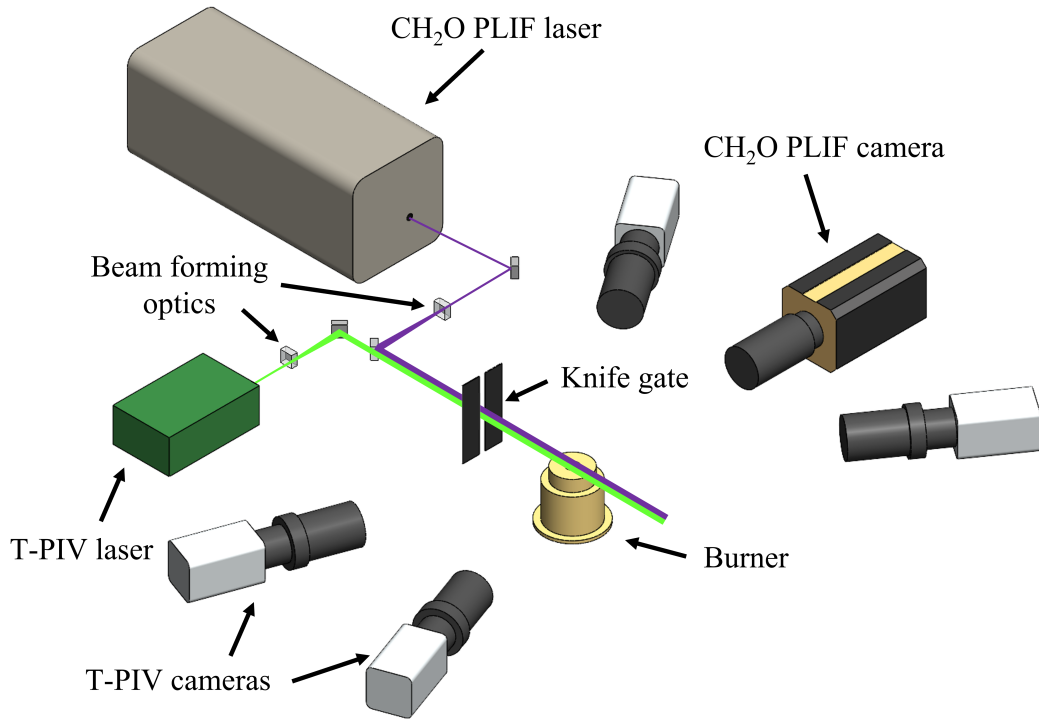


Figure 2.4: Laser diagnostics for “standard-resolution” velocity measurement. Long-distance microscopes replace TPIV camera lenses in “high-resolution” TPIV configuration.

the measurements are first taken under “standard-resolution”, followed by measurements in a “high-resolution” configuration. A total of 1,000 simultaneous TPIV and PLIF measurements are made at each test case.

### 2.3.1 Tomographic Particle Image Velocimetry

Measurements of the flow field are necessary for understanding various fluid dynamic behaviours, including inter-scale energy transfer. PIV is a non-intrusive technique used for measurement of instantaneous velocity fields [78]. At its core, PIV is measurement of tracer particle displacement, as shown in Figure 2.5. The flow is seeded with tracer particles and the plane of interest is illuminated twice in a short time interval. Monochromatic light from a pulsed laser is typically used as the light source in PIV experiments [78, 79]. The laser beam is shaped into a thin plane using a set of beam-forming optics, which il-

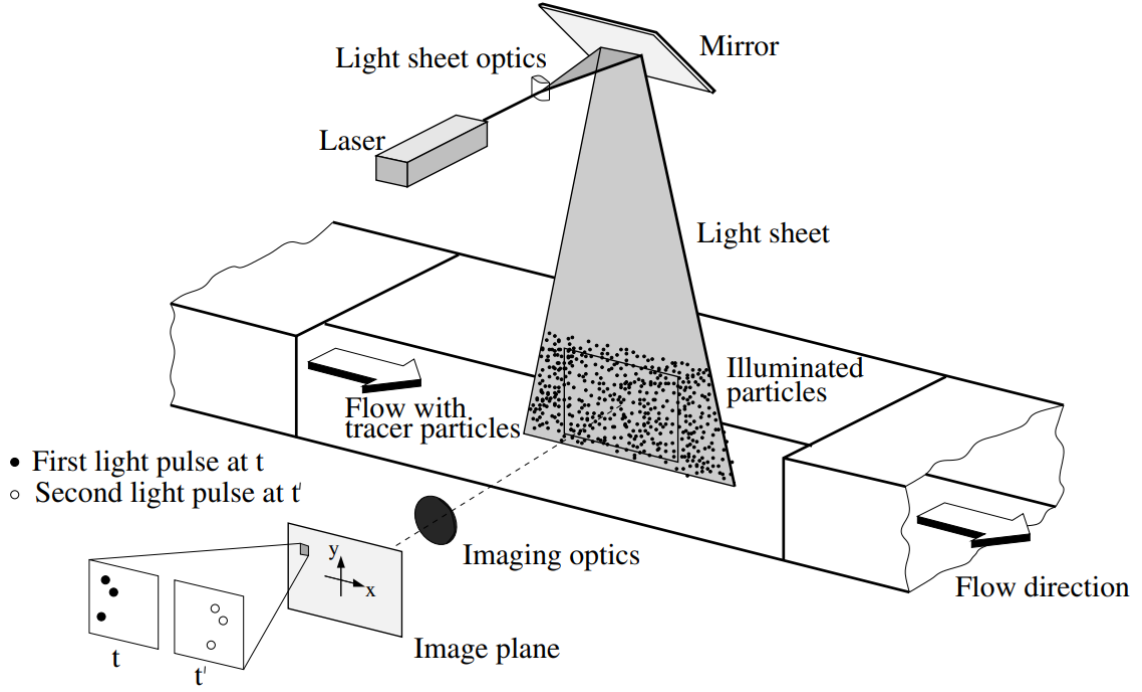


Figure 2.5: The basic principle of PIV [78].

illuminates the region of interest inside the flow. One or more recording devices (typically digital cameras) capture the light scattered by the tracer particles onto a sequence of images, which are used to evaluate the particle displacement during the elapsed time interval. Both frames are subdivided into small interrogation regions and the displacement of particles within each region is measured through cross-correlation of these regions to find the mean displacement that gives the maximum correlation [79].

In its simplest configuration, PIV uses a single camera as shown in Figure 2.5, and captures the velocity field on the illuminated plane (i.e. 2D). Moreover, only two in-plane components of the velocity vectors are captured, as measurement of out-of-plane velocity is not possible with a single camera. Stereoscopic PIV (SPIV) is a variant of PIV that uses two cameras with independent lines-of-sight to measure all three velocity components along the plane of interest. There exists a disparity between two velocity fields obtained by each camera, which allows one to compute the plane-normal velocity component that causes the disparity [80]. However, the measurements are constrained to a two dimensional

plane, similar to PIV.

Unfortunately, even SPIV is not sufficient to fully describe the instantaneous state of turbulence, which is intrinsically three-dimensional. To do so, all nine components of the velocity gradient tensor must be known to compute key fluid dynamic quantities, such as vorticity, strain-rate, divergence, and tensor invariants. Using SPIV, only six (in-plane) derivatives can be calculated from the measured velocity field; the out-of-plane gradients remain unknown. While SPIV may be sufficient for study of axisymmetric and quasi-2D flows, most realistic flows require a three dimensional diagnostic.

Several 3D velocimetry techniques have been developed, with TPIV emerging as a popular method to obtain high quality velocity measurement in a variety of flows [81, 82]. Unlike in PIV and SPIV setups, TPIV involves illuminating the flow using a laser slab, with a thickness typically up to one-quarter the height of the illuminated volume [83]. Three or more cameras (typically four) simultaneously capture the laser scattering from seed particles at different and independent viewing angles. These views are used to obtain three-dimensional representation of the particle field (tomograms) via an iterative algebraic tomographic reconstruction technique such as the Multiplicative Algebraic Reconstruction Technique (MART) [83]. The analysis of particle motion within the pair of tomograms is performed by three-dimensional cross-correlation, similar to PIV and SPIV.

To date there have been many studies that utilized TPIV in measurement of non-reacting and reacting flows. For example TPIV was used to study the interaction between turbulent boundary layers and shock waves [84], vorticity generation in a cylindrical wake [85]; Violato *et al.* [86] used TPIV to explore the three dimensional pattern of the flow transition of jets issued from a circular and chevron-exit nozzle jet and its implications on sound production. In reacting flows, TPIV was used to examine vorticity-strain rate interaction in turbulent partially premixed jet flames [6], measure turbulent flame structure and dynamics [8], and study lifted jet flames [87]. The use of TPIV in reacting flows presents an additional set of challenges, such as variation of seeding density across the flame front, increased

imaging noise, and beam steering through index of refraction gradients in the flame [8].

Currently available PIV systems have proved to be adequate for capturing the large-scale flow features; however, there are further difficulties in properly characterizing small-scale flow behaviour in high Re number flows. For an accurate description of small scale turbulent motion, a spatial resolution of three times the Kolmogorov scale ( $3\eta$ ) is required [88, 89]. In this context, micro-PIV ( $\mu$ -PIV) is a promising technique that enables measurement of small scale fluid behaviour.

$\mu$ -PIV is yet another variant of PIV which offers a sufficiently high spatial resolution to describe the micro-scale behavior of the flow by using a microscope instead of standard imaging lenses [78].  $\mu$ -PIV was introduced in 1998 to measure velocity fields in micro-scale fluidic devices [90], and can achieve the spatial resolution in the range from  $10^{-4}$  to  $10^{-7}$  m [78]. Microscopes offer high magnification and numerical aperture, but suffer from a narrow depth-of-field and a limited field-of-view. Out-of-plane particle motion can also have a significant impact on particle image blur and the quality of cross-correlation because the thickness of common laser sheets usually exceeds the narrow depth of field [91].

### *Optical Layout*

In this thesis, both TPIV and  $\mu$ -TPIV setups are used to maximize the dynamic range in space and in velocity. The  $\mu$ -TPIV setup is identical to the TPIV setup shown in Figure 2.4 but the standard lenses are replaced with long-distance microscopes to achieve a higher spatial resolution. Two measurements are performed for each operating test condition - one using TPIV and the other using  $\mu$ -TPIV. Since the two datasets are obtained independently and at a low repetition rate, the results can only be interpreted in a statistical sense.

The TPIV system consisted of four high-resolution sCMOS cameras (Andor Zyla 5.5 and Neo 5.5,  $2048 \times 2048$  px,  $6.5 \mu\text{m}$  pixel size) and a dual head Nd:YAG laser (Quintel Evergreen 200, 532 nm, 10 Hz, 200 mJ/pulse). A series of lenses and a knife edge gate shaped the beam into a collimated rectangular beam with a thickness of 5.5 mm for TPIV



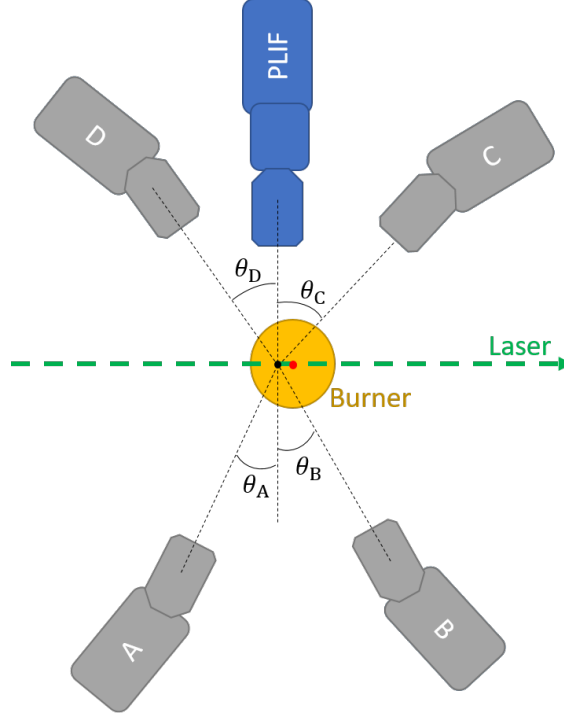


Figure 2.6: Camera orientations with respect to the laser propagation direction.

and 1 mm for  $\mu$ -TPIV. The thickness of the sheet is defined as the full-width-half-maximum (FWHM) of the intensity; the thickness was measured using a beam-profiling camera as demonstrated later in this section. The two pulses were separated by a variable time delay ( $3 \mu\text{s}$  -  $16 \mu\text{s}$  for TPIV, and  $1 \mu\text{s}$  -  $7 \mu\text{s}$  for  $\mu$ -TPIV), which was set appropriately for each test condition to allow sufficient particle displacement between TPIV frames for accurate velocity calculation. Mie scattering from the  $\text{Al}_2\text{O}_3$  particles, with a Stokes number below 0.03, was captured by the imaging system. The Stokes number was based on a conservative Kolmogorov time scale, which resulted in a flow tracking accuracy better than 1% [92].

Table 2.3: Orientations of cameras around the domain of interest.

Configuration	$\theta_A$	$\theta_B$	$\theta_C$	$\theta_D$	$\theta_{\text{PLIF}}$
Low-resolution	$13^\circ$	$14^\circ$	$31^\circ$	$31^\circ$	$0^\circ$
High-resolution	$12^\circ$	$14^\circ$	$19^\circ$	$20^\circ$	$0^\circ$

Each camera was equipped with either a macro lens (Tamron, 180 mm,  $f/\# = 2.8$ ) for standard-resolution data or an infinity-corrected long-distance microscope (Infinity K2,

CF-1/B objectives,  $f/\# = 38$ ) for high-resolution data. The cameras were positioned on both sides of the laser sheet as shown in Figure 2.6. The viewing angles between  $12^\circ$  and  $31^\circ$  to ensure cameras had independent views of the flow and minimize the reconstruction error; exact values are shown in Table 2.3. The lenses/microscopes were mounted to the cameras using Scheimpflug adapters (LaVision) to prevent image blurring during off-axis imaging.

### *Imaging Lenses*

The difference between the use of a standard lens and a microscope is in the magnification, and consequently spatial resolution, of the resultant image. Standard lenses typically have magnification  $M \leq 1$ , while microscopes offer magnifications  $M \geq 1$ . While the resultant spatial resolution given by the microscope is much greater, the field of view and working distance are typically very small. To avoid thermal issues while imaging reacting flows, a long-distance microscope is used for high resolution measurements.

There are critical differences in the imaging characteristics between the infinity corrected microscopes and single photographic-type lenses that are typically used for optical diagnostics. Specifically, the depth-of-field (DOF) and the diffraction-limited spot size ( $d_{\text{blur}}$ ) produced by an infinity-corrected microscope are described by the set of equations appropriate for microscopy [78]

$$d_{\text{blur}} = 2.44 \times M \times \lambda \times f/\#, \quad (2.2)$$

$$\text{DOF} = \frac{n\lambda}{\text{NA}^2} + \frac{ne}{\text{NA} \cdot M}, \quad (2.3)$$

where  $M$  is the magnification,  $\lambda$  is the wavelength of imaged light,  $n$  is the index of refraction of fluid between the objective lens and the object,  $e$  is the smallest distance that can be resolved by the detector (i.e. pixel spacing), and NA is the numerical aperture of the objective lens (interpreted as a measure of light-gathering ability and resolving power).

Table 2.4: Estimated  $d_{\text{blur}}$  and DOF for Infinity K2 microscope with CF1/B objective. Values used in computation:  $M = 0.8$ ,  $f = \text{WD} = 388 \text{ mm}$ ,  $\lambda = 532 \text{ nm}$ ,  $e = 6.5 \text{ }\mu\text{m}$ ,  $n = 1$ .

Aperture (mm)	NA	$f/\#$	$d_{\text{blur}} (\mu\text{m})$	$d_{\text{blur}} (\text{px})$	DOF (mm)
38	0.049	10	5.3	0.8	0.4
29	0.037	13	6.9	1	0.6
19	0.024	20	10.6	1.6	1.2
10	0.013	39	20.1	3.1	3.8

The  $f/\#$  can be approximated as  $f/\# \approx \frac{1}{2\text{NA}}$  for small NA and imaging in air [78].

Table 2.4 shows the theoretical  $d_{\text{blur}}$  and DOF across a range of aperture settings (which can be continuously adjusted) for the Infinity K2 long-distance microscope with CF1/B objective; these predictions were verified prior to “production measurements”. The chosen setting of  $f/\# \approx 39$  allowed to capture the entire width of approximately 1 mm thick laser sheet with an appropriate margin, while keeping the blurred particle image size small. The size of most particle images ranged between 3 and 5 pixels in the pre-processed images (due to additional optical effects).

It should be noted that significant optimization of the optics and laser illumination is required to balance competing effects of diffraction limited particle image size and limited depth of field at high magnifications. Interested readers are referred to author’s previous publication for an in-depth overview of how these factors are balanced to obtain high quality particle images and reconstructed tomograms under high magnifications [75].

#### *Seeding Density, Ghost Intensity, and Laser Profile*

The concentration of tracer particles is a significant factor in determining the resultant resolution of velocity measurements. As the frames containing raw particle images are broken up into numerous interrogation windows, it is necessary to have well defined images of tracer particles within each window. The probability of detecting a valid vector increases with a larger number of particle pairs within the interrogation box; thus, flows with a large tracer particle concentrations are desirable, with a minimum of five suggested by Raffel *et*

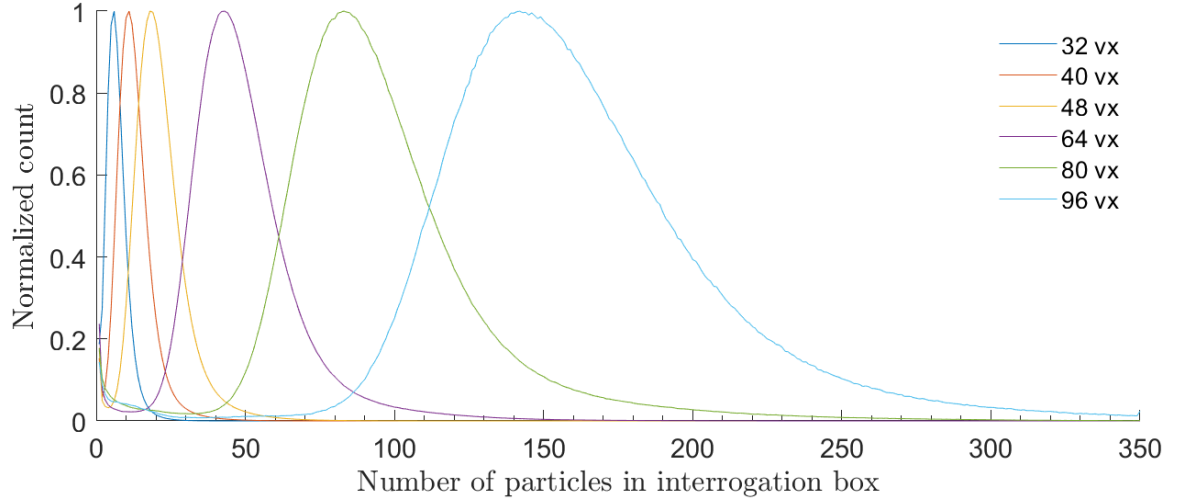


Figure 2.7: Distribution of particle counts per interrogation box from a typical tomographic reconstructed particle field (case D-E100-S3-U05 used).

*al.* [78].

To choose an optimal seed density, the flow rate through a fluidized bed seeder was tuned for every test condition to ensure sufficient particle density is present. The criteria for choosing an adequate flow rate through the seeder was determined by examining instantaneous particle images using a commercial PIV software (LaVision DaVis 8.4). After pre-processing of raw images and tomographic reconstruction, the 3D particle tomograms were used to count the number of particles within interrogation boxes of various sizes. Interrogation boxes considered were between 32 vx and 96 vx. The distribution of particle counts per interrogation box was normalized by the maximum count and compared to similar distributions obtained using different interrogation box sizes. The normalized histograms are shown in Figure 2.7 and seeding density statistics are summarized in Table 2.5.

Table 2.5: Seeding density statistics for case D-E100-S3-U05.

Box Size (vx)	Mean (vx)	Median (vx)	Mode (vx)	Standard Deviation (vx)
32	6.1	6	5	3.7
40	11.9	11	10	6.1
48	20.4	19	17	9.2
64	48.4	46	42	19.6
80	95.2	89	82	36.4
96	160.8	154	141	36.4

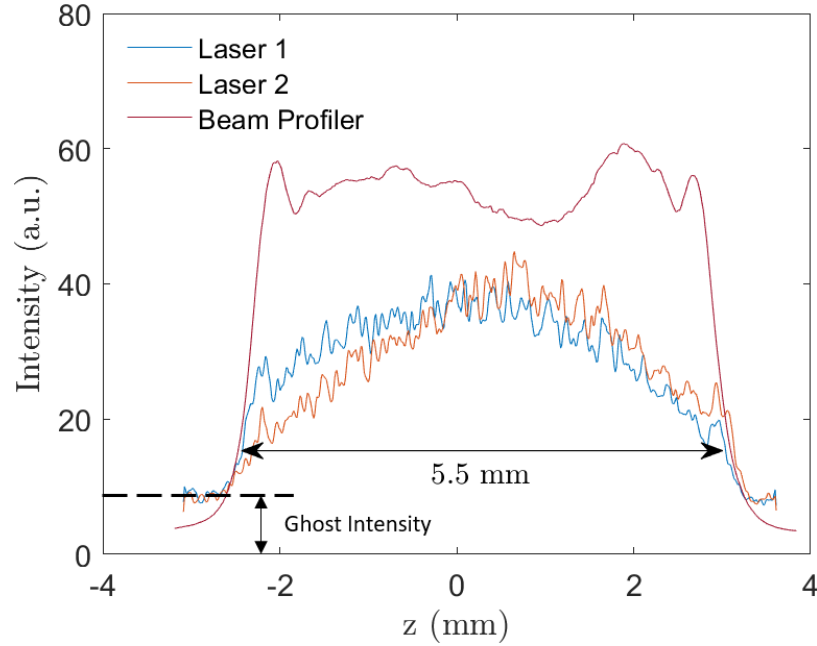


Figure 2.8: Reconstructed z-intensity profile from TPIV tomograms, compared to the beam profiler (case D-E100-S3-U05 used).

To assure strong cross-correlation, five to ten real particles need to be inside each interrogation box. Results show that the smallest box size of 32 vx contains a sufficient number of particles with a median of six particles per interrogation box. Seeding density at other test conditions was checked prior to data acquisition through visual evaluation of the raw images.

The velocity fields occasionally contained small regions of low seed particle count that lead to velocity vectors having weak correlation (correlation coefficient  $< 0.5$ ) or no computed vectors. These data points have been omitted from the analysis below. Moreover, the large region in the outer recirculation zone where the seeded reactant jet mixes with the ambient air, effectively reducing the seed density and producing low-quality velocity vectors was excluded from analysis. As this region did not contain the flame, its exclusion does not impact the results. The mean correlation value of the data used for analysis was between 0.7 – 0.8 across the three cases.

The second issue to consider in TPIV specifically is the “ghost intensity”. An artifact of tomographic reconstruction known as “ghost” particles diminishes the quality of the recon-

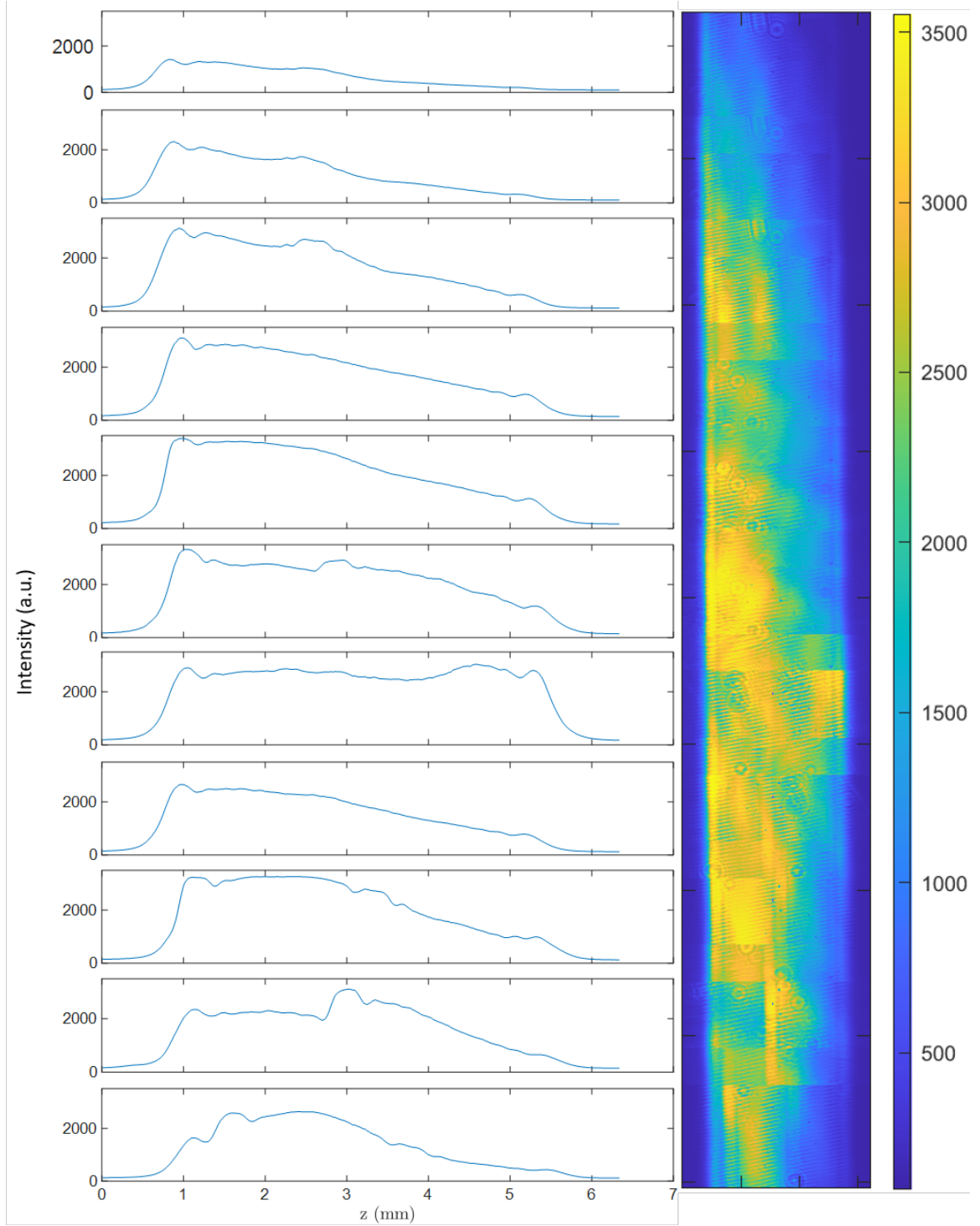


Figure 2.9: Aggregate of TPIV beam profiles and vertically averaged profiles for individual snapshots.

struction above a particle concentration of about 0.05 particles per pixel [83]. The ghost particles are created during 3D particle field reconstruction, wherein the reconstruction

algorithm creates more possible solutions for particle positions than the number of physical particles [83]. Introducing additional camera views reduces the ambiguities in particle position estimation, allowing higher seed densities to be used. However, an accurate reconstruction at higher seed densities is possible as long as most particles are projected onto well distinct images [83].

To estimate the ghost intensity,  $z$ -intensity profile of the tomographic reconstruction may be used to evaluate the ghost intensity [93]. Figure 2.8 shows the instantaneous  $z$ -intensity profiles generated from by the two tomograms in one frame pair used for TPIV; each frame corresponds to illumination of the flow by the Quantel Evergreen laser. The signal-to-background ratio of the  $z$ -intensity profile is defined as the ratio of the intensity inside the illuminated volume to the intensity outside the volume [93]. The intensity of the ghost particles remains constant in the out-of-plane direction; thus, the intensity outside the limits of the laser sheet is related to the ghost particle intensity. The “ghost intensity” is represented by the average intensity in the tails of the  $z$ -intensity profile in Figure 2.8; this is the region of space not illuminated by the laser. The estimated “ghost level” are between 20%-50%. To improve the accuracy of the results, only the middle portion of the illuminated slab is used, where the ghost level is less than 25%.

Additionally, the quality of tomographic reconstruction may be evaluated by comparing the extracted  $z$ -intensity profile to a reference measurement of the beam. In Figure 2.8 is shown a vertically averaged beam profile in the middle portion of the beam. Beam profile images were obtained using a beam profiler (Newport LBP2). Due to a limited beam profiler field of view, measurements were taken in sections as the beam profiling camera was traversed vertically using a translation stage; Figure 2.9 shows the mean aggregate beam profile that is obtained by stitching individual sections at different heights. Also shown are vertically averaged beam profiles for each section. The aggregate image is fairly noisy, but it gives a qualitative image of the entire TPIV beam. Since the laser slab is formed using knife edges, the two boundaries can be clearly identified and measured. While the beam

profile resembles a top-hat, the  $z$ -intensity profile from TPIV tomograms in Figure 2.8 appears like a smoothed top-hat. The reconstructed  $z$ -profiles are compared against vertically averaged beam profiler intensity in Figure 2.8. There is a good agreement between the widths of two  $z$ -intensities profiles and the mean beam profiler measurement.

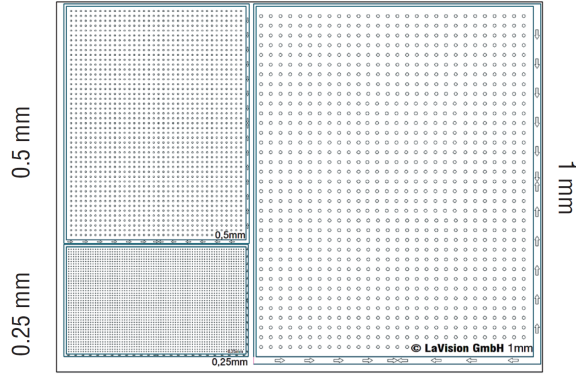
### *Calibration*

To obtain an accurate calculation of the velocity field and map simultaneous diagnostics to the physical space, a proper calibration must be performed. The process of calibration is necessary for generating a map from the object space to image space. When multiple cameras are imaging the same region of space, a unique mapping function is generated for each camera. The requirement on the precision of the calibration procedure is significantly stricter for TPIV than that for SPIV, and additional calibration corrections need to be utilized in the form of 3D self-calibration [94].

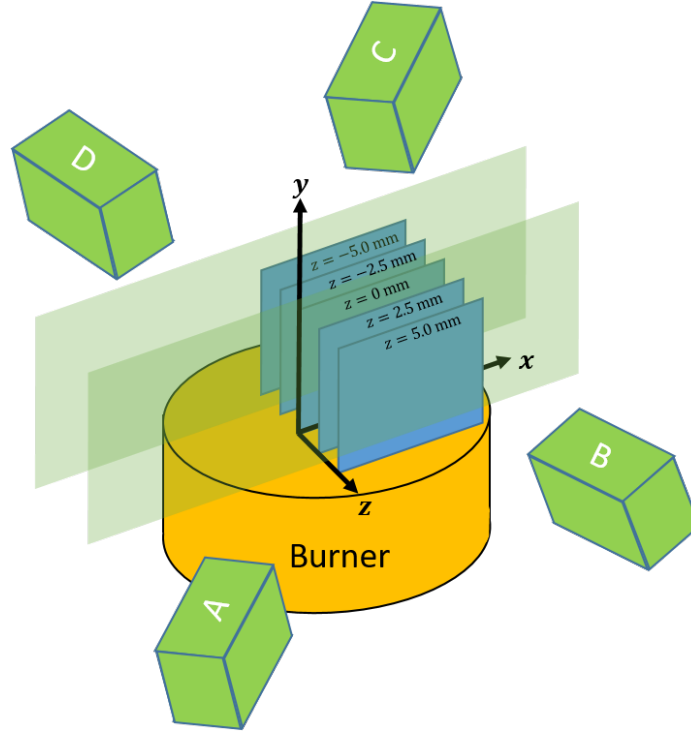
Calibration has a strong effect on the quality of the reconstructed particle field. A 3D calibration plate used conventionally for PIV, SPIV, and TPIV measurements has proven to be inadequate for  $\mu$ -TPIV, since the small field of view and high resolution of the imaging system does not capture enough calibration points and blurs the out-of-focus objects, as was previously shown [75]. The limited depth-of-field of long-range microscopes causes the calibration dots on the offset plane of the calibration target to lose contrast and appear out-of-focus. Here, a special micro-calibration plate was obtained from LaVision (MP 50 x 38), as shown in Figure 2.10a. The calibration plate has three sets of dots (spaced 0.25 mm, 0.5 mm, and 1 mm apart) printed on a 1.5 mm thick glass plate, allowing the dot matrix to be viewed from both sides of the calibration plate. For an accurate calibration, it is suggested that at least 10 to 15 dots in each direction is present in a calibration image, which is satisfied using this calibration target. For TPIV, the pattern with 1 mm dot spacing is used, while for  $\mu$ -TPIV the 0.5 mm dot pattern is used.

TPIV calibration requires calibration images acquired at different positions through





(a) Calibration plate.



(b) Location of calibration planes.

Figure 2.10: Calibration setup of the laser diagnostics.

the depth of the laser-illuminated volume. To obtain a three-dimensional calibration, the micro-calibration plate was mounted onto a micrometer-driven linear translation stage and calibration images were obtained at different  $z$ -positions; target images were recorded by the four TPIV cameras at five equally spaced  $z$ -planes, as shown in Figure 2.10b. For TPIV, steps of 2.5 mm were taken; for  $\mu$ -TPIV steps of 1 mm were taken between the planes. Sample calibration images are shown in Figure 2.11.

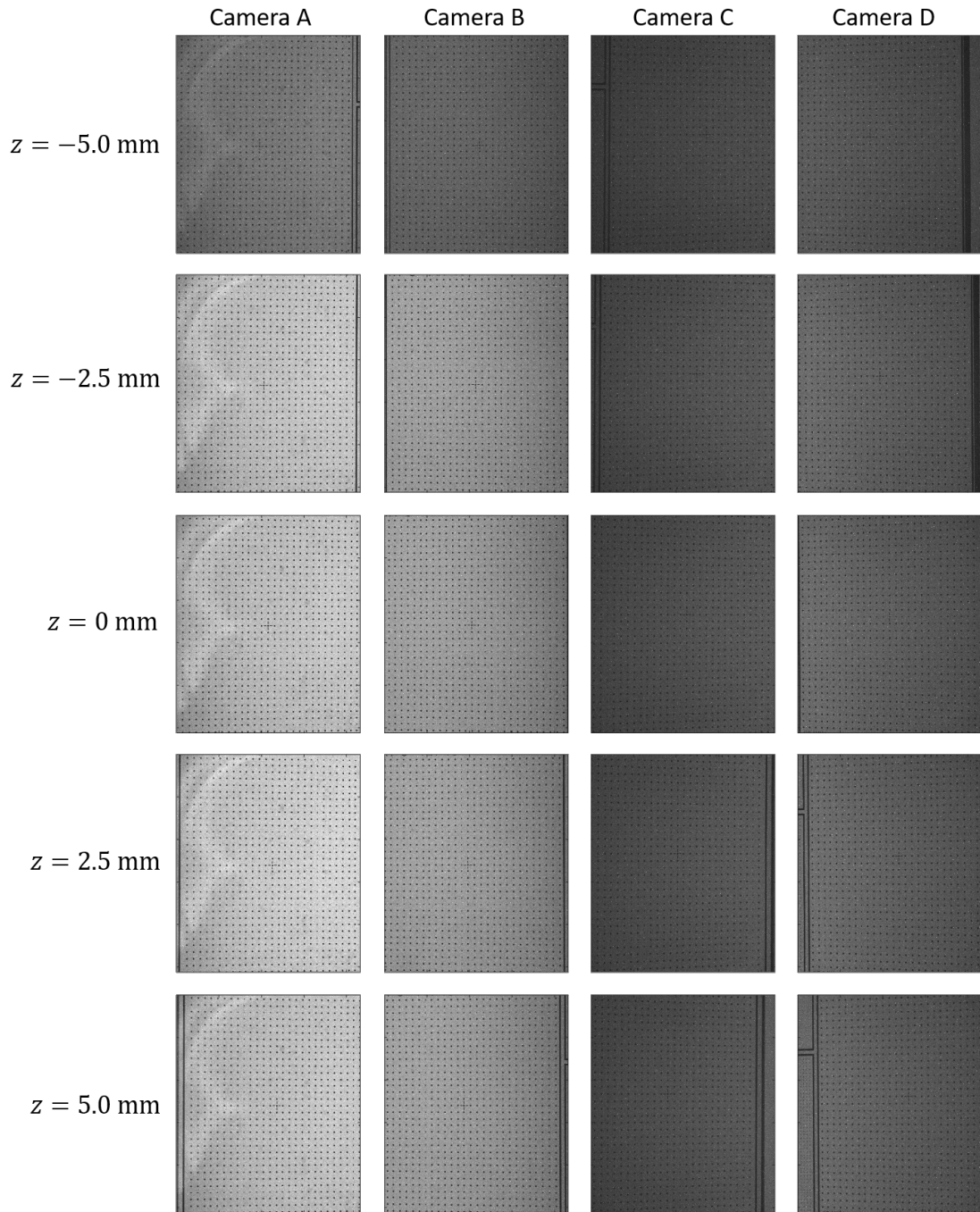


Figure 2.11: Calibration images for TPIV.

The initial calibration was then refined by running a volumetric self-calibration until the triangulation error was one the order of sub-pixel (typically below 0.05 px). This is done by iteratively performing triangulation of brightest particles in the flow, computing

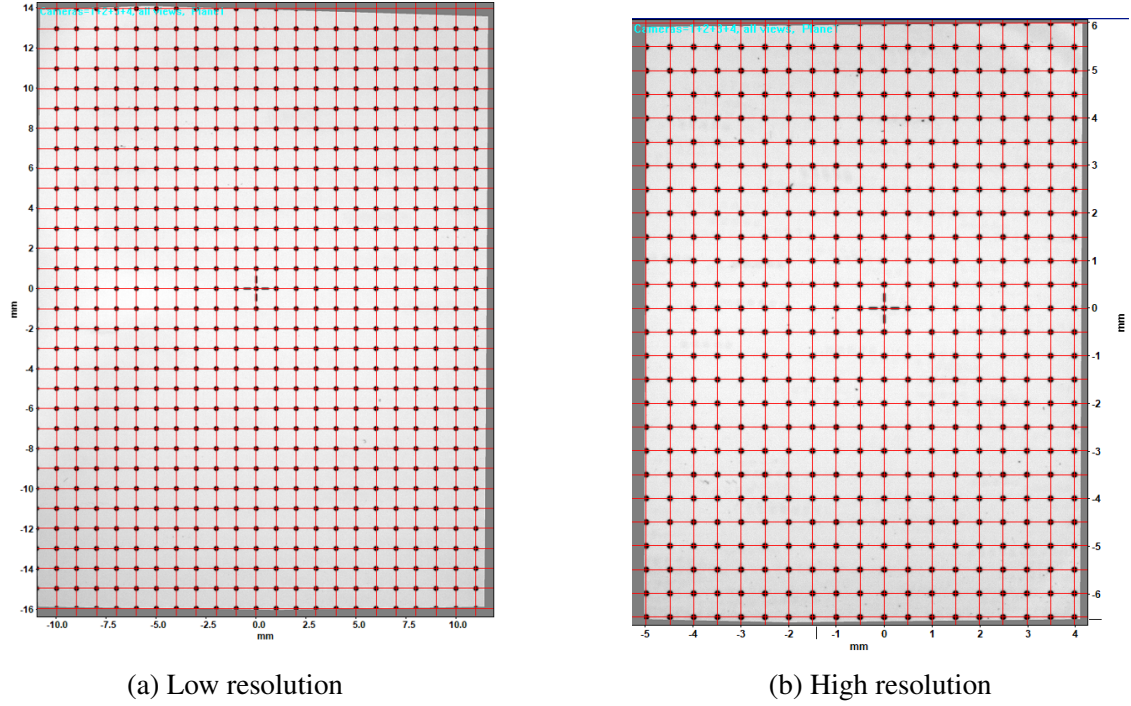


Figure 2.12: Corrected images from TPIV camera calibration.

the triangulation error, and applying correction to the calibration. The self-calibration is repeated to all the test cases taken during a single day; a separate calibration exists for each day of data acquisition. The quality of calibration is evaluated by ensuring the reconstructed  $z$ -intensity profiles match the reference beam profile, as shown in Figure 2.8. The final corrected calibration images are shown in Figure 2.12 for TPIV and  $\mu$ -TPIV setups.

### *Processing of Raw Data*

Calculation of the volumetric velocity fields from the Mie scattering images was performed in commercial software (LaVision DaVis 10.2) via direct cross-correlation using an adaptive evaluation algorithm. Cross-correlation of the reconstructed particle tomograms was performed using an iterative scheme. First, larger interrogation boxes are used to obtain the coarse flow field. The size of the interrogation box is gradually decreased with each pass as the calculated velocity field is refined. Multiple final interrogation box sizes are considered for TPIV and  $\mu$ -TPIV datasets, which are summarized in Table 2.6. Note that, for all cases

the overlap of 75% was used to maximize the number of samples in each direction.

Table 2.6: Summary of final interrogation box sizes and the corresponding vector resolutions.

Set	Interrogation Box (vx)	Resolution ( $\mu\text{m}$ )	Vector Spacing ( $\mu\text{m}$ )
TPIV	32	380	95
	64	760	190
	96	1140	285
$\mu$ -TPIV	32	158	40
	64	316	80

Vector post-processing is performed after each iteration. During multi-pass post-processing, the number of spurious vectors was reduced through application of a universal outlier detection, removal, and insertion algorithm. No post-processing is done after the final pass, except for removing spurious vectors that have a cross-correlation coefficient below 0.3. Typically, the velocity fields are smoothed after cross-correlation; however, doing so essentially applies an additional filter that can potentially skew computation of inter-scale energy transport  $\alpha_{\text{sfs}}$ .

### 2.3.2 CH<sub>2</sub>O Planar Laser Induced Fluorescence

Fluorescence is the spontaneous emission of radiation from an upper energy level of an atom or molecule after it has been excited, usually by electromagnetic radiation of higher energy [95]. PLIF offers high resolution planar measurements of a wide range of species and is often used in combustion diagnostics. Laser-induced excitation is often performed using the ultra-violet range of electromagnetic spectrum; wavelength of the emitted light is longer than that of the excitation, often emitting in near ultra-violet or visible ranges.

While it is possible to obtain quantitative measurements of the target species concentration using PLIF, this requires knowledge of multiple optical parameters and a more rigorous measurement approach. The goal of this dissertation, however, is to identify the flame structure and the flame's position inside the turbulent flow. Therefore, qualitative measurements are sufficient to identify regions where CH<sub>2</sub>O exists. While no quantitative species

concentration can be obtained from the measurements, the relative concentrations can be evaluated in a qualitative manner from the raw PLIF intensities.

### *Chemistry of CH<sub>2</sub>O*

In hydrocarbon-air combustion, formaldehyde is a product of fuel pyrolysis that is consumed rapidly during the formation of HCO in the final stages of oxidation. For methane-air flames, CH<sub>2</sub>O is a good indicator of the instantaneous thermal flame width (i.e.  $\delta_L^0 \approx (T_p - T_r)/\max(|\nabla T|)$ , where  $T_r$  and  $T_p$  are reactant and product temperatures), as the reactant-facing side of the CH<sub>2</sub>O-containing region matches with decomposition of methane and the product side corresponds to the thin regions of rapid heat release [96, 97]. Figure 2.13 shows the variation of CH<sub>2</sub>O mole fraction and fluid density versus position in a freely propagating laminar flame at atmospheric conditions and  $\phi = 0.75$ ; progress variable defined in terms of fluid temperature  $c_T = (T - T_r)/(T_p - T_r)$  is also shown. These calculations were performed using Chemkin with the GRI3.0 chemical model. Clearly, the concentration of formaldehyde increases with  $c_T$  and reduces to zero at  $c_T \geq 0.9$ . Similarly, the major variation in fluid density occurs in the region where CH<sub>2</sub>O exists. Consequently, the boundaries of the CH<sub>2</sub>O-containing regions can be used to identify the region of density gradient and demarcate the flame edges. Dem *et al.* [98] has also performed Raman scattering measurements in the same combustor configuration studied here and at similar flow conditions, finding that the species and temperature profiles closely matched those of a laminar flame and supporting this flamelet-like mapping.

It should be noted that the regions occupied by CH<sub>2</sub>O are typically representative of the preheat region of the premixed methane/air flame. CH<sub>2</sub>O PLIF is often combined with OH PLIF to identify the thin reaction zone [37, 96, 97]. Since the primary pathway for HCO production and heat release involves reactions with CH<sub>2</sub>O and OH (i.e.  $\text{CH}_2\text{O} + \text{OH} \rightarrow \text{HCO} + \text{H}_2\text{O}$ ), the overlap between CH<sub>2</sub>O and OH is used to identify the reaction layer, which was shown to nearly coincide with region of heat release [97]. However, since

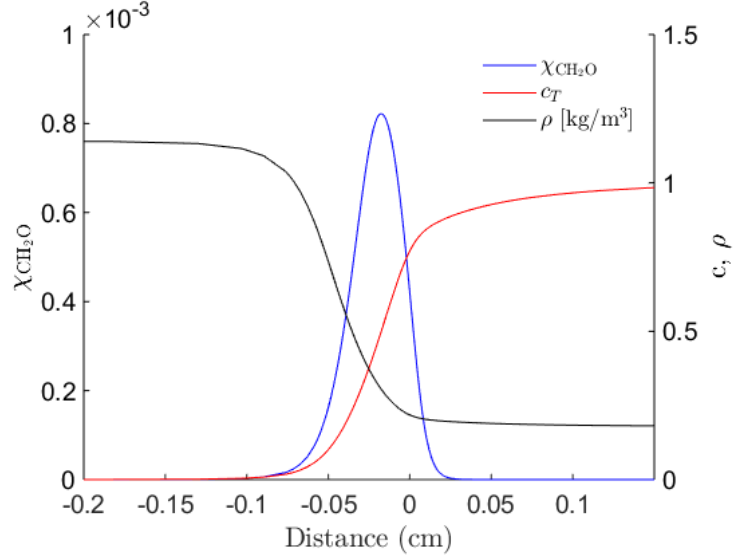


Figure 2.13: Variation of  $\text{CH}_2\text{O}$  mole fraction, temperature-based progress variable, and fluid density in a laminar premixed flame at  $\phi = 0.75$ .

filtering is required for the computation of  $\alpha_{\text{sfs}}$  and the thickness of the reaction layer is on order  $\mathcal{O}(10^{-1})\delta_L^0$ , the details of the reaction zone are not significant in this dissertation and only  $\text{CH}_2\text{O}$  PLIF is used.

### *Optical Layout*

The main challenge of performing  $\text{CH}_2\text{O}$  PLIF is its intrinsic low signal-to-noise ratio of the images. While there are many excitation schemes for  $\text{CH}_2\text{O}$  PLIF, the most common is the utilization of the third-harmonic output of a Nd:YAG laser at a frequency of 355 nm [8]. Unfortunately, the excitation of the  $4_0^1$  transition results in a low fluorescence signal per unit laser fluence. The issue of low signal strength is aggravated when simultaneous PIV measurements are made. Most commonly used  $\text{TiO}_2$  solid seed particles in PIV measurements were found to fluoresce after being illuminated by a 355 nm pulse, particularly at high laser energies. To mitigate the particle fluorescence problem,  $\text{Al}_2\text{O}_3$  solid seed particles were used since its broadband fluorescence is much weaker than that of  $\text{TiO}_2$ . Moreover, a custom optical formaldehyde filter was used to isolate the  $\text{CH}_2\text{O}$  fluorescence. The filter is an 11-band bandpass filter optimized to capture the peaks of formaldehyde emission over

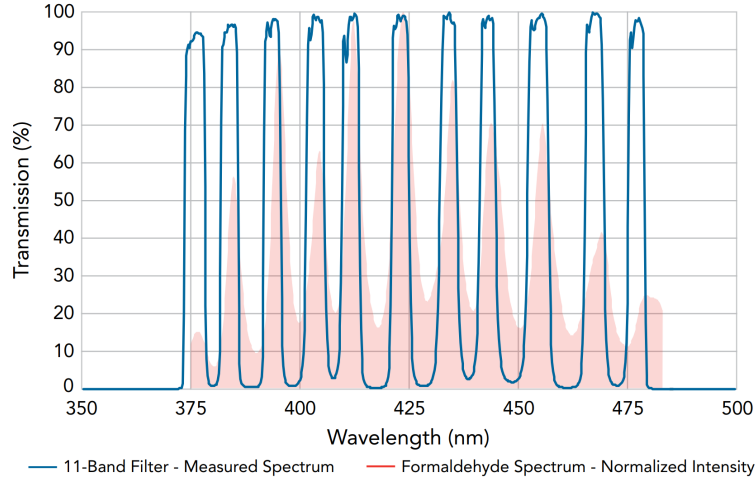


Figure 2.14: The measured spectra of the 11-band filter designed for imaging formaldehyde, overlaid with the emission spectra of  $\text{CH}_2\text{O}$  [99]

the 380 - 480 nm wavelength range, as shown in Figure 2.14 [99].

The  $\text{CH}_2\text{O}$  PLIF system consisted of a frequency tripled Nd:YAG laser (Quanta-Ray PRO-250-10, 355 nm, 10 Hz, 300 mJ/pulse) and an intensified high-resolution sCMOS camera (Lambert Instruments TRiCAM S20 3 ns,  $1200 \times 1920$  px) with a macro objective lens (Tamron,  $f = 180$  mm,  $f/\# = 2.8$ ), as demonstrated in Figure 2.4 and Figure 2.6. Measurements of instantaneous formaldehyde distribution were made along the central plane of the TPIV volume with a field of view of  $30 \times 30$  mm simultaneously with TPIV for the reacting cases. The laser excited the  $A - X_0^1$  transition of  $\text{CH}_2\text{O}$  in a bandwidth around 355 nm. The intensifier gate time was set to 100 ns to minimize the background luminosity and amplifier noise.

### *Measurement Resolution*

The resolution of the  $\text{CH}_2\text{O}$  PLIF measurement is determined by the maximum of the thickness of the laser sheet and the modulation transfer function (MTF) of the entire imaging system. The thickness of the sheet was measured by traversing the knife edge across the sheet and recording the laser power, as demonstrated in Figure 2.15. The measurements are taken at five locations, spanning the width of PLIF field of view (i.e. equidistantly spaced

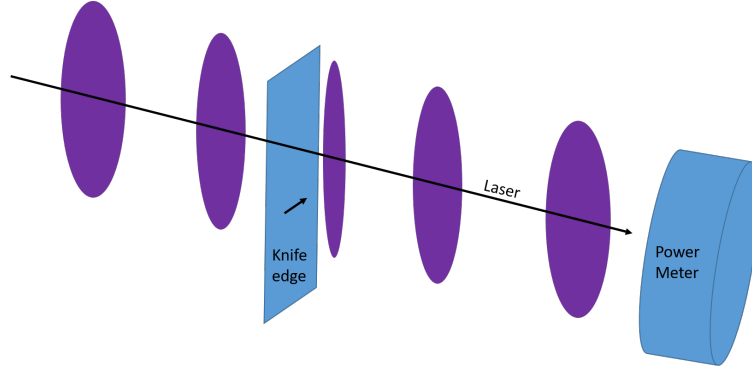


Figure 2.15: Schematic representation of laser sheet thickness measurement using knife edge traversal technique.

through 30 mm along laser propagation direction).

Figure 2.16a shows the laser power measurements at the five indicated locations. The data is least-square fitted to an error function of the form

$$\text{erf } z = \frac{2}{\sqrt{\pi}} \int_0^z \exp^{-t^2} dt. \quad (2.4)$$

Specifically, the four scaling parameters to the error function  $I(z) = w_1 + w_2 \text{erf}(w_3 z + w_4)$  are found through least-squares fitting and are shown as dashed curves in Figure 2.16a. The derivative of the error function is the Gaussian function, i.e.

$$g(z) = a \exp^{-\frac{(z-b)^2}{2c^2}}, \quad (2.5)$$

where  $a$ ,  $b$ , and  $c$  are the parameters of the function. Figure 2.16b shows the computed beam profiles from the derivatives of the fitted profiles. Clearly, the profiles are very similar, which indicates that the PLIF field of view is located within the confines of the laser beam waist. The beam thickness can be taken as the full-width-half-maximum of the profile or using 10%-90% of maximum intensity. The FWHM thickness ranges from 600  $\mu\text{m}$  - 630  $\mu\text{m}$  (5% variation), while the 10%-90% method gives 950  $\mu\text{m}$  - 1025  $\mu\text{m}$  (7% variation). Since the fluorescence signal originates throughout the entire volume that is illuminated by the laser, it is more accurate to estimate the laser sheet thickness as approximately 1 mm in



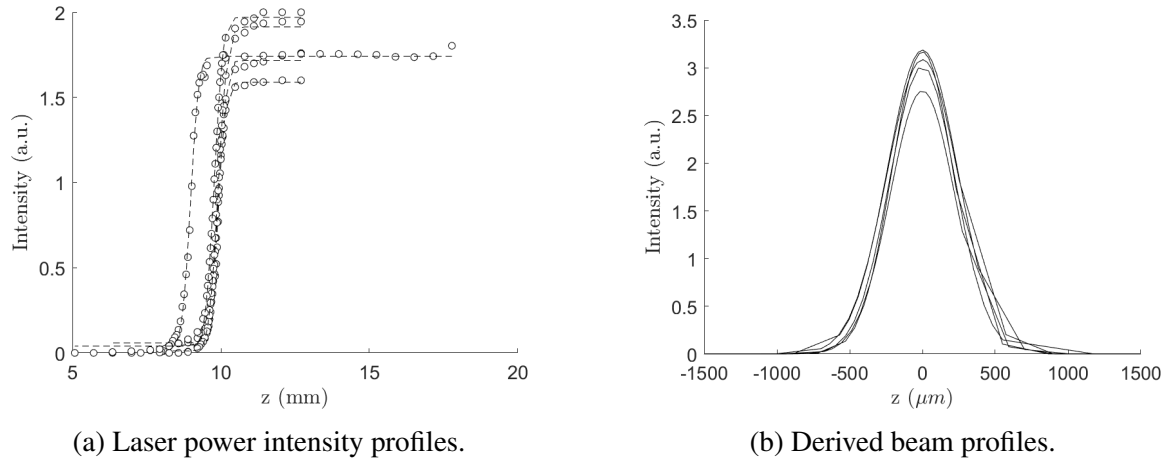


Figure 2.16: The laser power intensity profiles for  $\text{CH}_2\text{O}$  PLIF measured at 5 locations.

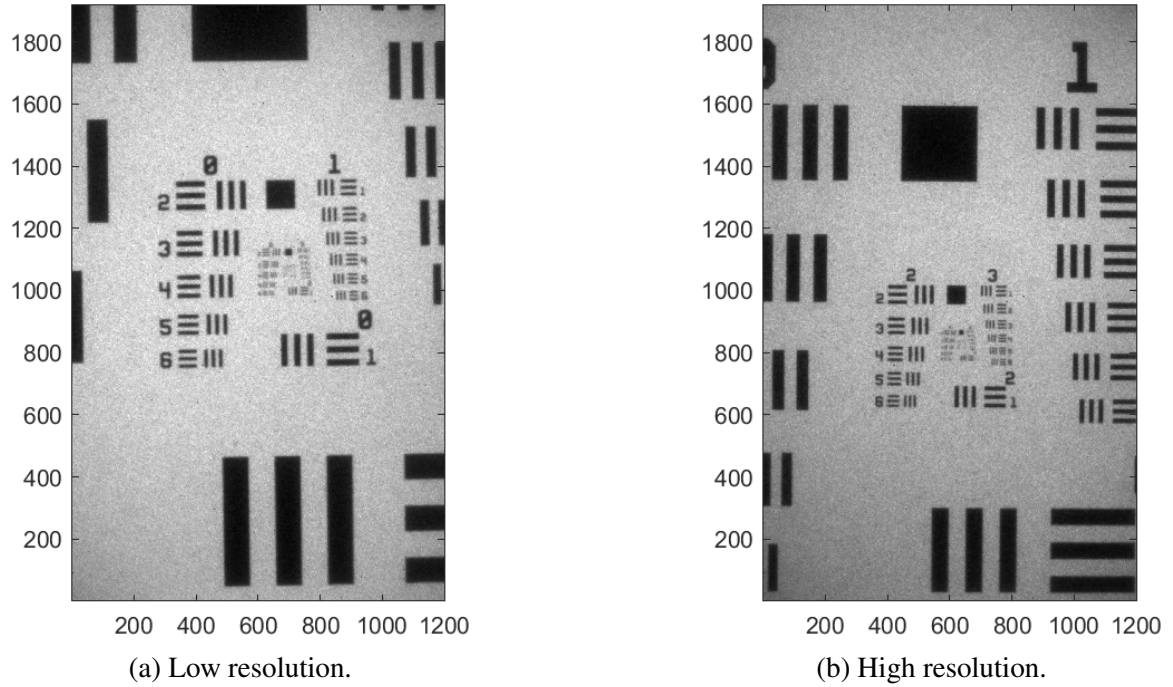


Figure 2.17: Images of the 1951 USAF resolution target in TPIV and  $\mu$ -TPIV configurations.

thickness with 7% variation along the propagation direction in the field of view.

Finally, the laser sheet thickness should be compared to in-plane resolution of the PLIF image. Resolution test targets can be used to measure the resolution of an imaging system. These usually consist of reference line or dot patterns with well-defined thicknesses and spacings. The targets imaged by the optical system and the largest set of non-

distinguishable lines determines the resolving power of a given system. In this dissertation, 1951 USAF resolution test targets is used to measure in-plane resolutions.

Figure 2.17 shows the images of the resolution test target, taken by the intensified PLIF camera, in the TPIV and  $\mu$ -TPIV configurations. For low resolution, line pairs beyond group 2 element 1 (4 lp/mm  $\approx$  125  $\mu$ m) are indiscernible; for high resolution, line pairs beyond group 4 element 1 (16 lp/mm  $\approx$  31.25  $\mu$ m) are indiscernible. Overall, the resolution of the PLIF images can be interpreted as 1 mm since the thickness of the laser sheet is larger than measured in-plane resolution.

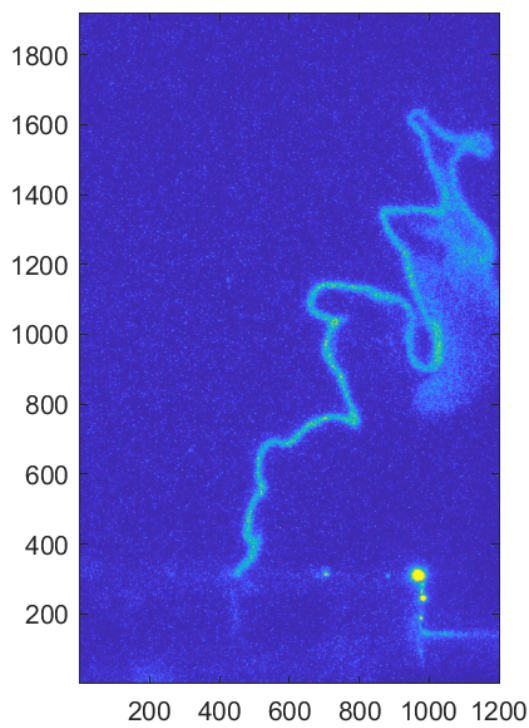
### *Background Corrections*

Before CH<sub>2</sub>O images can be processed further, a series of background corrections must be made to reduce image noise. Other than shot noise, the main sources of noise in a recorded PLIF image include (1) “dark” or thermal noise in the imaging sensor, which can be reduced by cooling the cameras; (2) background noise from scattered laser light (Rayleigh signal or reflections); and (3) luminosity from the flame. A series of reference images were taken prior to measurements to eliminate these sources of noise during background corrections.

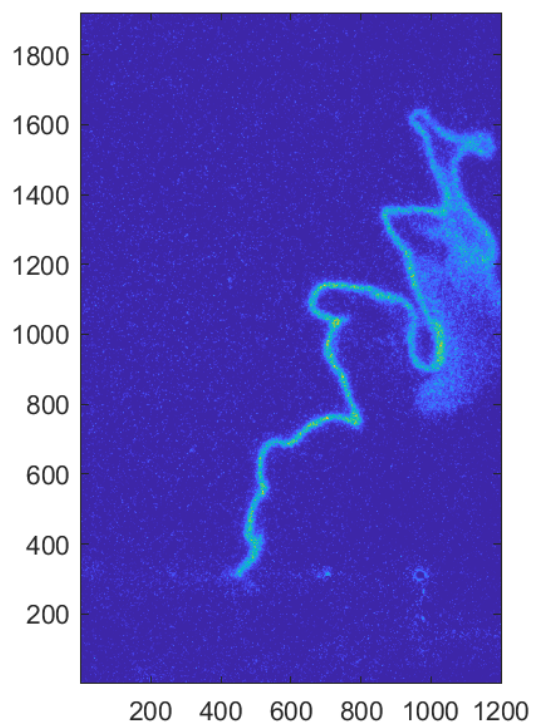
Noise due to background reflections and flame luminosity can be measured by recording a set of images without the tracer particles, but with the flame and laser present. The dark noise is measured by taking a set of images with the lens cap covering the camera lens. White background is also measured by imaging a uniform surface (a back-lit uniform LED panel); this allows to capture variations on the image from a non-varying source of light. This can be particularly significant in the corners of the image due to the vignetting effect of the optical system.

The CH<sub>2</sub>O images were pre-processed using a set of image processing steps to compensate for the effects of the known error sources. Mathematically, the corrected signal is

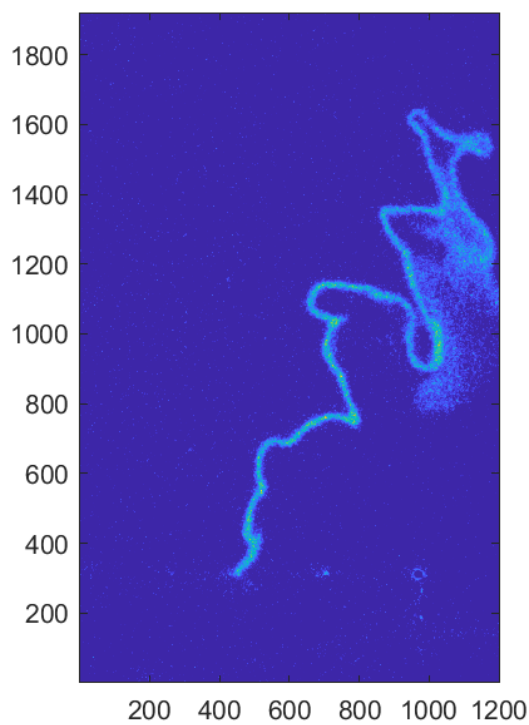
$$I_{\text{corr}} = \frac{I - N_{\text{background}} - N_{\text{dark}}}{N_{\text{white}} - N_{\text{dark}}}, \quad (2.6)$$



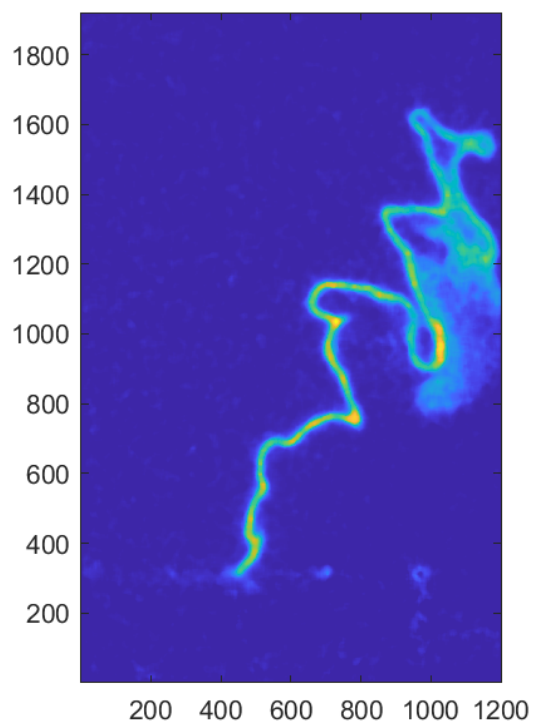
(a) Raw image.



(b) Step 1: Background subtracted.



(c) Step 2: Flat field corrected.



(d) Step 3: Median filtered.

Figure 2.18: CH<sub>2</sub>O PLIF image pre-processing.

where  $I$  is the intensity of the raw image,  $N_{\text{background}}$  is the mean background noise image,  $N_{\text{dark}}$  is the dark field noise, and  $N_{\text{white}}$  is the white field image. Figure 2.18 demonstrates the series of images obtained after individual correction step. The mean background image is subtracted from the raw image, remove most of the laser reflections from the surface of the burner while reducing the background intensity. Flat field correction (Equation 2.6) further removes background noise and corrects for non-uniform sensitivity of the sensor to uniform light. Finally, the  $21 \times 21$  median filter is applied to remove “salt and pepper” noise. The last step removes particle fluorescence and greatly enhances the PLIF signal-to-background ratio. The resultant signal-to-background ratio of the corrected PLIF images ranges from 15 to 30.

The last series of steps are meant to remove features that are not part of the flame. First, the 80th percentile of the image data was subtracted from the raw frames and all negative values are set to zero. Since the flame occupies a small portion of the flow (approximately 10%-20% of the image area), most values outside the flame have low image intensity; subtracting 80th percentile removes any remaining weak reflections and particle fluorescence. Finally, the image is cropped to only focus on the region that overlaps with the TPIV field of view. In Chapter 3, the corrected PLIF images are used to identify the boundaries of the flame, estimate the local fluid properties, and calculate the combustion progress variable.

## CHAPTER 3

### ANALYSIS METHODS

In Chapter 2, the details of the experimental setup, laser diagnostics, and application of corrections to raw data was presented. In this chapter, summary of various methods of using raw velocity fields and CH<sub>2</sub>O PLIF images to obtain  $\alpha_{\text{sfs}}$  is given. First the the method of deducing the density, temperature, and  $c$  fields from the CH<sub>2</sub>O PLIF data is presented. Next, the challenges of computing  $\alpha_{\text{sfs}}$  from simultaneous TPIV and CH<sub>2</sub>O PLIF are highlighted and the approach taken to overcome these difficulties is provided. Finally the method of identifying coherent flow structure is presented. The chapter closes with a brief overview of the approach taken to condition the results on relevant parameters while maintaining low uncertainty in the mean statistics.

Where applicable, the assessment of the impact of certain analysis choices and approximations on the final results is given. In particular, assessment is made on (a) the method of mapping CH<sub>2</sub>O PLIF data to  $c$ -fields, (b) the importance of including the density-gradient terms in  $\alpha_{\text{sfs}}$ , (c) the choice of filter type (i.e. box vs. Gaussian), and (d) the impact of using multiple planes of velocity field that do not overlap with  $c$ -fields. This assessment is performed by computing the results with these different (less accurate) choices/approximations and comparing the results to the ‘full’ calculation presented using JPFDs.

#### 3.1 Progress variable and density estimation

In order to compute  $\alpha_{\text{sfs}}$  and examine its flame-conditioned statistics, it is necessary to locate the velocity measurements within the flame structure;  $\alpha_{\text{sfs}}$  requires knowledge of the density field and flame-conditioning typically is done based on the reaction progress variable. Here, instantaneous progress variable and density fields are estimated from the CH<sub>2</sub>O PLIF measurements, taken at the center of the TPIV measurement volume ( $z =$

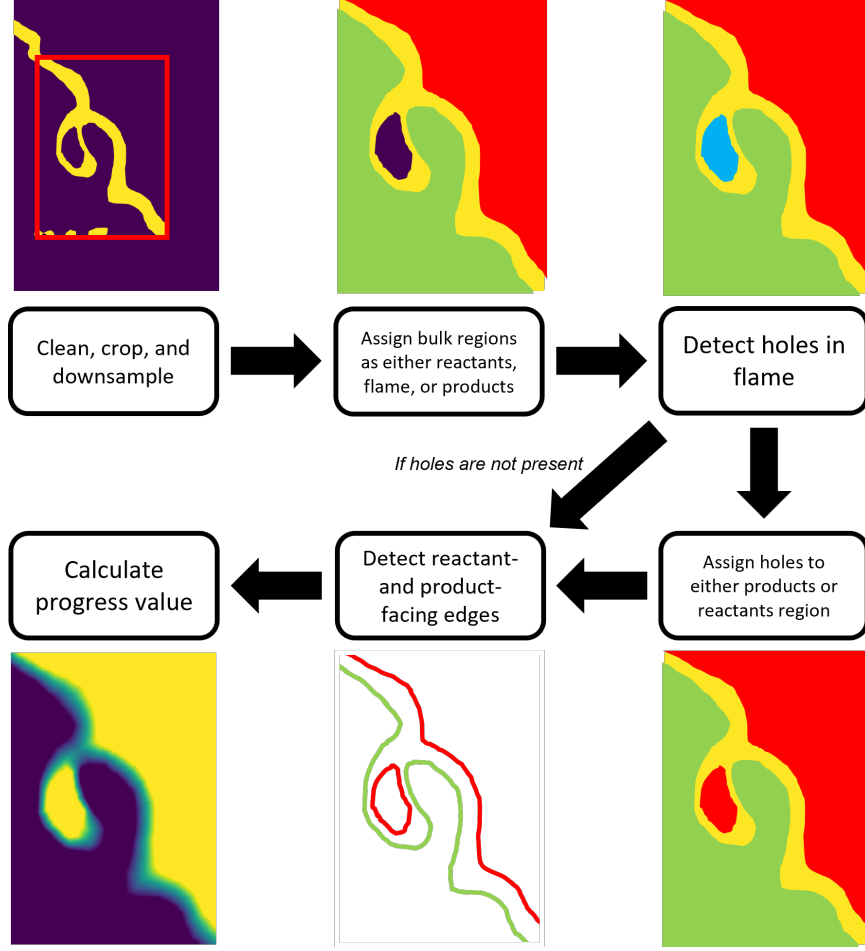


Figure 3.1: Schematic representation of mapping  $\text{CH}_2\text{O}$  to  $c$ .

0 mm).

Specifically, the distribution of formaldehyde is used to estimate the planar  $c$ -field. It was already demonstrated that the boundaries of the  $\text{CH}_2\text{O}$ -containing region capture most of the variation in mixture temperature and fluid density across a laminar flame. Therefore, it is reasonable to use the edges of  $\text{CH}_2\text{O}$ -containing region to identify the boundaries of the flame and *approximate* the combustion progress and local density internal to the flame for the turbulence conditions considered here.

To do so, a progress variable-like quantity is defined as

$$c = \frac{d - d_r}{d_p - d_r}, \quad (3.1)$$

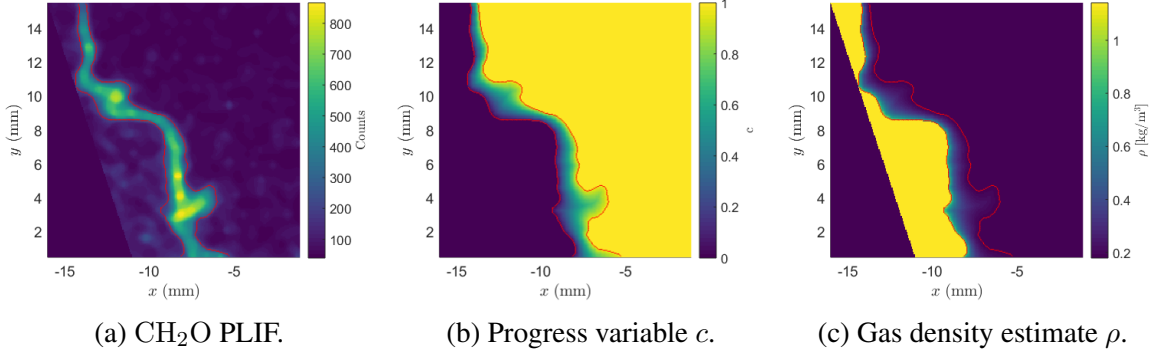


Figure 3.2: Illustration of instantaneous progress variable and density computation from planar CH<sub>2</sub>O distribution. Measurement from Case 1 is shown. Red lines show the boundaries of the two CH<sub>2</sub>O containing regions.

where  $d_r$  and  $d_p$  are the shortest in-plane distances from a given point  $d(x, y)$  inside the flame to the reactant- and product-facing edges of the CH<sub>2</sub>O-containing region, respectively. In other words, the intermediate  $c$  inside the flame is determined by using a linear fit between  $c = 0$  and  $c = 1$  based on the shortest distance from the given point to the nearest reactant and product edges. This process is shown schematically in Figure 3.1. The CH<sub>2</sub>O fields are first binned to the same resolution as the velocity fields and cropped to match the field of view. The image is then separated into regions of reactants ( $c = 0$ ), products ( $c = 1$ ), or the flame; pockets of combustion products and unburned reactants are identified and assigned to an appropriate region. Edge detection is performed by thresholding the gradient of binarized image. Lastly, the progress variable internal to the flame is obtained using Equation 3.1.

Figure 3.2(a) shows a typical instantaneous CH<sub>2</sub>O image, with two lines showing the reactant-facing and product-facing boundaries of the CH<sub>2</sub>O-containing region, which separate reactants ( $c \approx 0$ ), the flame ( $0 \lesssim c \lesssim 1$ ), and the products ( $c \approx 1$ ). The resultant progress variable field is shown in Figure 3.2(b) and the density field is shown in Figure 3.2(c). The local fluid properties are computed based on a flamelet assumption, i.e. assigning the local density to be the same as an equivalent laminar flame at the same value of  $c$ .

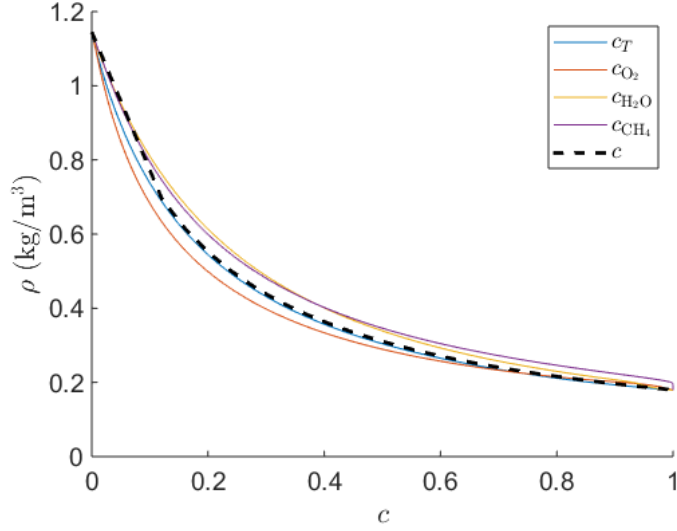


Figure 3.3: CH<sub>2</sub>O and  $\rho$  mapping to  $c$ .

To ensure that the density variation computed using the CH<sub>2</sub>O-based  $c$ -field is physically reasonable,  $\rho$  is plotted against  $c$ ,  $c_T$ , and various  $c_i = (\chi_i - \chi_{i,r})/(\chi_{i,p} - \chi_{i,r})$  based on the select species mole fractions ( $\chi_{i,r}$  and  $\chi_{i,p}$  are the mole fractions of species  $i$  in the reactants and products, respectively), as shown in Figure 3.3. The similarity between the density profiles demonstrates that the density variation across the flame is adequately estimated and is physically reasonable.

It is emphasized that the mapping between CH<sub>2</sub>O and the local fluid properties ( $\rho$  and  $T$ ) clearly is not exact; this is not a high-fidelity density field measurement technique. The uncertainty in the measured density fields could potentially affect  $\alpha_{\text{sfs}}$ . Note that the detailed method of computing  $\alpha_{\text{sfs}}$  is described in Section 3.2. The uncertainty in  $\rho$  and  $T$  arises from the mapping of  $c$  to locations internal to the flame and estimation of fluid properties from  $c$ . The sensitivity of the results to the uncertainty associated with mapping  $c$  and  $\rho$  to the position inside the flame is assessed by re-performing the analysis using a different mapping method. Specifically,  $\alpha_{\text{sfs}}$  is computed using two different methods of CH<sub>2</sub>O PLIF- $c$  mapping: (i) assigning a linearly-interpolated value of  $c$  between the reactant- and product-facing edges of the CH<sub>2</sub>O-containing region (i.e. interpolated), and



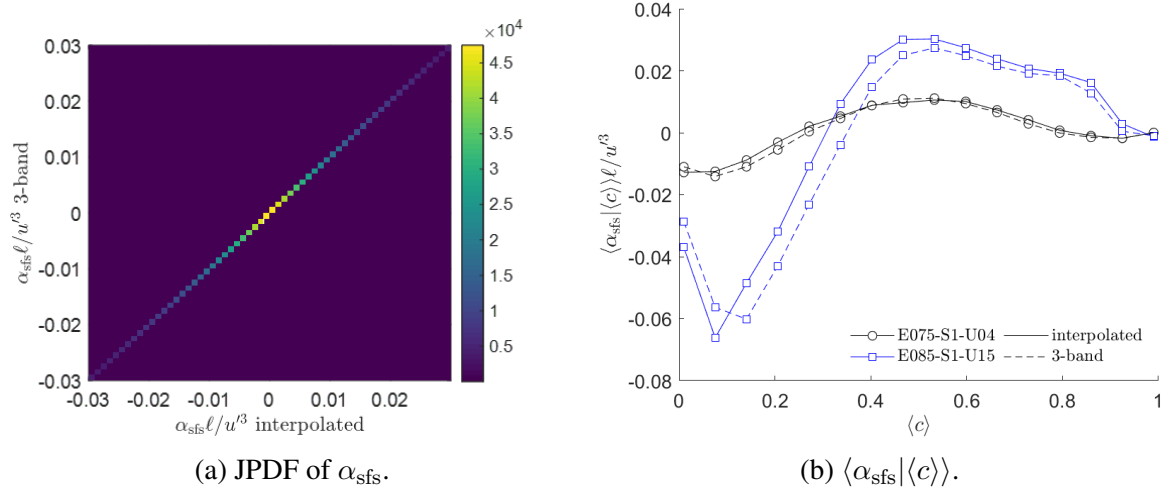


Figure 3.4: Comparison of the  $\alpha_{\text{sfs}}$  computed using different PLIF- $c$  mapping methods;  $\Delta/\delta_L^0 = 1.5$ .

(ii) assigning the  $\text{CH}_2\text{O}$ -containing region to  $c = 0.5$ , the reactants to  $c = 0$ , and products to  $c = 1$  (i.e. 3-band).

Figure 3.4(a) shows the JPDF of instantaneous  $\alpha_{\text{sfs}}$ , computed using the two aforementioned methods; there is a strong correlation between the two methods. Figure 3.4(b) shows the  $\langle \alpha_{\text{sfs}} | \langle c \rangle \rangle$  for cases E075-S1-U04 and E085-S1-U15, as filtered using  $\Delta/\delta_L^0 = 1.5$ . Conditioning  $\alpha_{\text{sfs}}$  on  $\langle c \rangle$  allows to compare the two methods across a continuous range of progress variable values. Evidently, the  $\langle \alpha_{\text{sfs}} | \langle c \rangle \rangle$  profiles, computed using the two methods, are qualitatively and quantitatively similar, with the difference not exceeding more than 15% between the profiles. It can thus be concluded that the sensitivity of  $\alpha_{\text{sfs}}$  to the mapping method is minimal and the interpretation of the results does not change with the method of mapping position in the flame to  $c$  and  $\rho$ .

The inter-scale energy transfer  $\alpha_{\text{sfs}}$  is effectively independent of the specific density field estimation method used due to the spatial filtering operation inherent to the analysis. That is, as long as the density field transitions from the density of the reactants to the density of the products in some reasonable manner over the measured flame position, calculations of  $\alpha_{\text{sfs}}$  do not depend on the detailed density distribution. All discussions and conclusions presented below are independent of the density mapping procedure.

### 3.2 Computation of $\alpha_{\text{sfs}}$

Computation of the mean cross-scale energy rate requires 3D velocity and density fields. While TPIV measurements provide 3D velocity fields, the estimate of the density field is only available on a single plane. Therefore, conservation of mass is used to produce an approximate measurable equation for  $\alpha_{\text{sfs}}$ .

For notational simplicity, the residual stress tensor is re-expressed as  $\mathcal{T}_{ij} = \bar{\rho} a_{ij}$ , where  $a_{ij} \equiv \widetilde{u_i u_j} - \tilde{u}_i \tilde{u}_j$ . Then,  $\alpha_{\text{sfs}}$  may be separated into

$$\alpha_{\text{sfs}} = -\frac{\tilde{u}_i}{\bar{\rho}} \frac{\partial \mathcal{T}_{ij}}{\partial x_j} = -\underbrace{\tilde{u}_i \frac{\partial a_{ij}}{\partial x_j}}_1 - \underbrace{a_{ij} \frac{\tilde{u}_i}{\bar{\rho}} \frac{\partial \bar{\rho}}{\partial x_j}}_2. \quad (3.2)$$

Hence, to calculate  $\alpha_{\text{sfs}}$  exactly, the local gradients of the filtered density are required. Since only planar density data is available from the experiment, the out-of-plane density gradient  $\partial \bar{\rho} / \partial x_3$  must be estimated to compute Term 2 in Equation 3.2. The out-of-plane density gradient can be approximated from the Favre-filtered continuity equation as

$$\frac{\partial \bar{\rho}}{\partial x_3} = \frac{1}{\tilde{u}_3} \left[ -\bar{\rho} \left( \frac{\partial \tilde{u}_1}{\partial x_1} + \frac{\partial \tilde{u}_2}{\partial x_2} + \frac{\partial \tilde{u}_3}{\partial x_3} \right) - \tilde{u}_1 \frac{\partial \bar{\rho}}{\partial x_1} - \tilde{u}_2 \frac{\partial \bar{\rho}}{\partial x_2} - \frac{\partial \bar{\rho}}{\partial t} \right]. \quad (3.3)$$

Using the filtering approach described below, all terms on the right of Equation 3.3 are measured except the time derivative of the filtered density. However, since the goal is to examine ensemble averaged statistics, the contribution of the unsteady density term to the mean cross-scale energy transfer is expected to be negligible in a statistically stationary turbulent flow. Specifically, consider the ensemble mean of Term 2 in Equation 3.2; taking a closer look at the unsteady portion of this expansion, i.e.

$$\left\langle a_{i3} \frac{\tilde{u}_i}{\bar{\rho}} \frac{1}{\tilde{u}_3} \frac{\partial \bar{\rho}}{\partial t} \right\rangle = \left\langle \underbrace{a_{i3} \frac{\tilde{u}_i}{\tilde{u}_3}}_g \frac{\partial \ln \bar{\rho}}{\partial t} \right\rangle = \left\langle g \frac{\partial \ln \bar{\rho}}{\partial t} \right\rangle. \quad (3.4)$$

Decomposing each term into mean ( $\langle \cdot \rangle$ ) and fluctuating ( $\cdot'$ ) components,

$$\left\langle g \frac{\partial \ln \bar{\rho}}{\partial t} \right\rangle = \left\langle \langle g \rangle \frac{\partial \langle \ln \bar{\rho} \rangle}{\partial t} \right\rangle + \left\langle \langle g \rangle \frac{\partial (\ln \bar{\rho})'}{\partial t} \right\rangle + \left\langle g' \frac{\partial \langle \ln \bar{\rho} \rangle}{\partial t} \right\rangle + \left\langle g' \frac{\partial (\ln \bar{\rho})'}{\partial t} \right\rangle \quad (3.5)$$

$$= \left\langle g' \frac{\partial (\ln \bar{\rho})'}{\partial t} \right\rangle, \quad (3.6)$$

where the first three terms are zero either due to the fact that time derivative of a statistic is zero in a steady flow (i.e.  $\partial \langle \cdot \rangle / \partial t = 0$ ), or because the mean of a fluctuation is also zero (ex.  $\langle (\ln \bar{\rho})' \rangle = 0$ ). It can be shown that the other terms in the expansion of Term 2 follow a similar expansion but result with an extra term; using the second-to-last term in Equation 3.3 as an example,

$$\left\langle a_{i3} \frac{\tilde{u}_i \tilde{u}_2}{\bar{\rho} \tilde{u}_3} \frac{\partial \bar{\rho}}{\partial x_2} \right\rangle = \left\langle \underbrace{a_{i3} \frac{\tilde{u}_i \tilde{u}_2}{\tilde{u}_3}}_h \frac{\partial \ln \bar{\rho}}{\partial x_2} \right\rangle \quad (3.7)$$

$$= \langle h \rangle \frac{\partial \langle \ln \bar{\rho} \rangle}{\partial x_2} + \left\langle h' \frac{\partial (\ln \bar{\rho})'}{\partial x_2} \right\rangle. \quad (3.8)$$

Since the flow is not homogeneous or isotropic, large gradients in mean and fluctuating densities are expected across the shear layers (i.e. the location of flames in presented configuration). Consequently, assuming  $\mathcal{O}(h) \approx \mathcal{O}(g)$ , the unsteady portion of this expansion is expected have negligible contributions as compared to other terms in the expansion. As a result, the unsteady density term is dropped in the present analysis.

The values of  $\alpha_{\text{sfs}}$  presented in this dissertation are calculated using Equation 3.2 and Equation 3.3 directly. However, it is useful to analyze these equations in somewhat more detail to demonstrate reason behind the robustness of the analysis to the assumptions made. After substitution of Equation 3.3 into Equation 3.2,  $\alpha_{\text{sfs}}$  can be written as

$$\alpha_{\text{sfs}} = -\tilde{u}_i \frac{\partial a_{ij}}{\partial x_j} + \underbrace{\frac{\tilde{u}_i}{\tilde{u}_3} \widetilde{u_i u_3} \frac{\partial \tilde{u}_k}{\partial x_k} - 2k \frac{\partial \tilde{u}_k}{\partial x_k}}_A + \underbrace{\frac{\tilde{u}_i}{\bar{\rho}} \frac{\partial \bar{\rho}}{\partial x_m} \left( \widetilde{u_i u_3} \frac{\tilde{u}_m}{\tilde{u}_3} - \tilde{u}_i \tilde{u}_m \right)}_B + \frac{\tilde{u}_i a_{i3}}{\bar{\rho} \tilde{u}_3} \frac{\partial \bar{\rho}}{\partial t}, \quad (3.9)$$

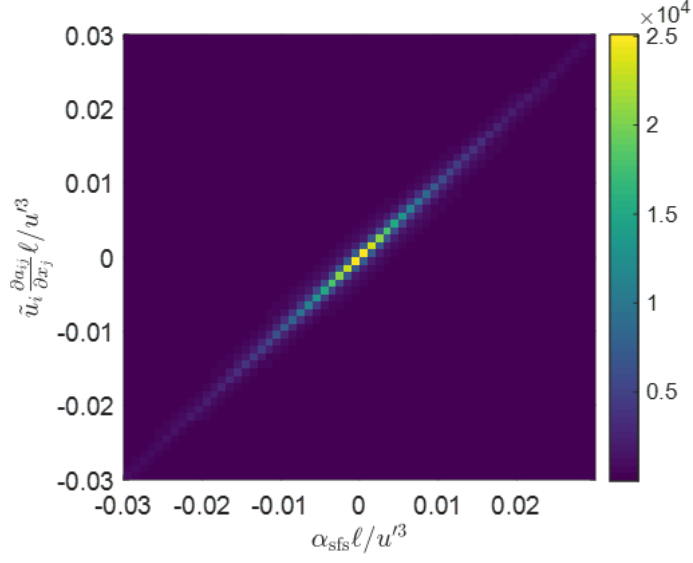


Figure 3.5: JPDF of  $\alpha_{\text{sfs}}$  computed using Equation 3.2 and Equation 3.3 vs. Equation 3.10 for case E085-S1-U15.

where  $m = 1, 2$ . Groups  $A$  and  $B$  each contain two terms having similar forms, *e.g.* if  $\widetilde{u_i u_3} = \tilde{u}_i \tilde{u}_3$ , then  $B = 0$ . The measurements showed that, both instantaneously and on average,  $A$  and  $B$  are small compared to the leading term on the right of Equation 3.9. Hence, taking the ensemble average of terms involving the time derivative to be small, the ensemble mean  $\langle \cdot \rangle$  cross-scale energy transfer can be approximately expressed as

$$\langle \alpha_{\text{sfs}} \rangle \approx - \left\langle \tilde{u}_i \frac{\partial a_{ij}}{\partial x_j} \right\rangle. \quad (3.10)$$

This approximation states that the contribution of the density gradients (i.e. Term 2 in Equation 3.2) is negligible; the Favre-filtered fluctuating velocities are the primary contributors to  $\langle \alpha_{\text{sfs}} \rangle$ . Figure 3.5 shows the JPDF of instantaneous  $\alpha_{\text{sfs}}$  calculated using Equation 3.2 and Equation 3.3 versus using Equation 3.10, demonstrating negligible difference between these methods.

It is also noted that the 3D filtering is performed by projecting the planar density field approximation through the  $z$ -extent of the filter. Due to the complexity of the flame geometry, there is potential concern regarding the effect of flame orientation with respect to the

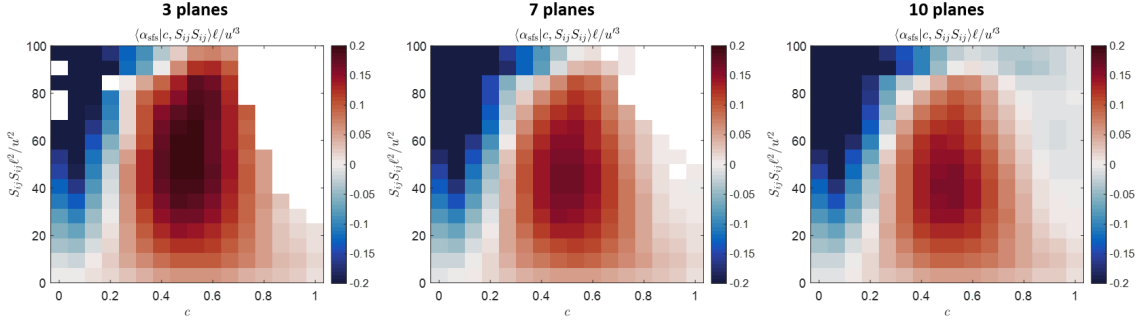


Figure 3.6: Convergence of doubly-conditioned statistics with  $\Delta/\delta_L^0 = 1.5$  for E085-S1-U15.

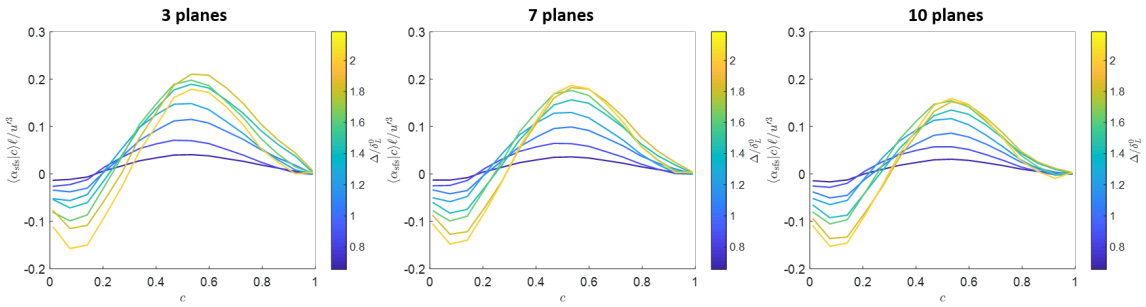


Figure 3.7: Convergence of  $\langle \alpha_{\text{sf}} | c \rangle$  for E085-S1-U15.

laser sheet on the results. When the flame is oriented significantly off-perpendicular with respect to the laser illumination, the assumption of constant density in  $z$ -direction would appear to yield a significant error. To address this concern, the analysis for  $\alpha_{\text{sf}}$  is performed using different number of planes. Note that *for the purpose of filtering*, the density field in the measurement plane is assumed to be representative of the 3D density field. This assumption is again borne out by the independence of the ultimate  $\alpha_{\text{sf}}$  results to the density field processing. Moreover, the reduction in the number of planes will exclude  $\alpha_{\text{sf}}$  from the outer planes which have a higher uncertainty associated with their distance from the PLIF plane. If the results compiled using different numbers of planes have a significant qualitative difference, it can be concluded that flame misalignment introduces a significant error.

Figure 3.6 shows the doubly-conditioned statistics for case E085-S1-U15 with  $\Delta/\delta_L^0 = 1.5$ , where three, seven, and ten planes were used (centered about the PLIF plane). The

main difference between the results is the number of non-converged bins is greater for the smaller number of planes. The region that is most sensitive to the number of planes used is  $c \gtrsim 0.6$  and  $S_{ij}S_{ij} \gtrsim 60 - 100$ . This is expected since the strain-rates associated with turbulence in the combustion products is typically lower than in reactants. Figure 3.7 shows a similar set of plots for  $\langle \alpha_{\text{sfs}} | c \rangle$  for the same case at variable  $\Delta/\delta_L^0$ . Again, while there are minor differences between the results, the form of the plots did not change significantly and the observed trends are qualitatively the same; there is a slight increase in the maximum magnitude of the mean back-scatter. These observations were consistent across the other test cases.

Hence, the main trends and conclusions of the paper are robust to the assumptions regarding the number of planes used in the analysis. Nevertheless, the analysis is performed only on the three central planes to remove any uncertainty associated with calculating  $\alpha_{\text{sfs}}$  in the outer planes. The smallest filter size considered is three vectors; therefore the use of three planes is appropriate.

### 3.3 Filtering

The filtering operation is performed instantaneously on the planar density and volumetric velocity fields using a spatial top hat filter kernel  $\mathcal{G}$

$$\mathcal{G}(\mathbf{x} - \mathbf{r}) = \begin{cases} \frac{1}{\Delta^3} & \text{if } |\mathbf{x} - \mathbf{r}| \leq \frac{\Delta}{2} \\ 0 & \text{otherwise.} \end{cases} \quad (3.11)$$

Note that in physical space, the convolution  $(\bar{\cdot}) = \mathcal{G} * (\cdot)$  is equivalent to a local volumetric average over a box with a side length  $\Delta$ . In the case of density fields, filtering is performed on a three-dimensional field, where the planar density data is replicated in the out-of-plane dimension. The filter lengths is varied from a minimum of 3 vectors up to the thickness of the TPIV measurement volume; the upper size limit depends on the size of the

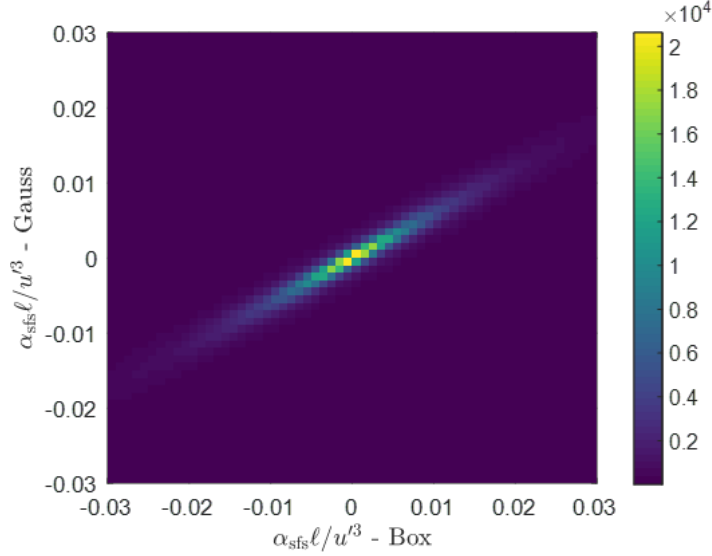


Figure 3.8: JPDF of  $\alpha_{\text{sfs}}$  computed using box filter vs. Gaussian filter for E085-S1-U15.

interrogation box used.

While the choice of a top hat filter is arbitrary, the underlying physical interpretation is independent of the choice of filter kernel. To demonstrate,  $\alpha_{\text{sfs}}$  results obtained using a box filter are compared to results obtained using a Gaussian kernel with standard deviation of  $\Delta/2$  at  $\Delta/\delta_L^0 = 1.5$ . Figure 3.8 shows the JPDF between  $\alpha_{\text{sfs}}$  computed using two different filters. Gaussian-filtered  $\alpha_{\text{sfs}}$  is linearly correlated to box-filtered  $\alpha_{\text{sfs}}$ , but with a non-unity slope. That is,  $|\alpha_{\text{sfs}}|$  with the Gaussian kernel is lower-than but proportional-to  $|\alpha_{\text{sfs}}|$  with the top hat kernel. Hence, it can be concluded that the sign and *relative* magnitude of  $\alpha_{\text{sfs}}$  does not depend strongly on the filter type, though the absolute magnitude does depend on the filter type. Box filter is used for the purposes of this dissertation, since the filter type does not affect the phenomenological interpretation of the results.

### 3.4 Identification of coherent structures

Presence of the coherent flow structures can disturb the turbulent flame and potentially result in enhanced inter-scale energy transfer. To evaluate the impact of such structures on turbulent combustion, the coherent structures have to be identified first.

There are many vortex-identification methods, the most popular of which are the  $Q$ -,  $\lambda_2$ -,  $\Delta$ -, and the  $\lambda_{ci}$ -criteria [100–103]. However, only the  $\Delta$ - and  $\lambda_{ci}$ -criteria are directly extendable to compressible flows [104]. Moreover, these two methods are frame independent and only identify regions where circular or spiralling streamlines occur; regions of high vorticity but no local spiralling motion, such as shear layers, are ignored [105]. The  $\lambda_{ci}$ -criteria is used here because it also provides a physically meaningful measure of the strength of local swirling motion. It should be noted that the objective here is to identify the extent of the vortex boundary and all methods gave similar vortex visualizations.

The  $\lambda_{ci}$ -criterion identifies coherent swirling eddies as spatial regions in which the velocity gradient tensor  $\partial u_i / \partial x_j$  has a complex eigenvalue pair ( $\lambda_{cr} \pm i\lambda_{ci}$ ) [103, 105]. The imaginary part of the complex eigenvalue pair -  $\lambda_{ci}$  - is referred to as the swirling strength and it quantifies the strength of the local swirling motion [105]. Physically, the local flow is either stretched or compressed along the axis of the real eigenvector ( $\nu_r$ ), while the flow is swirling in the plane spanned by the real and imaginary parts of the complex eigenvector ( $\nu_{cr}$  and  $\nu_{ci}$ ).

Computation of  $\lambda_{ci}$  proceeds in two steps. First, the velocity fields are spatially smoothed through a convolution with a box filter. Finite-difference schemes tend to amplify noise, hence smoothing raw velocity fields reduces noise in the spatial velocity gradients and consequently  $\lambda_{ci}$ . Note that  $\lambda_{ci}$  fields are used to strictly identify the largest scale coherent structure; smoothing velocity retains large scale eddies while suppressing smaller structures that may arise due to noise. Moreover, the width of the box filter used did not affect the identification of flow structures (i.e.  $\lambda_{ci}$  computed after smoothing with  $\Delta = 21$ ,  $\Delta = 11$ , and  $\Delta = 6$  vector was very similar). While the magnitude of peak  $\lambda_{ci}$  decreased with  $\Delta$ , the largest eddies retained their size and shape.

Next, the eigenvalues and eigenvectors are computed on the central plane of the TPIV volume. Locations with three real eigenvalues were assigned a value of  $\lambda_{ci} = 0$  (i.e. no swirl); for complex eigenvalue pairs, positive  $\lambda_{ci}$  is taken. The data is further reduced by



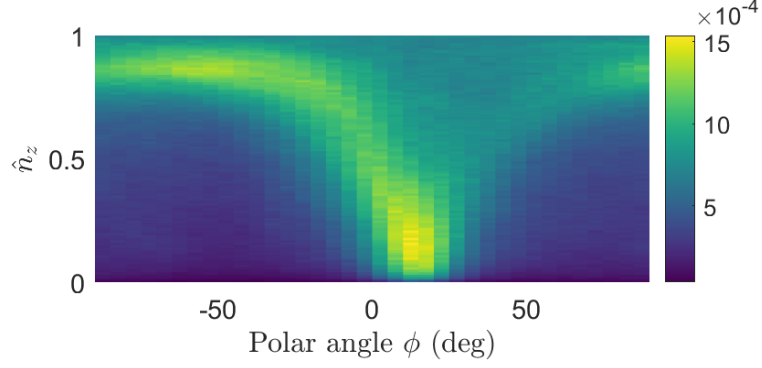


Figure 3.9: Joint probability density function of  $\hat{n}_z$  and the polar angle  $\phi$  of the normal vector in the  $x$ - $y$  plane.

eliminating locations where the axis of rotation was predominantly in the  $x$ - $y$  plane. To demonstrate the distribution of rotation axis orientations, the normal vector to the plane of rotation, defined as  $\hat{\mathbf{n}} = \boldsymbol{\nu}_{\text{cr}} \times \boldsymbol{\nu}_{\text{ci}}$ , is considered. Figure 3.9 shows the joint probability density function (PDF) of  $\hat{n}_z$  and the polar angle  $\phi$  of  $\hat{\mathbf{n}}$  in the  $x$ - $y$  plane. The locations with  $\phi \approx 0 - 25$  degrees were found to correspond to the large scale swirl induced by the burner. However, the locations with large  $\hat{n}_z$  correspond to coherent structures that rotate in plane. Therefore, locations with  $\hat{n}_z < 1/\sqrt{2}$  (where  $\hat{n}_z$  is the largest component) is set  $\lambda_{\text{ci}} = 0$  to isolate the structures of interest.

To extract the dominant coherent structures, the method of snapshot Proper Orthogonal Decomposition (POD) is used [106]. POD is a popular data analysis method to extract energetically and dynamically important features of the fluid flows, initially introduced by Lumley [107] and Sirovich [106] to separate coherent fluid motion from purely stochastic motion of turbulence.

POD constructs an optimal set of basis functions that captures as much of the data variance with as few basis functions as possible. Given a set of  $N$  measurements of the variable  $\xi(\mathbf{x}, t)$ , the fluctuating component ( $\xi' = \xi - \langle \xi \rangle$ ) can be approximated using  $P$  modes as

$$\xi'(\mathbf{x}, t) = \sum_{j=1}^P a_j(t) \phi_j(\mathbf{x}), \quad (3.12)$$

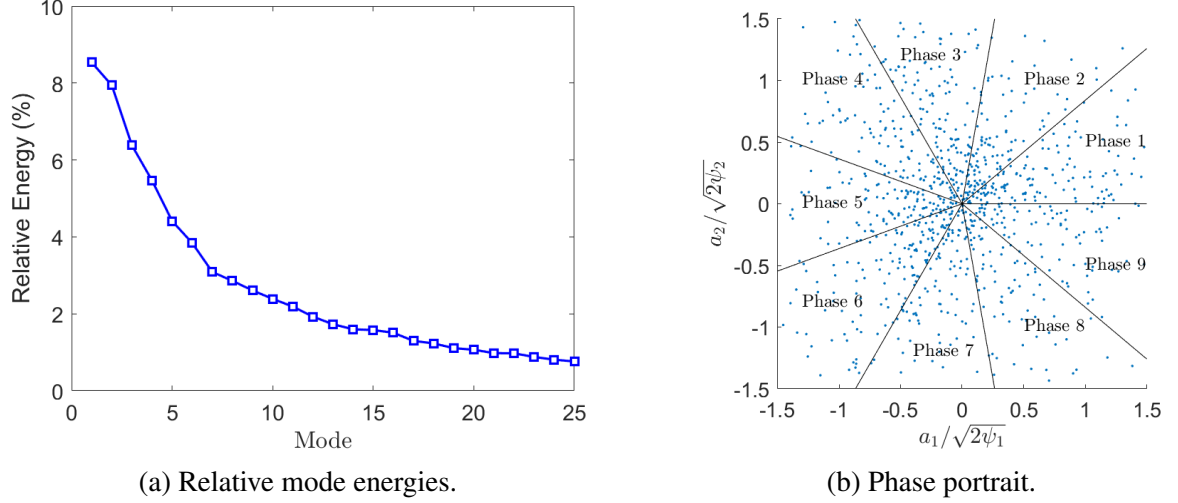


Figure 3.10: Distribution of eigenvalues  $\psi_i$  of POD analysis and phase portrait between coefficients of mode 1 and 2 for case E085-S1-U15.

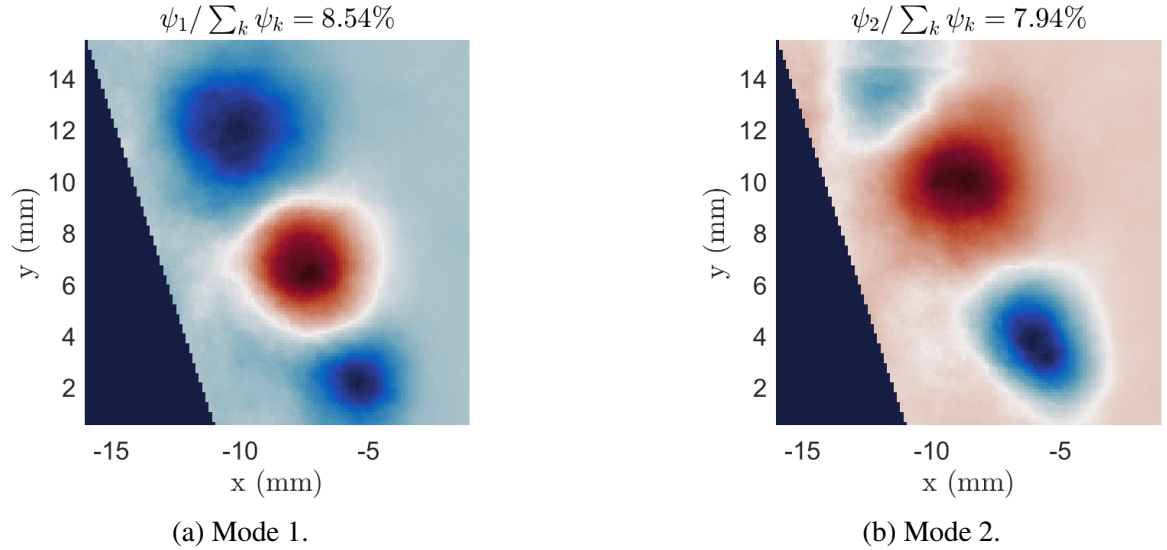


Figure 3.11: First two spatial POD modes for the reacting flow.

where  $\phi_j(\mathbf{x})$  and  $a_j(t)$  represent the spatial modes and their temporal coefficients, respectively. POD modes  $\phi_j$  are given by the eigenvectors of the covariance matrix  $\mathbf{R} = \mathbf{X}\mathbf{X}^T$ , where  $\mathbf{X}$  represents the  $N$  snapshots in a matrix form [108]. The eigenvalues ( $\psi_j$ ) are the mode energies, which describe how much of the variance in the original data is contained in a particular mode.

In this thesis,  $\lambda_{ci}$  is used as the quantity of interest for POD. Each realization is the planar snapshot of  $\lambda_{ci}$  on the central plane of the TPIV volume. Figure 3.10(a) shows a

representative relative energy content ( $\psi_i / \sum_k \psi_k$ ) of the first 25 modes from case E085-S1-U15. The first two modes have similar relative energy suggesting the pair forms a single convective vortex. Time coefficients for modes 1 and 2 can be used to construct a phase portrait, as is shown in Figure 3.10(b). Distribution of points along a unit circle implies existence of a coherent convective structure [109]. The observed scatter of data points in the phase portrait on a unit disk is an indication of 3D effects, cycle-to-cycle variations induced by strong turbulence, and other small-scale fluctuations [109]. The majority of the remaining modes had a low relative variance  $\psi_i / \sum_j \psi_j \leq 0.03$  and no other coherent pairs were identified.

Figure 3.11 shows the shape of the first 2 spatial modes in Figure 3.10. Both modes clearly show structures resembling vortices propagating along the inner shear layer; mode 2 is translated by approximately a quarter of the wavelength. This further confirms that the pair of identified modes forms a single convective vortex. Since the first two modes account for about 16.5% of variance, this vortex is identified as the dominant coherent structure.

The time coefficients from the identified modes (ex. modes 1 and 2) are used to obtain phase information of the periodic flow structure. This is done by phase-sorting individual measurements into nine equal “bins” based on the angle of the measurement in the  $a_1(t)$  and  $a_2(t)$  plane as shown in Figure 3.10(b), e.g. [110–113]. Phase-averaged quantities of interest  $q$  are calculated as

$$\langle q | \theta_i \rangle = \frac{1}{N_{\theta_i}} \sum_{k=1}^{N_{\theta_i}} q(t_k), \quad (3.13)$$

where  $\theta_i$  is the  $i$ -th range of phase angles and  $N_{\theta_i}$  is the ensemble size. This procedure allows for treatment of the phase as a clock signal for the dominant convective structure in absence of time-resolved measurements. In this work,  $\lambda_{ci}$ ,  $\alpha_{sfs}$ ,  $III$ , and  $c$  are the primary quantities of interest that are phase-averaged.

Figure 3.12 shows the profiles of  $\langle \lambda_{ci} | \theta_i \rangle$  at different phases of propagation in a reacting flow. Every second phase is shown for brevity and the dashed lines denote the phase-conditioned flame brush, i.e.  $0.1 < \langle c | \theta_i \rangle < 0.9$ . The vortex moves downstream along the

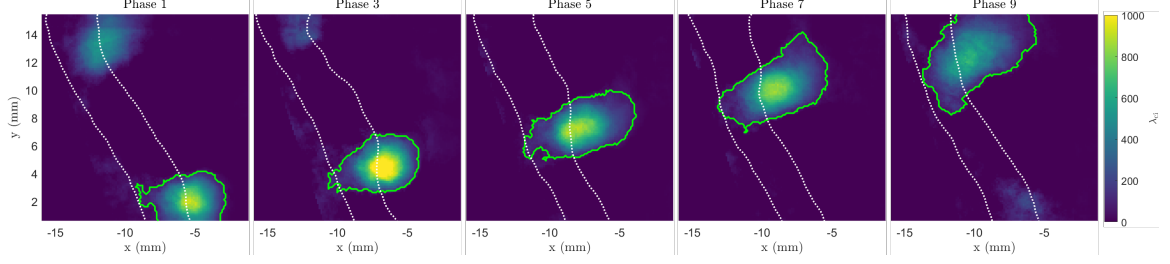


Figure 3.12: Phase averaged evolution of the dominant coherent vortex  $\langle \lambda_{ci} | \theta_i \rangle$ , with every second phase shown. White dashed curve represents  $\langle c | \theta_i \rangle = 0.1$  and  $0.9$ . Solid green curve is an isocontour of  $\langle \lambda_{ci} | \theta_i \rangle = \frac{1}{8} \langle \lambda_{ci} | \theta_i \rangle_{\max}$ .

inner shear layer between the flame and the recirculating products. The size of the vortex grows and the peak  $\lambda_{ci}$  decreases due to diffusion and flow dilatation as the vortex moves downstream. The structure and shape of the flame brush also changes in response to the presence of the vortex.

Previously, the dominant dynamic flow structure in this burner was identified as either a helical vortex core or a toroidal vortex, depending on the operating conditions [114]. The structure identified here corresponds to one of these shear layer vortex modes, though the exact mode cannot be identified due to the field of view, which only covers one half of the burner. Based on the operating conditions and results in Ref. [114], this is expected to be a helical mode. The POD on the non-reacting test case showed a similar set of modes and relative energies as the reacting flow, again consistent with the helical modes observed in all non-reacting cases in Ref. [114]. Regardless, the exact nature of the flow structure is not critical for the analysis presented here.

### 3.5 Data conditioning and convergence

The results presented in this dissertation are in terms of conditional PDFs and statistics of  $\alpha_{sfs}$ . To assess the influence of the local instantaneous flame, turbulence, and flow configuration, the data are first conditioned on various variables, including  $c$ ,  $S_{ij}S_{ij}$ ,  $\langle c \rangle$ ,  $\lambda_{ci}$ , and the region of space occupied by coherent eddies. The effects of combustion on mean dynamics of turbulence is conveniently represented by  $c$ -conditioned statistics. Similarly, the

regions of the flow dominated by turbulence can be identified using large rates of strain, or by the norm  $S_{ij}S_{ij}$ . This choice of flow conditioning is justified by Samgorinsky-type eddy viscosity models for LES. Either the swirling strength  $\lambda_{ci}$  or the location of large vortices can be used to isolate the effects of coherent structures of the results. Furthermore, results are conditioned on  $\langle c \rangle$  to assess the impact of the overall turbulent flame brush. Effects of multiple phenomena can be examined by conditioning on two or more variables.

Both conditional statistics and PDFs require binning the data. The uncertainty in the ensemble averaged conditional statistics is dictated by the convergence. Convergence is most challenging for the doubly-conditioned statistics due to the larger number of bins. Hence, to ensure that the reported doubly-conditioned means are converged: (1) the bin size was set to provide a reasonable number of samples across the range of measured values and (2) the presented data excludes any bins in which the expected uncertainty in the mean is more than 15% of the reported value (ex.  $\langle \alpha_{sfs} | c, S_{ij}S_{ij} \rangle \pm \sigma / \sqrt{N}$ , where  $\sigma$  and  $N$  are the standard deviation and number of samples used for the conditional mean).

This is nicely demonstrated in Figure 3.6, where the convergence is determined by the number of samples used (from more  $z$ -planes) to generate doubly-conditioned statistics. The main difference between the results is that the number of non-converged bins is greater for the smaller number of planes. Regions of high  $c$  and high  $S_{ij}S_{ij}\ell/u'^2$  occur less frequently than other combinations of flame and turbulence conditions; hence there are fewer number of samples to fully converge the mean statistics in this region.

Singly-conditioned results use the same range of  $c$  and  $S_{ij}S_{ij}$  values and bins of identical size as in multiple-conditioned analysis. The presented results typically use a total of 10-20 bins in each conditioning variable, which provided adequate resolution and good convergence across a reasonable range of measured values.

Another important consideration is the number of bins used when conditioning on instantaneous  $c$ . While the singly- and doubly-conditioned results may be converged in terms of the statistics for each bin, there is also uncertainty associated with the range of progress

variables represented by each bin. For example, one may use 100 bins between  $c = 0$  and  $c = 1$  (i.e. each bin representing  $\Delta c = 0.01$  in progress variable space), which will result in singly-conditioned statistic  $\langle \cdot | c \rangle$  with large sampling rate in  $c$ . However, oversampling in  $c$ -space may not yield useful results if the measurement of  $c$  has a lower resolution; a lower sampling rate in  $c$ -conditioned statistic is more meaningful when resolution of  $c$  measurement is low. A greater sampling is generally desired if the measurement resolution allows for greater  $c$ -sampling; however, a larger number of bins will have smaller number of samples in each bin, which will reduced the convergence in each bin. Consequently, the number of bins must be balanced with convergence.

Given that progress variable is estimated from the CH<sub>2</sub>O PLIF measurements, resolution of CH<sub>2</sub>O PLIF dictates the width of the  $c$ -bins used in conditional analysis. In Section 3.1, method of estimating  $c$  from distribution of formaldehyde in the flow field was presented. Using a CH<sub>2</sub>O- $c$  distribution in a representative laminar flame, the values at the boundaries of the reactants-CH<sub>2</sub>O-zone and CH<sub>2</sub>O-zone-products can be easily mapped to well-defined  $c$ . However, the accuracy of assigning  $c$  inside the flame requires more consideration.

Since there is a good agreement between  $c$ ,  $c_T$ , and  $c_i$  in a laminar premixed flame (see Figure 3.3), the resolution in  $c$  is expected to be on the order of the spatial resolution associated with CH<sub>2</sub>O-PLIF. Using the measured in-plane spatial resolution for low resolution and high resolution camera configurations, the number of non-overlapping samples within a spatial region corresponding to the thickness of the laminar flame can be computed as

$$\Delta c \propto \frac{\Delta x_i}{\delta_L^0}, \quad (3.14)$$

where  $\Delta x_i$  represents the spatial in-plane resolution. Based on the measured in-plane resolutions of the intensified cameras used for CH<sub>2</sub>O PLIF, the expected resolution of progress variable is approximately 0.1 - 0.2 in low resolution configuration and 0.03 - 0.06 in high

resolution set-up, depending on the equivalence ratio considered. For consistency, a value of  $\Delta c = 0.1$  was chosen for analysis of results across the test conditions and spatial resolutions.

It should be noted that the above stated resolution is valid in regions where the thickness of the flame does not deviate significantly from the thickness of an equivalent laminar flame. These regions can be easily identified by examining raw measurements of  $\text{CH}_2\text{O}$  distribution inside the flow field; the flame maintains uniform thickness (see Figure 2.18). In regions of flame-vortex interactions or inside highly turbulent flames, the preheat zone of the flame was previously demonstrated to broaden due to strong mixing induced by the turbulence or coherent flow structures [37]. In these regions, the resolution, as defined by Equation 3.14, is not applicable since the structure of the flame under consideration does not correspond to the one of the unstretched laminar flame. Nevertheless, the enhanced mixing of energy and species internal to the flame is expected to smooth out unknown variations in  $c$ . For the purposes of this thesis, bins of  $\Delta c = 0.1$  are maintained across all regions of the flame. It should also be noted that in broadened regions of the flame, the same  $\Delta c$  will represent a larger region of space, partially accounting for the unknown variation in temperature and species across the broadened turbulent flame surface.

## CHAPTER 4

### DECONVOLUTION

A requirement in computing  $\alpha_{\text{sfs}}$  is that the velocity and density fields under consideration are spatially resolved. Consequently, experimental measurements of  $\alpha_{\text{sfs}}$  are limited to flames of low to moderate turbulence intensity, in which the entire spectral content of the velocity field can be captured. This requires the spatial resolution of the measurement to be higher than the smallest length scale of turbulence (i.e. the dissipation scale  $\lambda_\nu \approx 6\eta$ , where  $\eta$  is the Kolmogorov length scale [115, 116]). When velocity fields are captured using TPIV with insufficient resolution to measure the smallest velocity scales, a filtering operation is imposed by the measurement at scale  $\Delta$  related to the interrogation box. This can be expressed mathematically as

$$\tilde{u}_i(\mathbf{x}) = u_i(\mathbf{x}) * \mathcal{G}(\mathbf{x}) + n(\mathbf{x}), \quad (4.1)$$

where  $\tilde{u}_i$  is the measured velocity,  $u_i$  is the true velocity,  $\mathcal{G}$  is the filter imposed by the TPIV operation, and  $n$  represents the noise added during the measurement and TPIV cross-correlation. The filter kernel corresponds to a spatial filter of unknown shape and width on the order of the final interrogation box volume over which the particle motion is averaged. In highly turbulent flows, the measurement represents a filtered velocity which either removes or attenuates the spectral content beyond the measurement cutoff wavenumber; note that non-spectral cutoff filters also attenuate spectral content below the cutoff.

As a result, fully resolved velocity field must be first estimated (i.e.  $u_i \approx u_i^*$ ) from the available velocity measurements via *deconvolution* prior to computation of  $\alpha_{\text{sfs}}$ . There are two considerations that must be addressed for reliable deconvolution in the context of this thesis. First, the primary objective here is not the accuracy of  $u^*$ , but of  $\alpha_{\text{sfs}}$ . Specifically,



$u_i^*$  obtained using these deconvolution methods will be used to calculate  $\mathcal{T}_{ij} \approx \widetilde{u_i^* u_j^*} - \tilde{u}_i \tilde{u}_j$  and consequently  $\alpha_{\text{sfs}}$ . Second, the knowledge of filter characteristics imposed by the measurement, such as its shape and size, is desired for accurate deconvolution. However, these characteristics are often unknown and difficult to estimate, as is the case with particle image velocimetry. Despite its widespread use, little is known about its effective filter kernel  $\mathcal{G}_{\text{PIV}}$ .

The goal of this chapter is to address these two issues in the context of TPIV measurements. Specifically, the objectives are to (i) evaluate the applicability of established deconvolution methods towards estimating cross-scale energy transfer, and (ii) attempt to identify the filter kernel associated with TPIV. DNS of a turbulent premixed flame, supplied by Dr. Peter Hamlington, will be used as a baseline for both objectives. Sensitivity of  $\alpha_{\text{sfs}}$  to deconvolution methods and filter shapes and sizes will be evaluated by comparing true and estimated  $\alpha_{\text{sfs}}$ . The filter kernel will be evaluated by simulating a TPIV measurement using DNS velocity fields and computing  $\mathcal{G}_{\text{PIV}}$  from fully-resolved and filtered velocity fields. The following sections give a brief overview of the deconvolution methods and TPIV filter kernel estimation technique considered.

## 4.1 Brief Overview of Deconvolution Methods

Deconvolution is commonly used in signal and image processing (e.g. [117]) to reverse the distortions by the measurement instrument or the environment. Formally, deconvolution is the inverse convolution operation and can be expressed similarly to Equation 1.15 as

$$q^*(\mathbf{x}, t) = \mathcal{Q} * \bar{q}(\mathbf{x}, t) = \int_{-\infty}^{\infty} \bar{q}(\mathbf{x}', t) \mathcal{Q}(\mathbf{x} - \mathbf{x}') d\mathbf{x}', \quad (4.2)$$

where  $\mathcal{Q} = \mathcal{G}^{-1}$  is the deconvolution kernel in physical space and  $q^*(\mathbf{x}, t)$  is the deconvolved scalar quantity. Similarly, Favre deconvolution is expressed as

$$q^*(\mathbf{x}, t) = \frac{\mathcal{Q} * \overline{\rho q}}{\mathcal{Q} * \bar{\rho}}. \quad (4.3)$$

It should be highlighted that the deconvolved quantity of interest is simply an approximation of the true unfiltered quantity of interest ( $q^* \approx q$ ). For differential filters, a class of filters where  $\bar{q}$  and  $q$  are connected via a linear differential equation, Germano [118] noted that the exact deconvolution is possible but the deconvolution operator is not bounded and the solution is unstable to high-frequency perturbations. Unfortunately, deconvolution is an ill-posed problem; multiple solutions to the forward problem (i.e.  $\bar{u} = \mathcal{G} * u$ ) are possible and the stability of  $\mathcal{Q}$  is often violated due to the sensitivity of the operation to noise and uncertainties in the filtered quantity [119]. In reality, noise is introduced into the measurement (see Equation 4.1), the details of which may be unknown. Typically, the estimate of the deconvolved signal  $q^*$  will worsen with lower signal-to-noise ratio; however, knowing even some details of the added noise can improve the estimate of  $q$  [120]. Some sort of regularization is typically applied in different deconvolution methods, which can be performed in either physical space or in the frequency domain.

Recently, deconvolution methods have started to appear in LES of reacting and inert flows to approximate unfiltered quantities and provide closure to sub-grid-scale terms with impressive results [74, 119, 121–123]. Approximate and constrained iterative reconstruction algorithms were applied in a substantially different flow configurations, involving a multi-component fuel flame to model the progress variable variance and progress variable scalar flux. Importantly, the operating conditions used in these studies involved a highly complex flame structure with a wide heat release zone and overlapping individual species reaction zones, thus presenting a stringent test case [61]. These deconvolution methods are based on mathematical arguments and provide an approximation to the inverse filtering

operation. Few to no assumptions are made regarding the reconstructed flow field or the physics of the problem, which makes this approach amenable to a wide range of operating conditions and configurations.

This section provides a brief overview of the popular deconvolution methods that will be tested. Later, these methods will be applied to the measured velocity fields to obtain  $u_i^*$  and estimate  $\alpha_{\text{sfs}}$ . To ensure that  $\alpha_{\text{sfs}}$  is physically reasonable and insensitive to processing parameters, each method will be processed using a range of appropriate processing choices. Furthermore, the  $\alpha_{\text{sfs}}$  results will be compared across the different methods to verify that the best estimate of  $\alpha_{\text{sfs}}$  is independent of the deconvolution method.

#### 4.1.1 Normal and Wiener Deconvolution

The basic premise of normal and Wiener deconvolution is the convolution theorem, which states that convolution in one domain (ex. time or space) is equal to pointwise product in the other space (frequency or wavenumber) [119]

$$u_i(x) * \mathcal{G}(x) = \mathcal{F}^{-1}\{\mathcal{F}\{u_i\} \cdot \mathcal{F}\{\mathcal{G}\}\}, \quad (4.4)$$

where  $\mathcal{F}$  and  $\mathcal{F}^{-1}$  are forward and inverse Fourier transform operators, respectively. This allows one to easily extract the original data by performing algebraic operations in the Fourier domain; this is typically referred to as *normal deconvolution*. In the case of Equation 4.1, the true velocity field can be computed as

$$u_i(x) = \mathcal{F}^{-1} \left\{ \frac{\mathcal{F}\{\tilde{u}_i\}}{\mathcal{F}\{\mathcal{G}\}} - \frac{\mathcal{F}\{n\}}{\mathcal{F}\{\mathcal{G}\}} \right\}. \quad (4.5)$$

In the ideal case, in which the filter kernel is known and noise is absent from the measurement ( $n = 0$ ), the original data can be easily recovered from the first term on the right hand side. However, noise is always present in experimental measurements and hence needs to be accounted for. Unfortunately, Fourier coefficients of  $\mathcal{G}$  are typically small at

high wavenumbers which leads to significant amplification of noise during deconvolution.

To address the noise issue in deconvolution, Wiener proposed to find a *Wiener filter*  $\mathcal{W}$ , such that the difference between the deconvolved estimate  $u_i^*$  and the true  $u_i$  is minimized [120]; this process is referred to as *Wiener deconvolution*. The Wiener filter is the solution to the minimum mean square error optimization problem, which can be written as [123]

$$\min_{u_i^*} \epsilon(k) = E \{ |\mathcal{F}\{u_i\}(k) - \mathcal{F}\{u_i^*\}(k)|^2 \}, \quad (4.6)$$

where  $E$  denotes the expectation operation. The estimate for the deconvolved solution is assumed to be of form  $u_i^* = \tilde{u}_i * \mathcal{W}$ , where the measurement is convolved with the Wiener filter. The solution to the minimization problem above is the Wiener filter [120]

$$\begin{aligned} \mathcal{W}(k) &= \frac{\mathcal{F}\{\mathcal{G}\}^*(k)\mathcal{S}(k)}{|\mathcal{F}\{\mathcal{G}\}(k)|^2\mathcal{S}(k) + \mathcal{N}(k)} \\ &= \frac{\mathcal{F}\{\mathcal{G}\}^*(k)}{|\mathcal{F}\{\mathcal{G}\}(k)|^2 + \eta(k)}, \end{aligned} \quad (4.7)$$

where  $\mathcal{S}(k) = E\{|\mathcal{F}\{u_i\}|^2\}$  and  $\mathcal{N}(k) = E\{|\mathcal{F}\{n\}|^2\}$  are the mean power spectral densities of the original data and noise, respectively;  $\eta(k) = \mathcal{N}(k)/\mathcal{S}(k)$  is the inverse of signal-to-noise ratio. Superscript  $(\cdot)^*$  represent complex conjugation. The Wiener filter uses the characteristics of the original data and the added noise to reduce the impact of noise on deconvolution. Note that as  $\mathcal{N}(k) \rightarrow 0$ ,  $\mathcal{W}(k)$  converges to the exact inverse of the filter. At frequencies with low signal-to-noise ratio ( $1/\eta \rightarrow 0$ ),  $\mathcal{W}(k) \rightarrow 0$ ; the Wiener filter attenuates frequencies according to their signal-to-noise ratio. The bandwidth of the Wiener filter is identical to the exact filter inverse; however, the amplitude of  $\mathcal{W}(k)$  is bounded, such that the inversion operation is well defined.

It should be noted that for successful inversion of filtering operation using Wiener deconvolution, the knowledge of signal and noise characteristics is required. While the spectral content of the signal can be calculated from the measured data, knowledge of the noise characteristics is often unknown. In these cases, application of Wiener deconvolu-

tion requires one to provide a good estimate for noise properties to obtain a reasonable deconvolution solution.

#### 4.1.2 Scale-Similarity (SS)

Scale-similarity method is based on the Bardina's LES model [13, 124] (see Chapter 1) and it is one of the simplest and time-effective deconvolution methods. In the context of deconvolution, the true velocity field is approximated by the filtered velocity itself

$$u_i^* = \tilde{u}_i. \quad (4.8)$$

The original LES model, first introduced by Bardina *et al.* [124] and based on physical arguments, assumes that the structure of the velocity field below  $\Delta$  is similar to that above  $\Delta$ . Consequently,  $\mathcal{T}_{ij}$  is expected to be similar to  $\mathcal{T}_{ij}^{\Delta_T}$ , the residual stress-tensor constructed from  $\tilde{u}_i$  and filtered at the test scale  $\Delta_T > \Delta$  [3], i.e.

$$\mathcal{T}_{ij} \approx \mathcal{T}_{ij}^{\Delta_T} = \hat{\rho} \left( \overline{\tilde{u}_i \tilde{u}_j} - \check{\tilde{u}_i} \check{\tilde{u}_j} \right), \quad (4.9)$$

where  $(\hat{\cdot}) = \mathcal{G}^{\Delta_T} * (\cdot)$  and  $(\check{\cdot}) = \widehat{\rho(\cdot)} / \hat{\rho}$ . The above expression essentially states that the momentum flux across  $\Delta$  is approximately equal to the net momentum flux across  $\Delta_T$  when the two filters are similar in size (often taken as  $\Delta_T = 2\Delta$ ). The similarity model has been proven accurate in many *a priori* DNS studies and is frequently combined with the Smagorinsky model to yield more physically reasonable LES results [3]. In a similar fashion, the self-similarity model can be applied to TPIV velocity fields to estimate  $\alpha_{\text{sfs}}$  across  $\Delta$ ; the raw velocity fields can be explicitly filtered using a box or Gaussian filter of size larger than the interrogation box used for TPIV cross-correlation. It should be noted, however, that  $\mathcal{T}_{ij}^{\Delta_T}$  effectively represents the momentum flux across  $\Delta_T$  and it may be more accurate to estimate  $\alpha_{\text{sfs}}$  across  $\Delta_T$  than across  $\Delta$  using the scale-similarity method.

### 4.1.3 Approximate Gaussian Method (AGM)

Another method to obtain an estimate for the true velocity field, first proposed by Katopodes *et al.* [59], is based on the Taylor series expansion of  $u_i$ . This technique aims at obtaining a higher-order approximation to the full velocity field  $u_i$  and  $\mathcal{T}_{ij}$ , which is particularly desirable for applications in complex flows. Here, the multi-dimensional Taylor expansion is first applied to the unfiltered velocity [121]

$$u_i(x'_j, t) = u_i(x_j, t) + (x'_k - x_k) \frac{\partial u_i(x_j, t)}{\partial x_k} + \frac{1}{2} (x'_k - x_k)(x'_l - x_l) \frac{\partial^2 u_i(x_j, t)}{\partial x_k \partial x_l} + \dots \quad (4.10)$$

Consider an anisotropic Gaussian filter kernel

$$\mathcal{G}_G(x, y, z) = \frac{6^{3/2}}{\pi^{3/2} \Delta_x \Delta_y \Delta_z} \exp \left( -\frac{6x^2}{\Delta_x^2} - \frac{6y^2}{\Delta_y^2} - \frac{6z^2}{\Delta_z^2} \right), \quad (4.11)$$

where  $\Delta_x$ ,  $\Delta_y$ , and  $\Delta_z$  are the filter sizes in three spatial coordinates. It should be noted that a similar decomposition can also be performed on filters of other shapes. Convolution (Equation 1.15) of the Gaussian filter kernel with the Taylor series expansion of  $u_i$  results in [121]

$$\begin{aligned} \tilde{u}_i(\mathbf{x}, t) = & u_i(\mathbf{x}, t) + \frac{\Delta_x^2}{24} \frac{\partial^2 u_i(\mathbf{x}, t)}{\partial x^2} + \frac{\Delta_y^2}{24} \frac{\partial^2 u_i(\mathbf{x}, t)}{\partial y^2} + \frac{\Delta_z^2}{24} \frac{\partial^2 u_i(\mathbf{x}, t)}{\partial z^2} \\ & + \frac{\Delta_x^4}{1152} \frac{\partial^4 u_i(\mathbf{x}, t)}{\partial x^4} + \frac{\Delta_y^4}{1152} \frac{\partial^4 u_i(\mathbf{x}, t)}{\partial y^4} + \frac{\Delta_z^4}{1152} \frac{\partial^4 u_i(\mathbf{x}, t)}{\partial z^4} \\ & + \frac{\Delta_x^2 \Delta_y^2}{1728} \frac{\partial^4 u_i(\mathbf{x}, t)}{\partial x^2 \partial y^2} + \frac{\Delta_y^2 \Delta_z^2}{1728} \frac{\partial^4 u_i(\mathbf{x}, t)}{\partial y^2 \partial z^2} + \frac{\Delta_x^2 \Delta_z^2}{1728} \frac{\partial^4 u_i(\mathbf{x}, t)}{\partial x^2 \partial z^2} + \mathcal{O}(\Delta^6). \end{aligned} \quad (4.12)$$

Due to symmetry, terms with odd powers of  $x$ ,  $y$ , and  $z$  are eliminated; application of an asymmetric filter kernels would retain all of the partial derivatives in the above expression. Rearranging Equation 4.12 for  $u_i$  and using the expression recursively leads to an

approximate deconvolution operation [121]

$$\begin{aligned}
u_i(\mathbf{x}, t) = & \tilde{u}_i(\mathbf{x}, t) - \frac{\Delta_x^2}{24} \frac{\partial^2 \tilde{u}_i(\mathbf{x}, t)}{\partial x^2} - \frac{\Delta_y^2}{24} \frac{\partial^2 \tilde{u}_i(\mathbf{x}, t)}{\partial y^2} - \frac{\Delta_z^2}{24} \frac{\partial^2 \tilde{u}_i(\mathbf{x}, t)}{\partial z^2} \\
& + \frac{\Delta_x^4}{1152} \frac{\partial^4 \tilde{u}_i(\mathbf{x}, t)}{\partial x^4} + \frac{\Delta_y^4}{1152} \frac{\partial^4 \tilde{u}_i(\mathbf{x}, t)}{\partial y^4} + \frac{\Delta_z^4}{1152} \frac{\partial^4 \tilde{u}_i(\mathbf{x}, t)}{\partial z^4} \\
& + \frac{5\Delta_x^2\Delta_y^2}{1728} \frac{\partial^4 \tilde{u}_i(\mathbf{x}, t)}{\partial x^2\partial y^2} + \frac{5\Delta_y^2\Delta_z^2}{1728} \frac{\partial^4 \tilde{u}_i(\mathbf{x}, t)}{\partial y^2\partial z^2} + \frac{5\Delta_x^2\Delta_z^2}{1728} \frac{\partial^4 \tilde{u}_i(\mathbf{x}, t)}{\partial x^2\partial z^2} \\
& + \mathcal{O}(\Delta^6).
\end{aligned} \tag{4.13}$$

This approach allows to express the unfiltered velocity field in terms of the measured quantities at all locations of interest. For a symmetric and uniform filter ( $\Delta = \Delta_x = \Delta_y = \Delta_z$ ), the approximate deconvolution operator is simplified to

$$\begin{aligned}
u_i(\mathbf{x}, t) = & \tilde{u}_i(\mathbf{x}, t) - \frac{\Delta^2}{24} \nabla^2 \tilde{u}_i(\mathbf{x}, t) + \frac{\Delta^4}{1152} \left( \frac{\partial^4 \tilde{u}_i(\mathbf{x}, t)}{\partial x^4} + \frac{\partial^4 \tilde{u}_i(\mathbf{x}, t)}{\partial y^4} + \frac{\partial^4 \tilde{u}_i(\mathbf{x}, t)}{\partial z^4} \right) \\
& + \frac{5\Delta^4}{1728} \left( \frac{\partial^4 \tilde{u}_i(\mathbf{x}, t)}{\partial x^2\partial y^2} + \frac{\partial^4 \tilde{u}_i(\mathbf{x}, t)}{\partial y^2\partial z^2} + \frac{\partial^4 \tilde{u}_i(\mathbf{x}, t)}{\partial x^2\partial z^2} \right) + \mathcal{O}(\Delta^6).
\end{aligned} \tag{4.14}$$

The above approximate deconvolution may be used in explicit or implicit numerical formulations, using the second order derivative scheme. Note that the accuracy of this approximation depends on the series truncation order and can be improved by retaining the higher order terms. Moreover, this approach is based on purely mathematical basis and the form of the unfiltered velocity field is not assumed beforehand unlike the self-similarity approach. Domingo *et al.* [121] has proved that the model for  $\mathcal{T}_{ij}$ , obtained via Taylor expansion, is an exact solution to the transport equations for  $\mathcal{T}_{ij}$  to a known accuracy. At this point, it is worth noting the form of  $\mathcal{T}_{ij}$  obtained using the Taylor expansion [121]

$$\mathcal{T}_{ij} \approx \widetilde{u_i^* u_j^*} - \tilde{u}_i \tilde{u}_j = \underbrace{\widetilde{\tilde{u}_i \tilde{u}_j} - \tilde{u}_i \tilde{u}_j}_{\text{Bardina}} - \frac{\Delta^2}{24} \widetilde{\tilde{u}_i \nabla^2 \tilde{u}_j} - \frac{\Delta^2}{24} \widetilde{\tilde{u}_j \nabla^2 \tilde{u}_i}. \tag{4.15}$$

This indicates that, to second order in  $\Delta$ , Equation 4.15 reduces to the scale similarity

model of Bardina *et al.* [124]. Because the self-similarity and Taylor decomposition methods are derived based on physical and mathematical arguments, respectively, the similarity between the two approaches is encouraging. More importantly, this demonstrates that the Taylor decomposition method yields a physically reasonable approximation.

#### 4.1.4 Approximate Deconvolution Model (ADM)

One of the earliest attempts at deconvolution using in LES is the approximate deconvolution model (ADM) proposed by Stolz *et al.* [125]. ADM is an iterative method, derived from the van Cittert filter [119], that involves repeated filtering of the measurement

$$u_i^{\nu+1} = u_i^\nu + (\tilde{u}_i - \mathcal{G} * u_i^\nu), \quad (4.16)$$

where  $\nu$  is the number of iterations used and which determines the strength of deconvolution. The van Cittert algorithm repeatedly adds detail to the current estimate, where the added detail is the difference between the measurement and the filtered estimate. Iterations are started by setting the first estimate to the measurement. Alternatively, the deconvolution operator can be derived recursively from the van Cittert filter and written in an explicit form as

$$\mathcal{Q}_N^{ADM} = \sum_{\nu=0}^N (I - \mathcal{G})^\nu, \quad (4.17)$$

where  $I$  is the identity operator, and  $N$  is the number of iterations. The approximate deconvolved quantity of interest is obtained through  $q^* = \mathcal{Q}_N^{ADM} * \tilde{q}$  [125].

In practice, the geometric series in Equation 4.17 is truncated at a finite  $N$ , thereby ignoring the higher frequencies that are more sensitive to perturbations; the model first recovers the lower frequency components [126]. Note that truncation of an infinite series is a form of regularization of ill-posed problems [125]. A good compromise between the accuracy of the solution and the computational cost of ADM is achieved with  $N = 5$  [125]. Typically, a higher number of iterations tends to amplify the image noise to a point where



the solution becomes indistinct.

ADM has many advantages, including rapid deblurring, no smoothness restrictions, simple mathematical operations, and additional information. However, it is sensitive to noise and the algorithm becomes unstable if  $N$  exceeds a certain limit, as analyzed in detail in Refs. [119, 123] for non-reacting LES.

#### 4.1.5 Regularized Deconvolution

Finally, the regularized deconvolution method (RDM) can be used to obtain  $u_i^*$ . This technique typically applies some type of regularization to ensure that the solution is bounded and does not violate conservation laws [126]. This approach is based on the generalized *Tikhonov* regularization problem [123], i.e.

$$u_i^* = \arg \min \left( \underbrace{\|\tilde{u}_i - \tilde{\mathcal{G}} * u_i^*\|_2}_{\text{deconvolution}} + \underbrace{\gamma \|\mathbf{\Gamma} u_i^*\|_2}_{\text{regularization}} \right), \quad (4.18)$$

where  $\mathbf{\Gamma}$  is the Tikhonov matrix and  $\gamma$  is the regularization parameter. The deconvolution term in Equation 4.18 ensures that the error between  $\tilde{q}^*$  and  $\tilde{q}$  is minimal, while the role of the regularization term is to promote the desired characteristics in  $q^*$  via  $\mathbf{\Gamma}$ ;  $\gamma$  is used to moderate the influence of  $\mathbf{\Gamma}$ . Two common Tikhonov matrices are the identity and the Laplacian operator [119]. The former promotes solutions with a small Euclidian norm, while the latter enforces spatially smooth fields (small second derivatives).

The RDM methodology is not restricted to Tikhonov regularization. Other methods, such as Tikhonov-Lavrentiev regularization can also be applied to the measured data [119]. This approach has been successfully applied to reconstruct the subfilter scale scalar fields in the implicitly-filtered LES of reacting flows [74, 123].

Table 4.1: Physical model parameters of the highly turbulent premixed methane–air flame simulated in the present study.

$\mathcal{D}$	$256 \times 256 \times 4096$	Number of cells
	$0.7 \text{ cm} \times 0.7 \text{ cm} \times 11.2 \text{ cm}$	Physical Dimensions
$\Delta x$	$0.70037 \text{ cm}$	Cell size
$\varepsilon$	$1.32 \times 10^6 \text{ erg/cm}^3\text{s}$	Energy injection rate
$U_\delta$	$469.3 \text{ cm/s}$	Turbulent velocity at scale $\delta_L$
$U$	$1182 \text{ cm/s}$	Turbulent velocity at scale $L$
$U_{rms}$	$1359 \text{ cm/s}$	Turbulent r.m.s. velocity
$U_l$	$785 \text{ cm/s}$	Unburned integral velocity
$l$	$2.05 \times 10^{-1} \text{ cm}$	Integral length
$\eta$	$1.382 \times 10^{-3} \text{ cm}$	Kolmogorov length scale in reactants
$\tau_{ed}$	$5.922 \times 10^{-4} \text{ s}$	Eddy turnover time $L/U$
$Da$	$0.19$	Damkohler number
$Ka$	$142$	Karlovitz number



Figure 4.1: Instantaneous snapshot of gas density along the central slice of the DNS volume. The red rectangle represents the region of interest used for deconvolution analysis.

## 4.2 Test Setup and Data Analysis

The direct numerical simulation used in this study is identical to that described by Darragh *et al.* [127, 128] for the Lagrangian analysis of enstrophy dynamics and analysis of particle pair dispersion in turbulent premixed flames. The authors have kindly shared the dataset for this study and the readers are referred to the aforementioned references for further details of the numerical setup. The details of the DNS simulation are summarized in Table 4.1. A sample snapshot of local gas density is show in Figure 4.1.

### 4.2.1 Deconvolution Analysis

The region of interest for deconvolution method comparison was isolated to a  $106 \text{ vx} \times 106 \text{ vx} \times 43 \text{ vx}$  ( $2.9 \text{ mm} \times 2.9 \text{ mm} \times 1.2 \text{ mm}$ ) in the region where the flame is present (see the red region in Figure 4.1). A reduced domain of interest was considered due to high

numerical cost of deconvolution analysis; convolution of a  $N_c \times N_c \times N_c$  domain with an  $M \times M \times M$  kernel requires  $\mathcal{O}(N_c^3 \times M^3)$  multiplications. The domain of comparison was chosen such that each dimension is at least three times the size of the test filter kernel used for comparison (i.e.  $3\Delta_T$ ).

Comparison between  $\alpha_{\text{sfs}}$  and  $\alpha_{\text{sfs}}^*$  is performed along the central portion of the comparison domain (i.e. within  $\Delta_T$ ). In the context of this thesis,  $\alpha_{\text{sfs}}^*$  is the inter-scale energy transfer deduced from deconvolution. The unresolved velocity fields used for deconvolution are obtained by filtering fully-resolved fields at scale  $\Delta$ . However, comparison between  $\alpha_{\text{sfs}}$  and  $\alpha_{\text{sfs}}^*$  is performed at the test filter scale  $\Delta_T > \Delta$ .

To perform deconvolution, velocity and density fields representative of experimental measurements must first be obtained (i.e.  $\tilde{u}_i$  and  $\bar{\rho}$ ). This is achieved using the fully resolved fields, which are filtered using a representative filter kernel and downsampled. Specifically, (i) the DNS velocity and density fields are filtered using a simulated TPIV filter of size  $\Delta$  (here, only  $\Delta = 5$  vx and  $\Delta = 7$  vx box filters are considered), (ii) the filtered velocity and density fields are downsampled at a rate corresponding to representative TPIV overlap (0%, 50%, 75%, or 100%), and (iii) random noise is added at each location. Figure 4.2 shows the sampling filter  $\Delta$ , test filter  $\Delta_T$ , and the sampling locations at target overlaps for  $\Delta = 7$  vx.

Deconvolution of simulated measurements is performed using the four techniques outlined in the previous section: SS, AGM, ADM, and RDM. Each method uses the simulated measurements to estimate the fully resolved fields (i.e.  $u_i^*$  and  $\rho^*$ ) at the same sampling locations as the simulated measurements. The deconvolved velocity fields are then used to estimate the cross-scale energy transfer  $\alpha_{\text{sfs}}^*$  across a test scale  $\Delta_T$  (box filter kernel), which was fixed at  $\Delta_T = 14$  vx in the original DNS grid (i.e. the physical region represented by  $\Delta_T$  was fixed while the number of points varies based on the measurement down-sampling).

A few comments on the deconvolution methods are warranted here. The AGM and

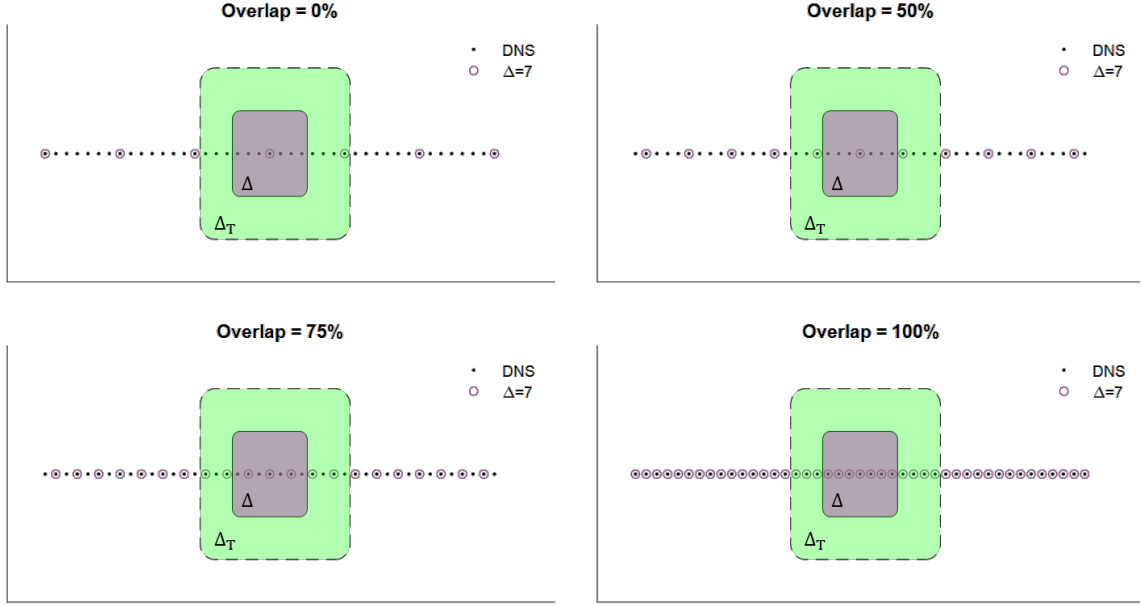


Figure 4.2: Schematic representation of the DNS grid and the sampling grid in a single dimension for overlaps typically used for TPIV. Grey and green blocks depict the  $\Delta$  and  $\Delta_T$  filters.

ADM deconvolution was performed in accordance to Equation 4.15 and Equation 4.17, respectively. It is noted that the ADM approach requires at least two points in the physical region represented by  $\Delta$ ; hence only large overlaps are used for ADM (75% and 100%). In scale similarity method, the approximation  $\mathcal{T}_{ij} \approx \mathcal{T}_{ij}^{\Delta_T}$  is not used;  $\mathcal{T}_{ij}^{\Delta_T}$  is computed directly since comparison of  $\alpha_{\text{sfs}}^*$  with  $\alpha_{\text{sfs}}$  is done at scale  $\Delta_T$ . The RDM approach allows for the solution to be super-sampled (finer sampling than the original measurement). In this study, the same grid as DNS was used for RDM, but the deconvolved results were downsampled back to the measurement grid for  $\alpha_{\text{sfs}}$  comparisons. Here,  $\Gamma$  is taken as the Laplacian operator with  $\gamma = 0.1$ .

#### 4.2.2 Identification of TPIV Filter

There are multiple ways to estimate the shape of the filter kernel, given the filtered and the original – unfiltered – velocity fields. However, both of these fields must be known. A known velocity field, either from DNS or analytical, is used as the unfiltered baseline. To

obtain  $\tilde{u}_i$ , the TPIV algorithm must be used to replicate TPIV cross-correlation.

A pair of particle tomograms is generated from the analytical velocity field by creating a pair of three-dimensional arrays, which represent a discretized physical volume in space. Then, simulated particles are randomly “seeded” through this volume, and then convected based on the velocity of the field at each particle’s individual location; a fourth-order Runge-Kutta (RK4) method time-marching scheme is used. Note that the seeding is done proportionally to the local gas density and each particle was assigned a Gaussian intensity profile of 5 voxels wide. The time separation between two tomogram snapshots was set to  $5 \mu\text{s}$ . These settings represent the recommended targets for TPIV, including average particle density of 7-10 particles per target interrogation box and an average particle displacement distance of  $1/4 - 1/3$  of the interrogation box width [78]. The tomograms are then uploaded to LaVision DaVis 8.4 for cross-correlation. With the knowledge of  $u_i$  and  $\tilde{u}_i$ , it is possible to estimate  $\mathcal{G}_{\text{TPIV}}$ . Here, three methods are considered.

#### *Fourier Inversion*

This approach utilizes the convolution theorem (Equation 4.4) and is similar to normal deconvolution, except the unknown is the convolution kernel

$$\mathcal{G}(x) = \mathcal{F}^{-1} \left\{ \frac{\mathcal{F}\{\tilde{u}_i\}}{\mathcal{F}\{u_i\}} \right\}. \quad (4.19)$$

Since no additional noise is added, it is theoretically possible to obtain an estimate for the filter kernel. However, the cross-correlation of TPIV also introduces some noise that may render the Fourier method inaccurate; TPIV noise may be due to peak-locking, bias due to ghost particles, and uncertainty due to insufficient particle count inside the interrogation box.

### Regularized Optimization

An alternative method is to iteratively search for a filter kernel that minimizes the difference between the measurement and the filtered true data. This method mimics the regularized deconvolution method; however, the goal of the optimization problem is to identify the filter, not the original velocity fields, i.e.

$$\mathcal{G}_{\text{PIV}} = \arg \min (\|u_i * \mathcal{G} - \tilde{u}_i\|_2 + \gamma \|\mathbf{\Gamma} \mathcal{G}\|_2). \quad (4.20)$$

The regularization used here includes constraining the norm of the filter to be unity, enforcing isotropy of the filter, and maintaining a positive value at the center of the filter. For computational efficiency, a one-dimensional radial profile was used in optimization. Prior to each optimization pass, a three-dimensional filter was generated by revolving the radial profile and normalizing appropriately. It should be noted that the radial  $\mathcal{G}_{\text{PIV}}$  profile was weighted by the weighing function  $w(r) = r^2$  to compensate for larger number of points contained in a spherical shell of radius  $r$ . DNS velocity fields were also used as the baseline for this approach.

### Step Response

The last method examines the step response in the velocity field to obtain a one-dimensional estimate for the filter kernel, similar to the approach taken by Elsinga *et al.* [129]. Figure 4.3 shows the procedure used to estimate  $\mathcal{G}_{\text{PIV}}$  using this method. Here, a one-dimensional “step” flow and is used as the baseline velocity field.

First, a one-dimensional flow with a step in  $x$ -velocity (horizontal) is created as shown in Figure 4.3(a); the velocity is set to  $U_x = \pm 10$  m/s above and below the step, respectively. Only a single component of velocity is considered in this study. Next, a pair of particle tomograms is generated for the imposed velocity field (Figure 4.3(b)). Tomograms were generated at a resolution of  $512 \times 512 \times 512$  vx with 75,000 total particles over a cube with

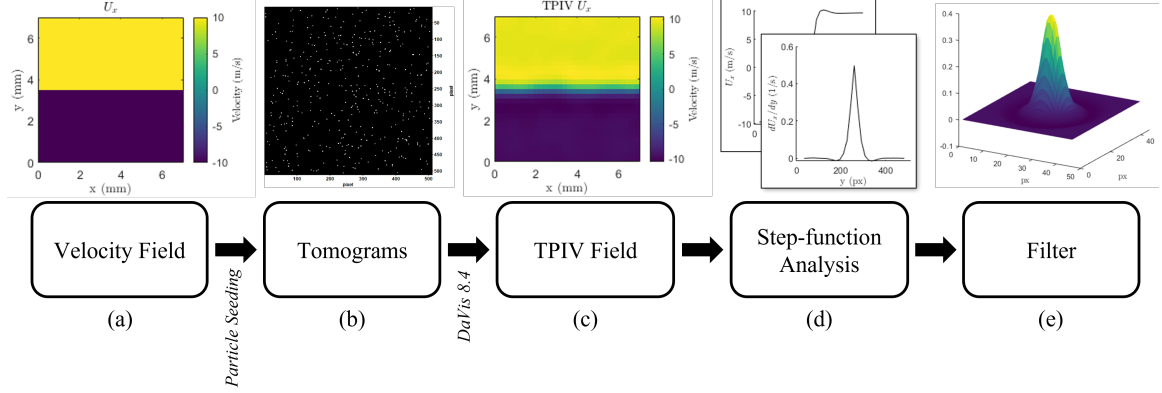


Figure 4.3: A flowchart for the process to obtain the TPIV filter from an analytical velocity field.

a side length of 7 mm, effectively quadrupling the number of cells of a single  $x - y$  plane of DNS. After cross-correlation of tomograms in LaVision DaVis 8.4,  $\tilde{u}_i$  are obtained. The resulting TPIV velocity fields, shown in Figure 4.3(c), were averaged across the two homogeneous directions ( $x$  and  $z$ ), to obtain a one-dimensional mean velocity profile across the step, as shown schematically in Figure 4.3(d). By spatial differentiation of the measured mean displacement field with respect to  $y$  and normalizing it with the step height, the normalized pulse response, or  $\mathcal{G}_{\text{PIV}}$ , is obtained [129]. The one-dimensional profile is revolved in 3D to give an estimate for  $\mathcal{G}_{\text{PIV}}$  (Figure 4.3(e)) to be used in validation.

Processing of tomograms and calculation of TPIV velocity fields through direct cross-correlation was performed using the LaVision DaVis 8.4 software. Two different interrogation boxes were used to investigate how the filter would scale with interrogation box size; namely 24 vx and 64 vx with an overlap of 75%. The software’s native universal outlier detection and removal algorithm was also used. Validation of the TPIV convolution kernel was done by comparing the DNS velocity fields filtered using  $\mathcal{G}_{\text{PIV}}$  to the same velocity field generated by TPIV cross-correlation; the identical process is used to generate TPIV velocity fields, as described above.

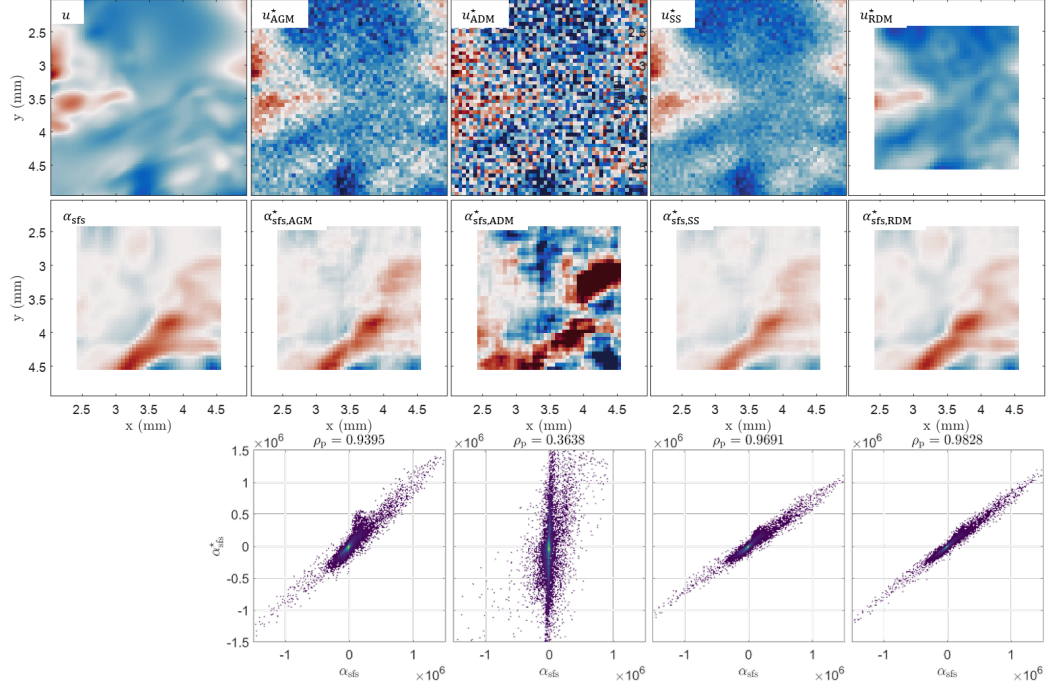
### 4.3 Application of Deconvolution Methods on DNS

Sample results of deconvolution are shown in Figure 4.4 for  $\Delta = 7$  vx and 75% overlap. The left column shows the fully resolved velocity and  $\alpha_{\text{sfs}}$  across  $\Delta_T = 7$  vx and  $\Delta_T = 14$  vx, obtained directly from DNS and downsampled to the measurement grid. The remaining columns show the deconvolved velocity  $u_i^*$  and estimated  $\alpha_{\text{sfs}}^*$  obtained from the various methods described in Section 4.1. The bottom row shows the joint PDF between true  $\alpha_{\text{sfs}}$  and  $\alpha_{\text{sfs}}^*$  for each deconvolution method.

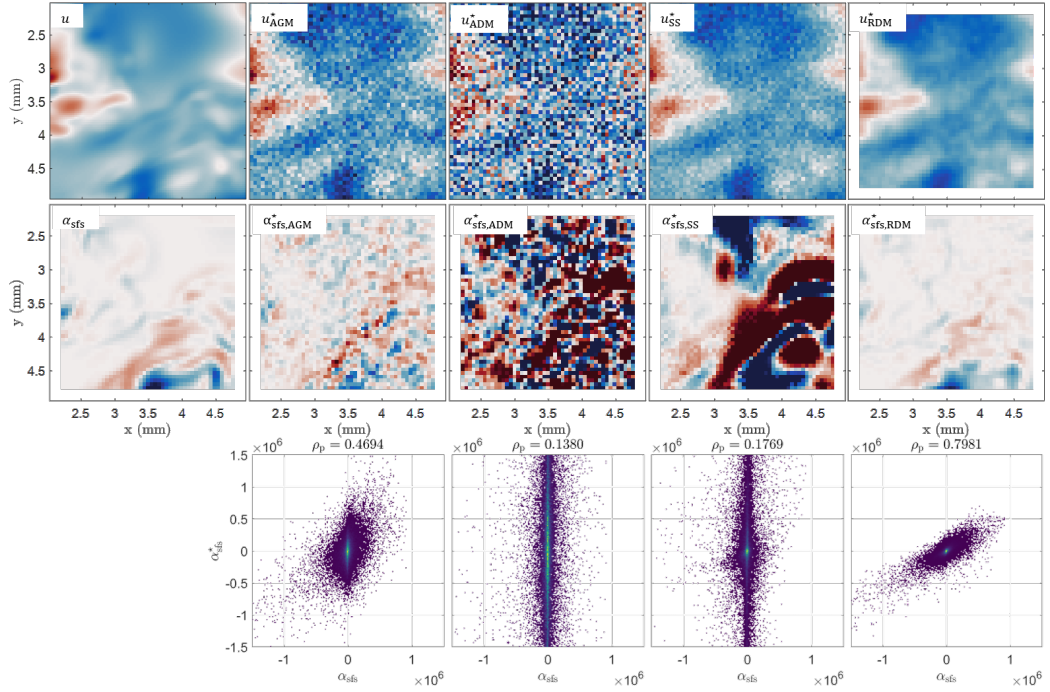
The first trend to note is that the deconvolved velocity for  $\Delta_T = 14$  vx retains the large scale features; however, the presence of the noise in the filtered velocity propagates into the deconvolved solution. Note that the filtered velocity for all case is represented by  $u_{\text{SS}}^*$ , since scale-similarity method assumes  $u_i^* = \tilde{u}_i$ . The AGM solution adds the second spatial derivative to filtered velocity, viz.  $u_{\text{AGM}}^* = \tilde{u}_i + (\Delta^2/24)\partial_{k,k}\tilde{u}_i$ , which is amplifies noise present in the measurement. The ADM solution uses Van Cittert iterations, which converge if  $\|I - \mathcal{G}\| < 1$  in Equation 4.17 [130]. This is equivalent to  $1 - \hat{\mathcal{G}} < 1$  in wavenumber space, where  $\hat{\mathcal{G}}$  is the Fourier transform of  $\mathcal{G}$ . Since the box filter is a sinc function in wavenumber space, this condition is not satisfied, which leads to significant oscillations in the solution. Finally, the RDM solution shows the greatest resistance to noise because optimization penalizes non-smooth solutions while trying to minimize the deconvolution error at all locations simultaneously.

Comparison of  $\alpha_{\text{sfs}}$  and  $\alpha_{\text{sfs}}^*$  shows a good qualitative agreement for AGM, SS, and RDM methods. The degree of correlation is indicated in the joint PDFs by the Pearson correlation coefficient  $\rho_p$  in Figure 4.4. Similar to deconvolved velocities,  $\alpha_{\text{sfs}}^*$  features look similar to  $\alpha_{\text{sfs}}$  for  $\Delta_T = 14$  vx, with AGM and ADM methods containing more noise than SS and RDM. Convolution of deconvolved fields with  $\mathcal{G}$  at  $\Delta_T$  attenuates any high-frequency content in  $u_i^*$ , including measurement noise, leading to similarity of  $\alpha_{\text{sfs}}^*$  across deconvolution methods. Due to the oscillatory nature of ADM, noise in  $u_{\text{ADM}}^*$  is





(a)  $\Delta_T = 14 \text{ vx}$ .



(b)  $\Delta_T = 7 \text{ vx}$ .

Figure 4.4: Comparison of deconvolved velocity and estimated  $\alpha_{\text{sfs}}$  using four deconvolution methods. Top row:  $u$ -velocity; middle row:  $\alpha_{\text{sfs}}$  across  $\Delta_T$ ; bottom row: joint PDF between  $\alpha_{\text{sfs}}$  and  $\alpha_{\text{sfs}}^*$ . Left column shows true velocity and  $\alpha_{\text{sfs}}$ .

significantly larger than other methods, resulting in  $\alpha_{\text{sfs},\text{ADM}}^*$  being largely overestimated. Nevertheless,  $\alpha_{\text{sfs},\text{ADM}}^*$  retains major  $\alpha_{\text{sfs}}$  structures and the corresponding sign of  $\alpha_{\text{sfs}}$ . The AGM, SS, and RDM methods show a very strong correlation ( $\rho_p > 0.9$ ) of  $\alpha_{\text{sfs}}^*$  to  $\alpha_{\text{sfs}}$ , with SS method under-predicting the magnitude of cross-scale energy transfer slightly. This is likely due to repeated filtering of the fully-resolved velocity field in the scale-similarity approach; other methods attempt to reconstruct the higher frequency content in  $u_i^*$  prior to convolution with  $\Delta_T$ .

Comparison of deconvolution results between  $\Delta_T = 7 \text{ vx}$  and  $\Delta_T = 14 \text{ vx}$  clearly demonstrates the sensitivity of  $\alpha_{\text{sfs}}^*$  to  $\Delta_T$ . While  $u_i^*$  appears qualitatively very similar between two target scales,  $\alpha_{\text{sfs}}^*$  is significantly different from  $\alpha_{\text{sfs}}$  when  $\Delta_T = \Delta$ . In particular, there is more noise in  $\alpha_{\text{sfs}}^*$ , the local magnitude of  $\alpha_{\text{sfs}}^*$  is overestimated, and large-scale structures are less similar to true structures. JPDFs further supports these observations; the magnitude of  $\alpha_{\text{sfs}}^*$  is significantly larger than  $\alpha_{\text{sfs}}$ , and noise widens the trendline shown in the JPDF. Moreover, estimation of  $\alpha_{\text{sfs}}^*$  is also sensitive to the deconvolution methods when  $\Delta_T = \Delta$  as the observed predictions are less similar amongst each other than for a larger  $\Delta_T$ . The best estimate is provided by RDM; however, large scale  $\alpha_{\text{sfs}}$  are not reconstructed to the same accuracy as compared to  $\Delta_T = 14 \text{ vx}$ . Since AGM and ADM methods are more sensitive to noise, it is not surprising that the noise propagates to  $\alpha_{\text{sfs}}^*$ . Interestingly, the scale-similarity approach over-estimates the magnitude of  $\alpha_{\text{sfs}}^*$  the most among the considered deconvolution methods. In fact, the shape and magnitude of the  $\alpha_{\text{sfs}}$  structures is more similar to the ones at  $\Delta_T = 14 \text{ vx}$ . This observation is expected, since the scale-similarity method uses information at the test filter scale to estimate  $\mathcal{T}_{ij}^\Delta$ . In conclusion, use of deconvolution methods near the original filter scale should be avoided due to high uncertainties in  $\alpha_{\text{sfs}}^*$ . When considering larger test scales  $\Delta_T > \Delta$ , AGM, SS, and RDM provide very similar results; the scale-similarity method can be used since it has the lowest numerical cost.

To gain additional insight, the trends of the correlation coefficient with downsampling

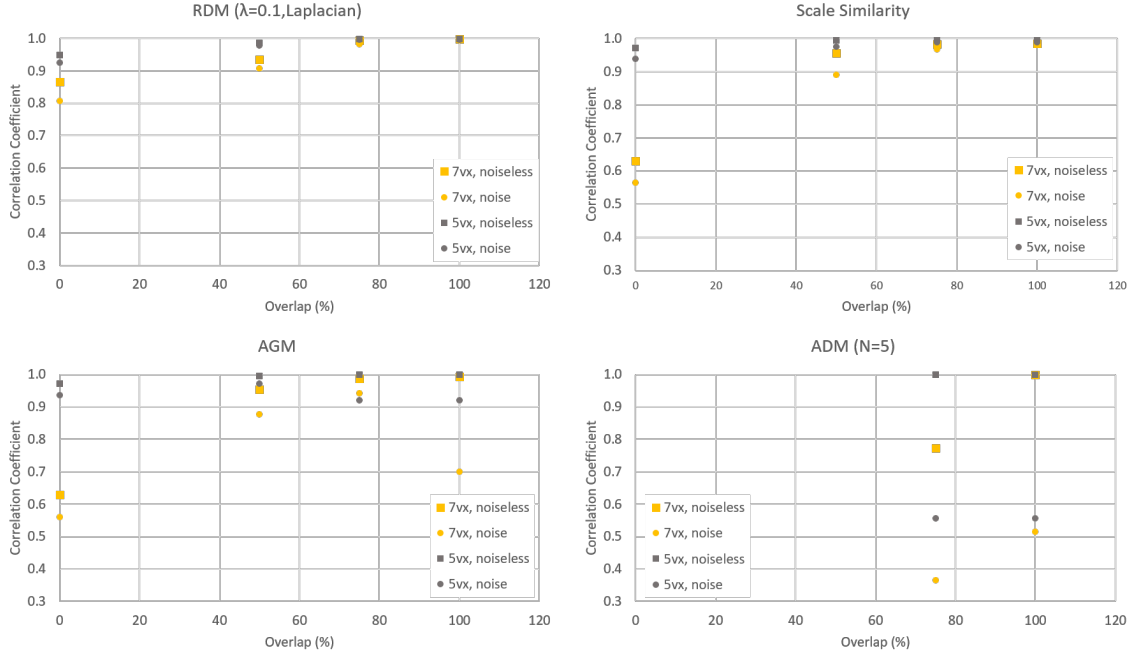


Figure 4.5: Variation of correlation coefficient between  $\alpha_{\text{sfs}}$  and  $\alpha_{\text{sfs}}^*$  across  $\Delta_T = 14$  vx with filter overlap, size of the measurement filter, and presence of noise for the four deconvolution methods.

rate, size of measurement filter  $\Delta$ , and presence of noise are analyzed. Figure 4.5 shows the variation of the correlation coefficient with filter overlap for the four deconvolution methods and using  $\Delta = 5$  vx and  $\Delta = 7$  vx. Presence of noise clearly decreases the strength of correlation when other parameters are held constant. The impact of noise on correlation is greatest in ADM results, due to inherent amplification of noise when using a spatial box filter. Generally, presence of noise reduces the correlation by approximately 0.1 across the conditions studied here; the reduction becomes more significant at lower overlap.

From Figure 4.5, it can be clearly seen that lower overlap (lower down-sampling) leads to a reduction of correlation between  $\alpha_{\text{sfs}}^*$  and  $\alpha_{\text{sfs}}$ , where a significant drop occurs at 0% overlap. This is likely due to the fact that a smaller number of points is used when convolving  $u_i^*$  with  $\Delta_T$ . For example, deconvolution using  $\Delta$  with 0% overlap uses the information only available at a single measurement location (see Figure 4.2) and further filtering at  $\Delta_T$

uses two neighboring measurement locations. In contrast, a measurement with a 75% overlap uses 3 points for deconvolution and 7 points for test filtering. Consequently, a larger number of samples reduces the variance of the test-filtered velocity at any given location, effectively increasing the confidence in the measurements and reducing the effect of noise on  $\alpha_{\text{sfs}}^*$ .

Finally, the correlation coefficients for  $\Delta = 5 \text{ vx}$  are universally greater than those for  $\Delta = 7 \text{ vx}$ . This suggests that the ratio of measurement filter to test filter  $\Delta/\Delta_T$  may be important. For a small  $\Delta/\Delta_T$  the test filter is significantly larger than the original measurement filter and it tends to remove structures smaller than  $\Delta_T$ , including those deconvolved using  $\Delta$ . As a result, in the limit  $\Delta/\Delta_T \rightarrow 0$ , the details of deconvolution are irrelevant and  $u_i^* = \tilde{u}_i$  should be sufficient to approximate  $\alpha_{\text{sfs}}$ . On the other hand, at  $\Delta/\Delta_T \approx 1$ , the test filter retains most flow structures obtained via deconvolution and hence the deconvolution methods dictate the accuracy of  $\alpha_{\text{sfs}}^*$ .

#### 4.3.1 Target test filter range

Application of more sophisticated deconvolution methods (AGM, ADM, and especially RDM) to estimate  $\alpha_{\text{sfs}}$  across the measurement length scale  $\Delta$  is cost-prohibitive. However, the scale-similarity method allowed computation of  $\alpha_{\text{sfs}}^*$  in a reasonable time frame, albeit at larger test filter scales. In this dissertation, the scale-similarity method is used for deconvolution and the range of scales considered is  $\Delta_T > \Delta$ . The goal of this section is to identify the target filter scales at which  $\alpha_{\text{sfs}}$  can be reliably estimated using not fully resolved TPIV velocity and an unknown  $\mathcal{G}_{\text{PIV}}$ . Since scale-similarity applies the filtering operation twice, the focus here will be on the effect of repeated filtering on the accuracy of  $\alpha_{\text{sfs}}$  estimate.

For most filter kernels of interest in LES, filtering attenuates or removes high frequency content from the input signal. Consequently, repeated filtering tends to smooth the signal more with each additional pass, unless the filter kernel is the sharp spectral cutoff filter of a

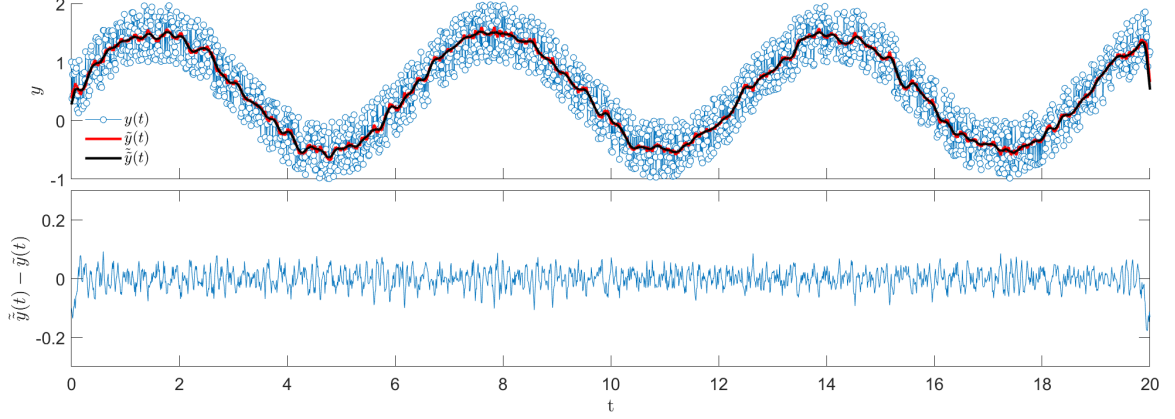


Figure 4.6: Demonstration of double filtering a noisy sine wave using a spatial box filter of width  $\Delta = 15$ . Top: original signal (blue circles), filtered signal (red), and doubly filtered signal (black). Bottom: difference between single- and doubly-filtered signal.

fixed size. As a result, repeated filtering of the quantity of interest generally does not yield the originally filtered input like it does for the averaging operation

$$\tilde{\tilde{u}} \neq \tilde{u}. \quad (4.21)$$

This is demonstrated in Figure 4.6, where an example sine wave superimposed with uniform noise, *viz.*  $y(t) = \sin(t) + \mathcal{U}(0, 1)$ , is filtered twice using a spatial box filter of  $\Delta = 15$  samples. Clearly, the high frequency noise is attenuated in  $\tilde{y}(t)$  and  $\tilde{\tilde{y}}(t)$  traces, but the single-filtered and double-filtered traces are not the same. The bottom plot of Figure 4.6 shows the difference between singly- and doubly-filtered traces ( $\tilde{\tilde{y}}(t) - \tilde{y}(t)$ ), which is clearly non-zero. Thus, it is vital to evaluate the uncertainty of the final result to the effects of repeated filtering. The analysis that follows proceeds in the following manner: first, velocity fields of different resolutions are filtered and compared to each other to identify the scale at which the details of the original TPIV measurement kernel are insignificant; and second, the inter-scale energy transfer is evaluated across a target filter scale  $\Delta_T$  using velocity fields of different resolution to determine the sensitivity of the result to the original TPIV kernel size.

To begin, let's consider the velocity field that is filtered twice, first using the filter kernel

$\mathcal{G}_{\text{PIV}}$  (across  $\Delta$ ), the details of which may not be fully known, and second using  $\mathcal{G}$  (across  $\Delta_{\text{T}}$ ) with known parameters:, i.e.

$$\hat{u}_i = \underbrace{\mathcal{G} * \mathcal{G}_{\text{PIV}}}_{\mathcal{G}_{\text{T}}} * u_i. \quad (4.22)$$

Due to the associative property of convolution, the above operation can be re-expressed as  $\hat{u}_i = \mathcal{G}_{\text{T}} * u_i$ , where  $\mathcal{G}_{\text{T}}$  is the convolution of  $\mathcal{G}$  with  $\mathcal{G}_{\text{PIV}}$ . This is equivalent to performing a single convolution of  $u_i$  with  $\mathcal{G}_{\text{T}}$ . In instances where only limited knowledge of the filter details is available in the smaller kernel ( $\mathcal{G}_{\text{PIV}}$  in Equation 4.22), performing a second convolution with a larger filter kernel  $\mathcal{G}$  may allow one to disregard the details of the smaller filter when computing  $\hat{u}_i$ .

First, the difference between  $\mathcal{G}$  and  $\mathcal{G}_{\text{T}}$  is examined. Figure 4.7 shows  $\mathcal{G}_{\text{PIV}}$ ,  $\mathcal{G}$ , and  $\mathcal{G}_{\text{PIV}} * \mathcal{G}$  for a range of  $\Delta_{\text{T}}/\Delta$  size ratios. The three most commonly used filter kernels used in LES are considered for the hypothetical  $\mathcal{G}_{\text{PIV}}$  kernel: box, Gaussian, and sharp spectral cutoff filters. The size of all three  $\mathcal{G}_{\text{PIV}}$  kernels are kept the same. The test filter  $\mathcal{G}$  is a spatial box, the size of which is increased. Clearly, for a sufficiently large  $\Delta_{\text{T}}/\Delta$ , the difference between  $\mathcal{G}$  and  $\mathcal{G}_{\text{T}}$  is negligible. When  $\mathcal{G}_{\text{PIV}}$  is a box and Gaussian filters, which are spatially local, the convergence occurs for lower  $\Delta_{\text{T}}/\Delta$  than for the spatially non-local sharp spectral cutoff filter.

Quantification of the difference between  $\mathcal{G}$  and  $\mathcal{G}_{\text{T}}$  can be done by computing the root-mean-square of the residual between the two filter kernels, i.e.

$$\text{RMS}_{\mathcal{G}-\mathcal{G}_{\text{T}}} = \sqrt{\frac{1}{N} \sum_i^N \left[ \frac{\mathcal{G}(x_i) - \mathcal{G}_{\text{T}}(x_i)}{1/\Delta} \right]^2}. \quad (4.23)$$

Note that the residual is normalized by the amplitude of the box  $\mathcal{G}_{\text{PIV}}$  to enforce independence from  $\Delta$ . Figure 4.8 shows  $\text{RMS}_{\mathcal{G}-\mathcal{G}_{\text{T}}}$  between  $\mathcal{G}_{\text{T}}$  and  $\mathcal{G}_{\text{PIV}}$  in Figure 4.7; the

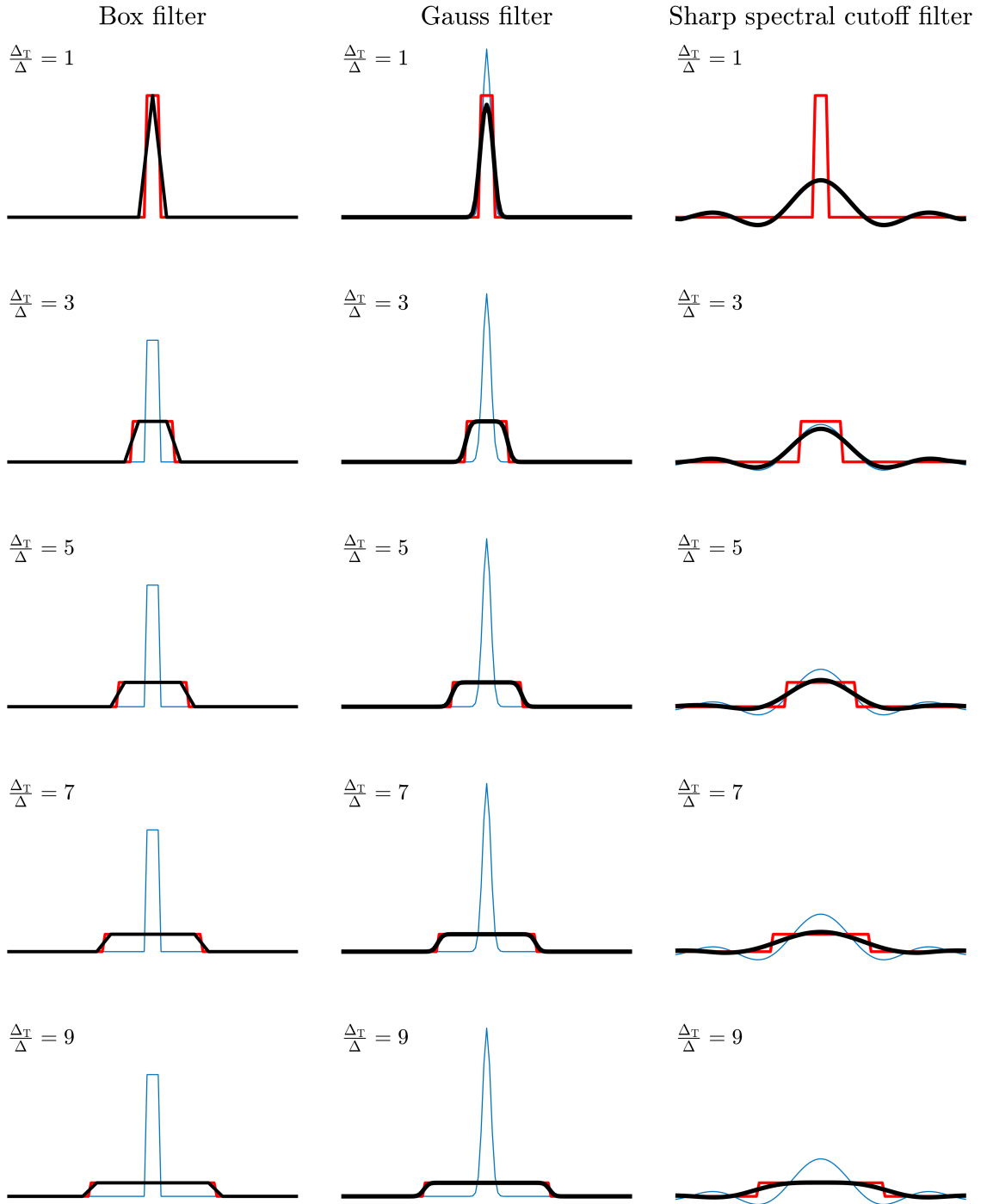


Figure 4.7: Convolution of a box filter  $\mathcal{G}$  (red) with a hypothetical TPIV filter  $\mathcal{G}_{\text{PIV}}$  (blue) that has a shape of a box (left column), Gaussian (middle column), and sharp spectral cutoff (right column). Black curve shows the result of the convolution  $\mathcal{G} * \mathcal{G}_{\text{PIV}}$ .

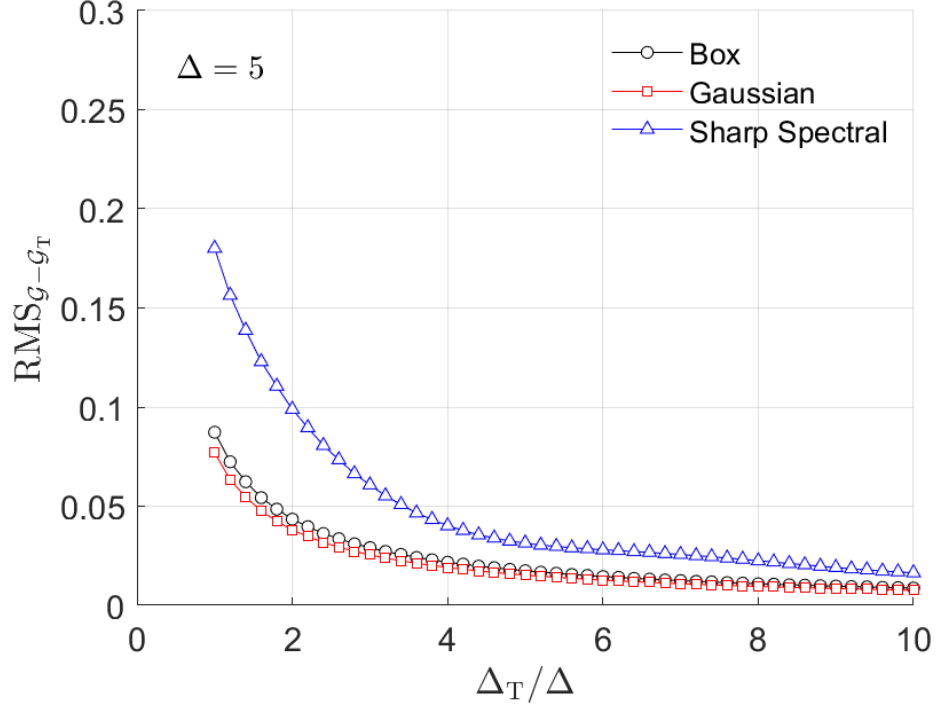


Figure 4.8: Trends in doubly-filtered convolution kernel.

observed variation is identical for other  $\Delta$ . The main trend to be observed is that the RMS reduces with increasing  $\Delta_T/\Delta$ , regardless of the filter shape used for  $\mathcal{G}_{PIV}$ . Clearly, the details of the initial filter kernel have diminishing effect when considering the cutoff scale significantly larger than the scale imposed by  $\mathcal{G}_{PIV}$ . The non-local nature of the sharp spectral cutoff filter results in larger RMS as compared to box and Gaussian filters, but all three RMS curves approach zero at sufficiently large  $\Delta_T/\Delta$ .

Thus, given not fully resolved velocity fields  $\tilde{u}_i$ , it is possible to accurately estimate filtered velocity  $\hat{\tilde{u}}_i$  at a sufficiently large  $\Delta_T/\Delta$ . The observed trend suggests that  $\mathcal{G} * \mathcal{G}_{PIV} \rightarrow \mathcal{G}$  as  $\Delta_T/\Delta \rightarrow \infty$ . Equivalently, the above limit can be interpreted as  $\hat{\tilde{u}}_i \approx \hat{u}_i$  since the details of the initial filter become negligible. From Figure 4.8, for ratios  $\Delta_T/\Delta \gtrsim 2-4$ , the RMS monotonically decreases towards zero, and hence the test filter scale should be at least  $\Delta_T/\Delta \approx 2$  when using the self-similarity method.

To verify this asymptotic behavior, DNS velocity fields and  $\alpha_{sfs}$  need to be also compared. To do so, the DNS velocity is Favre filtered using box, Gaussian, and spectral cutoff



filters of same width  $\Delta$  to obtain  $\tilde{u}_i$ ; standard normal noise is also added to each velocity component ( $\sigma = 1$ ) and gas density ( $\sigma = 0.05$ ). The three results are filtered the second time using a larger box filter of width  $\Delta_T$  to obtain  $\hat{\tilde{u}}_i$  and  $\alpha_{\text{sfs}}^* = \frac{1}{\bar{\rho}} \frac{\partial}{\partial x_j} (\widehat{\tilde{u}_i \tilde{u}_j} - \hat{\tilde{u}}_i \hat{\tilde{u}}_j)$ . Comparison is then made between  $\hat{\tilde{u}}_i$  and  $\hat{u}_i$ , and between  $\alpha_{\text{sfs}}^*$  and  $\alpha_{\text{sfs}} = \frac{1}{\bar{\rho}} \frac{\partial}{\partial x_j} (\widehat{u_i u_j} - \hat{u}_i \hat{u}_j)$  for  $\Delta_T/\Delta = 1, 3, 5$ , and 10 in Figure 4.9.

Doubly-filtered velocity fields are nearly identical to singly-filtered velocity at all filter scale ratios. While some noise can be seen in  $\hat{\tilde{u}}_i$  at  $\Delta_T = \Delta$ , large-scale structures are clearly distinguishable and two velocities become increasingly more similar with increasing  $\Delta_T/\Delta$ .

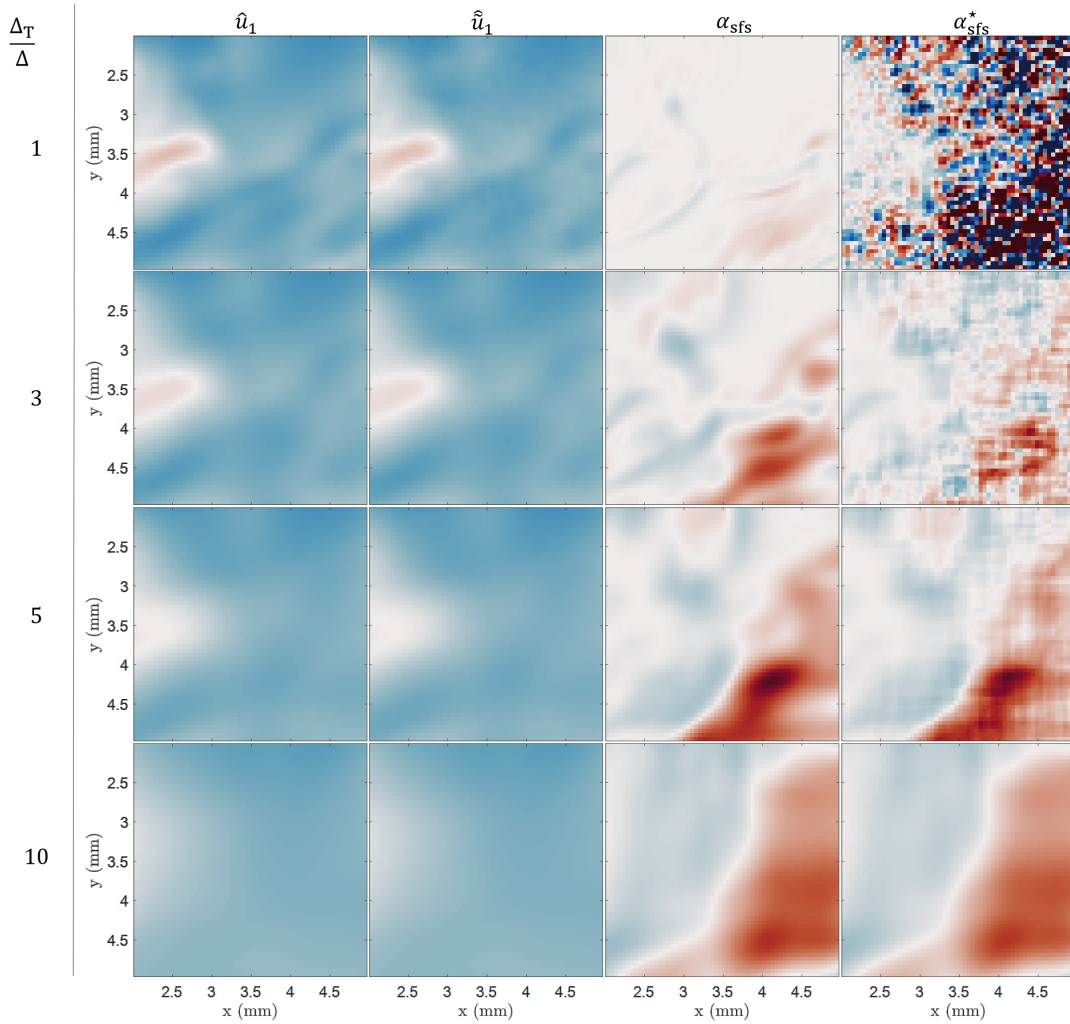


Figure 4.9: Comparison of filtered velocity fields and  $\alpha_{\text{sfs}}$  across  $\Delta_T$  with estimates obtained by filtering the results twice. Here, both  $\Delta_T$  and  $\Delta$  are box filters.

However, similarity between velocities does not guarantee similarity in any of the derived quantities. The right two columns of Figure 4.9 shows a comparison between  $\alpha_{\text{sfs}}^*$  and  $\alpha_{\text{sfs}}$  for the same filter scale ratios. Clearly, the presence of noise in the measurement contaminates  $\alpha_{\text{sfs}}^*$  at  $\Delta_T = \Delta$ , such that no discernible features can be identified. Nevertheless, the similarity between true and estimated inter-scale energy transfer improves with increasing  $\Delta_T/\Delta$ ; the estimates are usable for  $\Delta_T/\Delta \gtrsim 3$ . Note that the estimates for  $\alpha_{\text{sfs}}$  below this threshold are strongly affected by imposed noise. This analysis was repeated with added noise and both sets of results (velocity and inter-scale energy transfer) were nearly identical for all scale ratios.

Finally, difference between true and estimated velocities and  $\alpha_{\text{sfs}}$  are quantified using root-mean-square approach, similar to Equation 4.23. Figure 4.10 shows the RMS variation for velocity and  $\alpha_{\text{sfs}}$  with filter scale ratio. The observed trend is similar to Figure 4.8, where the RMS decreases with increasing  $\Delta_T/\Delta$  asymptotically. Consequently, the self-similar deconvolution is increasingly more accurate for larger filter scales. In this thesis, the minimum target filter scale is thus  $\Delta_T = 3\Delta$  to ensure the validity of the results.

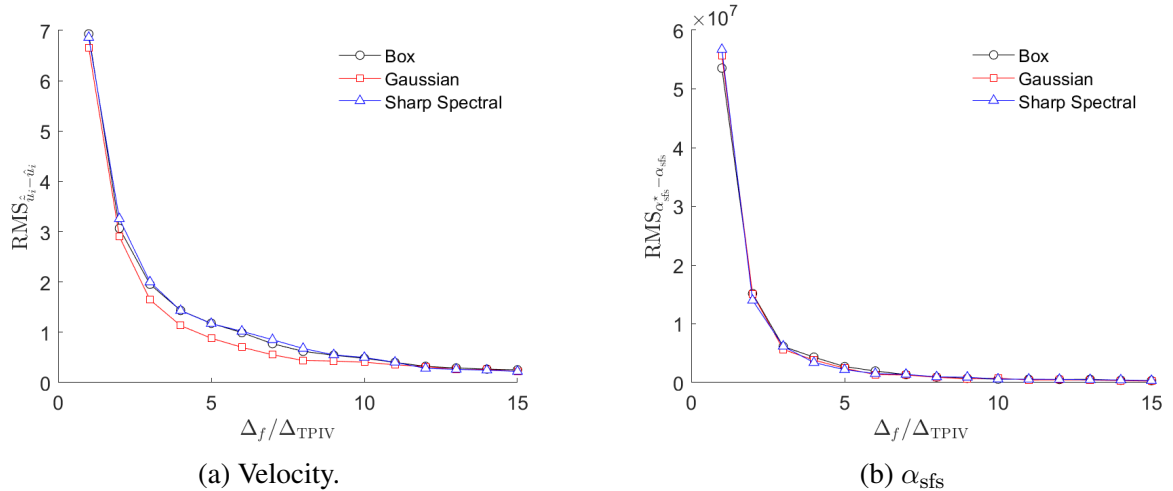


Figure 4.10: Variation of RMS residual of filtered velocity and  $\alpha_{\text{sfs}}$  with filter scale ratio.

#### 4.4 Estimation of PIV filter kernel

In the previous section it was demonstrated that the self-similarity method can be used to accurately estimate  $\alpha_{\text{sfs}}$  at resolutions three times larger than the measurement resolution, regardless of knowledge of the filter kernel. Nevertheless, the accuracy of deconvolution can be improved if the shape of the filter kernel is known. In this section, an attempt is made to identify the characteristics of the filter kernel associated with TPIV using the methods described in Section 4.2.2.

Figure 4.11 shows the central slice of  $\mathcal{G}_{\text{PIV}}$  identified using the Fourier inversion, regularized optimization, and step response methods. The three profiles are clearly different, with differences in size and one-dimensional shape of the kernel. The direct inversion in Fourier space results in a filter kernel that essentially uses points in the immediate neighbourhood of the sample location. Moreover, there is substantial noise at larger radii, which is introduced by TPIV cross-correlation. The regularized optimization and step response profiles are more similar in shape, taking on both positive and negative values, but the relative size of the shape is different. The corresponding shape of the filter resembles the Mexican-hat Gauss profile reported by Elsinga *et al.* [129] and Westerweel [131]; however, their procedure used a higher IB overlap when computing the filter shape.

It should be stated that the optimization approach was highly sensitive to various processing parameters. A large portion of optimization trials resulted in filter shapes that sig-

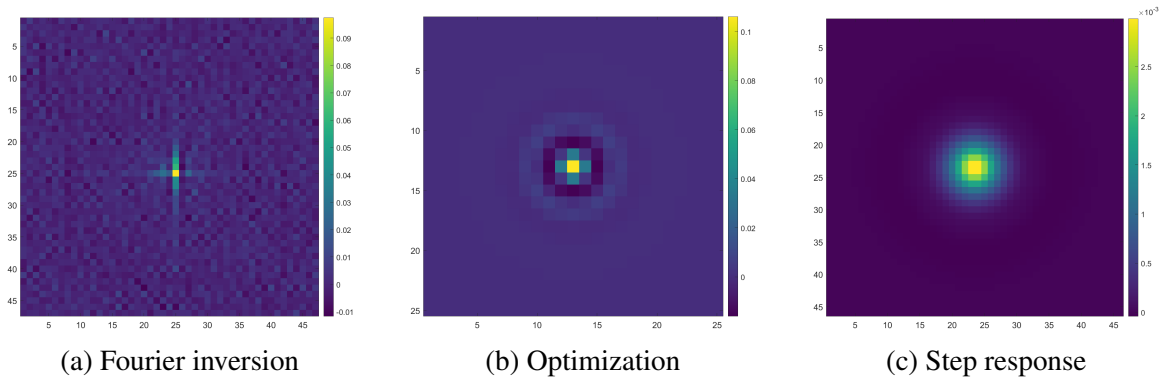


Figure 4.11: Central slice of the identified filter kernels with IB of 24 vx.

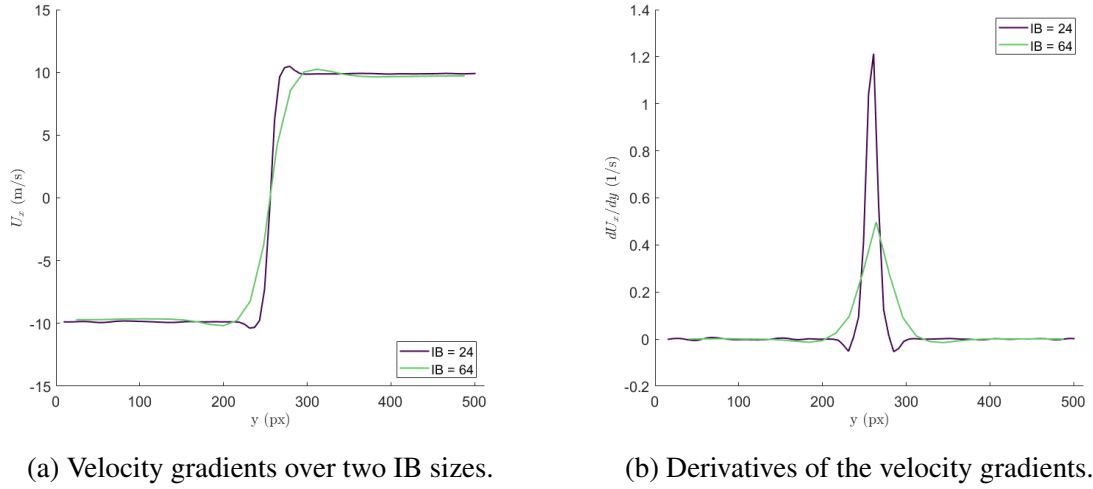


Figure 4.12: One dimensional profiles of the result from applying TPIV on the step-response velocity field.

nificantly diverged from the Mexican-hat Gauss. Among parameters varied were changes in the initial condition for the optimizer, filter kernel size, and TPIV interrogation box size. Additionally, each solution resulted in a relatively large convergence error, indicating that the solution may not be the most optimal. This indicates that finding a universally appropriate TPIV filter is also an ill-posed problem. Thus, while the Mexican hat filter shape appears promising, additional evidence is needed to prove its validity.

Hence, evaluation of how the filter shape varies with IB size can only be done for the step response approach. The mean one-dimensional TPIV velocity profile across the step and its derivative are shown in Figure 4.12 for two IB sizes considered. The mean velocity profile shows an overshoot across the step, similar to findings in Ref. [129]. Clearly, the width of the convolution kernel increases and amplitude decreases as IB size is increased. Moreover, the amplitude of oscillating tails is reduced for a larger IB size. It is noted that the width of the central peak corresponds to the size of the interrogation box used in TPIV.

Since there is no consensus on the shape of the filter amongst the estimation methods used, it cannot be stated with certainty which prediction is correct. However, a comparison can be made between the TPIV velocities and the original velocity fields filtered using the obtained shapes; only the optimization and step response results are considered here.

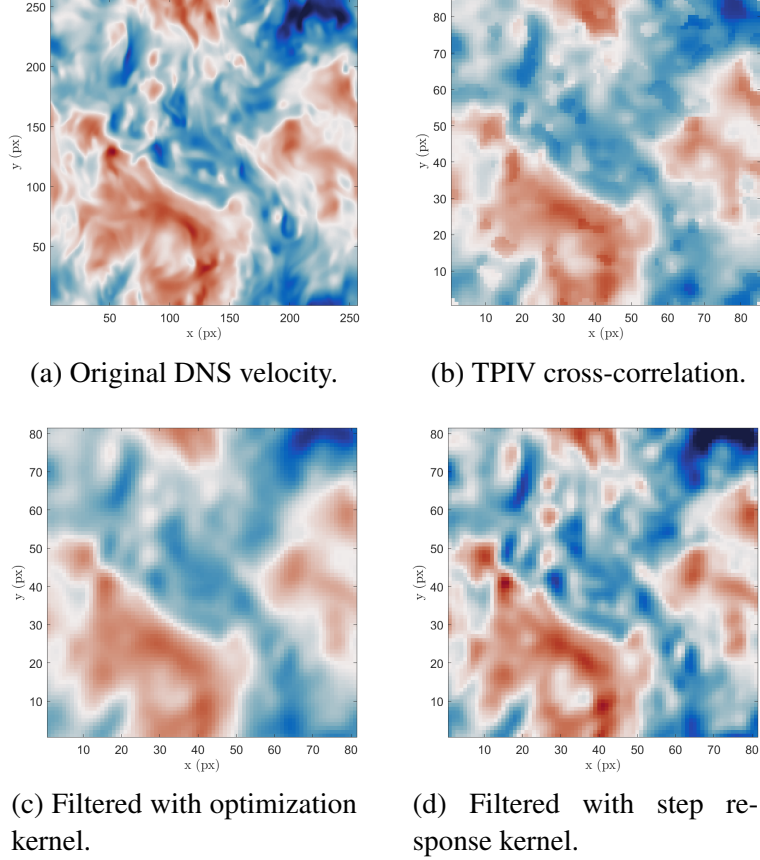


Figure 4.13: Original and filtered velocity fields. Filtering is performed using estimated  $\mathcal{G}_{\text{PIV}}$ , corresponding to IB of 24 vx. Filtered velocity is compared to the TPIV velocity field.

Application of the three-dimensional  $\mathcal{G}_{\text{PIV}}$  on a fully-resolved DNS field is displayed in Figure 4.13; these filtered fields are compared with the corresponding TPIV field. Note that only the  $x$ -component of velocity is included for brevity; other velocity components show similar results. While the filtered fields look similar to the TPIV result, neither method matches the TPIV field exactly. The large-scale velocity structures are captured well, but the details of smaller structures are different for the two methods. The optimization kernel tends to smooth the finer scale details in the flow and reduce the velocity magnitude. On the other hand, the step response kernel does not smooth the smaller structures sufficiently, and the result is more similar to the original DNS data rather than TPIV velocity.

For a more quantitative comparison, joint PDF between TPIV velocity  $\tilde{u}_i$  and  $u_i * \mathcal{G}_{\text{PIV}}$

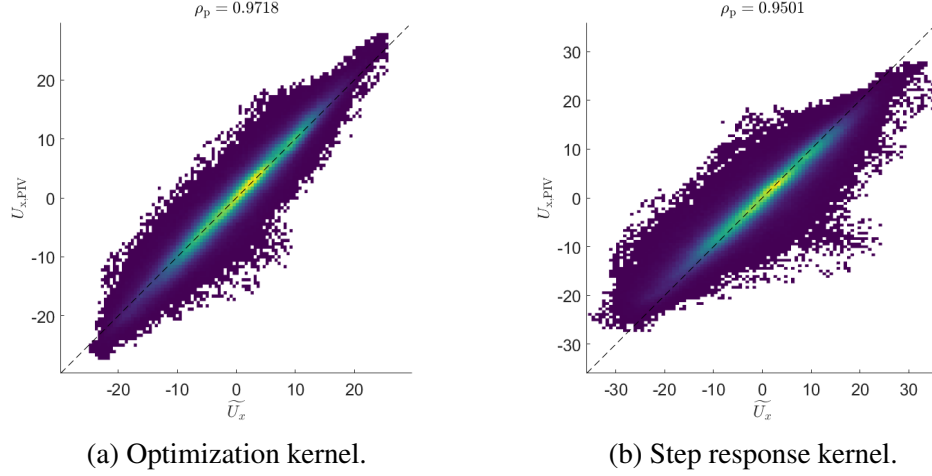


Figure 4.14: Original and filtered velocity fields. Filtering is performed using estimated  $\mathcal{G}_{\text{PIV}}$ , corresponding to IB of 24 vx. Filtered velocity is compared to the TPIV velocity field.

are constructed and shown in Figure 4.14, along with the computed correlation coefficient. The joint PDFs indicate a strong correlation between the filtered DNS fields and TPIV results, with  $\rho_p > 0.95$  in both cases. As observed earlier, the step response kernel tends to over-estimate the magnitude of the TPIV velocity.

There are a few key takeaways from this investigation. Firstly, the three methods used to identify the TPIV filter kernel all resulted in different shapes; no consensus was found. The Fourier inversion and regularized optimization methods were found to be sensitive to noise and processing parameters. The most-likely shape is the Mexican hat-Gaussian profile given by the step response approach. Second, the application of the filter estimates results in the velocity fields that are qualitatively similar at large scales to the velocity given by cross-correlation in TPIV. However, there are significant differences at finer scales. As was demonstrated in the previous section, presence of even minor noise can introduce significant amplification in  $\alpha_{\text{sfs}}^*$ , especially at small filter ratios. In conclusion, the exact shape of the TPIV filter kernel remains unclear. The results below are presented in terms of either directly measured  $\alpha_{\text{sfs}}$  from the fully-resolved measurements or as  $\alpha_{\text{sfs}}^*$  at filter scales that are at least three times larger than the resolution of TPIV measurement.

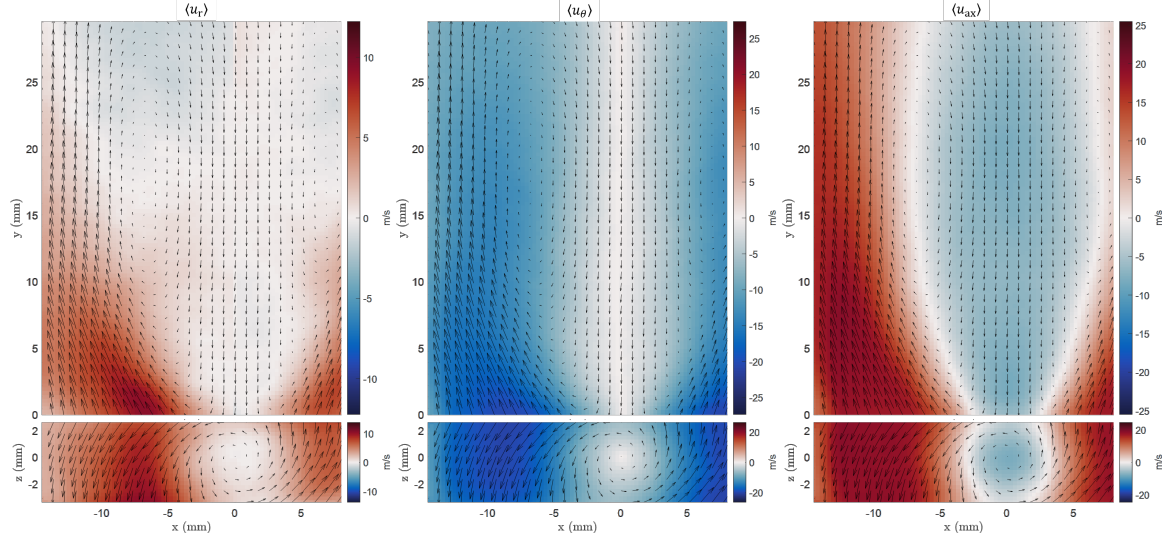
## CHAPTER 5

### CHARACTERIZATION OF THE FLOW AND FLAMES

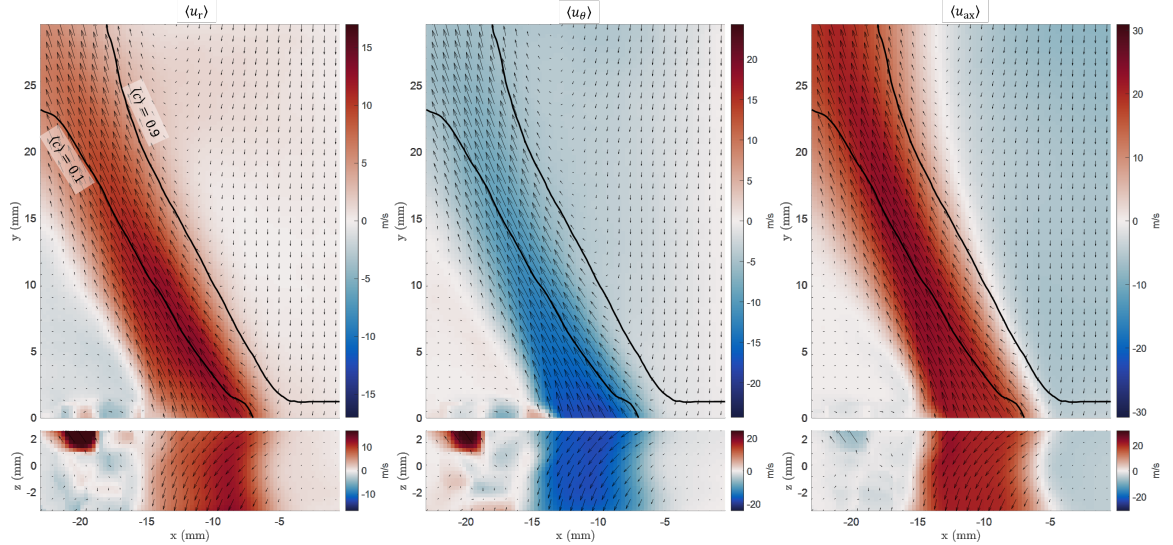
This chapter describes the characterization of the flow field and turbulence of the swirl burner. The discussion is broken into three main sections. In the first section, the details of the mean flow are presented for all three swirlers and independence of the controlling parameters -  $U_j$ ,  $\mathcal{S}$ , and  $\phi$  - is evaluated. Results are presented in the cylindrical coordinate frame, which allows for measurement of the actual swirl number of each swirler; a rough estimate of the mean radial pressure gradient is also obtained. In the second section, turbulence characteristics, specifically  $\ell$ ,  $Re$ , and  $\eta$  are measured. Comparison between the different estimates for the integral length scale are also made. The last section describes the procedure for determining whether the high-resolution velocity measurements are fully resolved; fully-resolved cases allow for direct measurement of  $\alpha_{sfs}$ .

#### 5.1 Characterization of the flow field

In Chapter 2, different swirler geometries and operating conditions were presented; however, no measurements of the actual flow conditions were given. Additionally, it was stated that the magnitude of turbulence intensity, radial pressure gradients, and density gradients can be controlled in a relatively independent manner. Finally, there is an expected difference between the geometrical swirl number and the measured swirl number. In this section, ensemble averaged velocity fields are examined to determine the swirl numbers for the three configurations, assess independence between the controlling parameters, and determine the experimental flow conditions.



(a) Non-reacting flow (D-N075-S3-U20).



(b) Reacting flow (D-E100-S3-U20).

Figure 5.1: Mean velocity fields in cylindrical coordinates of equivalent non-reacting and reacting flows along the  $z = 0$  mm and  $y = 1$  mm planes. Every third velocity vector is shown. Flame brush is denoted by the contours at  $\langle c \rangle = 0.1$  and  $\langle c \rangle = 0.9$ .

### *Effects of controlling parameters on mean flow*

Shown in Figure 5.1 are the mean velocity fields under reacting and non-reacting conditions along the central  $z = 0$  mm plane and cross-sectional plane at  $y = 1$  mm; mean velocity field and contours of the flame brush are overlaid onto each reacting plot. Note that the field of view was shifted for reacting conditions to ensure that the left branch of the symmetrical



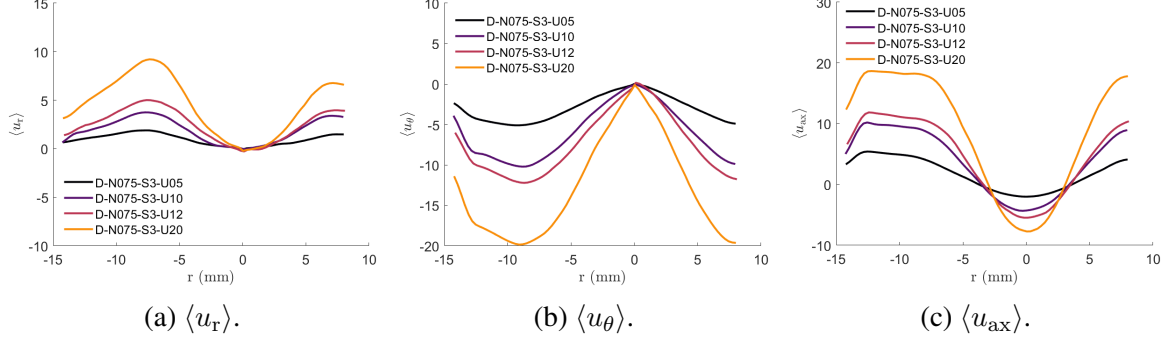


Figure 5.2: Radial profiles of mean velocity components along  $y = 1$  mm and  $z = 0$  mm line in a series of non-reacting flows as  $U_j$  is varied;  $S$  and chemistry are fixed.

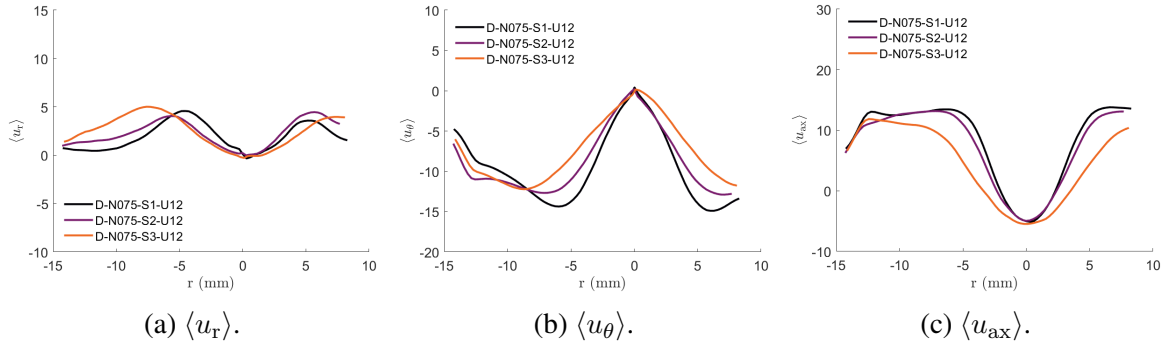


Figure 5.3: Radial profiles of mean velocity components along  $y = 1$  mm and  $z = 0$  mm line in a series of non-reacting flows as  $S$  is varied;  $U_j$  and chemistry are fixed.

flame fits completely inside the image. Cylindrical coordinates are used to evaluate the experimental swirl number and compare flow conditions across operating conditions. The radial, azimuthal, and axial velocity components are computed as

$$u_r = \vec{u} \cdot \hat{r}, \quad u_\theta = \vec{u} \cdot (\hat{y} \times \hat{r}), \quad u_{ax} = u_y, \quad (5.1)$$

where  $\hat{r}$  and  $\hat{y}$  are the unit vectors in radial and axial directions; here, Cartesian  $y$ -axis aligns with the axial coordinate in cylindrical coordinate frame.

In both cases (i.e. reacting and non-reacting), there is significant radial and azimuthal fluid motion that creates the central recirculation zone, characterized by mean downward axial fluid motion and lower velocity magnitude in the vicinity of the central axis of the burner. Presence of the flame results in a wider recirculation zone as can be clearly seen

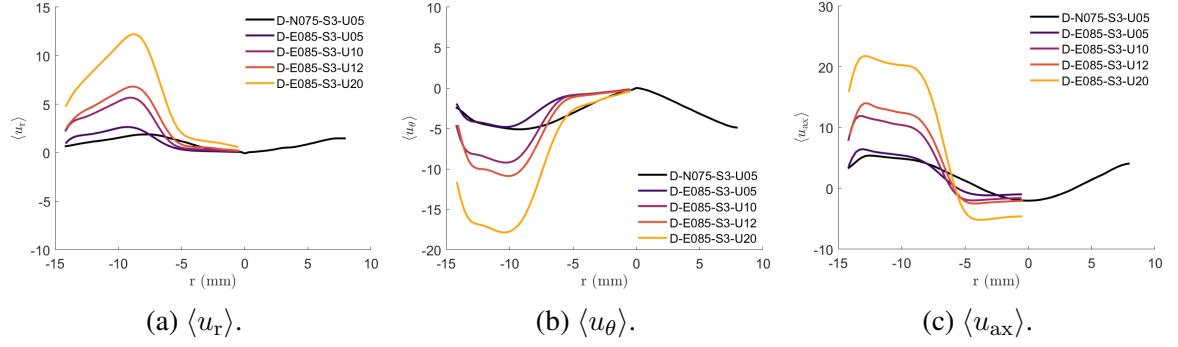


Figure 5.4: Radial profiles of mean velocity components along  $y = 1$  mm and  $z = 0$  mm line in a series of reacting flows as  $U_j$  is varied;  $\mathcal{S}$  and  $\phi$  are fixed.

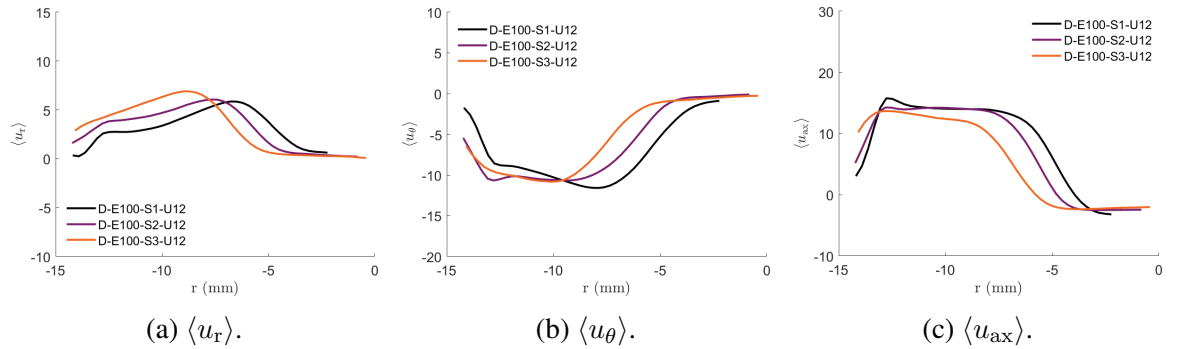


Figure 5.5: Radial profiles of mean velocity components along  $y = 1$  mm and  $z = 0$  mm line in a series of reacting flows as  $\mathcal{S}$  is varied;  $U_j$  and  $\phi$  are fixed.

on the transverse slice of  $\langle u_{ax} \rangle$ ; the radius of  $\langle u_{ax} \rangle = 0$  m/s contour is 2 – 3 mm larger in the reacting case. Similar conclusion can be drawn by examining other components of the mean velocity field. Enlargement of the central recirculation zone is due to the fluid expansion across the flame, which forces the swirling jet outwards; the radial and azimuthal components of velocity persist further downstream in reacting conditions than in an equivalent non-reacting flow. At the nozzle exit, the velocity magnitude is similar between reacting and non-reacting flows.

Evaluation of independence between  $\mathcal{S}$ ,  $U_j$ , and  $\phi$  is done by comparison of one-dimensional radial profiles of  $\langle u_r \rangle$ ,  $\langle u_\theta \rangle$ , and  $\langle u_{ax} \rangle$ ; profiles are taken along the  $y = 1$  mm and  $z = 0$  mm line to avoid noise due to laser reflections from the burner.

Figure 5.2 and Figure 5.3 compare the effects of varying  $U_j$  and  $\mathcal{S}$  in non-reacting flows. Recall that the conditions were defined such that  $U_j$  should reflect the magnitude of

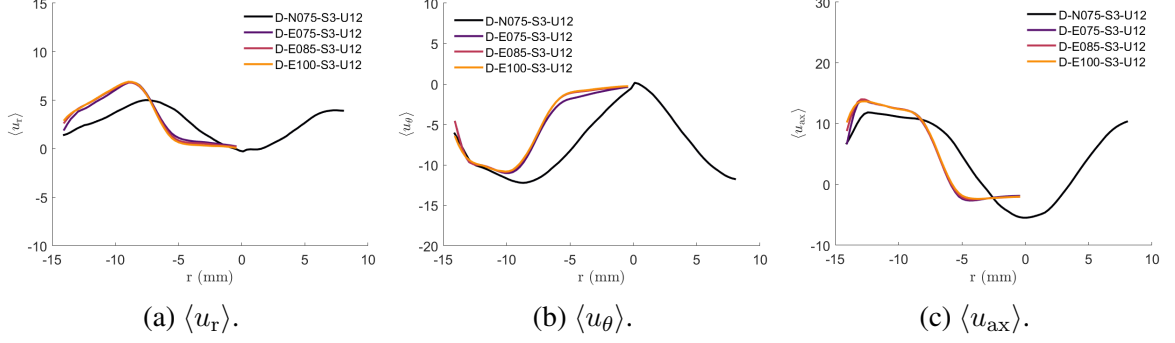


Figure 5.6: Radial profiles of mean velocity components along  $y = 1$  mm and  $z = 0$  mm line in a series of reacting flows as  $\phi$  is varied;  $U_j$  and  $\mathcal{S}$  are fixed.

the velocity vector under the assumption of negligible radial velocity and uniform velocity across the inflow jet, i.e.  $U_j \approx (u_{ax}^2 + u_\theta^2)^{1/2}$  in the inflow. Assuming that  $\mathcal{S} \propto u_\theta / u_{ax}$ ,

$$\frac{U_j}{u_{ax}} \propto (1 + \mathcal{S}^2)^{1/2}. \quad (5.2)$$

This is borne out in the data, when compensating for the non-uniform nature of the real flow; measurements of  $\mathcal{S}$  are presented below. Furthermore, the jets had non-negligible  $u_r$ , meaning that the actual velocity magnitudes were greater than  $U_j$ . Within the CRZ ( $|r| \leq 5$  mm), the magnitude of  $\langle u_{ax} \rangle$  also increases with  $U_j$ , while  $\langle u_r \rangle$  and  $\langle u_\theta \rangle$  tend to zero across all flow rates. Note that the magnitude of  $\langle u_{ax} \rangle$  in the jet is similar to the target jet velocity (ex. U10 in case name for  $U_j = 10$  m/s). The primary influence of  $\mathcal{S}$  on the mean velocity field is to push the jet radially outward with increasing  $\mathcal{S}$ , as is expected. As a result, the central recirculation zone is also widened. This is demonstrated by the shifted peak in all three mean velocity magnitudes in Figure 5.3.

Figure 5.4 to Figure 5.6 show the effects of varying  $U_j$ ,  $\mathcal{S}$ , and  $\phi$  in the reacting flows. Similar to the non-reacting flows, the effect of increasing  $U_j$  results in larger magnitudes of all three velocity components. Furthermore, the location of the jet is shifted radially outward as compared to the non-reacting flow, as was observed earlier. It should be noted that the transition between the jet and the central recirculation zone for reacting flows is akin to a step as compared to smooth transition in a non-reacting flow. Likewise, increase

Table 5.1: Statistics of swirl number measurements.

	Non-reacting cases		Reacting cases		All cases	
Swirler	$\mu_S$	$\sigma_S$	$\mu_S$	$\sigma_S$	$\mu_S$	$\sigma_S$
$S_1$	0.50	0.02	0.49	0.01	0.50	0.02
$S_2$	0.56	0.02	0.56	0.01	0.56	0.02
$S_3$	0.64	0.01	0.59	0.01	0.61	0.03

in  $S$  at constant  $U_j$  and  $\phi$  results in a radially outward shift of the jet and larger central recirculation zone. Finally, at fixed  $U_j$  and  $S$ , the change in  $\phi$  appears to have no effect on the mean flow profile as demonstrated in Figure 5.6. This indicates that  $\phi$  can be used to modulate the strength of the density gradients independently from turbulence intensity and mean flow field.

#### *Measurement of swirl number*

Mean velocity fields can also be used to measure the swirl number. Equation 2.1 is simplified to

$$S = \frac{\int_0^R \rho u_{ax} u_\theta r^2 dr}{R \int_0^R \rho u_{ax}^2 r dr}, \quad (5.3)$$

where the pressure term is disregarded. Note that at small Mach numbers,  $(p - p_\infty) \ll \rho u_{ax}^2$ .

In this thesis, evaluation of the swirl number is performed in the mean sense:

$$S \approx \frac{\int_0^R \langle \rho \rangle \langle u_{ax} \rangle \langle u_\theta \rangle r^2 dr}{R \int_0^R \langle \rho \rangle \langle u_{ax} \rangle^2 r dr}. \quad (5.4)$$

Mean profiles of  $\langle \rho \rangle$ ,  $\langle u_{ax} \rangle$ , and  $\langle u_\theta \rangle$  are taken along the  $y = 1$  mm plane and geometric radius of the nozzle  $R = 14.375$  mm is used. It is noted that using the ensemble means ignores the density-velocity correlation in the reacting cases and the velocity-velocity correlations across all cases. Nevertheless, Equation 5.4 is a good first-order approximation for  $S$  for the purposes of this thesis.

Figure 5.7 shows the distribution of measured swirl numbers on a box and whiskers plot for the three swirler geometries; basic statistics of measured  $S$  are summarized in Table 5.1.

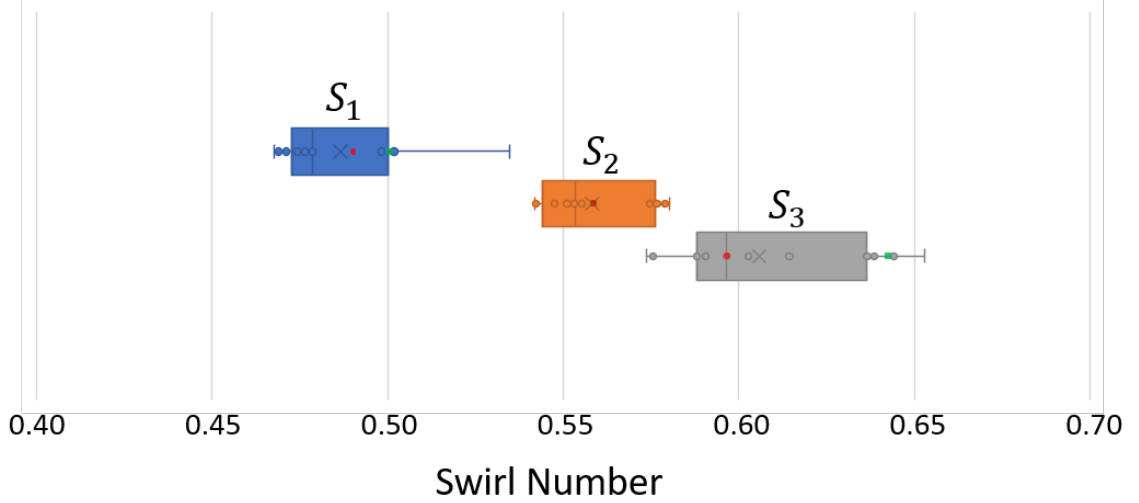


Figure 5.7: Box and whiskers plot of the measured swirl numbers in both reacting and non-reacting flows. Marker 'x' denotes the mean across all cases for each swirler; red circle represents the mean across reacting cases; green square represents the mean across non-reacting cases.

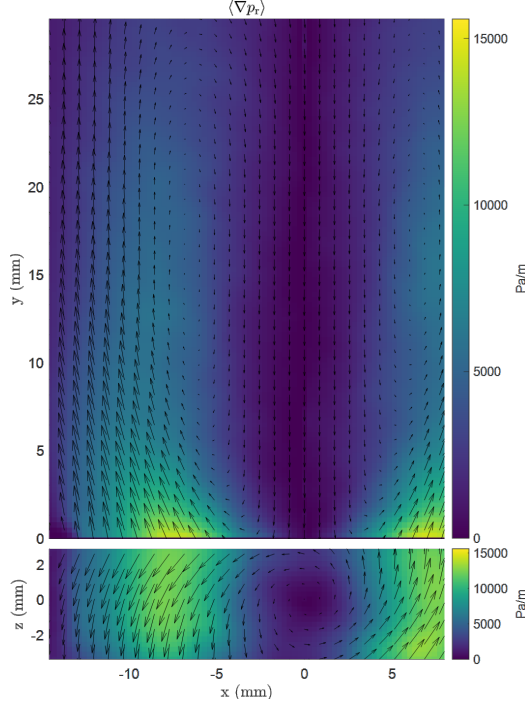
While there exists variation in the measured swirl number, the sample standard deviation is small for each swirler and there is minimal overlap between the swirler geometries. The single measurement for  $S_3$  that overlaps with  $S_2$  measurements in Figure 5.7 is for case D-E075-S100-U05; this is the test case with the lowest flow rate and largest uncertainty in mass flow rates. Mean swirl number from non-reacting flows is either equal to or slightly than mean swirl number from reacting flows. More importantly, the observed velocity fields have shown sufficient variation to distinguish the three different swirlers.

#### *Estimation of radial pressure gradient*

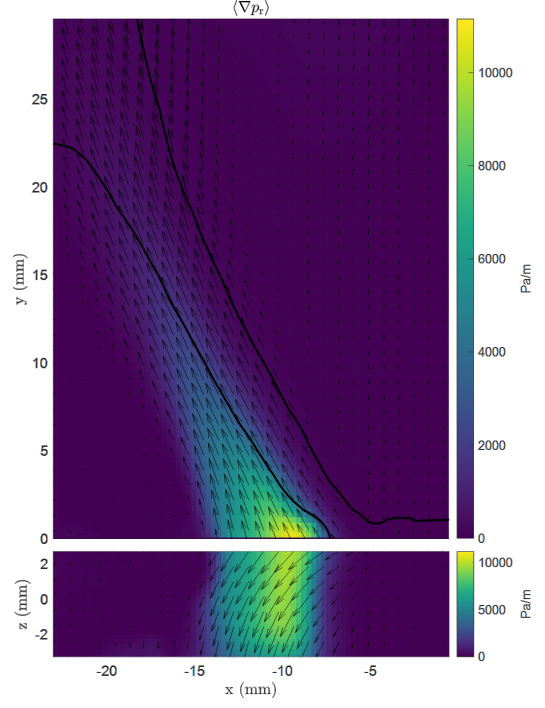
Lastly, the magnitude of the radial pressure gradient associated with the swirling motion can be estimated using the radial momentum equation

$$\frac{\partial p}{\partial r} = \rho \frac{u_\theta^2}{r}. \quad (5.5)$$

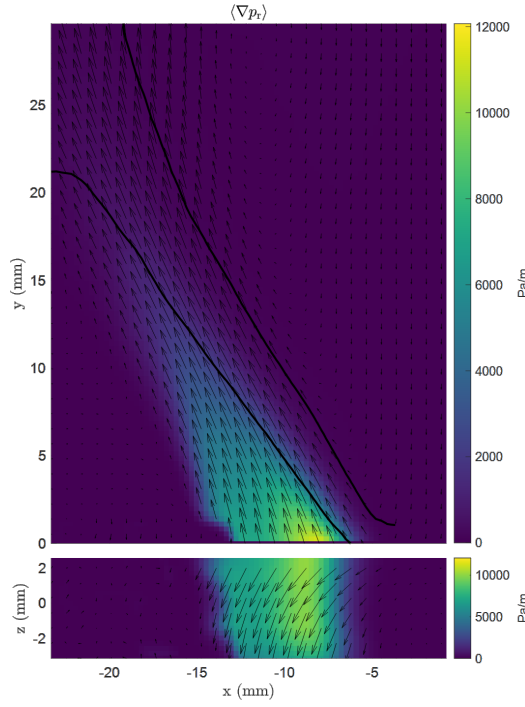
Only mean pressure fields are considered in this dissertation and the mean radial pres-



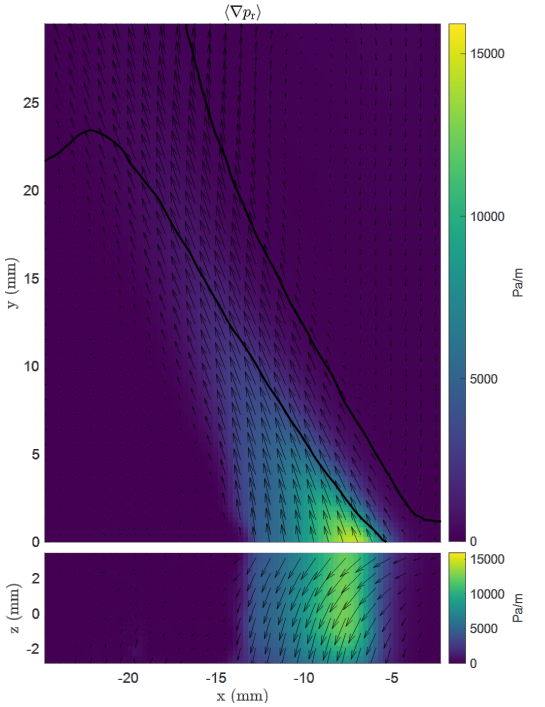
(a) D-N075-S100-U10



(b) D-E100-S100-U10



(c) D-E100-S075-U10



(d) D-E100-S055-U10

Figure 5.8: Profiles of the mean radial pressure gradient along  $z = 0$  mm and  $y = 1$  mm planes for different swirl numbers. Flame brush is denoted by the contours at  $\langle c \rangle = 0.1$  and  $\langle c \rangle = 0.9$ .

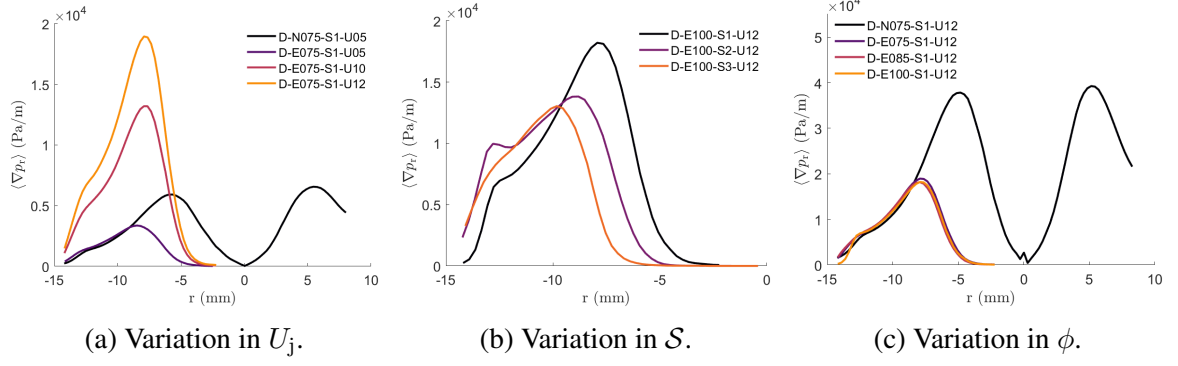


Figure 5.9: Radial profiles of mean radial pressure gradient along  $y = 1$  mm and  $z = 0$  mm line in a series of reacting flows where  $\phi$ ,  $U_j$ , and  $S$  are varied.

sure gradient is estimated as

$$\left\langle \frac{\partial p}{\partial r} \right\rangle \propto \langle \rho \rangle \frac{\langle u_\theta \rangle^2}{r}. \quad (5.6)$$

It should be noted that averaging operation on the left hand side of Equation 5.5 will result in additional correlation terms on the right hand side, which are not considered here. Here, Equation 5.6 is used to identify regions of the flow with substantial mean pressure gradients  $\langle \nabla p_r \rangle$ .

Figure 5.8 shows the distribution of  $\langle \nabla p_r \rangle$  in a non-reacting flow and reacting flows at three different swirl numbers. Clearly, the regions with non-zero radial pressure gradient are inside the jet. This region is wider for a non-reacting flow than in an equivalent reacting flow due to a smaller central recirculation zone. In the reacting flows, the regions with large  $\langle \nabla p_r \rangle$  lie immediately upstream of the reactant edge of the flame brush for all three swirlers. Hence, significant up-scale inter-scale energy transfer is expected in regions where instantaneous flame occupies regions of significant flow-induced pressure-gradients.

Figure 5.9 summarizes the effect of  $U_j$  and  $S$ , and  $\phi$  on the radial pressure gradients. This is again done by plotting  $\langle \nabla p_r \rangle$  along the  $z = 0$  mm and  $y = 1$  mm line. The main trends are similar to the earlier observations: (1) magnitude of  $\langle \nabla p_r \rangle$  increases with  $U_j$ , (2) increase in  $S$  shifts the observed peak in  $\langle \nabla p_r \rangle$  radially outward, (3) no observable change with  $\phi$ . Additionally, the magnitude of maximum  $\langle \nabla p_r \rangle$  in non-reacting flow is larger than in an equivalent reacting flow due to a lower fluid density at the same radial coordinate; the

profiles are identical in region occupied by the reactant jet at larger  $r$ . Also, the magnitude of peak  $\langle \nabla p_r \rangle$  is reduced with increasing  $\mathcal{S}$ . This is due to the lower flow rates used at larger  $\mathcal{S}$  in an attempt to match  $U_j$ .

## 5.2 Characterization of turbulence conditions

Here, key turbulence properties, such as  $\ell$ ,  $Re$ , and  $\eta$ , are presented. Integral length scale is an important turbulence quantity, which represents the length scale at which turbulence accepts energy from the mean flow and at which most of turbulent kinetic energy exists. There are multiple ways to estimate  $\ell$  from experimental data. In some cases, a suitable scale can be defined by the physical constraints of the flow domain (ex. diameter of a pipe in a turbulent pipe flow is on the order of the largest eddies in the flow) [132]. Otherwise,  $\ell$  can be defined in terms of the correlation of velocity fluctuations at two points, separated by a certain distance. Since many quantities, such as  $Ka$ ,  $Re$ , and  $\eta$  are derived from  $u'$  and  $\ell$ , it is critical to accurately estimate these two quantities for proper turbulence characterization.

Definition of the integral length scale is based on the integral of the autocorrelation function

$$\ell = \int_0^\infty R_{ii}(r, t) dr, \quad (5.7)$$

where  $R_{ii}(r, t)$  is the autocorrelation of velocity fluctuations at points separated by distance  $r$ , i.e.

$$R_{ii}(r) = \frac{\langle u_i(x_i, t) u_i(x_i + r, t) \rangle}{\langle u_i^2 \rangle}. \quad (5.8)$$

The autocorrelation function is longitudinal if  $r$  is parallel to  $u_i$  ( $R_{LL}$ ) and transverse if  $r$  is perpendicular to  $u_i$  ( $R_{TT}$ ). Since the swirling flow under consideration is anisotropic, the measurement of  $\ell$  must be with the relevant portion of the turbulent flow. In swirling flows and swirl-stabilized flames, turbulence is strongest in the inner shear layer between the central recirculation zone and the reactant jet; this is also the location of the flame brush in the reacting flows. Thus, turbulence characterization measurements are taken in the inner



shear layer, near the exit plane of the nozzle.

Figure 5.10(a) shows a representative distribution of the RMS velocity fluctuations  $u'$  along the central  $z = 0$  mm plane in a reacting flow. Clearly, the most intense velocity fluctuations occur inside the inner and outer shear layers; however, only the inner shear layer is considered since no reactions occur across the outer shear layer between the jet and ambient atmosphere. Overlaid onto the plot is a red line of maximum  $u'$  at axial location between  $y = 0$  mm and  $y = 15$  mm inside the shear layer. Black dotted lines are perpendicular to the line of maximum  $u'$  and intersect at target axial distances from  $y = 0$  mm to  $y = 5$  mm. Variation of  $u'$  along these lines is shown in Figure 5.10(c).

Shown in Figure 5.10(b) are  $R_{LL}$  across the shear layer at several downstream locations. The longitudinal velocity component is obtained by projecting the instantaneous velocity onto the black dotted lines in Figure 5.10(a). Note that  $R_{ii}(r) = 0$  indicates that velocity fluctuations are not correlated at  $r$ . Consequently, the integration domain in Equation 5.7 can be specified in different manners: use the entire available domain ( $\ell_{\text{all}}$ ), integrate up to a minimum in  $R_{ii}$  ( $\ell_{R-\text{min}}$ ), integrate up to the first zero-crossing ( $\ell_{R-0}$ ), or integrate up to  $1/e$  ( $\ell_{R-1/e}$ ) [132]. Estimates of the integral length scale using the autocorrelation of longitudinal velocity gives an estimate for  $\ell$  between 1.8 mm and 3 mm, which encloses the approximations given by the other two methods in Figure 5.10.

It is common to estimate the integral length scale as the characteristic width of the shear layer as either the full-width-at-half-maximum of  $u'$  or as a difference between coordinates of reference points in the mean velocity profile (ex.  $\ell \approx \langle U \rangle_{0.9} - \langle U \rangle_{0.1}$ , where subscripts represent the percentage of the mean characteristic velocity difference across the shear layer). These two approaches are demonstrated in Figure 5.10(c-d); both approaches give similar estimates for  $\ell$ . Moreover, at the condition presented here, there is very little variation with axial distance.

Since all three methods give similar estimates, the integral length scale is estimated using the autocorrelation method with entire available integration domain. Summary of the

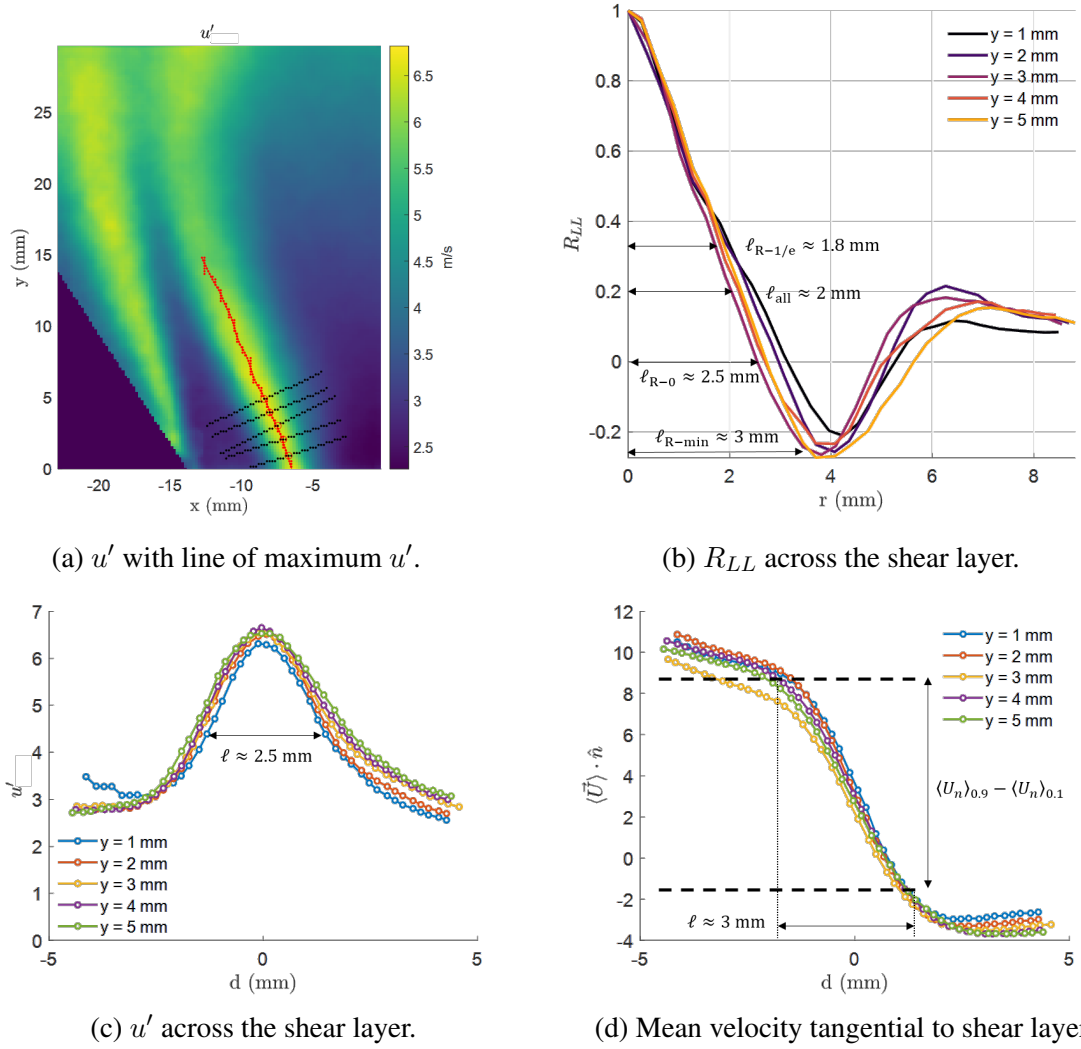


Figure 5.10: Turbulence characterization inside the inner shear layer for case E085-S2-U10.

measured  $\ell$ ,  $u'$ ,  $Re$ ,  $Ka$ , and  $\eta$  are given in Table 5.2. The Karlovitz number is calculated using Equation 1.12; Reynolds number is estimated as  $Re = u'\ell/\nu_r$ , where the kinematic viscosity is taken to be that of the reactants. The laminar flame properties, namely the laminar flame speed  $s_L^0$  and flame thickness  $\delta_L^0$  were calculated in Cantera using a freely propagating flame model with the GRI3.0 chemical mechanism. All test conditions are visually presented on the premixed combustion regime diagram in Figure 5.11, clearly showing that the proposed test conditions lie in the thin reaction zone regime.

Table 5.2: Measured properties of turbulence and mean flow. The cases marked with \* are those, for which the high resolution velocity dataset is fully resolved.

Case	$\langle \nabla p_r \rangle$ (Pa/m)	$\ell$ (mm)	$u'$ (m/s)	Re	Ka	$\eta$ ( $\mu\text{m}$ )
E075-S1-U04*	$0.30 \times 10^4$	2.0	2.5	50	11	102
E075-S1-U05*	$0.34 \times 10^4$	1.9	2.6	56	21	95
E075-S1-U10*	$1.30 \times 10^4$	1.4	5.7	90	71	48
E075-S1-U12*	$1.90 \times 10^4$	1.4	7.2	109	111	42
E075-S1-U15	$2.40 \times 10^4$	1.3	9.4	135	124	33
E085-S1-U05*	$0.33 \times 10^4$	1.2	2.4	32	14	90
E085-S1-U10*	$1.30 \times 10^4$	1.7	5.4	101	40	53
E085-S1-U12*	$1.80 \times 10^4$	1.6	6.7	116	57	44
E085-S1-U15*	$2.40 \times 10^4$	1.4	8.7	134	89	36
E085-S1-U20*	$5.00 \times 10^4$	1.2	12.5	168	164	26
E085-S1-U25*	$6.20 \times 10^4$	1.3	15.1	217	212	23
E085-S1-U27	$7.40 \times 10^4$	1.2	16.6	220	254	21
E100-S1-U05*	$0.34 \times 10^4$	2.5	2.3	64	6	111
E100-S1-U10*	$1.30 \times 10^4$	1.6	5.2	90	27	54
E100-S1-U12*	$1.80 \times 10^4$	1.5	6.2	101	37	46
E100-S1-U20	$4.60 \times 10^4$	1.8	12.1	246	89	30
E075-S2-U05*	$0.28 \times 10^4$	1.9	2.6	54	20	96
E075-S2-U10*	$1.00 \times 10^4$	1.7	5.0	94	59	56
E075-S2-U12*	$1.40 \times 10^4$	1.7	6.1	113	78	49
E085-S2-U05*	$0.27 \times 10^4$	1.2	1.8	23	9	112
E085-S2-U10*	$0.99 \times 10^4$	2.0	4.5	100	28	64
E085-S2-U12*	$1.40 \times 10^4$	1.4	5.9	93	49	48
E085-S2-U17	$3.20 \times 10^4$	2.1	7.5	173	122	44
E100-S2-U05*	$0.28 \times 10^4$	1.4	1.8	28	6	118
E100-S2-U10*	$0.98 \times 10^4$	1.5	4.2	71	20	62
E100-S2-U12*	$1.40 \times 10^4$	1.1	5.5	68	35	47
E075-S3-U05*	$0.26 \times 10^4$	1.5	2.2	37	18	102
E075-S3-U10*	$0.98 \times 10^4$	0.9	5.3	51	87	46
E075-S3-U12	$1.40 \times 10^4$	1.3	6.3	90	94	44
E085-S3-U05*	$0.24 \times 10^4$	1.4	1.8	29	9	114
E085-S3-U10*	$0.93 \times 10^4$	1.4	4.5	69	33	59
E085-S3-U12*	$1.30 \times 10^4$	1.4	6.0	92	51	47
E085-S3-U20	$3.50 \times 10^4$	1.3	11.0	153	134	29
E100-S3-U05*	$0.26 \times 10^4$	1.5	1.5	26	4	135
E100-S3-U10*	$0.93 \times 10^4$	1.1	4.2	52	24	57
E100-S3-U12*	$1.30 \times 10^4$	0.9	5.4	56	37	46
E100-S3-U20	$3.40 \times 10^4$	1.2	10.4	142	85	30

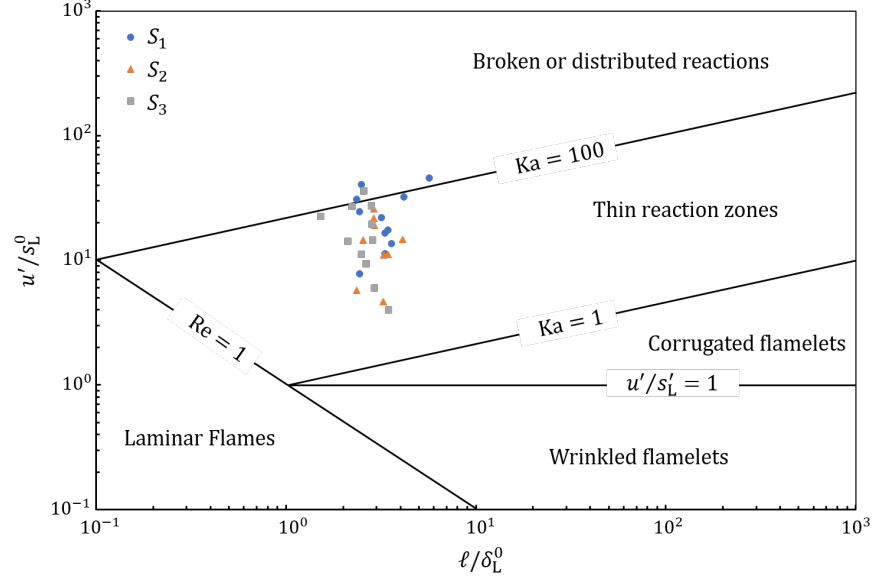


Figure 5.11: Proposed test conditions plotted on a turbulent premixed combustion regime diagram by Peters [23].

### 5.3 Determination of fully-resolved cases

To directly compute  $\alpha_{\text{sfs}}$ , fully-resolved velocity fields are required. When measured velocity fields are not fully-resolved, various terms in Equation 1.27 and Equation 1.28 can be under-estimated and lead to erroneous conclusions. Thus, it is critical to identify cases, which do not suffer from under-resolution for which  $\alpha_{\text{sfs}}$  can be computed directly.

Under-resolution results in a systematic reduction in the measured gradients, which is also affected by the numerical methods used for smoothing and gradient calculation. Thus, any term that involves computation of a spatial derivative (ex.  $\alpha_{\text{sfs}}$  and  $\alpha_\nu$ ) can be potentially under-estimated when using under-resolved velocity measurements. The impact of resolution is assessed by calculating vector fields using interrogation volume lengths ranging from 96 vx to 32 vx and comparing the results. It is noted that there was a large increase in measurement noise at interrogation boxes smaller than 32 vx due to insufficient particle count inside individual interrogation boxes, as was demonstrated in Section 2.3.1.

Figure 5.12 shows joint probability density functions of the velocity field and its gradients (up to third order) with interrogation box lengths of 40 vx and 32 vx for cases

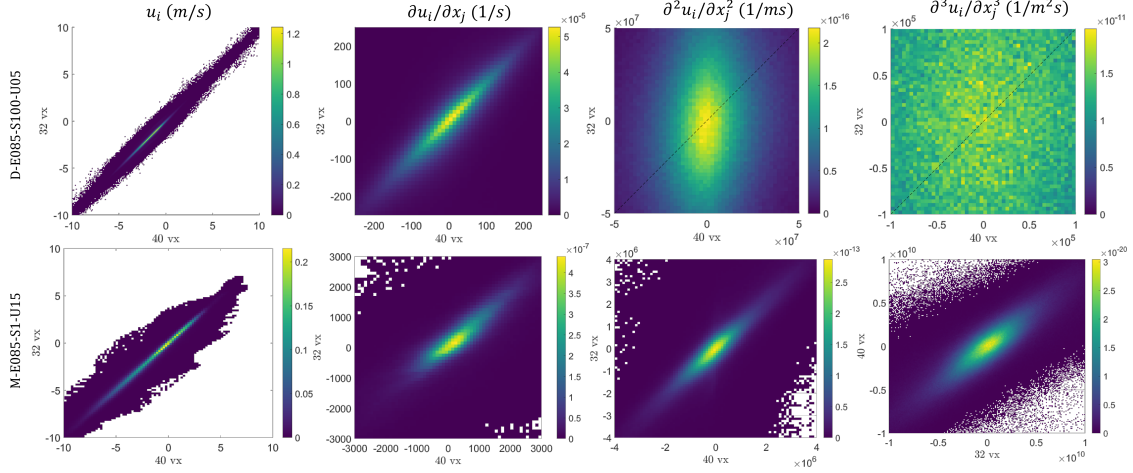


Figure 5.12: Joint probability density plots of  $u_i$ ,  $\partial u_i / \partial x_j$ ,  $\partial^2 u_i / \partial x_j^2$ ,  $\partial^3 u_i / \partial x_j^3$ , as computed using 32 vx and 40 vx grids for cases E085-S100-U05 and E085-S1-U10. Low resolution dataset used for E085-S100-U05 (top row); high resolution dataset used for E085-S1-U10 (bottom row).

E085-S100-U05 and E085-S1-U10; convergence for case E085-S100-U05 was evaluated using the “standard-resolution” TPIV measurements, while case E085-S1-U10 used a high-resolution TPIV setup. Comparison between different resolutions also uses different grids; therefore, the results obtained using smaller interrogation box were downsampled to the coarser grid for comparison.

While the velocity measurements ( $u_i$ ) are nearly perfectly correlated for both low- and high-resolution datasets, the differences in convergence can be observed for JPDFs of higher-order derivatives of velocity ( $\partial^n u_i / \partial x_j^n$ ). The higher-order derivatives are associated with higher noise; hence magnitudes of the derivative are typically larger for finer grids. From Figure 5.12, it is evident that for cases with not fully-resolved velocity measurements, deviations begin to manifest in second-order velocity derivatives. Specifically, the line of main correlation on the JPDF thickens and the slope of the line deviates from unity. When comparing the third-order derivative, no discernible correlation can be observed. In this case, the low resolution dataset for E085-S100-U05 is labeled as not-fully converged, for which  $\alpha_{\text{sfs}}$  needs to be compute using scale-similarity deconvolution.

In contrast, the high-resolution dataset shows that all gradients up to third order show a

meaningful correlation with a unity slope in the JPDF. In this case, the velocity dataset is labeled as converged. Note that the turbulence conditions (higher jet velocity) is greater for E085-S1-U15 using high-resolution than for E085-S100-U05 using low-resolution data. Despite more intense turbulence conditions, a higher-resolution dataset allows one to directly compute  $\alpha_{\text{sfs}}$ .

For the purposes of this thesis, spatial derivatives of order larger than two are not considered. This is due to the fact that such gradients are not required for analysis of the inter-scale energy dynamics. As shown in Equation 1.27,  $\alpha_\nu = \frac{\tilde{u}_i}{\bar{\rho}} \frac{\partial \tilde{\tau}_{ij}}{\partial x_j}$  requires computation of the second derivative of velocity ( $\tau_{ij} \propto \frac{\partial u_i}{\partial x_j}$ ). Since no other term in the transport equation require a higher-order derivative of velocity, it is sufficient to ensure that derivatives up to second order are converged.

Since both high- and low-resolution measurements are available for each test condition, the “standard-resolution” datasets are used primarily for computation of  $\alpha_{\text{sfs}}^*$  using the scale-similarity method across larger filter scales; high-resolution datasets are used to directly compute  $\alpha_{\text{sfs}}$ . For each high-resolution dataset, JPDFs akin to Figure 5.12 are generated to ensure that the dataset is indeed converged. Any dataset which does not show a clear correlation and a unity slope is excluded from the study. The conditions that have a fully-resolved dataset are marked with an asterisk (\*) in Table 5.2.

## CHAPTER 6

### INTER SCALE ENERGY TRANSPORT

The analysis of  $\alpha_{\text{sfs}}$  below is presented in the following manner. First, instantaneous and mean fields of  $\alpha_{\text{sfs}}$  are examined qualitatively. Next is the discussion of the statistics of  $\alpha_{\text{sfs}}$  (PDFs, conditional means, skewness, etc.) conditioned on the reaction progress variable and fluid strain-rate at a fixed filter width of  $\Delta/\delta_L^0 = 1.5$  for three select cases. These results demonstrate the overall physical trends and prevalence of back-scatter within the flame. Comparisons to the non-reacting cases clearly reveal the impact of combustion on the cross-scale kinetic energy dynamics. Next, the impact of the filter scale on the observed results is addressed, which has implications regarding the range of scales over which flame-generated kinetic energy is influential. Followed is the discussion of how the simultaneous action of turbulence, combustion, and coherent flow structures affect the inter-scale energy transfer. Finally, the effects of swirl number, jet velocity, and equivalence ratio on inter-scale energy transfer are evaluated by comparing  $c$ -conditioned statistics at a fixed filter scale. The chapter closes with an examination of how  $\alpha_{\text{sfs}}$  is correlated to the swirl-induced pressure gradient and the turbulent Reynolds number. A scaling is proposed that reflects the impact of swirl-induced pressure gradients in swirl flames relative to DNS of statistically planar flames in HIT.

#### 6.1 Instantaneous and mean $\alpha_{\text{sfs}}$ fields

First, the instantaneous and mean  $\alpha_{\text{sfs}}$  fields are examined qualitatively. Shown in Figure 6.1 are the instantaneous  $\alpha_{\text{sfs}}$  fields along the central plane of the burner for both reacting and non-reacting conditions at increasing jet velocity; the filter used is  $\Delta = 2.3$  mm. Dark blue patches in both sets of data represent locations that were excluded from the analysis due to insufficient seed particle concentration for accurate velocity calculation.

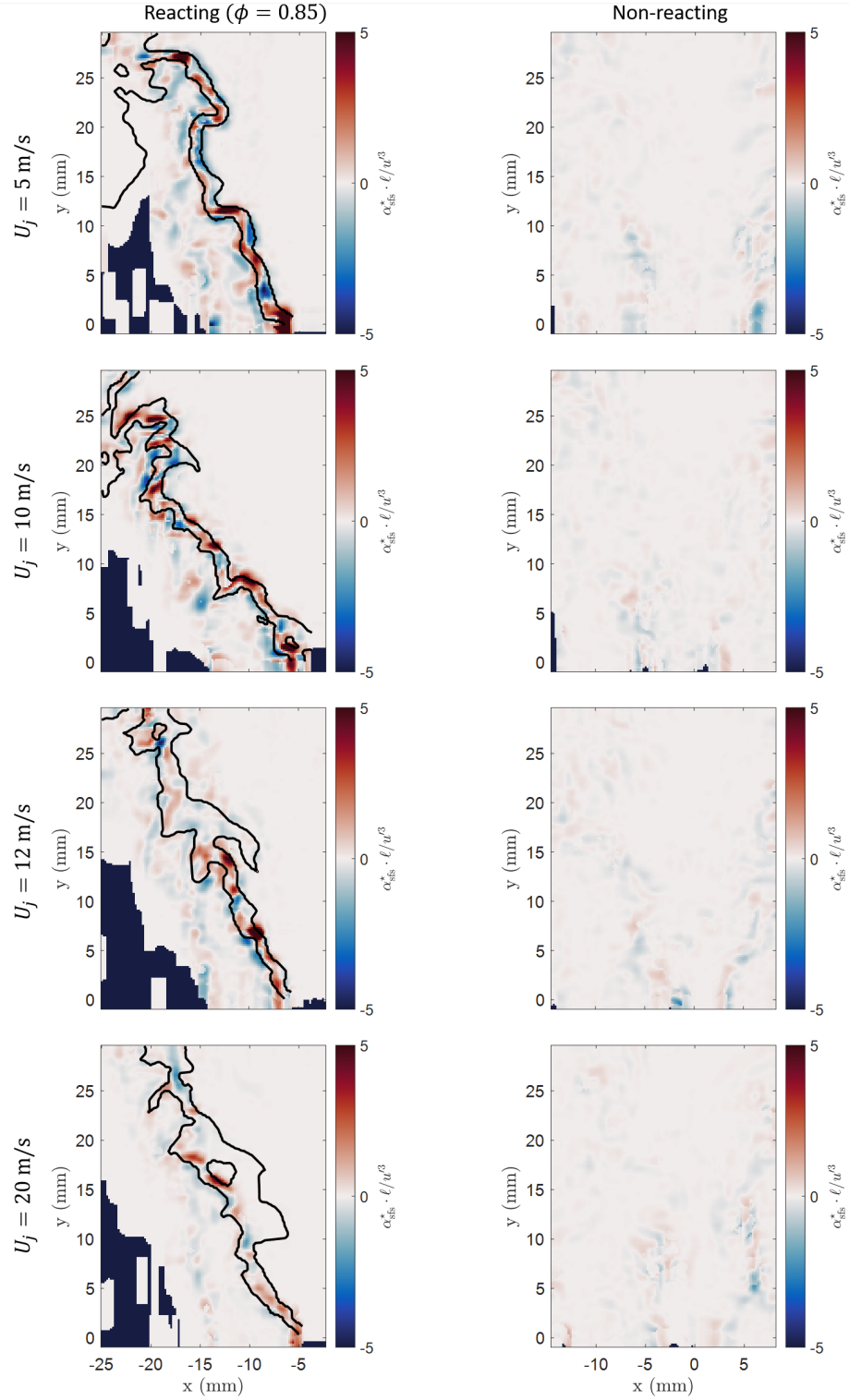


Figure 6.1: Instantaneous inter-scale energy transfer  $\langle \alpha_{\text{sfs}}^* \rangle \cdot \ell / u^3$  for  $S_1$  swirler across at  $\Delta = 2.3$  mm ( $\Delta / \delta_L^0 = 4.7$  for reacting cases). Black contours denote  $c = 0.1$  and  $c = 0.9$ . Left column: reacting flow at  $\phi = 0.85$ ; right column: non-reacting flow.



Clearly, both positive and negative values of  $\alpha_{\text{sfs}}$  appear throughout the flow instantaneously under non-reacting and reacting conditions. For non-reacting flow, the regions of larger  $|\alpha_{\text{sfs}}^*|$  appear systematically inside the inner shear layers between the reactant jet and the inner recirculation zone; significant  $|\alpha_{\text{sfs}}^*|$  is also visible in the outer shear layer for  $U_j = 5$  m/s. In the constant density flows,  $\alpha_{\text{sfs}}^*$  typically attains large magnitudes in regions of locally high strain-rates, which are more distributed in space for low Reynold number flows. In the reacting flows, regions of large  $\alpha_{\text{sfs}}^*$  are primarily within the inner shear layer across all of the test cases considered; there is also non-negligible  $\alpha_{\text{sfs}}^*$  in the outer shear layer, which merges with the inner shear layer downstream of the nozzle.

It should be noted that the presence of the flame alters the flow structure due to gas expansion across the flame; the position of the shear layer is displaced radially outward in the reacting cases. Changes in the local fluid properties and chemical composition also has an effect on the local  $\alpha_{\text{sfs}}^*$ . For example,  $|\alpha_{\text{sfs}}^*|$  is relatively small in the central recirculation zone of the reacting flows since this region contains combustion products; the increased viscosity across the flame increases  $\eta$  and leads to attenuation of small-scale kinetic energy in the products. On the other hand,  $|\alpha_{\text{sfs}}^*|$  varies significantly in the reactant jet and inside the instantaneous flame, regions where the temperature and viscosity are lower.

The region of highest  $|\alpha_{\text{sfs}}^*|$  is concentrated within the instantaneous flame for the reacting cases; the magnitude of  $\alpha_{\text{sfs}}^*$  internal to the flame is significantly larger compared to the reactant jet, the outer shear layer, or any region in an equivalent non-reacting flow. Furthermore, the normalized magnitude of inter-scale energy transfer  $\alpha_{\text{sfs}}^* \cdot \ell / u'^3$  decreases with increasing  $U_j$ . Hence, combustion has a non-negligible effect on the magnitude and distribution of  $\alpha_{\text{sfs}}^*$ , and it's effect depends on the strength of turbulence in the flow. Furthermore, Figure 6.1 shows that internal to the flame, energy backscatter generally appears more frequently than forward scatter, suggesting that combustion and energy backscatter are correlated.

Another important observation is regarding the structure of  $\alpha_{\text{sfs}}$  inside the flame. At

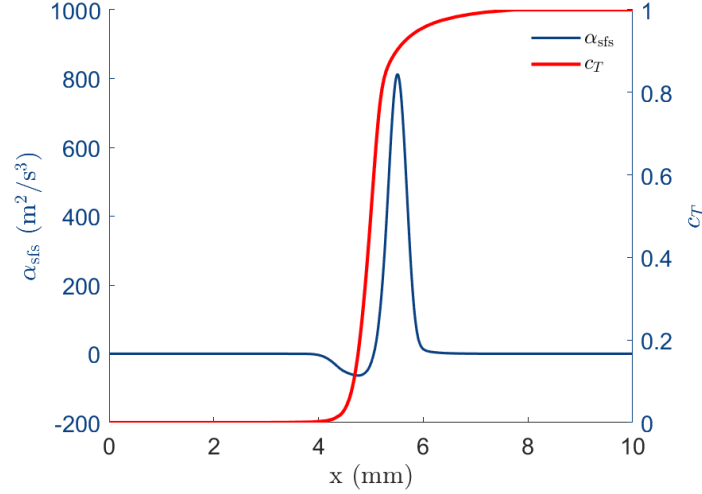


Figure 6.2: One dimensional  $\alpha_{sfs}$  across a premixed methane-air laminar flame at  $\phi = 0.75$ . Profiles of density, temperature, and axial velocity used to compute  $\alpha_{sfs}$  were obtained using Cantera; filtering performed using a box filter of width  $\Delta = 1.5$  mm or  $\Delta/\delta_L^0 = 2.6$ .

the lowest jet flow velocity ( $U_j = 5$  m/s), there appears to be a band-like positive  $\alpha_{sfs}^*$  structure across the flame, which become less coherent at higher jet velocities. There is also significant forward energy cascade near the reactant and product facing edges of the flame. To explain this, a 1D laminar flame we is considered, for which a 1D  $\alpha_{sfs}$  can be computed as

$$\alpha_{sfs} = -\frac{\tilde{u}}{\bar{\rho}} \frac{\partial}{\partial x_j} \bar{\rho}(\widetilde{uu} - \tilde{u}\tilde{u}). \quad (6.1)$$

Figure 6.2 shows the one-dimensional  $\alpha_{sfs}$  across a representative laminar premixed flame. It clearly shows a region of forward scatter at early stages of combustion, followed by a region of strong energy backscatter inside the flame. Hence, this behavior represents  $\alpha_{sfs}$  dynamics in the absence of turbulence, and one can expect a similar structure in weakly turbulent flames. This is likely what is observed for lower  $U_j$  cases. There is also significant forward-scatter following the band of backscatter. Since the instantaneous flame is located inside the shear layer, it is likely that fluctuating strain-rates cause forward energy scatter in the region following the site of significant heat-release.

At greater jet flow velocities, these bands of positive and negative  $\alpha_{sfs}^*$  appear to break up, such that regions of positive and negative  $\alpha_{sfs}^*$  occur in patches. Moreover, the width of

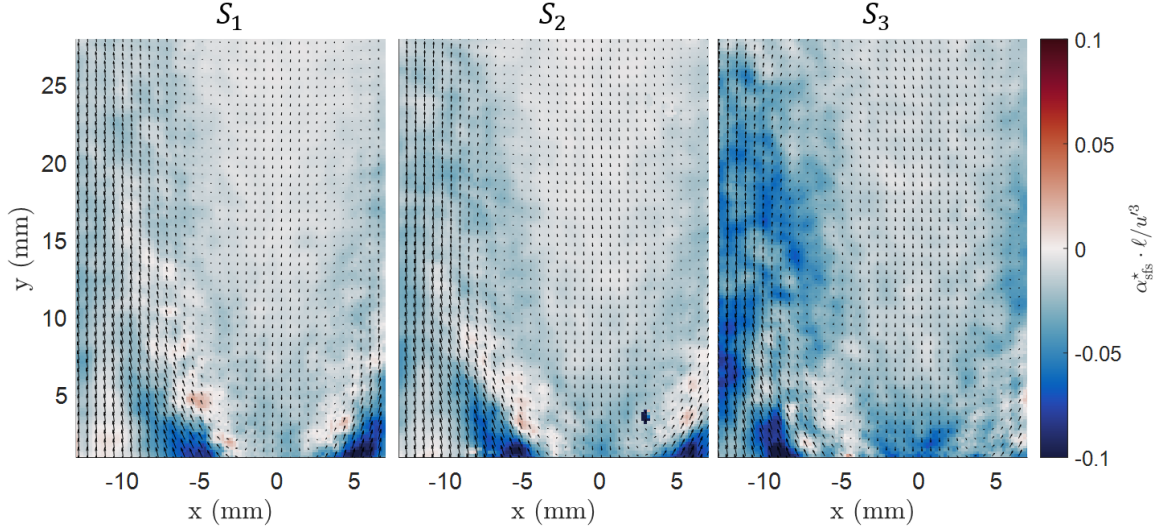


Figure 6.3: Mean inter-scale energy transfer  $\langle \alpha_{\text{sfs}}^* \rangle \cdot \ell / u'^3$  for non-reacting flows at  $U_j = 5$  m/s for three available swirlers;  $\alpha_{\text{sfs}}^*$  computed at  $\Delta = 2.3$  mm.

the flame increases at larger  $U_j$ , suggesting that there is stronger fluid mixing inside the turbulent shear layer that can potentially explain the break-up of  $\alpha_{\text{sfs}}^*$  structures. Nevertheless, the direction of inter-scale energy transfer is predominantly upwards (positive  $\alpha_{\text{sfs}}^*$ ) inside the flame.

#### *Mean $\alpha_{\text{sfs}}^*$*

The above results have demonstrated existence of strong backscatter inside the flame and existence of  $\alpha_{\text{sfs}}^*$  structure across such a flame. Next, the mean distributions of  $\alpha_{\text{sfs}}^*$  are considered for different  $\mathcal{S}$  and  $U_j$ . Figure 6.3 and Figure 6.4 show the distribution of mean inter-scale energy transfer  $\langle \alpha_{\text{sfs}}^* \rangle$  in the non-reacting and reacting flows, respectively. The black lines in the reacting case represent the  $\langle c \rangle = 0.1$  and  $\langle c \rangle = 0.9$  contours of the flame brush, which overlap with the shear layer as expected. In both reacting and non-reacting cases, the predominant flux of kinetic energy occurs within or in the vicinity of the shear layer.

In absence of combustion, the mean energy cascade is predominantly from large to small scales ( $\langle \alpha_{\text{sfs}}^* \rangle < 0$ ), which supports the Kolmogorov and Richardson phenomenology.

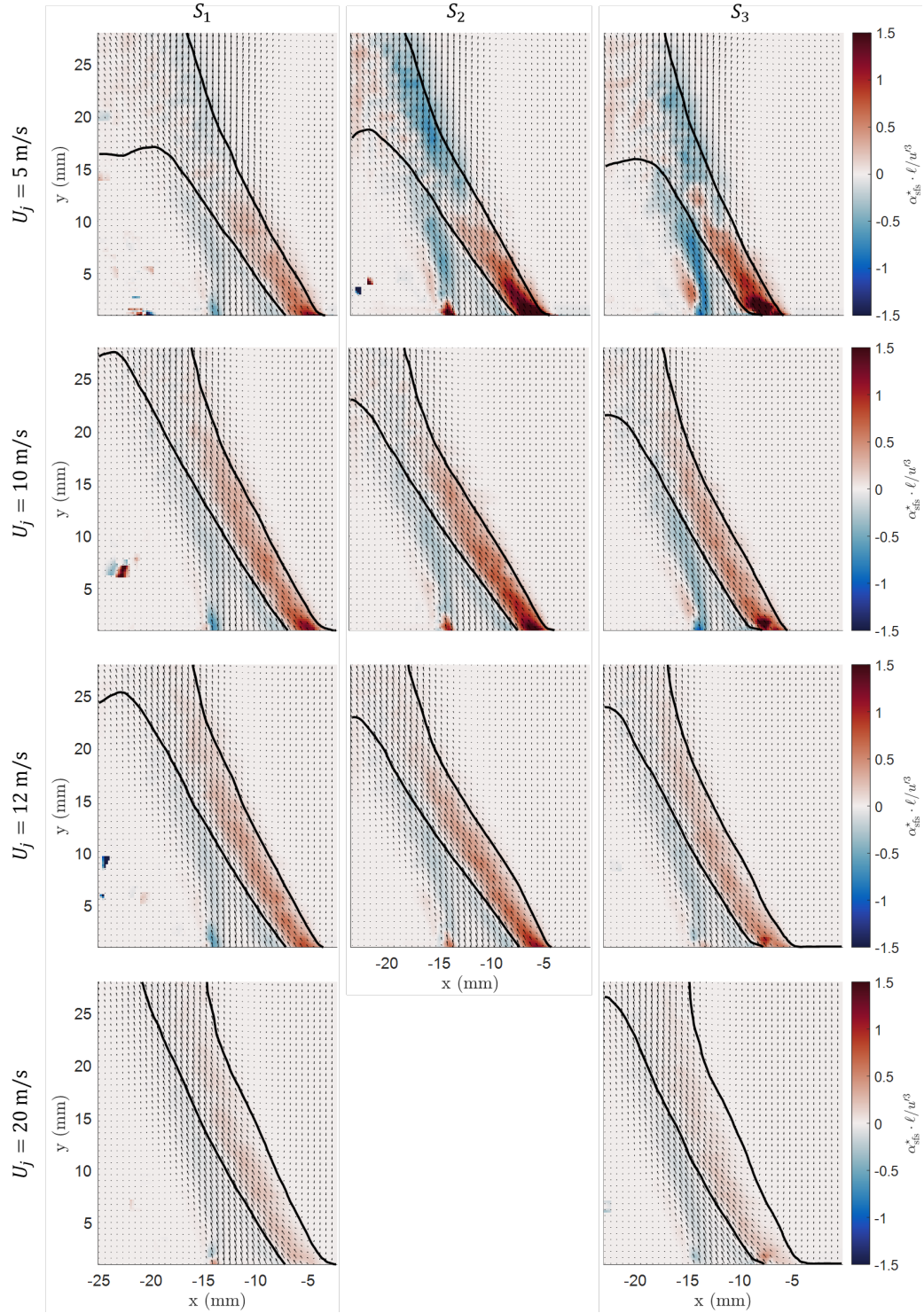


Figure 6.4: Mean inter-scale energy transfer  $\langle \alpha_{\text{sfs}} \rangle \cdot \ell / u'^3$  for  $\phi = 0.85$  at  $\Delta = 2.3$  mm ( $\Delta/\delta_L^0 = 4.7$ ). Black lines represent  $\langle c \rangle = 0.1$  and  $\langle c \rangle = 0.9$  contours of the flame brush.

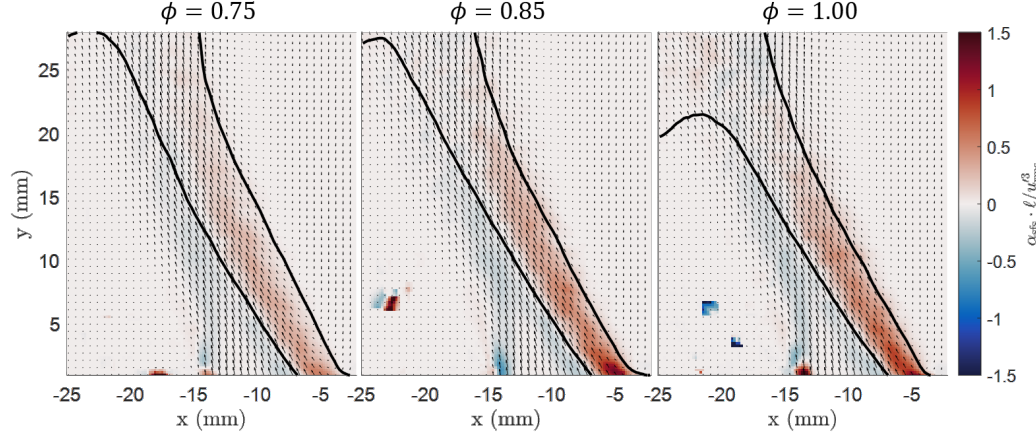


Figure 6.5: Mean inter-scale energy transfer  $\langle \alpha_{\text{sfs}} \rangle \cdot \ell / u^3$  for varying  $\phi$  using  $\mathcal{S}_1$  at  $U_j = 10$  m/s across  $\Delta = 2.3$  mm. Black lines represent  $\langle c \rangle = 0.1$  and  $\langle c \rangle = 0.9$  contours of the flame brush.

The magnitude of forward scatter is the greatest in the inner shear layer directly above the nozzle, with  $|\langle \alpha_{\text{sfs}}^* \rangle|$  decreasing with downstream distance. For the most part,  $\langle \alpha_{\text{sfs}}^* \rangle < 0$  everywhere in the flow, with the exception of the boundary between the inner shear layer and the inner recirculation zone. Since the filter scale lies near the energy input range of scales (i.e.  $\Delta$  is only slightly smaller than  $\ell$ ), positive patches of  $\langle \alpha_{\text{sfs}}^* \rangle$  exist as turbulent kinetic energy is created by mean shear. An increase in  $\mathcal{S}$  shows an increase in  $|\langle \alpha_{\text{sfs}}^* \rangle|$  and the inner shear layer is pushed radially outward; note that the flow rate is larger for higher  $\mathcal{S}$  at the same  $U_j$ , which resulted in the higher turbulent intensity, as is expected.

The reacting flow in Figure 6.4 shows significant differences in  $\langle \alpha_{\text{sfs}}^* \rangle$  as compared to the non-reacting flow. There is clear evidence of mean energy backscatter in all cases. Similar to the instantaneous measurements, there is a band of backscatter ( $\langle \alpha_{\text{sfs}}^* \rangle > 0$ ) inside the flame brush (between  $\langle c \rangle = 0.1$  and  $\langle c \rangle = 0.9$ ); a band of forward energy scatter ( $\langle \alpha_{\text{sfs}}^* \rangle < 0$ ) exists immediately upstream of the flame brush ( $\langle c \rangle < 0.1$ ). This structure is similar to the one observed across the laminar flame (see Figure 6.2). The magnitude of  $\langle \alpha_{\text{sfs}}^* \rangle$  generally decreases with downstream distance. There is an important difference in downstream  $\langle \alpha_{\text{sfs}}^* \rangle$  between weakly turbulent flames ( $U_j = 5$  m/s) and moderate to strongly turbulent flame ( $U_j = 10 - 20$  m/s). Specifically,  $\langle \alpha_{\text{sfs}}^* \rangle$  decreases from positive  $\langle \alpha_{\text{sfs}}^* \rangle$  to

zero with downstream distance for strongly turbulent flames, whereas there is a region of significant forward cascade at  $y \gtrsim 10$  mm for  $U_j = 5$  m/s. Since the downstream negative region of  $\langle \alpha_{\text{sfs}}^* \rangle$  is observed to change with  $S$ , this likely a result of the changing pressure field.

Finally, the effects of varying  $S$ ,  $U_j$ , and  $\phi$  on  $\langle \alpha_{\text{sfs}} \rangle$  are discussed briefly based on the mean distributions shown in Figure 6.4 and Figure 6.5. Firstly, increasing the jet velocity, and turbulent velocity fluctuations, generally results in a weaker normalized energy backscatter inside the flame brush. Nevertheless, the mean direction of inter-scale energy transfer is upwards inside the flame brush at all investigated operating conditions. Secondly, the effect of increasing the swirl number appears to depend on  $U_j$ ; the  $U_j = 5$  m/s cases are very different at three swirl numbers, while this variation is not noticable at larger  $U_j$ . It seems that the influence of  $S$  decreases as  $U_j$  increases. Finally, increasing  $\phi$  from lean to stoichiometric conditions increases the observed  $\langle \alpha_{\text{sfs}}^* \rangle$ , as demonstrated in Figure 6.5. This likely is due to the greater dilatation across the flame with increasing  $\phi$ . Further details on the effects of  $S$ ,  $U_j$ , and  $\phi$  will be discussed in Section 6.5.

## 6.2 $c$ - and $S_{ij}S_{ij}$ - conditioned statistics at $\Delta/\delta_L^0 = 1.5$

Here, three separate cases are considered for analysis of conditional statistics. For Section 6.2 to Section 6.4, all results are taken from conditions that are fully resolved and  $\alpha_{\text{sfs}}$  can be computed directly. The results below are presented in terms of conditional PDFs and statistics of  $\alpha_{\text{sfs}}$ . To assess the influence of the local instantaneous flame and flow configuration, the data are first conditioned on both  $c$  and  $S_{ij}S_{ij}$ . This choice of flow conditioning is justified by Samgorinsky-type eddy viscosity models for LES.

Figure 6.6 shows the mean doubly-conditioned cross-scale energy flux  $\langle \alpha_{\text{sfs}} | c, S_{ij}S_{ij} \rangle$  for three sample flames with fully-resolved flow field (cases E075-S1-U4, -U10, and E085-S1-U15) with  $\Delta/\delta_L^0 = 1.5$ ; also shown are the JPDFs of  $c$  and  $S_{ij}S_{ij}$  to demonstrate the probability of the flow occupying different points in the parameter space. The JPDFs show

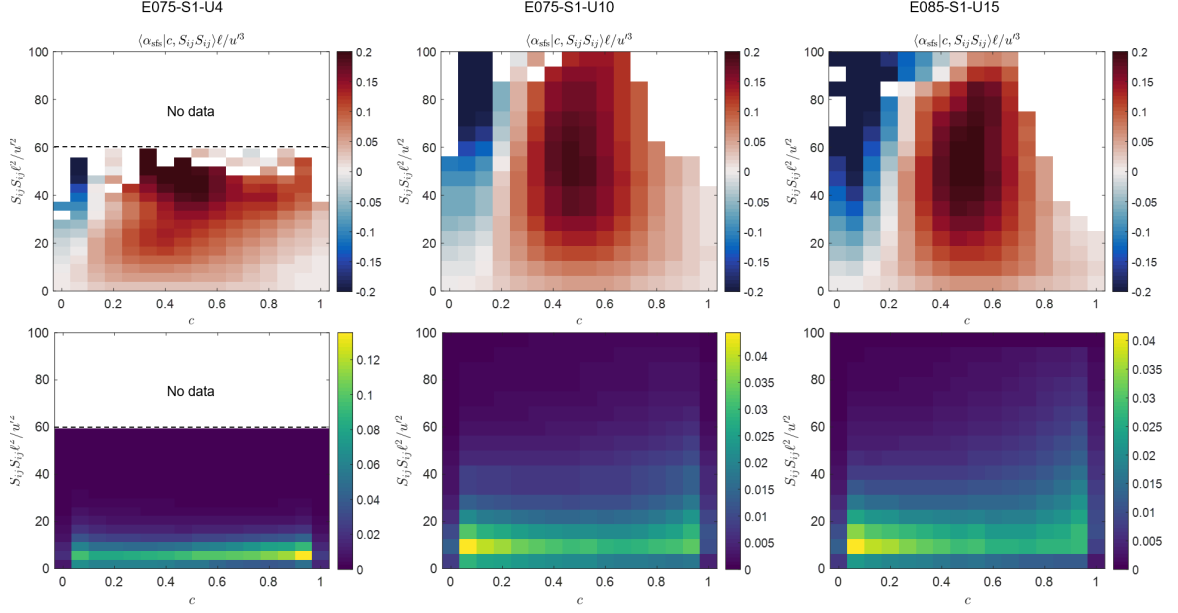


Figure 6.6: Doubly-conditioned statistics with  $\Delta/\delta_L^0 = 1.5$ . Top row: mean cross-scale energy transport as a function of progress variable and strain rate. Bottom row: JPDFs between progress variable and strain rate.

that the majority of measurements have normalized strain-rates well below the maximum measured strain-rate for which the data are considered converged.

Mean back-scatter is clearly present in all flames, and its normalized magnitude is similar across the turbulence intensities considered here. In the flame with the weakest turbulence (E075-S1-U4), energy is primarily transferred from small to large scales inside the flame, except for a small region at low  $c$  and (relatively) high  $S_{ij} S_{ij}$ . In the more turbulent flames, the range of measured strain rates is larger, with the exception of the region bounded by  $c \gtrsim 0.7$  and  $S_{ij} S_{ij} \ell^2 / u^2 \gtrsim 40$ . This is expected since the strain-rates associated with turbulence in the combustion products is typically lower than in the reactants. Mean forward-scatter occurs at higher strain rates for  $c \lesssim 0.2$ , though the probability of these strain-rates is low. Mean back-scatter occurs at locations internal to the flame structure where the majority of the data lie. The maximum back-scatter magnitude occurs internal to the flame surface, in the range  $0.4 \lesssim c \lesssim 0.6$ , which is consistent with previous DNS results [68].



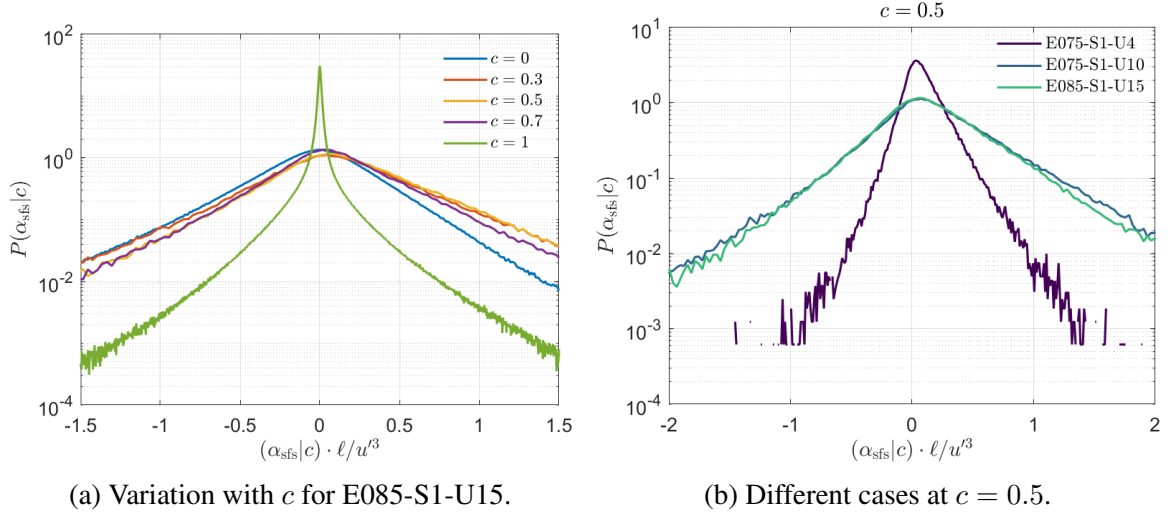


Figure 6.7: Probability density functions of  $\alpha_{\text{sfs}}$  conditioned on  $c$  with  $\Delta/\delta_L^0 = 1.5$ .

The general relationship between  $\langle \alpha_{\text{sfs}} \rangle$ ,  $c$ , and  $S_{ij}S_{ij}$  is quite similar between the three cases in the normalized coordinates, with the lower turbulence intensity case E075-S1-U4 being truncated along the strain-rate axis at  $S_{ij}S_{ij}\ell^2/u'^2 \approx 60$  and the more intense cases being truncated at  $S_{ij}S_{ij}\ell^2/u'^2 \approx 100$ . That is, there appears to be a parameter range below  $S_{ij}S_{ij}\ell^2/u'^2 \lesssim 100$  in which mean back-scatter occurs internal to the flame surface for all cases when  $\Delta/\delta_L^0 = 1.5$ . The absolute strain-rates at which mean back-scatter occurs increases with increasing turbulence intensity. Moreover, the normalized doubly-conditioned  $\langle \alpha_{\text{sfs}} \rangle$  obtain similar values between all cases, in the range of  $\langle \alpha_{\text{sfs}} \rangle \ell/u'^3 \approx 0.2$ . Within the range of commonly-occurring strain-rates,  $\langle \alpha_{\text{sfs}} \rangle$  is positive across essentially the entire range of progress variables, except at  $c \lesssim 0.1 - 0.15$ . Hence, back-scatter dominates within the flame structure for the conditions and configuration studied here.

Figure 6.6 showed that  $\alpha_{\text{sfs}}$  depends on both  $c$  and the turbulence. Additional insight can be gained by examining the PDFs of  $\alpha_{\text{sfs}}$ , conditioned on either  $c$  or  $S_{ij}S_{ij}$  individually. Figure 6.7(a) shows  $P(\alpha_{\text{sfs}}|c)$  for case E085-S1-U15, marginalized across  $S_{ij}S_{ij}$ . The range of  $\alpha_{\text{sfs}}|c$  decreases with increasing  $c$  due to suppression of small-scale motion as a result of flow dilatation and increased temperature (viscosity) across the flame. Towards the reactants, the most probable  $\alpha_{\text{sfs}}$  (maximum  $P(\alpha_{\text{sfs}}|c)$ ) is near zeros and the PDF is neg-



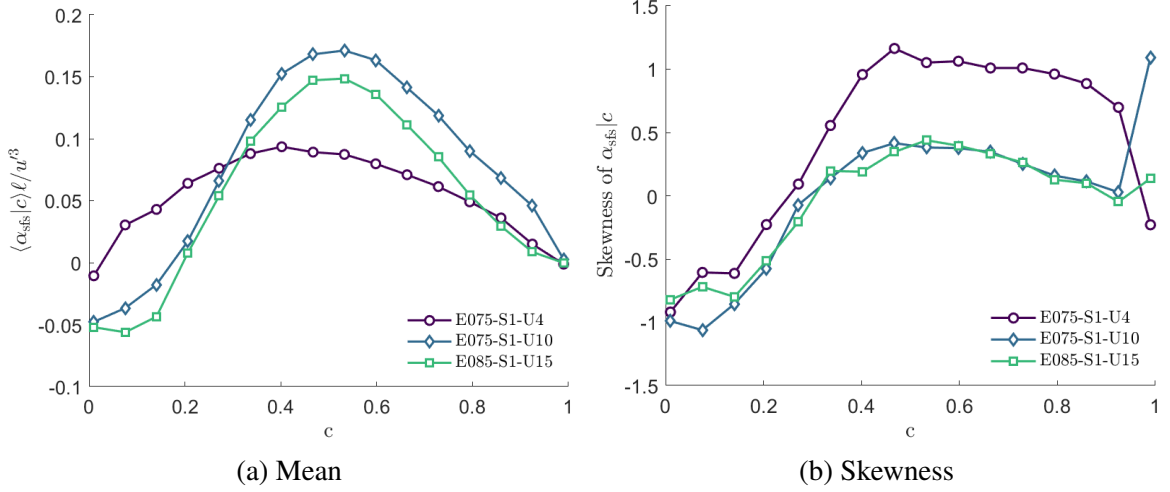


Figure 6.8: Mean and skewness of  $P(\alpha_{\text{sfs}}|c)$  with  $\Delta/\delta_L^0 = 1.5$ .

atively skewed, resulting in a negative  $\langle \alpha_{\text{sfs}} \rangle$ . Internal to the flame, the most probable  $\alpha_{\text{sfs}}$  shift towards positive values, with the maximum shift occurring around  $c \approx 0.5$ ; the most probable  $\alpha_{\text{sfs}}$  is positive (back-scatter) within the flame, even for the most turbulent case shown here. Figure 6.7(b) shows  $P(\alpha_{\text{sfs}}|c = 0.5)$  for the three cases under consideration. The range of normalized  $\alpha_{\text{sfs}}$  increases with higher flow rate (turbulence intensity) cases, with the two more turbulent cases showing very similar distributions. In all cases, the most probable  $\alpha_{\text{sfs}}|c = 0.5$  is positive.

The mean and skewness of  $\alpha_{\text{sfs}}|c$  versus  $c$  are shown in Figure 6.8 for the three cases. Increasing the bulk flow rate from case E075-S1-U4 to case E085-S1-U15, and hence increasing both the turbulence intensity and overall heat release rate, increases both the mean forward energy cascade toward the reactant side of the flame  $c \lesssim 0.1 - 0.2$  and mean back-scatter in the middle of the flame. The distribution for case E085-S1-U15 is similar to case E075-S1-U10, but the magnitude of normalized of back-scatter is reduced slightly for  $\langle \alpha_{\text{sfs}}|c \rangle$  in the range  $0.3 \lesssim c \lesssim 0.8$ . It is noteworthy that the magnitude of the mean back-scatter towards the middle of the flame is larger than that of the forward-scatter towards the reactants. The impact of jet velocity, swirl number, and equivalence ratio on inter-scale energy transfer is discussed in more detail in Section 6.5.

The PDFs for the three cases exhibit negative skewness for  $c \lesssim 0.3$ . While the least tur-

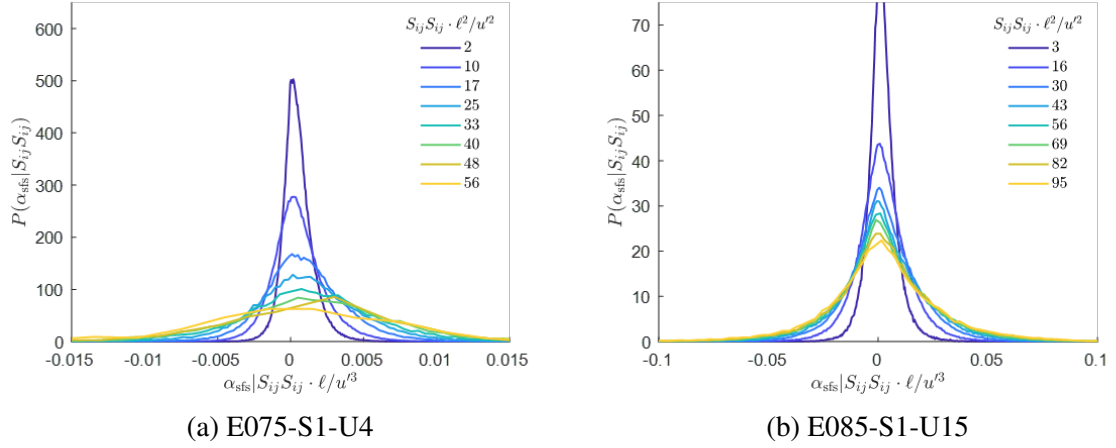


Figure 6.9: Probability density functions of  $\alpha_{\text{sfs}}$  conditioned on  $S_{ij}S_{ij}$  with  $\Delta/\delta_L^0 = 1.5$

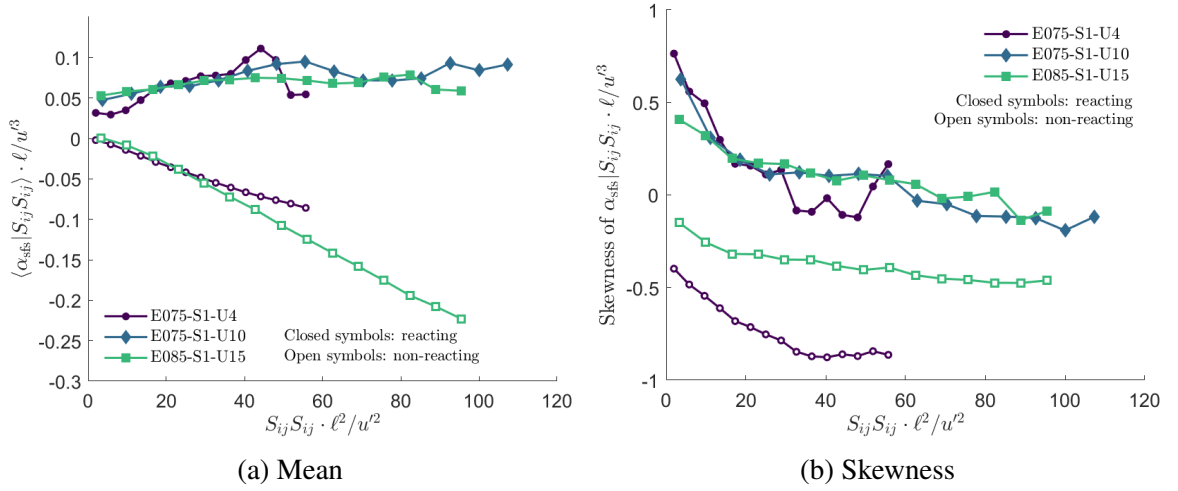


Figure 6.10: Mean and skewness of  $P(\alpha_{\text{sfs}}|S_{ij}S_{ij})$  with  $\Delta/\delta_L^0 = 1.5$ . Filled markers: reacting flow, empty markers: non-reacting flow.

bulent case E075-S1-U4 is positively skewed for higher  $c$ , cases E075-S1-U10 and E085-S1-U15 have near zero skewness. Hence, combustion both shifts the PDFs to higher values of  $\alpha_{\text{sfs}}$  and increases the skewness compared to what would occur without the flame. However, the positive mean  $\alpha_{\text{sfs}}$  at the higher turbulence intensities is due to a positive most-probable  $\alpha_{\text{sfs}}$  and elimination of negative skewness, as opposed to a positively skewed distribution.

Figure 6.6 showed that  $\alpha_{\text{sfs}}$  depends on both  $c$  and the turbulence. To further articulate the impact of local flow conditions, Figure 6.9 shows the probability density functions of

$\alpha_{\text{sfs}}$  conditioned on  $S_{ij}S_{ij}$  for cases E075-S1-U4 and E085-S1-U15. To reiterate, although PDFs are shown across the range of measured  $S_{ij}S_{ij}$  for each case, the majority of data occurred at  $S_{ij}S_{ij}\ell^2/u'^2 \lesssim 10$  for case E075-S1-U4 and  $S_{ij}S_{ij}\ell^2/u'^2 \lesssim 50$  for case E085-S1-U15. The PDFs indicate a positive most probable  $\alpha_{\text{sfs}}$ , with a trend towards zero as  $S_{ij}S_{ij}$  increases.

The mean and skewness of the PDFs are shown in Figure 6.10 for the three cases. Also included are the data for the non-reacting flows with the same volumetric flow-rates; these data allow explicit demonstration of the overall impact of the flame on  $\alpha_{\text{sfs}}$ . For the reacting cases, the  $\langle \alpha_{\text{sfs}} | S_{ij}S_{ij} \rangle$  profiles show mean back-scatter at all measured normalized strain-rates. Comparing the reacting and non-reacting cases, the non-reacting cases showed mean forward-scatter across the entire range of  $S_{ij}S_{ij}$ , consistent with the classical mean downward energy cascade in constant density flows. Importantly, there is a significant offset between the reacting and non-reacting cases, even at high strain rates. That is, even though the magnitude of mean back-scatter is lower than of forward-scatter in non-reacting flows, flame caused an increased probability and magnitude of intermittent back-scatter.

Figure 6.10(b) shows that the PDFs for the reacting cases are positively skewed at  $S_{ij}S_{ij}\ell^2/u'^2 \lesssim 60$  (where the majority of the data occur) and nearly symmetric for  $S_{ij}S_{ij}\ell^2/u'^2 \gtrsim 60$ . The trend is skewness with  $S_{ij}S_{ij}$  is approximately linear beyond  $S_{ij}S_{ij}\ell^2/u'^2 \gtrsim 40$ . In contrast, the non-reacting cases show negative skewness that is consistently below the reacting cases across all values of the strain-rate. These data confirm that combustion both shifts and skews the  $\alpha_{\text{sfs}}$  PDFs towards positive values.

### 6.3 Effect of filter size

The data above were all obtained with a filter size of  $\Delta/\delta_L^0 = 1.5$ , demonstrating the cross-filter energy transfer at a filter scale slightly greater than the laminar flame thickness. It also is instructive to consider the effect of changing the filter scale on the observed results. For example, if  $\langle \alpha_{\text{sfs}} \rangle$  is similar between filter scales  $\Delta_1$  and  $\Delta_2 > \Delta_1$ , this indicates that

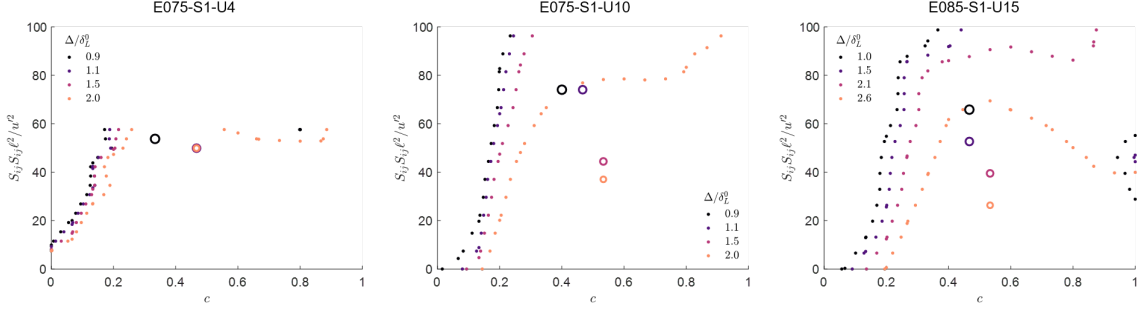


Figure 6.11: Contours (solid dots) where  $\langle \alpha_{\text{sfs}} \rangle = 0$  for increasing  $\Delta$ . Open circles indicate the location of maximum  $\langle \alpha_{\text{sfs}} \rangle$  for each  $\Delta$ .

kinetic energy transferred from smaller scales through  $\Delta_1$  is also transferred through  $\Delta_2$ . If  $\langle \alpha_{\text{sfs}} \rangle$  is lower at the larger filter scale, this may indicate accumulation of kinetic energy between the scales.

Figure 6.11 provides important attributes of the doubly-conditioned mean  $\alpha_{\text{sfs}}$  across a range of filter scales  $0.9 \leq \Delta/\delta_L^0 \leq 2.2$ . These plots summarize important features in the doubly-conditioned mean data that were shown in Figure 6.6 for  $\Delta/\delta_L^0 = 1.5$ . In particular, the solid dots represent the points where  $\langle \alpha_{\text{sfs}} | c, S_{ij} S_{ij} \rangle = 0$  and the open dots represent the location of maximum  $\langle \alpha_{\text{sfs}} | c, S_{ij} S_{ij} \rangle$  for each filter scale.

The main trend is that the range of strain-rates over which mean back-scatter occurs is reduced to lower values with increasing filter scale. Nevertheless, this range still encompasses the majority of the data as shown by the JPFDs in Figure 6.6, which are not affected by the filter scale. Positive  $\langle \alpha_{\text{sfs}} \rangle$  occurs at slightly higher  $c$  for increasing filter scale, but always occurs for  $c \gtrsim 0.2$ . Regarding the location of maximum  $\langle \alpha_{\text{sfs}} \rangle$ , the overall effect of increasing  $\Delta$  is to shift the location of maximum back-scatter to smaller strain rates and closer to the middle of the flame. Comparing cases E075-S1-U10 and E085-S1-U15, the range of normalized strain-rates over which mean back-scatter occurs is similar between cases at any given filter scale.

Figure 6.12 shows the variation of  $c$ -conditioned probability density functions with  $\Delta$  at  $c = 0$  and  $0.5$  for case E085-S1-U15. In the reactants, the PDFs are centered around zero and skewed slightly negatively, demonstrating net forward-scatter at all tested filter

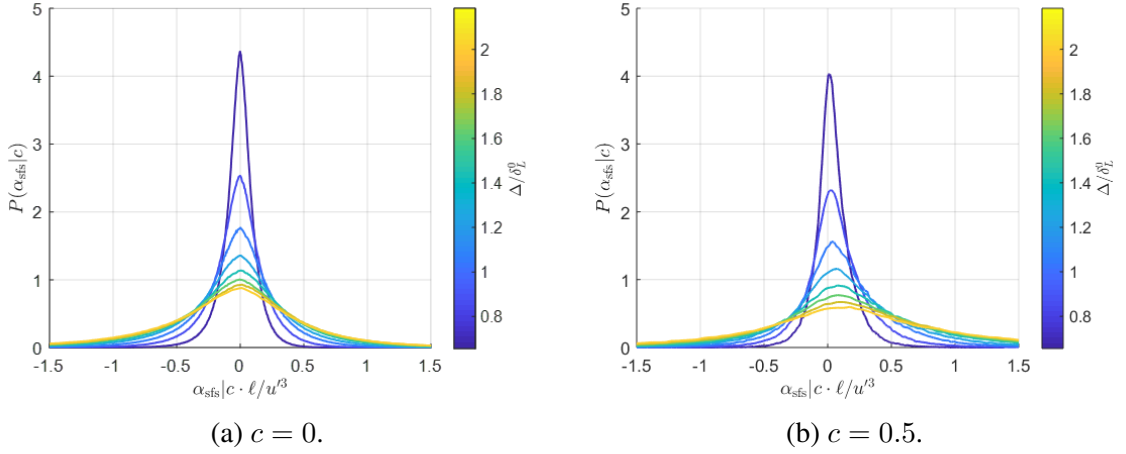


Figure 6.12: Probability density functions of  $\alpha_{\text{sfs}}$ , conditioned on progress variable, at different filter scales for E085-S1-U15.

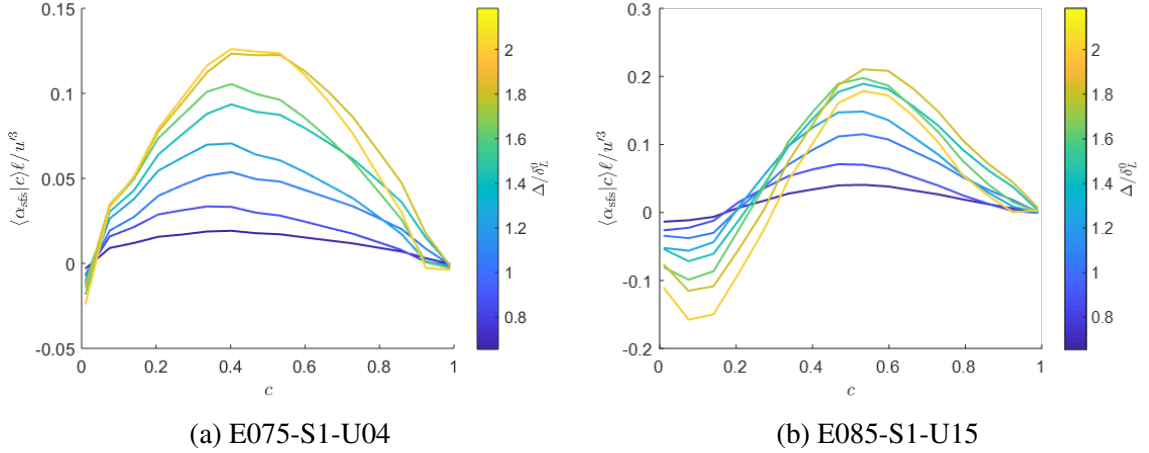


Figure 6.13: Variation of  $\langle \alpha_{\text{sfs}}|c \rangle$  with the filter scale.

scales. Inside the flame, the PDFs are positively shifted and skewed, demonstrating net back-scatter at all tested filter scales.

The impact of filter size on  $\alpha_{\text{sfs}}$  is further articulated in Figure 6.13, which shows the variation of  $\langle \alpha_{\text{sfs}}|c \rangle$  for various  $\Delta$  in cases E075-S1-U04 and E085-S1-U15. In the least turbulent case, mean forward-scatter is only observed at the reactant edge of the flame. Mean back-scatter occurs throughout the flame structure, peaking at around  $c \approx 0.5$  with a magnitude that increases with filter scale. This indicates that net more kinetic energy is transferred up-scale through larger filter scales in this weakly turbulent flame, at least to

$\Delta/\delta_L^0 = 2.2$ . Thus, for weakly turbulent flames, the local energy transfer dynamics are strongly influenced by thermal expansion across the range of filter scales studied.

The more turbulent case shows some similar attributes, but with some important differences. Forward-scatter is observed over a larger range of  $c$ -values, with this range increasing with increasing  $\Delta$ . While the magnitude of the forward-scatter at low  $c$  monotonically increased with increasing  $\Delta$ , the magnitude of the back-scatter appears to reach a maximum at around  $\Delta/\delta_L^0 \approx 1.8$ . Indeed, the increased  $c$ -range exhibiting negative  $\langle \alpha_{\text{sfs}} \rangle$  reduces the overall back-scatter for  $\Delta/\delta_L^0 \gtrsim 1.8$  in this flame. This result may indicate that the influence of the flame on kinetic energy dynamics is limited to a range of scales around the laminar flame thickness.

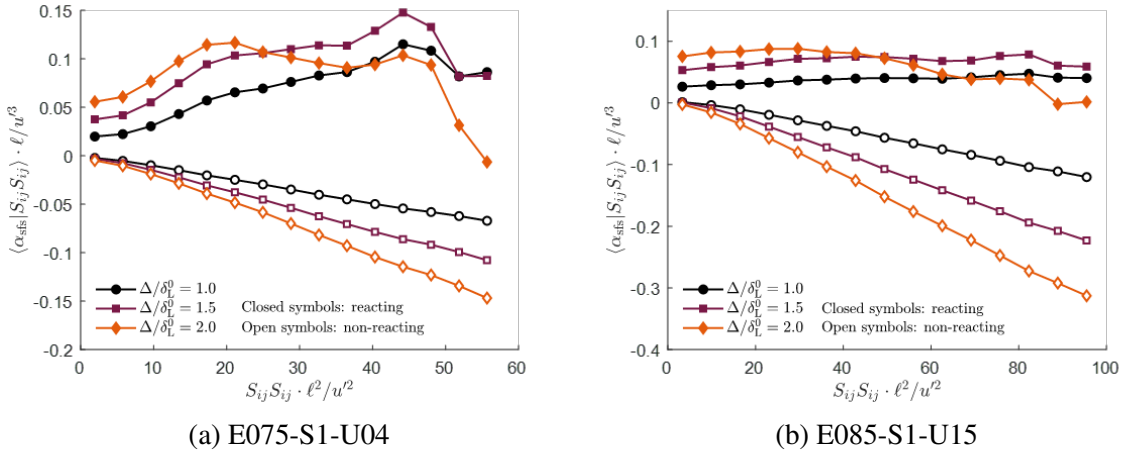


Figure 6.14: Mean of  $\alpha_{\text{sfs}}|S_{ij}S_{ij}|$  in reacting and non-reacting flows, as filtered using near the scales of the flame.

Finally, it is worth comparing the impact of filter-scale on the differences in  $\langle \alpha_{\text{sfs}} \rangle$  between reacting and non-reacting cases. To do so, Figure 6.14 presents  $\langle \alpha_{\text{sfs}}|S_{ij}S_{ij}|$  at  $\Delta/\delta_L^0 = 1.0, 1.5$ , and  $2.0$  for cases E075-S1-U04 and E085-S1-U15, similar to what was shown in Figure 6.10(a). In case E075-S1-U04, the reacting flows show mean back-scatter at all strain-rates and filter sizes, while the non-reacting cases show mean forward scatter. The magnitude of  $\langle \alpha_{\text{sfs}} \rangle$  generally increases with increasing filter size.

The data in case E085-S1-U15 exhibit somewhat more complicated behavior, but yield

similar overall conclusions. Increasing the filter scale generally increases the magnitude of  $\langle \alpha_{\text{sfs}} \rangle$ . For the reacting cases, positive  $\langle \alpha_{\text{sfs}} \rangle$  occurs for  $S_{ij}S_{ij}\ell^2/u'^2 \lesssim 100$ . The magnitude of  $\langle \alpha_{\text{sfs}} \rangle$  does not vary significantly with  $S_{ij}S_{ij}$  for  $\Delta/\delta_L^0 \lesssim 1.5$ , but starts to tend towards  $\langle \alpha_{\text{sfs}} \rangle < 0$  at higher strain rates when  $\Delta/\delta_L^0 = 2$ . Consistent with Figure 6.10(a), the  $\langle \alpha_{\text{sfs}} \rangle$  curves for the reacting cases are always above the curves for the non-reacting cases at the same strain-rates. Hence, even at local conditions for which combustion does not induce mean back-scatter, it does have a significant impact on the cross-scale energy transfer for the flames studied here.

## 6.4 Effect of Coherent Flow Structures

Thus far, only effects of combustion and turbulence on  $\alpha_{\text{sfs}}$  have been considered. However, there are also coherent flow structures that interact with the instantaneous turbulent flame and can have a significant effect on the inter-scale energy transfer in regions of flame-vortex interactions. In this section, results from a single case - E085-S1-U25 - are presented to demonstrate the effect of coherent vortex structures on the inter-scale energy transfer. First, the relationship between  $\alpha_{\text{sfs}}$  and  $\lambda_{\text{ci}}$  is considered on an instantaneous basis to demonstrate the effects of swirling eddies on local cross-scale energy transfer. Next, the impact of a single most dominant eddy on energy dynamics is performed by examining phase-averaged  $\lambda_{\text{ci}}$  and  $\alpha_{\text{sfs}}$ .

### 6.4.1 Instantaneous Data and Conditional Statistics

First, the relationship between  $\lambda_{\text{ci}}$ , the flame, and  $\alpha_{\text{sfs}}$  is examined on an instantaneous basis. Figure 6.15(a) shows a representative snapshot of  $\lambda_{\text{ci}}$ , overlaid with  $c = 0.1$  and  $c = 0.9$  contours as markers of the flame. A set of large-scale coherent swirling structures (eddies) intersects with the instantaneous flame. The flame generally is thicker and more curved at locations of flame/vortex interaction.

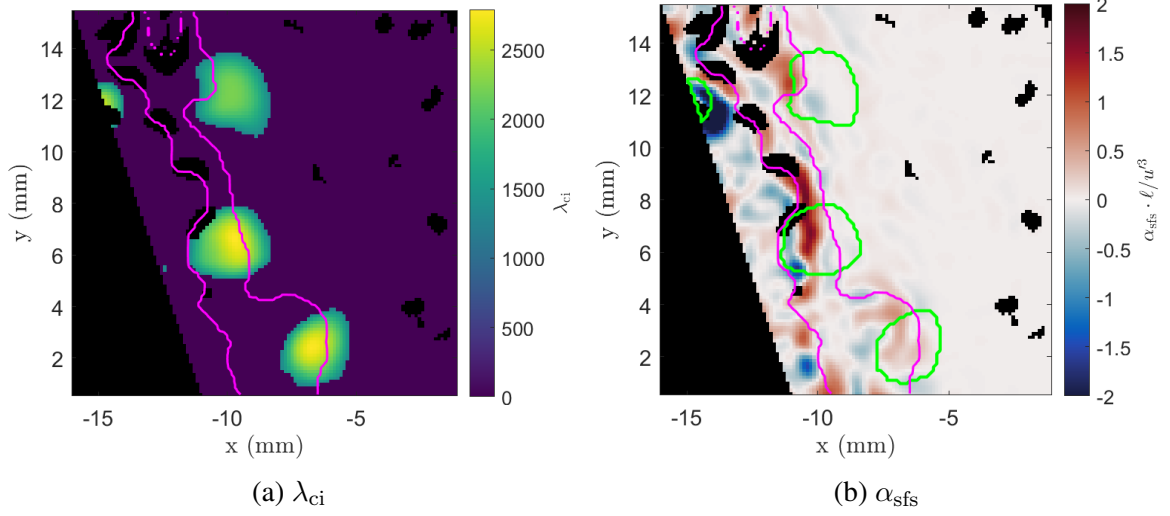


Figure 6.15: Instantaneous realization of  $\lambda_{ci}$  and  $\alpha_{sfs}$  for  $\Delta/\delta_L^0 = 1.5$ . Magenta curves correspond to  $c = 0.1$  and  $c = 0.9$  contours. Green curve is an isocontour of  $\lambda_{ci} = \frac{1}{2} \max(\lambda_{ci})$  at this instant. Regions that do not have valid velocity measurements are filled black.

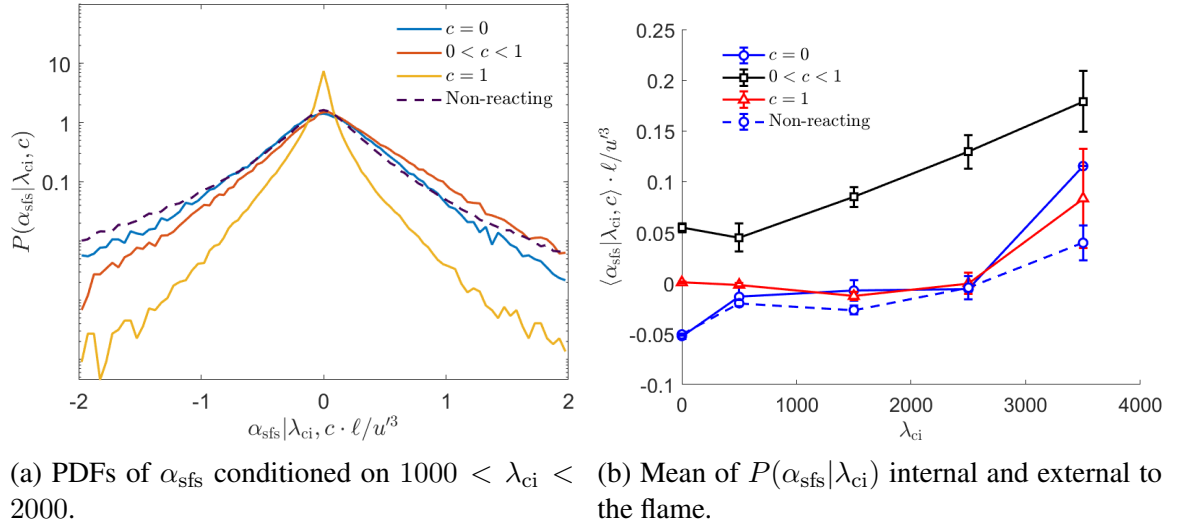


Figure 6.16: Variation of instantaneous  $\alpha_{sfs}$  with  $\lambda_{ci}$  for reacting and non-reacting flows.

Figure 6.15(b) shows the corresponding  $\alpha_{sfs}$  field with contours of the flame and eddies shown in magenta and green, respectively. Energy transfer occurs in both the up-scale (back-scatter, red) and down-scale (forward-scatter, blue) directions across the filter scale  $\Delta$ , with regions of energy back-scatter predominantly occur in the vicinity of the flame. The magnitude of  $\alpha_{sfs}$  is substantially lower in the products due to suppression of small-scale motion as a result of flow dilatation and increasing viscosity across the flame.



Since it is difficult to ascertain correspondence between the eddies and cross-scale energy transfer from this individual image, the conditional PDFs of  $\alpha_{\text{sfs}}$  are plotted in Figure 6.16(a); the PDFs are conditioned on moderate swirl ( $1000 < \lambda_{\text{ci}} < 2000$ ) and the reacting data are conditioned on the pure reactants ( $c = 0$ ), internal to the flame ( $0 < c < 1$ ) and in the burnt products ( $c = 1$ ). In the reactants and in non-reacting flow, the PDFs are nearly symmetric, indicating nearly equal forward- and back-scatter across  $\Delta$ . Similarly, the PDF in the products is nearly symmetric, but with reduced range of  $\alpha_{\text{sfs}}$  due to attenuation of turbulence at elevated temperature. Inside the flame, the PDF is positively skewed, indicating an increased probability of back-scatter.

To further articulate the simultaneous effects of the flame and eddies on  $\alpha_{\text{sfs}}$ , Figure 6.16(b) shows the conditional mean  $\langle \alpha_{\text{sfs}} | \lambda_{\text{ci}}, c \rangle$  for both the reacting and non-reacting flows (the PDFs in Figure 6.16(a) are from the data comprising the mean at  $\lambda_{\text{ci}} = 1500$  in Figure 6.16(b)). The error bars indicate the expected uncertainty in the mean based on the sample standard deviation and number of samples, approximating the statistics as normal. For the non-reacting case,  $\langle \alpha_{\text{sfs}} \rangle$  is negative for most values of  $\lambda_{\text{ci}}$ , obtaining a slightly positive value at locations of high swirl. The data in the reactants and products of the reacting case are qualitatively similar to the non-reacting case. Most interesting are the data within the flame, which clearly demonstrate the flame-induced mean back-scatter and that the back-scatter magnitude increases with the local swirling strength. Regions of locally high swirling strength are expected to correspond to local increases in reaction rate due to flame wrinkling and increased scalar gradients. Hence, the data are indicative of a positive correlation between locally-enhanced combustion chemistry and occurrence of back-scatter.

#### 6.4.2 Phase-Conditioned Analysis

The above results demonstrate how the presence of swirling eddies and flame affect the local cross-scale kinetic energy transfer. Now, the impact of the single most dominant

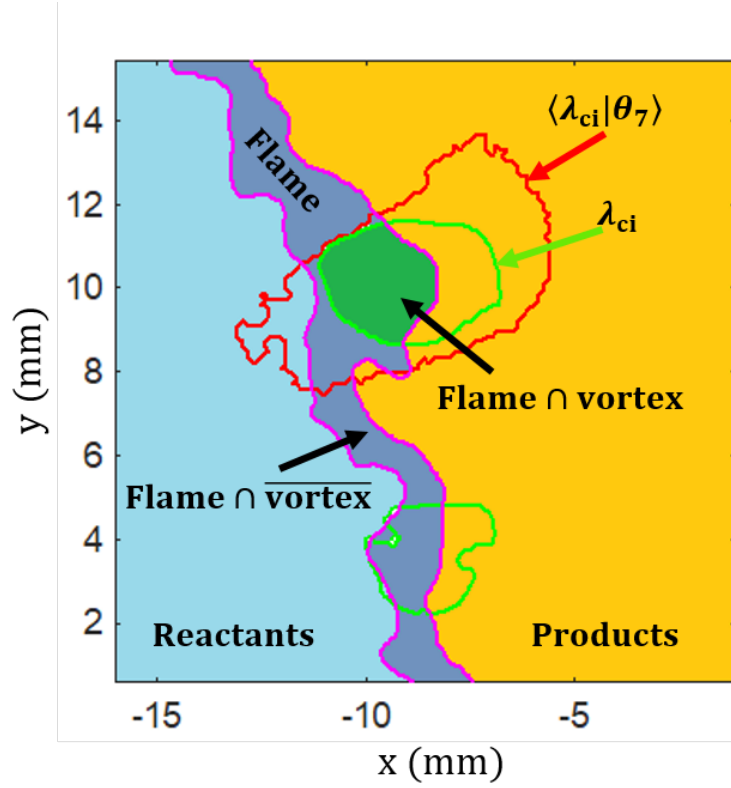


Figure 6.17: Schematic of the regions used for conditioning the phase-averaged statistics, taken from an instantaneous image at phase 7.

coherent structure on the energy dynamics is isolated, namely the periodic vortex identified from the POD (see Figure 3.12). To do so, the phase-averaged  $\lambda_{ci}$ ,  $\alpha_{sfs}$ , and  $c$  profiles generated using POD modes 1 and 2 in the reacting and non-reacting flows are examined.

Phase averaging is performed based on Equation 3.13, and further conditioning is done on specific spatial regions of interest. To demonstrate this, Figure 6.17 shows an instantaneous schematic of  $\lambda_{ci}$  and  $c$  in phase 7, showing the location of the phase-averaged vortex ( $\langle \lambda_{ci} | \theta_i \rangle$  - red contour), the location of the instantaneous vortex ( $\lambda_{ci}$  - green contour), and the region occupied by the flame ( $0 < c < 1$  - magenta contour). The size discrepancy between  $\lambda_{ci}$  and  $\langle \lambda_{ci} | \theta_7 \rangle$  is due to the strong turbulence in the flow that causes the periodic structure to fluctuate about its average position for each phase; these fluctuations grow with distance from the nozzle. Strong turbulence in the flow that makes the periodic structure fluctuate about its nominal position for each phase; these fluctuations are amplified with

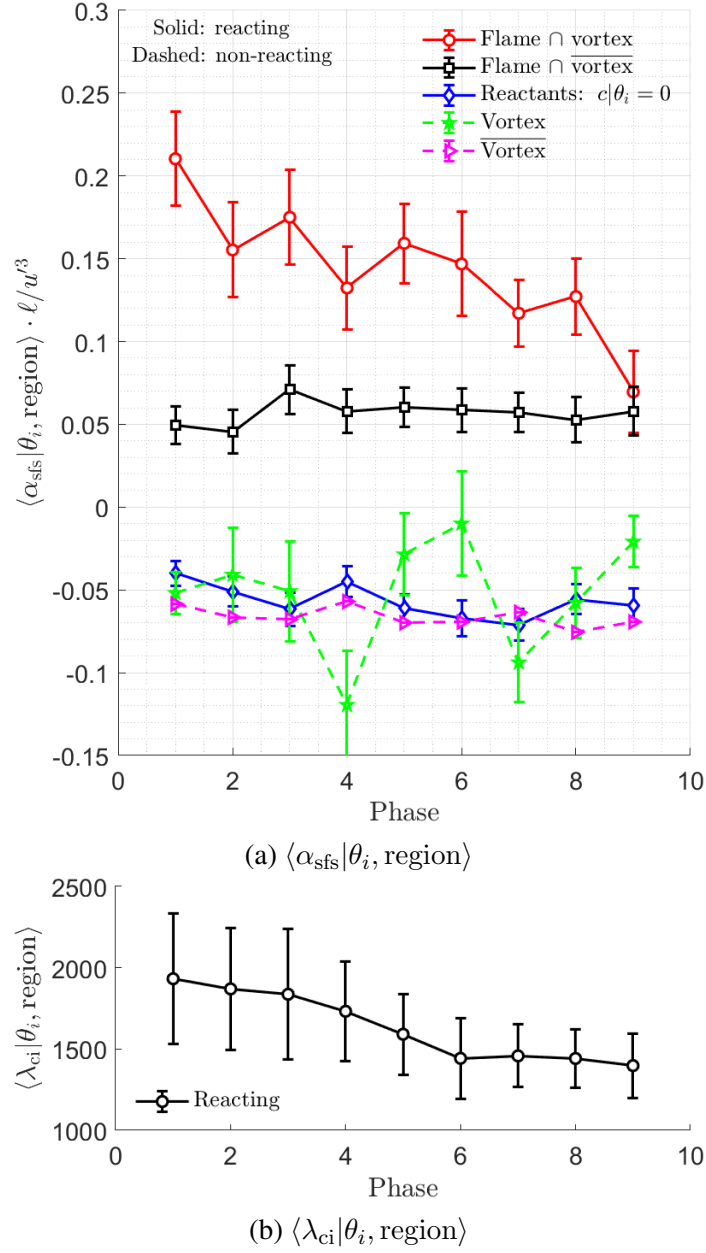


Figure 6.18: Phase-averaged statistics as a function of phase for the most dominant coherent structure in the reacting and non-reacting flows.

distance away from the nozzle. Figure 6.15(a) shows that instantaneous vortices are similar in size; however, in Equation 3.13 the size of the phase-averaged vortex grows with phase, suggesting that the trajectory of the coherent structure deviates more from its average path at later phases. The “flame  $\cap$  vortex” region (shaded green) represents the region where the flame,  $\lambda_{\text{ci}}$ , and  $\langle \lambda_{\text{ci}} | \theta_i \rangle$  intersect; the instantaneous vortex that lies outside the  $\langle \lambda_{\text{ci}} | \theta_i \rangle$  contour is not part of the periodic vortex and, hence, is not considered in this

analysis. The “flame  $\cap \overline{\text{vortex}}$ ” region (shaded purple) represents the locations inside the flame but external to the instantaneous vortex inside the  $\langle \lambda_{ci} | \theta_i \rangle$  contour. Also considered are regions “vortex” and “ $\overline{\text{vortex}}$ ”, which represent overlapping regions of  $\lambda_{ci}$  and  $\langle \lambda_{ci} | \theta_i \rangle$  and its complement set, respectively. Finally, the “reactants” region (shaded light blue) represents regions of  $c = 0$ . Data in the products (shaded orange) is not presented, as  $\alpha_{sfs}$  generally is low in this region due to the attenuated turbulence.

Figure 6.18(a) shows the phase-averaged  $\alpha_{sfs}$  in different regions of the flow as a function of phase. In the reactants and in the non-reacting flow,  $\langle \alpha_{sfs} | \theta_i \rangle$  is negative and no significant phase dependence is observed. For the non-reacting flow, the increased scatter for regions containing the periodic vortex likely is attributed to uncertainty and convergence. Broadly speaking, the non-reacting flow and non-reacting regions of the reacting flow both show mean forward-scatter across the filter scale.

The regions containing the flame show qualitative differences in  $\alpha_{sfs}$  compared to the non-reacting flows, with further qualitative differences between regions with and without the dominant periodic vortex. In the “flame  $\cap \overline{\text{vortex}}$ ” region,  $\langle \alpha_{sfs} | \theta_i, \text{flame} \cap \overline{\text{vortex}} \rangle$  is positive. This is consistent with our previous experimental findings [133] and other DNS studies [41, 68, 69], demonstrating that the flame leads to mean back-scatter at scales around the laminar flame thickness. Importantly, regions where the flame and periodic vortex intersect exhibit higher mean back-scatter compared to regions of the flame without the vortex present, i.e.  $\langle \alpha_{sfs} | \theta_i, \text{flame} \cap \text{vortex} \rangle > \langle \alpha_{sfs} | \theta_i, \text{flame} \cap \overline{\text{vortex}} \rangle$ .

The magnitude of  $\langle \alpha_{sfs} | \theta_i, \text{flame} \cap \text{vortex} \rangle$  decreases with phase. Figure 6.18(b) shows that the magnitude of the swirl, i.e.  $\langle \lambda_{ci} | \theta_i, \text{flame} \cap \text{vortex} \rangle$ , also decreases with phase as the vortex moves downstream. Hence, there is a correspondence between the swirling strength of the dominant periodic vortex and the mean back-scatter magnitude at locations of flame/vortex interaction. This result is consistent with the instantaneous data in Figure 6.16(b) and further articulates the simultaneous and complimentary effects of combustion and large-scale coherent vortices on kinetic energy back-scatter.

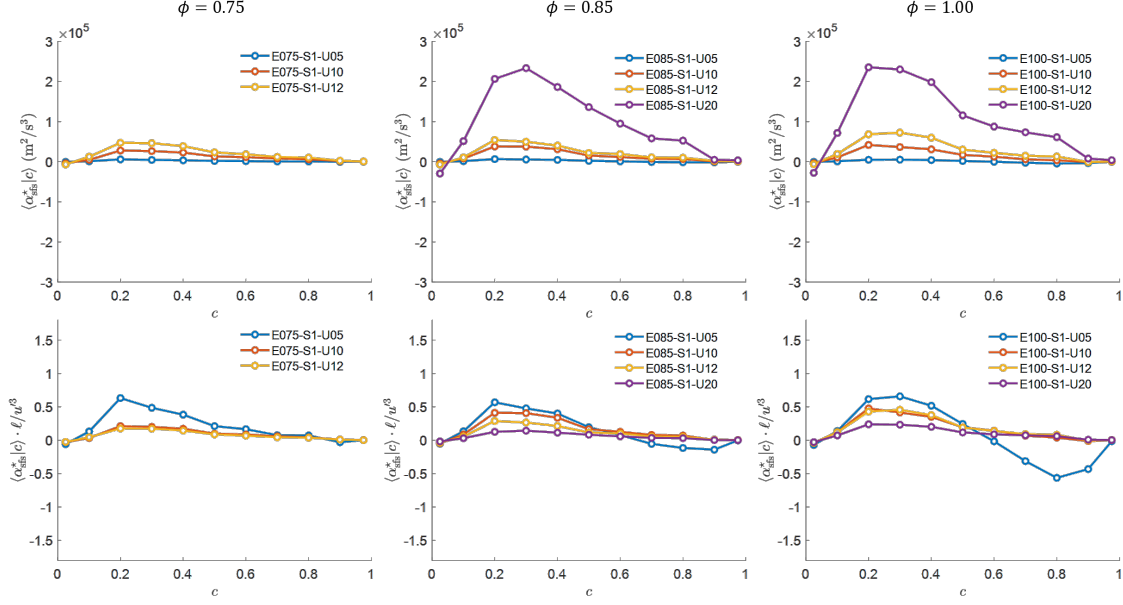


Figure 6.19: Variation of  $c$ -conditioned  $\alpha_{\text{sfs}}^*$  with  $U_j$  at  $\phi = 0.75, 0.85$ , and  $1.00$ ; swirl number fixed at  $\mathcal{S}_1$  and  $\alpha_{\text{sfs}}^*$  computed across  $\Delta = 1.1$  mm. Top row: non-normalized; bottom row: normalized by  $\ell/u^3$ .

## 6.5 Effects of swirl number, equivalence ratio, jet velocity, and mean pressure gradient

The results presented thus far have revealed the occurrence of mean kinetic energy backscatter internal to the flame structure, in agreement with DNS of statistically planar flames in HIT [41, 68, 69]. One of the objectives was to determine how energy backscatter is related to the three controlling parameters  $\mathcal{S}$ ,  $U_j$ , and  $\phi$ . In this section, variation of  $\alpha_{\text{sfs}}$  with individual controlling parameters is examined. This is done by varying one parameter and comparing  $\langle \alpha_{\text{sfs}} | c \rangle$  while keeping the other two parameters constant. For the analysis in this section, all results are computed using the scale-similarity approach outlined in Section 4.1; the results are presented for  $\alpha_{\text{sfs}}^*$ . This is to ensure consistent processing between all data sets used in the comparisons. For cases that were fully resolved, results using  $\alpha_{\text{sfs}}$  were compared to  $\alpha_{\text{sfs}}^*$  with negligible difference.

Figure 6.19 demonstrates the variation of mean  $c$ -conditioned  $\alpha_{\text{sfs}}^*$  with the jet flow velocity; normalized and non-normalized  $\langle \alpha_{\text{sfs}}^* | c \rangle$  plots at  $\phi = 0.75, 0.85$ , and  $1.00$  for swirler

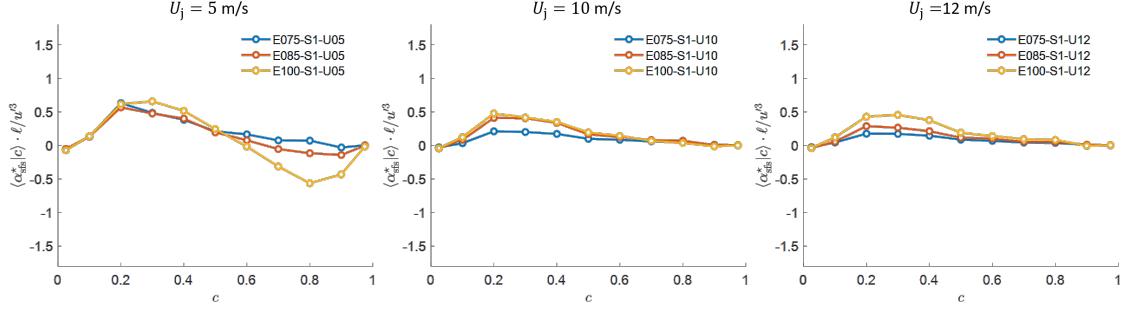


Figure 6.20: Variation of  $c$ -conditioned  $\alpha_{\text{sfs}}$  with  $\phi$  at  $U_j = 5, 10$ , and  $12$  m/s; swirl number fixed at  $S_1$  and  $\alpha_{\text{sfs}}$  computed across  $\Delta = 1.1$  mm.

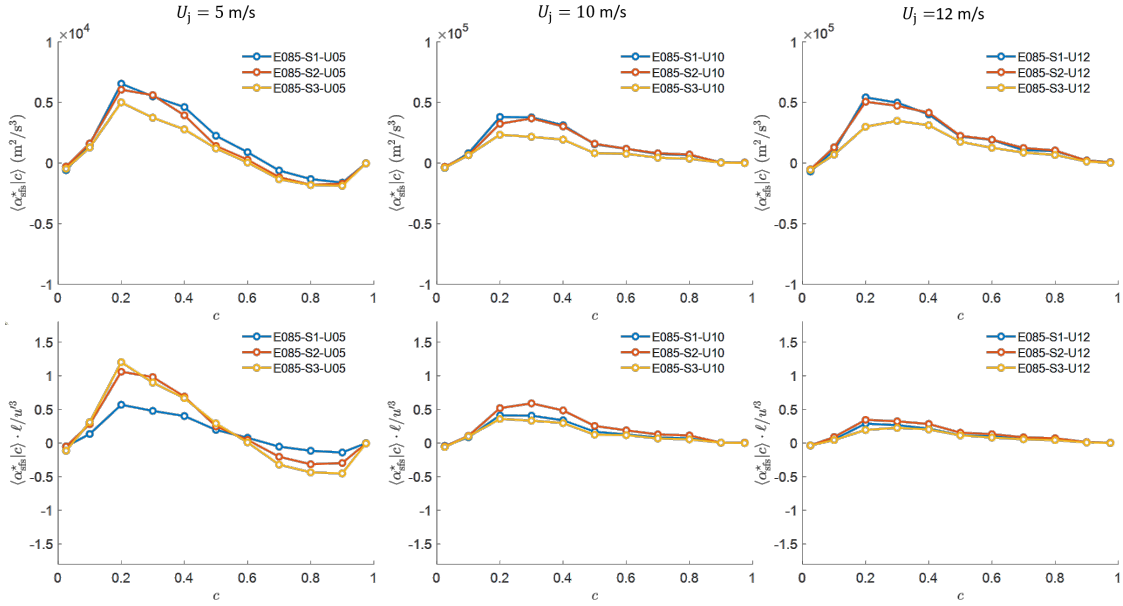


Figure 6.21: Variation of  $c$ -conditioned  $\alpha_{\text{sfs}}$  with  $S$  at  $U_j = 5, 10$ , and  $12$ ; equivalence ratio is fixed at  $0.85$  and  $\alpha_{\text{sfs}}$  computed across  $\Delta = 1.1$  mm. Top row: non-normalized; bottom row: normalized by  $\ell/u^3$ .

$S_1$  are shown. In general, the maximum magnitude of  $\langle \alpha_{\text{sfs}}^* | c \rangle$  increases with increasing  $U_j$  at all equivalence ratios. However, when normalized, the magnitude of  $\langle \alpha_{\text{sfs}}^* | c \rangle \cdot \ell/u^3$  decreases with  $U_j$ . Note that the normalization factor is the inverse of the rate at which turbulent kinetic energy is passed from large to small scales in constant-density non-reacting turbulent flow (i.e.  $\Pi \sim u'^3/\ell$ ). Hence, despite greater backscatter at larger  $U_j$ , the magnitude of backscatter relative to the expected turbulent kinetic energy input rate decreases. Increasing  $\phi$  slightly increased  $\alpha_{\text{sfs}}^*$  in general.

Figure 6.20 shows the variation of mean  $c$ -conditioned  $\alpha_{\text{sfs}}$  with  $\phi$  while keeping  $\mathcal{S}$  and  $U_j$  constant. Both, normalized and non-normalized plots are similar and only  $\langle \alpha_{\text{sfs}}^* | c \rangle \cdot \ell / u'^3$  is shown here. Although minimal, there is variation of  $\alpha_{\text{sfs}}$  with  $\phi$ ; increasing  $\phi$  tends to increase  $\langle \alpha_{\text{sfs}}^* | c \rangle \cdot \ell / u'^3$  slightly as mentioned above. Increasing  $\phi$  results in a larger density gradient and greater thermal expansion across the flame; this can serve as a means of redistributing turbulent kinetic energy.

Finally, the variation of  $\langle \alpha_{\text{sfs}}^* | c \rangle$  with the swirl number is demonstrated in Figure 6.21 while keeping  $U_j$  and  $\phi$  fixed. Interestingly, the magnitude of maximum  $\langle \alpha_{\text{sfs}}^* | c \rangle$  reduces with increasing  $\mathcal{S}$ ; no clear trend can be extracted from the normalized  $\alpha_{\text{sfs}}$  plots. However, since the flow rates were not identical across  $\mathcal{S}$  while maintaining  $U_j$  (mass flow rate was greater for  $\mathcal{S}_1$  than  $\mathcal{S}_2$  for the same  $U_j$ ), it is logical that the observed  $\langle \alpha_{\text{sfs}}^* | c \rangle$  is lower for larger  $\mathcal{S}$ . Moreover, the normalized profiles are increasingly similar at larger  $U_j$ , suggesting that the influence of the swirl number at larger  $U_j$  is decreased.

O'Brien *et al.* [68] suggest that the cause of back-scatter is ‘excess’ kinetic energy in the sub-filter-scales, created by SFS thermal-expansion in the form of  $\alpha_{\text{p}}^{\text{sfs}}$  (see Equation 1.28). It is noted that modification of the resolved-scale kinetic energy by inhomogeneous pressure fields occurs both directly through  $\alpha_{\text{p}} = \tilde{u}_i \frac{\partial \bar{P}}{\partial x_i}$  and indirectly through  $\alpha_{\text{p}}^{\text{sfs}} = \alpha_{\text{p}} - \overline{u_i \frac{\partial P}{\partial x_i}}$ ; the latter drives the kinetic energy back-scatter ( $\alpha_{\text{sfs}} > 0$ ) from SFS to resolved scales. In the flames of O'Brien *et al.* [68], approximately four times more resolved kinetic energy is produced via  $\alpha_{\text{p}}$  than by  $\alpha_{\text{sfs}}$  via  $\alpha_{\text{p}}^{\text{sfs}}$ .

The magnitude of the pressure gradient affects the magnitudes of  $\alpha_{\text{p}}$  and  $\alpha_{\text{p}}^{\text{sfs}}$ . For turbulent flames in HIT, the main sources of pressure gradients is due to thermal gas expansion across the flame  $\nabla p_{\text{f}} \propto \rho S_{\text{L}}^2 / \delta_{\text{L}}^0$  and due to Kolmogorov scale eddies  $\nabla p_{\eta} \propto \rho u_{\eta}^2 / \eta$ . In practical combustor geometries, there exist other sources of pressure gradients, including those induced by the large-scale flow and due to stochastic turbulent motions. If these pressure gradients are similar (or greater) in magnitude to those due to the flame, the kinetic energy dynamics induced by  $\alpha_{\text{p}}$  and  $\alpha_{\text{p}}^{\text{sfs}}$  could be significantly affected.

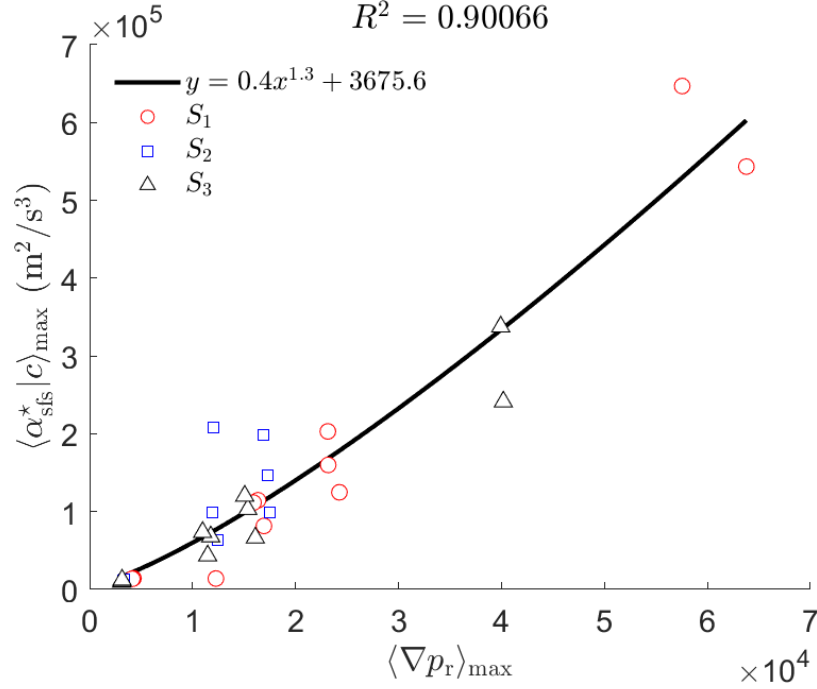


Figure 6.22: Scaling between maximum measured  $\langle \alpha_{\text{sfs}} | c \rangle$  and  $\langle \nabla p_r \rangle$ ;  $\Delta = 2.3$  mm.

Here, the mean radial pressure gradient induced by the swirling jet  $\langle \nabla p_r \rangle \propto \langle \rho \rangle \langle U_\theta \rangle^2 / R$  is considered, where  $R$  and  $U_\theta$  are the nozzle radius and bulk swirl velocity, respectively. To demonstrate whether  $\alpha_{\text{sfs}}$  depends on the magnitude of the mean pressure gradient induced by the swirling flow, maximum  $\langle \alpha_{\text{sfs}}^* | c \rangle$  from all test cases is plotted against the maximum mean pressure gradient  $\langle \nabla p_r \rangle$  on the central plane (see Figure 5.8); results are shown in Figure 6.22.

Clearly, increasing the magnitude of flow-induced pressure gradient correlates with increases in the magnitude of the energy backscatter. In fact, the power-law fit predicts that

$$\langle \alpha_{\text{sfs}}^* \rangle \propto \langle \nabla p_r \rangle^{1.3}, \quad (6.2)$$

with high confidence; the  $R^2$  goodness of fit is 0.9. Recall that the primary hypothesis was that presence of strong pressure gradients will result in larger small-scale pressure work (i.e.  $\frac{\partial \alpha_{\text{p}}^{\text{sfs}}}{\partial |\nabla \langle p \rangle|} > 0$ ). Although it was not possible to directly measure  $\alpha_{\text{p}}^{\text{sfs}}$ , it was shown that it has a direct effect on  $\alpha_{\text{sfs}}$  [68]. Hence, the trend in Figure 6.22 supports this hypothesis.



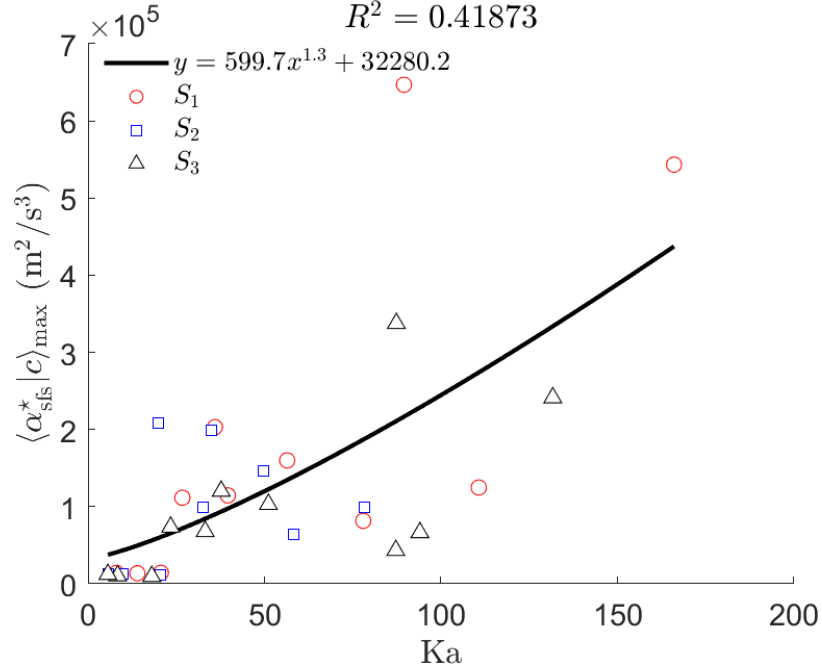


Figure 6.23: Scaling between maximum measured  $\langle \alpha_{\text{sfs}} | c \rangle$  and  $Ka$ ;  $\Delta = 2.3$  mm.

The main takeaway is that existence of pressure gradients due to sources other than the flame itself can have a significant impact on the magnitude of energy backscatter across the flame.

It can be shown that the ratio of the pressure gradients due to the swirl and gas-dynamic expansion scales as [57]

$$\frac{\nabla p_s}{\nabla p_f} \propto \frac{\rho U_\theta^2 / R}{\rho S_L^2 / \delta_L^0} \propto \frac{S^2}{1 + S^2} \frac{\ell}{R} \frac{S_L}{u'} Ka^2, \quad (6.3)$$

where we assume  $u' \propto U$ ,  $\ell = \text{const}$ , and  $S \propto U_\theta / U$ . For fixed combustor geometry ( $\ell$  and  $R$ ), Eq. (Equation 6.3) suggests that the significance of the swirl-induced pressure gradient is increased with  $S$  and  $Ka$ . At fixed turbulence and combustion conditions (i.e.  $S_L / u'$  and  $Ka$ ),  $\nabla p_f$  becomes decreasingly significant compared to  $\nabla p_s$  with increasing  $S$ . Exposure to a stronger pressure gradient is consequently expected to increase  $\alpha_p^{\text{sfs}}$ , which can lead to increased backscatter. However, further effort is required to verify the proposed scaling – and its impact on backscatter – through independent variations of  $S$  and  $Ka$ .

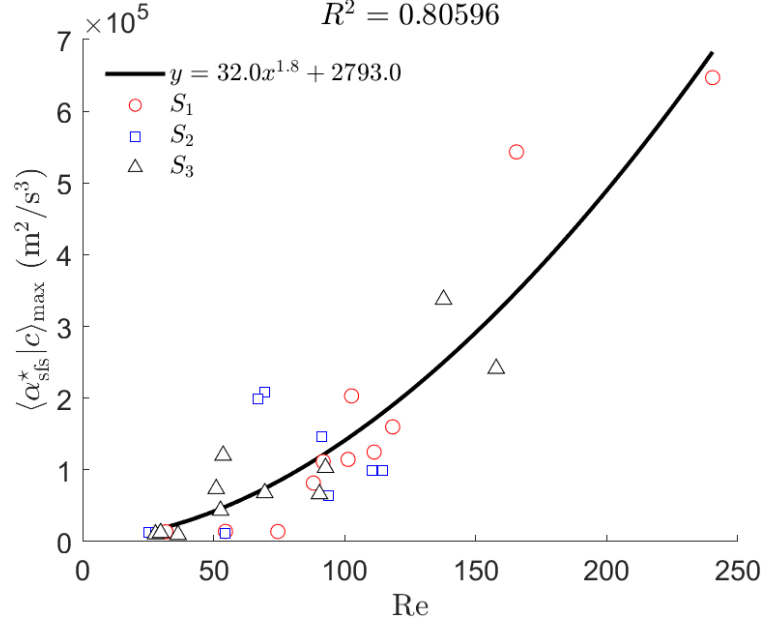


Figure 6.24: Scaling between maximum measured  $\langle \alpha_{\text{sfs}} | c \rangle$  and  $\text{Re}$ ;  $\Delta = 2.3$  mm.

Finally, the magnitude of backscatter is also expected to depend on the intensity of turbulence in the flow. A similar comparison to Figure 6.22 is performed between  $\langle \alpha_{\text{sfs}}^* | c \rangle$  and  $\text{Ka}$ , and between  $\langle \alpha_{\text{sfs}}^* | c \rangle$  and  $\text{Re}$ ; the scatter plots are shown in Figure 6.23 and Figure 6.24, respectively. In both cases, the magnitude of  $\langle \alpha_{\text{sfs}}^* | c \rangle_{\text{max}}$  increases with both  $\text{Ka}$  and  $\text{Re}$ . The power-law fits are

$$\langle \alpha_{\text{sfs}}^* \rangle \propto \text{Ka}^{1.3}, \quad (6.4)$$

$$\langle \alpha_{\text{sfs}}^* \rangle \propto \text{Re}^{1.8}, \quad (6.5)$$

although the goodness of fit for  $\text{Ka}$  scaling is relatively weak ( $R^2 < 0.5$ ), which leaves the relationship between  $\alpha_{\text{sfs}}$  and  $\text{Ka}$  inconclusive. The correlation between  $\langle \alpha_{\text{sfs}}^* | c \rangle_{\text{max}}$  and  $\text{Re}$  is strong and also indicates that more turbulent flames exhibit greater levels of energy backscatter. It should be noted that the Reynolds number and the magnitude of  $\langle \nabla p_r \rangle$  are related through  $U_j$  and hence are not independent in this study. Further work should decouple the flow-induced pressure gradients from the turbulence to study their effects on  $\alpha_{\text{sfs}}$  independently.

## CHAPTER 7

### CONCLUSIONS

The objective of this work was to experimentally measure  $\alpha_{\text{sfs}}$  and determine the relationship between the pressure field, turbulence conditions, heat-release rate, and inter-scale energy transfer in an aerospace-relevant configuration. This thesis has demonstrated the complex nature of inter-scale energy dynamics in a set of swirl-stabilized premixed flames. It was demonstrated that the swirl flows and swirl-stabilized flames induce large-scale pressure fields and generate large-scale coherent flow structures, both of which have a significant effect on the energy backscatter. The study has been performed experimentally; high-resolution velocity and density fields were measured using simultaneous TPIV and CH<sub>2</sub>O PLIF. The swirl number, jet velocity, and equivalence ratio were varied to control the magnitude of flow-induced pressure gradients, turbulence intensity, and magnitude of thermal expansion across the flame. The data acquired have allowed calculation of the kinetic energy transfer between SFS and resolved scales ( $\alpha_{\text{sfs}}$ ) under a wide range of operating conditions and in presence of naturally occurring coherent flow structures.

In cases when fully-resolved measurements were not available, the scale-similarity deconvolution method was applied to estimate the inter-scale energy transfer across the filter scales larger than the measurement scale (i.e.  $\alpha_{\text{sfs}}^*$  across  $\Delta_T > \Delta$ ). It was demonstrated that other common deconvolution methods give a similar result when  $\Delta_T \gtrsim 3\Delta$ . An attempt was also made towards identifying the shape of the filter kernel imposed by TPIV measurement; however, no conclusive shape was identified. Nevertheless, the sensitivity of  $\alpha_{\text{sfs}}^*$  to the measurement filter kernel was demonstrated to be negligible at larger  $\Delta_T/\Delta$ .

The inter-scale energy dynamics was predominantly analyzed in terms of PDFs and conditional statistics over a range of filter sizes around the laminar flame thickness. The main conclusions are summarized:

1. The non-reacting cases and non-reacting regions of the the reacting case (pure reactants and products) exhibited mean down-scale transfer of kinetic energy, i.e. forward-scatter, with nearly symmetric  $\alpha_{\text{sfs}}$  PDFs about  $\alpha_{\text{sfs}} = 0$ . This result further supports the classical phenomenologies of Richardson and Kolmogorov.
2. Mean kinetic energy backscatter occurs internal to the flame structure across the range of conditions studied here. The magnitude of the mean backscatter peaks towards the center of the flame structure ( $c \approx 0.5$ ). Mean forward-scatter did occur for  $c \lesssim 0.2$ .
3. Regardless of the local strain-rate and overall flow rate, combustion increased the mean  $\alpha_{\text{sfs}}$  compared to non-reacting cases with the same flow rates (which all exhibited mean forward-scatter).
4. The magnitude of the mean  $\alpha_{\text{sfs}}$ , normalized by the turbulence conditions, varied differently with operating conditions studied here, but remained positive (i.e. backscatter). This indicates that there are mechanisms that increase the SFS kinetic energy production via thermal expansion, and the consequent backscatter, that maintain their significance with increasing turbulence intensity in these swirl flames. A scaling was proposed to articulate the relative impact of swirl-induced pressure gradients compared to flame-induced pressure gradients, which generate the pressure-work source of kinetic energy.
5. The magnitude of mean backscatter generally increased with increasing  $\Delta$  over the range studied. This indicates that the flame significantly influences kinetic energy transfer across filter scales in the range of the laminar flame thickness, mean backscatter was observed at scales up to  $\Delta/\delta_L^0 = 4.7$  here.
6. The mean magnitude of the backscatter inside the flame was increased in regions of flame/vortex interaction, as demonstrated both through the instantaneous data and

statistics conditioned on the phase of the periodic vortex structure. Coherent structures were identified using the  $\lambda_{ci}$ -criterion and POD was performed on  $\lambda_{ci}$ -fields to isolate the most dominant periodic coherent vortex structure.

7. There was a correspondence between the magnitude of the local swirling strength and the mean backscatter magnitude. It is possible that the observed increased backscatter in regions of flame/vortex interaction is due to greater local heat release rates, though further measurements would be needed to confirm this.
8. Magnitude of maximum backscatter was observed to increase with the higher jet flow velocity, equivalence ratios close to 1, and decreasing swirl number. This demonstrates the complexity of inter-scale energy dynamics in a practical burner configuration and dependence on various operating parameters which need to be properly accounted for in LES of such configurations.
9. The maximum observed backscatter is positively correlated with the magnitude of flow-induced pressure gradient and  $Re$ . However, further work is required to independently evaluate the decouple the effects of turbulence and large-scale pressure gradients.

This study articulates the complicated influences of the flame and flow/flame interactions on turbulence dynamics around the flame scale, which should be considered in turbulence modeling. At this point, there is no clear analytical relationship between the global turbulent flame characteristics and energy backscatter. Such a relationship likely depends on specific conditions and configurations. Future LES studies using mixed models are encouraged to “turn off” backscatter to further articulate these effects.

The primary hypothesis that was stated was that the magnitude of energy backscatter will (i) increase with the magnitude of the persistent pressure gradient induced over the flame region by the large-scale fluid dynamics, (ii) will increase with magnitude of heat release across the flame, and (iii) decrease in larger  $Re_T$  flows. The results clearly demon-

strate that energy backscatter exists internal to the flame and that it depends on  $\phi$ ,  $U_j$ , and  $\mathcal{S}$ . The equivalence ratio, jet flow velocity, and swirl number served as proxy for the heat-release rate, the Reynolds number, and the magnitude of flow-induced pressure gradients, respectively.

Increasing equivalence ratio from lean ( $\phi < 1$ ) to stoichiometric ( $\phi = 1$ ) conditions resulted in larger  $\alpha_{\text{sfs}}$ . Since the rate of heat-release is maximum at stoichiometric conditions for  $\text{CH}_4$ -air flames, the observed trend supports the stated hypothesis. Changes in equivalence ratio have a direct effect on global flame characteristics, such as the rate of heat release, magnitude of thermal expansion, and adiabatic flame temperatures. For  $\text{CH}_4$ -air flames,  $\dot{q}$ ,  $T_{\text{ad}}$ , and flow divergence increases as the reactant mixture approaches stoichiometric conditions. Since the rate of energy production by mean shear at the large scales was held constant (i.e. same  $\text{Re}_T$ ) while varying  $\phi$ , greater heat-release rate at small length scales likely creates an imbalance in inter-scale energy transfer across scales on the order of laminar flame thickness.

Similarly, varying the rate of turbulent kinetic energy production at the large scales (via  $\text{Re}_T$ ) while maintaining  $\phi$  was shown to increase the magnitude of downscale energy cascade. In this work, variation of  $U_j$  changed both  $\text{Re}_T$  and  $\dot{q}$ ; hence the  $\alpha_{\text{sfs}}^*$  was normalized by expected forward energy cascade from measured  $u'$  and  $\ell$ . The results clearly demonstrate that normalized amount of energy backscatter is reduced as  $U_j$  is increased. Hence, the second part of the hypothesis is also supported by the results. Clearly, the ratio between the rate of turbulent kinetic energy production through mean shear to the rate of chemical energy release is an important parameter. Future studies should consider directly measuring these rates and correlating them to likelihood of observing backscatter.

Finally, presence of strong pressure-gradients due to large-scale flow features was demonstrated to have a non-negligible effect on observed  $\alpha_{\text{sfs}}$ , especially when compared to premixed flames in HIT. There was variation in  $c$ -conditioned  $\alpha_{\text{sfs}}$  profiles with  $\mathcal{S}$ ; however, the observed trends are a result of simultaneous variation in  $\mathcal{S}$  and  $U_j$ , as the two pa-

rameters could not be varied independently. Nevertheless, presence of large-scale mean pressure-gradient field was found to be positively correlated with larger backscatter values through a power-law relationship. In addition, regions of flame-vortex interactions were shown to have elevated rates of energy backscatter as opposed to regions with no coherent vortices. Pressure gradients associated with local swirling motion of the fluid internal to such coherent structures can contribute to the increased backscatter observed here. Hence, this thesis presents sufficient evidence to support the hypothesis that presence of strong pressure-gradients can lead to larger backscatter inside premixed  $\text{CH}_4$ -air flames.

The results presented herein are the first experimental measurements of inter-scale energy transfer in turbulent premixed flames to the author's knowledge. To accomplish this, state-of-the-art diagnostics were used to capture fully-resolved velocity fields. However,  $\alpha_{\text{sfs}}$  was directly computed only in moderately turbulent flows; deconvolution methods were used to approximate  $\alpha_{\text{sfs}}^*$  in such cases. While deconvolution is used in many fields of research, application of deconvolution on experimental velocity measurements is a fairly novel combination. As was demonstrated, different deconvolution methods can be used to compute  $u_i^*$  and  $\alpha_{\text{sfs}}^*$ ; however, there are large uncertainties associated with the estimate in presence of noise and when considering length scales similar to the those associated with the measurement, especially when computing quantities derived from  $u_i^*$ . In this thesis, scale-similarity method was shown to be the most cost-effective and one of more robust deconvolution methods; yet it was used in a fairly narrow range of scales ( $1 < \Delta_T/\delta_L^0 < 5$ ). While the considered deconvolution methods give good predictions in the absence of noise, the results were shown to be sensitive to noise in the data. Presence of noise in experimental data essentially prevented estimation of  $\alpha_{\text{sfs}}^*$  at test filter scales less than  $3\Delta$ . Further research should consider improving on deconvolution methods used here.

Additionally, the results presented herein rely on the assumptions used to approximate the density and progress variable fields from  $\text{CH}_2\text{O}$  fields. As was demonstrated, there is inherent uncertainty in the measurement of the progress variable that limits the size of the

$c$  bin when conditioning on progress variable is performed. The accuracy of  $c$ -bins can be estimated using the in-plane spatial resolution and laminar flame thickness; however this estimate is only reliable inside turbulent flames that have similar structure as laminar flames. In broadened turbulent flames or at sites of flame-vortex interactions, the structure of the flame is changed due to enhanced mixing. Using the same bin widths as in non-broadened flames can account for some uncertainty in  $c$  by representing larger portion of the flame; however, a more robust method of measuring  $c$  directly should be used if the variation across the flame is of interest. Further research should be done in quantifying the uncertainties associated with the estimate of progress variable in high  $Ka$  flames.

It is worth briefly discussing the effect of energy backscatter on the overall flame characteristics, such as the flame structure, flame speed, and local heat-release. The impact of backscatter on global flame behavior and characteristics is likely configuration and condition specific and this impact likely cannot be analytically answered. Moreover, the experimental measurements of the turbulent flame speed, flame structure, and other properties of turbulent flame already reflect the effect of the observed backscatter at the scales of the flame.

However, backscatter has a significant impact on the LES models, which rely on the knowledge of energy transfer mechanisms. As a result, it is important to consider what will be the effect of ignoring energy backscatter in turbulence closure models under reacting flow conditions. In the context of LES, the occurrence of backscatter can have a significant impact on the dynamics predicted by LES. For example, over-predicting dissipation in the subfilter scales reduces the predicted reaction rates and flame speed. Transferring energy upscale via backscatter will affect both the large-scale and small-scale turbulence and turbulence-flame interaction.

Overall, these experimental results provide additional evidence – complimentary to previous DNS – that LES closure methods that only predict SFS kinetic energy dissipation may not properly capture the flame-induced flow physics in conditions and configurations



that are relevant to practical devices. Indeed, the results indicate that  $\alpha_{\text{sfs}}$  is not solely determined by the flame and turbulence properties, but is influenced by the pressure field associated with the configuration being studied. Hence, the combined actions of the flame, turbulence, and swirling flow have a large impact on the turbulence dynamics in the swirl combustor studied here. Presented work was performed in a limited set of conditions. Specifically, the operating conditions across all test cases were at a fixed swirl number  $S < 0.65$  and moderate turbulence conditions ( $Ka < 120$ ). Future studies are also encouraged to explore other burner configurations to verify the results presented here and expand the range of operating conditions.

## 7.1 Future Work

In this work, important observations of energy backscatter and trends with controlling parameters were presented. While these results may provide meaningful insights for development of turbulence closure models for applications in turbulent reacting flows and understanding of energy dynamics in turbulent premixed flames, it also opens many potential research directions for future study.

Firstly, the equivalence ratio was used as a proxy for the heat-release rate. Future work should measure the rate of heat-release directly to verify the observed correlation between elevated energy backscatter and equivalence ratio. Moreover, direct measurements of  $\dot{q}$  would allow to compare rates of local heat release to those generated by classical turbulence production mechanisms. Such investigations could be enabled by advanced laser diagnostics that are becoming increasingly available today.

Secondly, further work is needed to investigate the mechanisms through which energy backscatter occurs. Such studies would require measurement of the terms in transport equations of both the filtered kinetic energy and sub-filter-scale kinetic energy equations. While this is possible using numerical simulations (i.e. DNS and LES), experimental measurements are more challenging since fully resolved velocity, pressure, and density fields must

be captured simultaneously.

Third, the mapping between the distribution of  $\text{CH}_2\text{O}$  and density and  $c$  can be improved by using alternative laser diagnostic techniques (ex. simultaneous  $\text{CH}_2\text{O}$  and OH PLIF or filtered Rayleigh scattering) to obtain quantitative measurements of  $c$  and  $\rho$ . Doing so will permit examination of finer variation of  $\alpha_{\text{sfs}}$  with  $c$ . Some advanced laser diagnostics, such as filtered Rayleigh scattering, are becoming more available and can enable direct measurement of temperature fields, from which other relevant thermodynamic parameters can be computed. Application of such diagnostics in conjunction with high-resolution TPIV can significantly improve the accuracy of the  $\alpha_{\text{sfs}}$  estimates.

Fourth, future work is also needed in improving the deconvolution methods as applied to experimental data. Common methods were considered here; however, the range of scales and parameters used was fairly narrow. Experimental data always contains noise and uncertainty, which must be accounted for when performing deconvolution as it can have significant effects on the results. Future studies should expand on the Improvement and development of new deconvolution methods, specifically for deconvolution of TPIV velocity fields would be invaluable for the experimental research in area of fluid mechanics and combustion.

Fifth, deconvolution methods applied to TPIV velocity measurements can benefit significantly if the TPIV filter kernel is known. While the attempt to identify such filter was made here, no conclusive shape was identified. Further work should use spatially resolved velocity fields from both DNS and experiments to identify the filter shape associated with TPIV. Moreover, further investigation is required to determine if the such filter kernel is sensitive to varying seeding density (i.e. representative of compressible and reacting flows).

Finally, further investigation is required into the effect mean energy backscatter has on the existing LES models. When possible, LES studies using mixed models that are able to “turn off” backscatter are encouraged to do so in order to further articulate these effects in reacting flows specifically. Lastly, such studies should investigate the parameter space

over which energy backscatter is expected to have a leading order impact on the large-scale dynamics of the flow in swirl-stabilized flames and other configurations.

# **Appendices**

## APPENDIX A

### SWIRL NUMBER CALCULATION FOR RADIAL SWIRLER

Swirl number is given by the ratio of azimuthal momentum flux over axial momentum flux

$$S = \frac{\int \rho u_{ax} u_{\theta} dA}{\int \rho u_{ax}^2 dA}, \quad (\text{A.1})$$

where  $u_{\theta}$  is the azimuthal velocity of the incoming flow from the channel and  $u_{ax}$  is axial velocity of the flow. Typically, the swirl number is evaluated over the nozzle cross-section; however, during the design of radial swirler, a cylindrical control surface is considered.

Figure A.1 shows a single radial channel intersecting the circular nozzle (represented by a section of a circle). The channel velocity  $u$  is assumed to be uniform across the channel width; radial and azimuthal components of velocity upon entering the nozzle are related to  $u$  via

$$u_{ax} = u_r = u \cos \theta, \quad (\text{A.2})$$

$$u_{\theta} = u \sin \theta, \quad (\text{A.3})$$

where  $\theta$  is the angle between the velocity of the channel flow and the radial vector at a given point in the entrance of the swirler. Since the flow enters the nozzle only through the radial channels, it can be assumed that  $u_{ax} = u_r$  due to conservation of mass.

An infinitesimal contribution to the swirl number per unit area is a function of angle  $\theta$ :

$$S(\theta) \propto \frac{\rho u_{ax} u_{\theta}}{\rho u_{ax}^2} = \frac{u_{\theta}}{u_{ax}} = \frac{u \sin \theta}{u \cos \theta} = \tan \theta. \quad (\text{A.4})$$

It is assumed that the swirl number can be represented by the momentum flux of a single

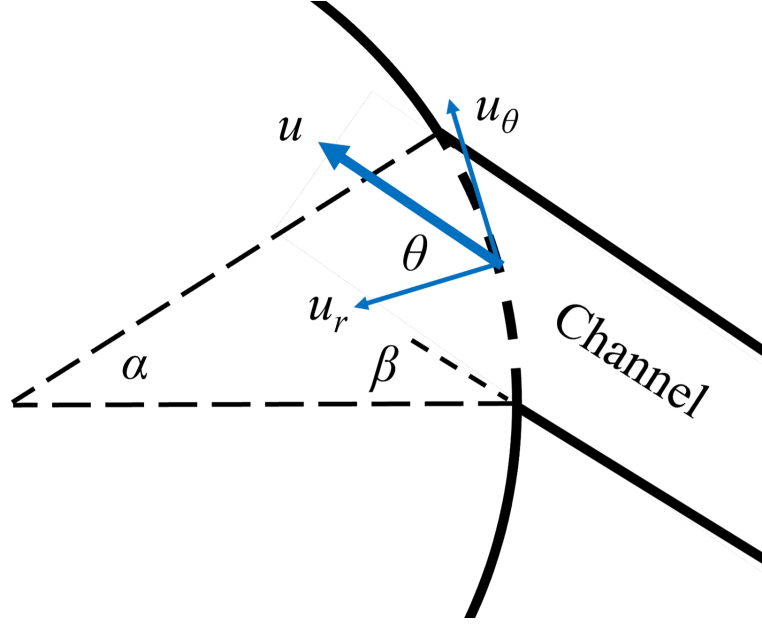


Figure A.1: Schematic of a singular channel in a swirler and relevant angles.

channel. Hence, the average swirl number can be computed across the channel as

$$S = \frac{1}{\alpha + \beta - \beta} \int_{\beta}^{\alpha + \beta} \tan \theta d\theta \quad (\text{A.5})$$

$$= \frac{1}{\alpha} \ln \left( \frac{\cos \beta}{\cos(\alpha + \beta)} \right), \quad (\text{A.6})$$

where integration is performed from  $\beta$  to  $\alpha + \beta$ , which represent the locations at which the channel walls intersect with the cylindrical nozzle wall. The actual swirl number is experimentally measured (see Section 5.1).

## REFERENCES

- [1] S. Turns, *An introduction to combustion: concepts and applications*. McGraw-Hill Education, 2011.
- [2] N. Swaminathan and K. N. C. Bray, *Turbulent premixed flames*, N. Swaminathan and K. N. C. Bray, Eds. Cambridge University Press, Apr. 2011, ISBN: 9780521769617.
- [3] C. Meneveau and J. Katz, “Scale-invariance and turbulence models for large-eddy simulation,” *Annual Review of Fluid Mechanics*, vol. 32, no. 1, pp. 1–32, Jan. 2000.
- [4] J. Driscoll, “Turbulent premixed combustion: flamelet structure and its effect on turbulent burning velocities,” *Progress in Energy and Combustion Science*, vol. 34, no. 1, pp. 91–134, Feb. 2008.
- [5] A. Steinberg, B. Coriton, and J. Frank, “Influence of combustion on principal strain-rate transport in turbulent premixed flames,” *Proceedings of the Combustion Institute*, vol. 35, no. 2, pp. 1287–1294, 2015.
- [6] B. Coriton and J. H. Frank, “Experimental study of vorticity-strain rate interaction in turbulent partially premixed jet flames using tomographic particle image velocimetry,” *Physics of Fluids*, vol. 28, no. 2, p. 025 109, Feb. 2016.
- [7] B. Coriton, A. M. Steinberg, and J. H. Frank, “High-speed tomographic PIV and OH PLIF measurements in turbulent reactive flows,” *Experiments in Fluids*, vol. 55, no. 6, p. 1743, Jun. 2014.
- [8] J. R. Osborne, S. A. Ramji, C. D. Carter, S. Peltier, S. Hammack, T. Lee, and A. M. Steinberg, “Simultaneous 10 kHz TPIV, OH PLIF, and CH<sub>2</sub>O PLIF measurements of turbulent flame structure and dynamics,” *Experiments in Fluids*, vol. 57, no. 5, p. 65, May 2016.
- [9] B. Bobbitt, S. Lapointe, and G. Blanquart, “Vorticity transformation in high Karlovitz number premixed flames,” *Physics of Fluids*, vol. 28, no. 1, p. 15 101, Jan. 2016.
- [10] B. Bobbitt and G. Blanquart, “Vorticity isotropy in high Karlovitz number premixed flames,” *Physics of Fluids*, vol. 28, no. 10, p. 105 101, Oct. 2016.
- [11] A. Steinberg, P. Hamlington, and X. Zhao, “Structure and dynamics of highly turbulent premixed combustion,” *Progress in Energy and Combustion Science*, vol. 85, p. 100 900, 2022.
- [12] P. Davidson, *Turbulence*. Oxford University Press, 2015, ISBN: 0198722591.

- [13] S. B. Pope, *Turbulent flows*. Cambridge University Press, 2000, ISBN: 0521598869.
- [14] L. F. Richardson, *Weather prediction by numerical process*. Cambridge University Press, 1922, ISBN: 0521680441.
- [15] H. Tennekes and J. Lumley, *A first course in turbulence*. The MIT Press, 1972.
- [16] J. Jiménez, A. A. Wray, P. G. Saffman, and R. S. Rogallo, “The structure of intense vorticity in isotropic turbulence,” *Journal of Fluid Mechanics*, vol. 255, no. -1, p. 65, Oct. 1993.
- [17] K. A. Buch and W. J. A. Dahm, “Experimental study of the fine-scale structure of conserved scalar mixing in turbulent shear flows. Part 2. Sc1,” *Journal of Fluid Mechanics*, vol. 364, pp. 1–29, Jun. 1998.
- [18] B. Ganapathisubramani, K. Lakshminarasimhan, and N. T. Clemens, “Investigation of three-dimensional structure of fine scales in a turbulent jet by using cinematographic stereoscopic particle image velocimetry,” *Journal of Fluid Mechanics*, vol. 598, pp. 141–175, Mar. 2008.
- [19] A. N. Kolmogorov, “The local structure of turbulence in incompressible viscous fluid for very large Reynolds numbers,” *Doklady Akademii Nauk SSSR*, vol. 30, no. 4, pp. 299–303, 1941.
- [20] S. G. Saddoughi and S. V. Veeravalli, “Local isotropy in turbulent boundary layers at high Reynolds number,” *Journal of Fluid Mechanics*, vol. 268, pp. 333–372, Jun. 1994.
- [21] A. N. Kolmogorov, “A refinement of previous hypotheses concerning the local structure of turbulence in a viscous incompressible fluid at high Reynolds number,” *Journal of Fluid Mechanics*, vol. 13, no. 1, pp. 82–85, May 1962.
- [22] C. K. Law, *Combustion physics*. Cambridge University Press, Sep. 2006, ISBN: 9780521870528.
- [23] N. Peters, *Turbulent combustion*. Cambridge University Press, Aug. 2000.
- [24] T. Poinso and D. Veynante, *Theoretical and numerical combustion*, 3rd ed. Bordeaux: Aquaprint, 2005.
- [25] Y. Zhou, “Degrees of locality of energy transfer in the inertial range,” *Physics of Fluids A: Fluid Dynamics*, vol. 5, no. 5, pp. 1092–1094, May 1993.



- [26] J. G. Brasseur and C.-H. Wei, “Interscale dynamics and local isotropy in high Reynolds number turbulence within triadic interactions,” *Physics of Fluids*, vol. 6, no. 2, pp. 842–870, Feb. 1994.
- [27] J. A. Domaradzki and D. Carati, “An analysis of the energy transfer and the locality of nonlinear interactions in turbulence,” *Physics of Fluids*, vol. 19, no. 8, p. 85 112, Aug. 2007.
- [28] J. I. Cardesa, A. Vela-Martín, S. Dong, and J. Jiménez, “The temporal evolution of the energy flux across scales in homogeneous turbulence,” *Physics of Fluids*, vol. 27, no. 11, p. 111 702, Nov. 2015.
- [29] F. Williams, “Criteria for existence of wrinkled laminar flame structure of turbulent premixed flames,” *Combustion and Flame*, vol. 26, pp. 269–270, Feb. 1976.
- [30] R. Borghi, “On the structure and morphology of turbulent premixed flames,” in *Recent Advances in the Aerospace Sciences*, Boston, MA: Springer US, 1985, pp. 117–138.
- [31] B. Zhou, C. Brackmann, Q. Li, Z. Wang, P. Petersson, Z. Li, M. Aldén, and X.-s. Bai, “Distributed reactions in highly turbulent premixed methane/air flames,” *Combustion and Flame*, vol. 162, no. 7, pp. 2937–2953, Jul. 2015.
- [32] A. M. Klimov, “Laminar flame in a turbulent flow,” *Prikladnoy Mekhaniki i Tekhnicheskoy Fiziki Zhurnal*, vol. 3, 1963.
- [33] A. M. Steinberg and J. F. Driscoll, “Straining and wrinkling processes during turbulence–premixed flame interaction measured using temporally-resolved diagnostics,” *Combustion and Flame*, vol. 156, no. 12, pp. 2285–2306, Dec. 2009.
- [34] A. N. Lipatnikov and J. Chomiak, “Molecular transport effects on turbulent flame propagation and structure,” *Progress in Energy and Combustion Science*, vol. 31, no. 1, pp. 1–73, Jan. 2005.
- [35] A. N. Lipatnikov, V. A. Sabelnikov, S. Nishiki, and T. Hasegawa, “Letter: Does flame-generated vorticity increase turbulent burning velocity?” *Physics of Fluids*, vol. 30, no. 8, p. 81 702, Aug. 2018.
- [36] T. M. Wabel, A. W. Skiba, J. E. Temme, and J. F. Driscoll, “Measurements to determine the regimes of premixed flames in extreme turbulence,” *Proceedings of the Combustion Institute*, vol. 36, no. 2, pp. 1809–1816, 2017.
- [37] T. M. Wabel, A. W. Skiba, and J. F. Driscoll, “Evolution of turbulence through a broadened preheat zone in a premixed piloted Bunsen flame from conditionally-

- averaged velocity measurements,” *Combustion and Flame*, vol. 188, pp. 13–27, Feb. 2018.
- [38] E. Mallard and H. L. Le Chatelier, “Recherches experimentales et theoriques sur la combustion des melanges gazeux explosifs,” *Annals of Mines*, vol. 8, no. 4, pp. 274–568, 1883.
  - [39] A. N. Lipatnikov and J. Chomiak, “Effects of premixed flames on turbulence and turbulent scalar transport,” *Progress in Energy and Combustion Science*, vol. 36, no. 1, pp. 1–102, Feb. 2010.
  - [40] A. Lipatnikov, *Fundamentals of premixed turbulent combustion*. CRC Press, 2012.
  - [41] C. A. Z. Towery, A. Y. Poludnenko, J. Urzay, J. OBrien, M. Ihme, and P. E. Hamlington, “Spectral kinetic energy transfer in turbulent premixed reacting flows,” *Physical Review E*, vol. 93, no. 5, May 2016.
  - [42] H. Kolla, E. R. Hawkes, A. R. Kerstein, N. Swaminathan, and J. H. Chen, “On velocity and reactive scalar spectra in turbulent premixed flames,” *Journal of Fluid Mechanics*, vol. 754, pp. 456–487, Aug. 2014.
  - [43] H. Kolla, X.-Y. Zhao, J. H. Chen, and N. Swaminathan, “Velocity and reactive scalar dissipation spectra in turbulent premixed flames,” *Combustion Science and Technology*, vol. 188, no. 9, pp. 1424–1439, Jun. 2016.
  - [44] S. H. R. Whitman, C. A. Z. Towery, A. Y. Poludnenko, and P. E. Hamlington, “Scaling and collapse of conditional velocity structure functions in turbulent premixed flames,” *Proceedings of the Combustion Institute*, vol. 37, no. 2, pp. 2527–2535, 2019.
  - [45] V. A. Sabelnikov, A. N. Lipatnikov, S. Nishiki, and T. Hasegawa, “Application of conditioned structure functions to exploring influence of premixed combustion on two-point turbulence statistics,” *Proceedings of the Combustion Institute*, vol. 37, no. 2, pp. 2433–2441, 2019.
  - [46] V. A. Sabelnikov, A. N. Lipatnikov, S. Nishiki, and T. Hasegawa, “Investigation of the influence of combustion-induced thermal expansion on two-point turbulence statistics using conditioned structure functions,” *Journal of Fluid Mechanics*, vol. 867, pp. 45–76, Mar. 2019.
  - [47] J. F. MacArt, T. Grenga, and M. E. Mueller, “Effects of combustion heat release on velocity and scalar statistics in turbulent premixed jet flames at low and high Karlovitz numbers,” *Combust. Flame*, vol. 191, pp. 468–485, May 2018.

- [48] ———, “Evolution of flame-conditioned velocity statistics in turbulent premixed jet flames at low and high Karlovitz numbers,” *Proceedings of the Combustion Institute*, vol. 37, no. 2, pp. 2503–2510, 2019.
- [49] P. H. Renard, D. Thévenin, J. C. Rolon, and S. Candel, “Dynamics of flame/vortex interactions,” *Progress in Energy and Combustion Science*, vol. 26, no. 3, pp. 225–282, Jun. 2000.
- [50] P. E. Hamlington, A. Y. Poludnenko, and E. S. Oran, “Interactions between turbulence and flames in premixed reacting flows,” *Physics of Fluids*, vol. 23, no. 12, p. 125 111, Dec. 2011.
- [51] N. Chakraborty, I. Konstantinou, and A. Lipatnikov, “Effects of Lewis number on vorticity and enstrophy transport in turbulent premixed flames,” *Physics of Fluids*, vol. 28, no. 1, p. 15 109, Jan. 2016.
- [52] V. Papapostolou, D. H. Wacks, N. Chakraborty, M. Klein, and H. G. Im, “Enstrophy transport conditional on local flow topologies in different regimes of premixed turbulent combustion,” *Scientific Reports*, vol. 7, no. 1, Sep. 2017.
- [53] A. N. Lipatnikov, V. A. Sabelnikov, S. Nishiki, and T. Hasegawa, “A direct numerical simulation study of the influence of flame-generated vorticity on reaction-zone-surface area in weakly turbulent premixed combustion,” *Physics of Fluids*, vol. 31, no. 5, p. 55 101, May 2019.
- [54] M. K. Geikie, Z. R. Carr, K. A. Ahmed, and D. J. Forliti, “On the flame-generated vorticity dynamics of bluff-body-stabilized premixed flames,” *Flow, Turbulence and Combustion*, vol. 99, no. 2, pp. 487–509, Jun. 2017.
- [55] M. K. Geikie and K. A. Ahmed, “Pressure-gradient tailoring effects on the turbulent flame-vortex dynamics of bluff-body premixed flames,” *Combustion and Flame*, vol. 197, pp. 227–242, Nov. 2018.
- [56] A. Kazbekov, K. Kumashiro, and A. Steinberg, “Enstrophy transport in swirl combustion,” *Journal of Fluid Mechanics*, vol. 876, 2019.
- [57] A. Kazbekov and A. Steinberg, “Flame- and flow-conditioned vorticity transport in premixed swirl combustion,” *Proceedings of the Combustion Institute*, vol. 38, no. 2, pp. 2949–2956, 2021.
- [58] A. Leonard, “Energy cascade in large-eddy simulations of turbulent fluid flows,” *Advances in Geophysics*, vol. 18, no. PA, pp. 237–248, Jan. 1975.
- [59] F. Katopodes, R. Street, and J. Ferziger, “A theory for the subfilter-scale model in large-eddy simulation,” Stanford, Tech. Rep., Jun. 2001.

- [60] J. Smagorinsky, “General circulation experiments with the primitive equations,” *Monthly Weather Review*, vol. 91, no. 3, pp. 99–164, 1963.
- [61] Z. M. Nikolaou, Y. Minamoto, and L. Vervisch, “Unresolved stress tensor modeling in turbulent premixed V-flames using iterative deconvolution: An a priori assessment,” *Physical Review Fluids*, vol. 4, no. 6, Jun. 2019.
- [62] J. Bardina, J. Ferziger, and W. Reynolds, “Improved turbulence models based on large eddy simulation of homogeneous, incompressible, turbulent flows,” Stanford University, Stanford, Tech. Rep., May 1983.
- [63] M. Germano, U. Piomelli, P. Moin, and W. H. Cabot, “A dynamic subgrid-scale eddy viscosity model,” *Physics of Fluids A: Fluid Dynamics*, vol. 3, no. 7, pp. 1760–1765, Jul. 1991.
- [64] P. Moin, K. Squires, W. Cabot, and S. Lee, “A dynamic subgrid-scale model for compressible turbulence and scalar transport,” *Physics of Fluids A: Fluid Dynamics*, vol. 3, no. 11, pp. 2746–2757, Nov. 1991.
- [65] S. Liu, C. Meneveau, and J. Katz, “On the properties of similarity subgrid-scale models as deduced from measurements in a turbulent jet,” *Journal of Fluid Mechanics*, vol. 275, Sep. 1994.
- [66] C. G. Speziale, “Galilean invariance of subgrid-scale stress models in the large-eddy simulation of turbulence,” *Journal of Fluid Mechanics*, vol. 156, no. 1, p. 55, Jul. 1985.
- [67] J. O’Brien, J. Urzay, M. Ihme, P. Moin, and A. Saghaffian, “Subgrid-scale backscatter in reacting and inert supersonic hydrogenair turbulent mixing layers,” *Journal of Fluid Mechanics*, vol. 743, pp. 554–584, Mar. 2014.
- [68] J. O’Brien, C. A. Towery, P. E. Hamlington, M. Ihme, A. Y. Poludnenko, and J. Urzay, “The cross-scale physical-space transfer of kinetic energy in turbulent premixed flames,” *Proceedings of the Combustion Institute*, vol. 36, no. 2, pp. 1967–1975, Jan. 2017.
- [69] J. Kim, M. Bassenne, C. A. Z. Towery, P. E. Hamlington, A. Y. Poludnenko, and J. Urzay, “Spatially localized multi-scale energy transfer in turbulent premixed combustion,” *Journal of Fluid Mechanics*, vol. 848, pp. 78–116, Jun. 2018.
- [70] F. Kaufman, “Chemical kinetics and combustion: intricate paths and simple steps,” *Symposium (International) on Combustion*, vol. 19, no. 1, pp. 1–10, Jan. 1982.

- [71] W. Meier, P. Weigand, X. Duan, and R. Giezen-danner-Thoben, “Detailed characterization of the dynamics of thermoacoustic pulsations in a lean premixed swirl flame,” *Combustion and Flame*, vol. 150, no. 1-2, pp. 2–26, Jul. 2007.
- [72] N. Syred, “A review of oscillation mechanisms and the role of the precessing vortex core (PVC) in swirl combustion systems,” *Progress in Energy and Combustion Science*, vol. 32, no. 2, pp. 93–161, Jan. 2006.
- [73] N. Syred and J. Beér, “Combustion in swirling flows: a review,” *Combustion and Flame*, vol. 23, no. 2, pp. 143–201, Oct. 1974.
- [74] Q. Wang and M. Ihme, “A regularized deconvolution method for turbulent closure modeling in implicitly filtered large-eddy simulation,” *Combustion and Flame*, vol. 204, pp. 341–355, Jun. 2019.
- [75] A. Kazbekov, *Enstrophy transport in premixed swirl flames*, Toronto, 2018.
- [76] Y. Huang and V. Yang, “Dynamics and stability of lean-premixed swirl-stabilized combustion,” *Progress in Energy and Combustion Science*, vol. 35, no. 4, pp. 293–364, Aug. 2009.
- [77] S. Candel, D. Durox, T. Schuller, J.-F. Bourgouin, and J. P. Moeck, “Dynamics of swirling flames,” *Annual Review of Fluid Mechanics*, vol. 46, no. 1, pp. 147–173, Jan. 2014.
- [78] M. Raffel, C. E. Willert, F. Scarano, C. J. Kähler, S. T. Wereley, and J. Kompenhans, *Particle image velocimetry*. Cham: Springer International Publishing, 2018, ISBN: 978-3-319-68851-0.
- [79] J. Westerweel, G. E. Elsinga, and R. J. Adrian, “Particle image velocimetry for complex and turbulent flows,” *Annual Review of Fluid Mechanics*, vol. 45, no. 1, pp. 409–436, Jan. 2013.
- [80] R. J. Adrian, “Twenty years of particle image velocimetry,” *Experiments in Fluids*, vol. 39, no. 2, pp. 159–169, Aug. 2005.
- [81] G. E. Elsinga, F. Scarano, B. Wieneke, and B. W. van Oudheusden, “Tomographic particle image velocimetry,” *Experiments in Fluids*, vol. 41, no. 6, pp. 933–947, Dec. 2006.
- [82] G. E. Elsinga and B. Ganapathisubramani, “Advances in 3D velocimetry,” *Measurement Science and Technology*, vol. 24, no. 2, p. 020 301, Feb. 2013.
- [83] F. Scarano, “Tomographic PIV: principles and practice,” *Measurement Science and Technology*, vol. 24, no. 1, p. 012 001, Jan. 2013.

- [84] R. A. Humble, G. E. Elsinga, F. Scarano, and B. W. van Oudheusden, “Three-dimensional instantaneous structure of a shock wave/turbulent boundary layer interaction,” *Journal of Fluid Mechanics*, vol. 622, pp. 33–62, Mar. 2009.
- [85] F. Scarano and C. Poelma, “Three-dimensional vorticity patterns of cylinder wakes,” *Experiments in Fluids*, vol. 47, no. 1, p. 69, Jul. 2009.
- [86] D. Violato and F. Scarano, “Three-dimensional evolution of flow structures in transitional circular and chevron jets,” *Physics of Fluids*, vol. 23, no. 12, p. 124 104, Dec. 2011.
- [87] J. Weinkauff, D. Michaelis, A. Dreizler, and B. Böhm, “Tomographic PIV measurements in a turbulent lifted jet flame,” *Experiments in Fluids*, vol. 54, no. 12, p. 1624, Dec. 2013.
- [88] O. R. H. Buxton, S. Laizet, and B. Ganapathisubramani, “The effects of resolution and noise on kinematic features of fine-scale turbulence,” *Experiments in Fluids*, vol. 51, no. 5, pp. 1417–1437, Nov. 2011.
- [89] N. A. Worth, T. B. Nickels, and N. Swaminathan, “A tomographic PIV resolution study based on homogeneous isotropic turbulence DNS data,” *Experiments in Fluids*, vol. 49, no. 3, pp. 637–656, Sep. 2010.
- [90] J. G. Santiago, S. T. Wereley, C. D. Meinhart, D. J. Beebe, and R. J. Adrian, “A particle image velocimetry system for microfluidics,” *Experiments in Fluids*, vol. 25, no. 4, pp. 316–319, Sep. 1998.
- [91] C. Eichler and T. Sattelmayer, “Premixed flame flashback in wall boundary layers studied by long-distance micro-PIV,” *Experiments in Fluids*, vol. 52, no. 2, pp. 347–360, Feb. 2012.
- [92] C. Tropea, A. Yarin, and F. John, *Springer handbook of experimental fluid mechanics*. Springer-Verlag GmbH, 2016, ISBN: 3662491621.
- [93] LaVision Inc, *Flowmaster tomographic PIV*, Gottingen.
- [94] B. Wieneke, “Volume self-calibration for 3D particle image velocimetry,” *Experiments in Fluids*, vol. 45, no. 4, pp. 549–556, Oct. 2008.
- [95] A. C. Eckbreth, *Laser diagnostics for combustion temperature and species*, 2nd. London: Taylor & Francis, 1996.
- [96] H. N. Najm, O. M. Knio, P. H. Paul, and P. S. Wyckoff, “A study of flame observables in premixed methane - air flames,” *Combustion Science and Technology*, vol. 140, no. 1-6, pp. 369–403, Dec. 1998.

- [97] T. M. Wabel, P. Zhang, X. Zhao, H. Wang, E. Hawkes, and A. M. Steinberg, “Assessment of chemical scalars for heat release rate measurement in highly turbulent premixed combustion including experimental factors,” *Combustion and Flame*, vol. 194, pp. 485–506, 2018.
- [98] C. Dem, M. Stöhr, C. M. Arndt, A. M. Steinberg, and W. Meier, “Experimental study of turbulence-chemistry interactions in perfectly and partially premixed confined swirl flames,” *Zeitschrift für Physikalische Chemie*, no. 4, pp. 569–595, 2014.
- [99] *Semrock 2017 master catalog*, 2017.
- [100] J. Hunt, A. Wray, and P. Moin, “Eddies, streams, and convergence zones in turbulent flows,” in *Center for Turbulence Research Report CTR-S88*, 1988, pp. 193–208.
- [101] J. Jeong and F. Hussain, “On the identification of a vortex,” *Journal of Fluid Mechanics*, vol. 285, pp. 69–94, Feb. 1995.
- [102] M. S. Chong, A. E. Perry, and B. J. Cantwell, “A general classification of three-dimensional flow fields,” *Physics of Fluids A: Fluid Dynamics*, vol. 2, no. 5, pp. 765–777, May 1990.
- [103] V. Kolář, “Vortex identification: new requirements and limitations,” *International Journal of Heat and Fluid Flow*, vol. 28, no. 4, pp. 638–652, Aug. 2007.
- [104] V. Kolár, “Compressibility effect in vortex identification,” *AIAA Journal*, vol. 47, no. 2, Feb. 2009.
- [105] J. Zhong, T. Huang, and R. Adrian, “Extracting 3D vortices in turbulent fluid flow,” *IEEE Transactions on Pattern Analysis and Machine Intelligence*, vol. 20, no. 2, 1998.
- [106] L. Sirovich, “Turbulence and the dynamics of coherent structures. I. Coherent structures,” *Quarterly of Applied Mathematics*, vol. 45, no. 3, pp. 561–571, 1987.
- [107] J. L. Lumley, *Stochastic tools in turbulence*. Academic Press, 1970.
- [108] K. Taira, S. L. Brunton, S. T. M. Dawson, C. W. Rowley, T. Colonius, B. J. McKeon, O. T. Schmidt, S. Gordeyev, V. Theofilis, and L. S. Ukeiley, “Modal analysis of fluid flows: an overview,” *AIAA Journal*, vol. 55, no. 12, pp. 4013–4041, Dec. 2017.
- [109] S. Depardon, J. J. Lasserre, L. E. Brizzi, and J. Borée, “Automated topology classification method for instantaneous velocity fields,” *Experiments in Fluids*, vol. 42, no. 5, pp. 697–710, Apr. 2007.

- [110] P. Gilge, J. R. Seume, and K. Mulleners, “Experimental analysis of multiscale vortex shedding in turbulent turbomachine blade wakes,” *AIAA Journal*, vol. 58, no. 12, pp. 5183–5190, Dec. 2020.
- [111] B. W. v. Oudheusden, F. Scarano, N. P. v. Hinsberg, and D. W. Watt, “Phase-resolved characterization of vortex shedding in the near wake of a square-section cylinder at incidence,” *Experiments in Fluids*, vol. 39, no. 1, pp. 86–98, Jul. 2005.
- [112] R. Perrin, M. Braza, E. Cid, S. Cazin, A. Barthet, A. Sevrain, C. Mockett, and F. Thiele, “Obtaining phase averaged turbulence properties in the near wake of a circular cylinder at high Reynolds number using POD,” *Experiments in Fluids*, vol. 43, no. 2-3, pp. 341–355, Aug. 2007.
- [113] M. Legrand, J. Nogueira, and A. Lecuona, “Flow temporal reconstruction from non-time-resolved data part I: mathematic fundamentals,” *Experiments in Fluids*, vol. 51, no. 4, pp. 1047–1055, Oct. 2011.
- [114] A. Steinberg, C. Arndt, and W. Meier, “Parametric study of vortex structures and their dynamics in swirl-stabilized combustion,” *Proceedings of the Combustion Institute*, vol. 34, no. 2, pp. 3117–3125, Jan. 2013.
- [115] M. Tsurikov and N. Clemens, “The structure of dissipative scales in axisymmetric turbulent gas-phase jets,” in *40th AIAA Aerospace Sciences Meeting & Exhibit*, Reston, Virgina: American Institute of Aeronautics and Astronautics, Jan. 2002.
- [116] Friehe C., C. W. Atta, and C. Gibson, “Jet turbulence dissipation rate measurements and correlations,” in *Physics*, Aug. 1971.
- [117] T. E. Gureyev, Y. I. Nesterets, A. W. Stevenson, and S. W. Wilkins, “A method for local deconvolution,” *Applied Optics*, vol. 42, no. 32, p. 6488, Nov. 2003.
- [118] M. Germano, “Differential filters of elliptic type,” *Physics of Fluids*, vol. 29, no. 6, p. 1757, 1986.
- [119] W. J. Layton and L. Rebholz, *Approximate deconvolution models of turbulence*. Springer Berlin Heidelberg, 2012.
- [120] N. Wiener, *Extrapolation, interpolation, and smoothing of stationary time series*. The MIT Press, 1949, ISBN: 9780262257190.
- [121] P. Domingo and L. Vervisch, “Large eddy simulation of premixed turbulent combustion using approximate deconvolution and explicit flame filtering,” *Proceedings of the Combustion Institute*, vol. 35, no. 2, pp. 1349–1357, 2015.



- [122] V. Moureau, P. Domingo, and L. Vervisch, "From large-eddy simulation to direct numerical simulation of a lean premixed swirl flame: filtered laminar flame-PDF modeling," *Combustion and Flame*, vol. 158, no. 7, pp. 1340–1357, Jul. 2011.
- [123] Q. Wang and M. Ihme, "Regularized deconvolution method for turbulent combustion modeling," *Combustion and Flame*, vol. 176, pp. 125–142, Feb. 2017.
- [124] J. Bardina, J. Ferziger, and W. Reynolds, "Improved subgrid-scale models for large-eddy simulation," in *13th Fluid and Plasma Dynamics Conference*, American Institute of Aeronautics and Astronautics, Jul. 1980.
- [125] S. Stolz and N. A. Adams, "An approximate deconvolution procedure for large-eddy simulation," *Physics of Fluids*, vol. 11, no. 7, pp. 1699–1701, Jul. 1999.
- [126] C. Mehl, J. Idier, and B. Fiorina, "Evaluation of deconvolution modelling applied to numerical combustion," *Combustion Theory and Modelling*, vol. 22, no. 1, pp. 38–70, Aug. 2017.
- [127] R. Darragh, C. A. Z. Towery, M. A. Meehan, and P. E. Hamlington, "Lagrangian analysis of enstrophy dynamics in a highly turbulent premixed flame," *Physics of Fluids*, vol. 33, no. 5, p. 055 120, May 2021.
- [128] R. Darragh, C. A. Towery, A. Y. Poludnenko, and P. E. Hamlington, "Particle pair dispersion and eddy diffusivity in a high-speed premixed flame," *Proceedings of the Combustion Institute*, vol. 38, no. 2, pp. 2845–2852, 2021.
- [129] G. Elsinga and J. Westerweel, "The point-spread-function and the spatial resolution of PIV cross-correlation methods," in *9th International Symposium On Particle Image Velocimetry – PIV'*, Tsukuba, Japan, Jul. 2011.
- [130] S. Stolz, N. A. Adams, and L. Kleiser, "The approximate deconvolution model for large-eddy simulation of compressible flows and its application to shock-turbulent-boundary-layer interaction," *Physics of Fluids*, vol. 13, no. 10, pp. 2985–3001, Sep. 2001.
- [131] J. Westerweel, "Digital particle image velocimetry: theory and application," Ph.D. dissertation, Delft University of Technology, Delft, Jun. 1993.
- [132] P. O'Neill, D. Nicolaides, D. Honnery, and J. Soria, "Autocorrelation functions and the determination of integral length with reference to experimental and numerical data," in *15th Australasian Fluid Mechanics Conference*, Sydney, Dec. 2004.
- [133] A. Kazbekov and A. Steinberg, "Physical space analysis of cross-scale turbulent kinetic energy transfer in premixed swirl flames," *Combustion and Flame*, vol. 229, 2021.